Trinity College Dublin
Coláiste na Tríonóide, Baile Átha Cliath
The University of Dublin

# Vertical Upflow Convective Boiling: Flow Regimes, Heat Transfer and EHD Augmentation


Munir Eraghubi

BSc, M Eng

Department of Mechanical and Manufacturing Engineering

Parson Building

Trinity College

Dublin 2

Ireland


A thesis submitted to the University of Dublin in partial fulfilment of the requirements for the degree of Ph. D

May 2018

# Declaration

I declare that I am the author of this thesis and that all work described herein is my own unless otherwise referenced. Furthermore, this work has not been submitted, in whole or part, to any other university or college for any degree or qualification.

I authorize the library of Trinity College Dublin to lend or copy this thesis.

Munir Eraghubi,

April 2018

# Summary

This work is to investigate the effect of electrohydrodynamic force on two-phase flow of HFE7000 refrigerant under convection boiling conditions. The experiment apparatus designed to facilitate the visualization of two-phase flow under EHD field. The test section made of sapphire tube, which allows for optical access to the flow, allows also for heat transfer. A transparent conductive layer of Indium Tin Oxide deposited on the outside surface of the sapphire tube, this (ITO) conductive layer works as sores of heat when connected to an electric power supply. A stainless steel rod runs concentrically along the inside of the sapphire tube and used as the high voltage electrode. The (ITO) layer connected to electrical ground to facilitate EHD force.

The present work is to contribute to the understanding of low quality vertical upflow convective boiling. To this end, measurements are analysed and boiling heat transfer is investigated in the context of boiling curves. Specifically, the influence of mass and heat flux on vertical upward flow are investigated, the results discussed in terms of the observed flow regimes. Finally the heat transfer coefficient results are compared with several existing correlations.

The forced convective boiling experiments with HFE-7000 were conducted for upward flow in a vertical tube at 1.2 bars, inlet subcooling of 2°C and mass flux ranging between 50 and 300 kg/($m^2$ s).

Initial tests were performed by fixing the flow rate and progressively increasing the heat flux prior to reaching the critical heat flux. A second set of identical tests were performed with a 3 mm diameter stainless steel rod positioned concentrically inside the tube to test the influence of moderate confinement.

However, once fully developed boiling conditions are achieved, the heat transfer is generally insensitive to the flow rate and moderate confinement. Seven well-established forced boiling heat transfer correlations have been applied to predict the heat transfer coefficient and the accuracy of these are discussed.

Flow regimes for various mass and heat fluxes have been visualized at the central region of the heated section using high speed videography. Three main flow patterns have been observed under different mass and heat fluxes: bubbly flow, bubbly-slug flow and churn flow. The measured boiling conditions were plotted on seven existing vertical flow pattern maps and the agreement discussed.

In the final phase of this study, EHD augmentation of the flow and heat transfer for vertical upflow convective boiling was investigated. To the best of knowledge, this is the first study of vertical upflow boiling with EHD augmentation that included local heat transfer measurements with detailed visualization of the flow regimes and phase interactions. The EHD enhancement of heat transfer measured during increasing heat flux, applied electric field strength and AC frequency.

# Acknowledgements

Firstly I want express my deep thanks and admiration to my supervisor Dr. Tony Robinson for all his guidance, patience, enthusiasm, understanding, and endless ideas. I have personal benefited from his knowledge of heat transfer in countless occasions. His ability to define the problems and finding the alternative solutions was amazing. Working with him has been rewarding and a privilege.

I would like to thank Gerry Byrne in the Thermo lab for all his assistance with my modification of the test rig and his problem solving ability. Thanks are due to Mick Reilly, Paul Normoyle, and Workshop staff for their high quality work and Gorgen for his help in Rig design.

I wish also to thank other department staff for their advice help and their contributions in various way including Dr. Tim Persoon, Dr. Seamus O'Shaughnessy, Dr. Tom Lupton, Dr. Nicolas Baudin and Dr. Sajad Alimohammadi.

Finally I want to thank my wife Zainab for her continual encouragement and support during these four years of been away from her family and friends. And most of all I have to thank my parents Mohammed and Salma for their support and patience.

# Table of Contents

# List of Figures

# List of Tables

# Nomenclature

**Latin Symbols**

| Symbols | Name | Units |
|---|---|---|
| A | area | $m^2$ |
| Bi | Biot number | - |
| Bo | Boiling number | - |
| $C_p$ | specific heat | J/(kg K) |
| Co | Convection number | - |
| d | test section diameter | m |
| $D_h$ | hydraulic diameter | m |
| f | friction factor | - |
| F | Convective enhancement factor | - |
| Fr | Froude number | - |
| E | Electric field strength | V/m |
| G | mass flux | kg/($m^2$ s) |
| g | Gravity and Acceleration | $m/s^2$ |
| $h_{fg}$ | latent heat | J/ kg |
| I | current | A |
| J | superficial velocity | m/s |
| k | thermal conductivity | W/(m K) |
| K | parameter in Taitel and Duckler map | - |
| h | heat transfer coefficient | W/($m^2$ K) |
| $\dot{m}$ | mass flow rate | kg/s |
| $M_d$ | Masuda number | - |
| Nu | Nusselt number | - |
| P | pressure | Pa |
| $R_e$ | Reynolds number | - |
| q” | heat flux | $W/m^2$ |
| $q_L$ | natural convection losses | $W/m^2$ |
| S | Suppression factor | - |
| S | slip ratio | - |

| | | |
|---|---|---|
| T | Temperature | °C |
| T | parameter in Taitel and Duckler map | - |
| V | voltage | V |
| u_ | Phase velocity | m/s |
| x | quality (dryness fraction) | - |
| $X_{tt}$ | Lockart-Martinelli parameter | - |

**Greek symbols**

| | | |
|---|---|---|
| α | void fraction | - |
| ε_ | Dielectric permittivity | F/m |
| $\lambda$ | gas-phase parameter, Baker flow map | - |
| μ | dynamic viscosity | kg/m.s |
| ρ | density | $kg/m^3$ |
| σ | surface tension, | N/m |
| ν | kinematic viscosity | $m^2/s$- |
| $\psi$ | liquid-phase parameter, Baker flow map | - |
| $\boldsymbol{\phi_l^2}$ | Friction Multipliers | - |

**Subscripts Subscipts**

| | |
|---|---|
| Cb | convection boiling |
| G | gas |
| i | inner |
| l | liquid |
| nb | nucleate boiling |
| o | outer |
| sat | saturation |
| sup | superheat temperature |
| tp | two phase |
| v | vapour |
| wall | wall |

# Chapter 1. Introduction

## 1.1 Flow Forced Convective Boiling

Flow boiling is a very effective technique for removing large amounts of heat at a targeted temperatures for a given mass flow rate of coolant due to the large latent heat of vaporization, the high heat transfer coefficients and relatively small inlet-to-outlet temperature differences compared to the single-phase flow [1]. Due to these and other reasons, forced boiling systems are broadly used in various industrial applications and very common in everyday life, including central heating, air conditioning, thermal power plants, nuclear reactors, water-cooled gas turbines, internal combustion engines, X-ray sources [2] [3], to name a few.

Flow boiling heat transfer is also used in space platforms and satellites design [4], where very efficient, compact and lightweight devices are required [5] [6]. Heat pipes, for example are used to transport heat from inside to outside the spacecrafts and satellites, and do not require gravity to operate. Figure 1-1 shows an experimental heat pipe payload onboard MIOSat.

As the physical sizes of electrical and electronic systems used in computers, cell phones, biomedical and defence applications decrease, the heat generated per unit volume increases significantly. Here, boiling can be a very effective heat transfer mechanism, which can maintain the temperature of electronics devices at safe temperatures using compact heat sinks [2] [7] [8] (see Figure 1-2 and Figure 1-3).

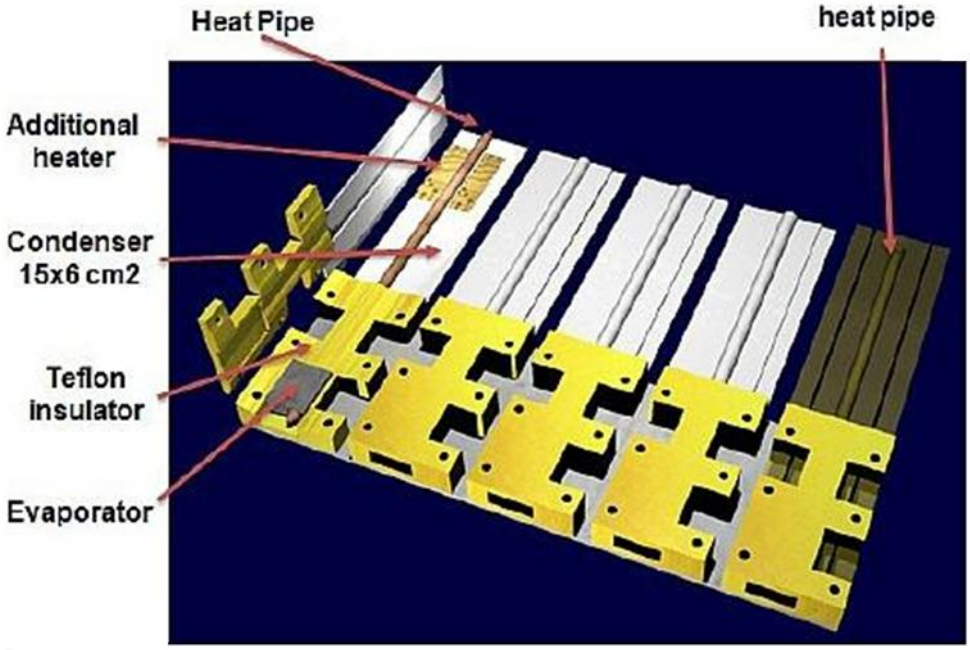


Figure 1-1. View of the experimental heat pipe payload onboard MIOSat [9]

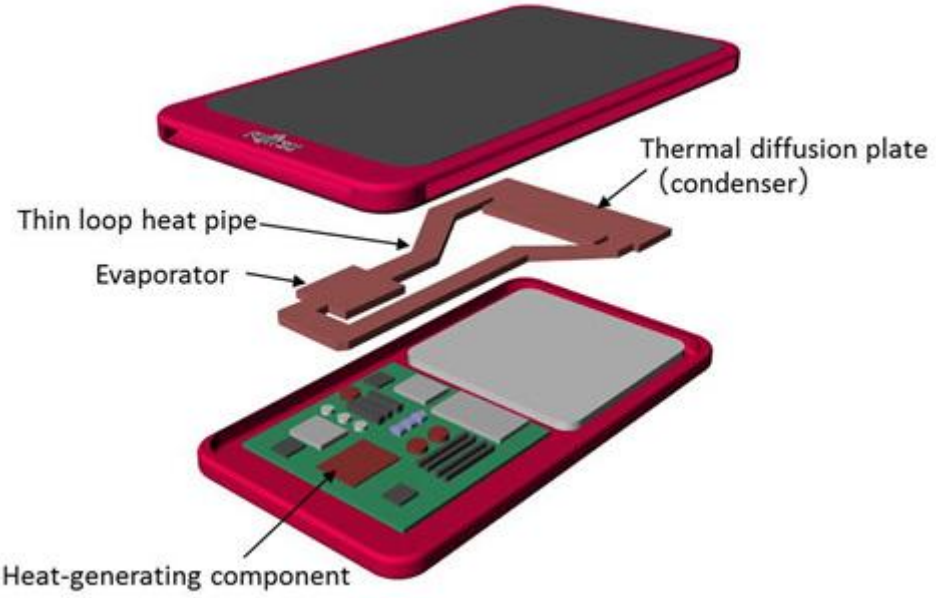


Figure 1-2. New thermal management concept for a smartphone equipped with a loop heat pipe [10]

Figure 1-3. Heat pipes built on P35 Express motherboards [11]

Flow boiling describes the boiling of flowing liquids along superheated surfaces whereby there is sufficient heat transfer to the fluid to cause vaporization. Generally, heat is transferred in flow boiling by either vaporization or nucleate boiling. For the later, formation, growth and detachment of discrete vapour bubbles on the superheated surface defines nucleate boiling-based flow boiling regimes. Conduction and convection through a liquid film in contact with the superheated surface with subsequent vaporization at the two-phase interface defines vaporization-based convective boiling regimes [12].

At low vapour qualities, the heat transfer coefficient depends strongly on the heat flux and the corresponding flow patterns are the bubbly and slug flows. In the bubbly flow regime, the repeated bubble formation and departure from the heated wall increases the flow mixing which enhances the heat transfer. Increased heat flux corresponds with increased vapour production whereby bubble coalescence increases to the point that vapour slugs form within the channel and the heat transfer can be a mix of nucleate boiling and conduction-convection-vaporization across a liquid film between the wall and the slug. Further increase in heat flux and vapour production causes instabilities that inhibit slug formation and instigate a churn flow regime where the heat transfer is characterizes by nucleate boiling and the chaotic tossing, stirring and mixing of the two phases [13].

In the high quality regions, forced convection is the main heat transfer mechanism with nucleate boiling being usually suppressed at qualities higher than 0.2. In this region the corresponding flow pattern is annular flow, where the heat is transferred by the conduction and convection modes across the liquid film while the evaporation takes place at the interface between the liquid and the vapour. The heat transfer coefficient is less dependent on the heat flux and tends to increase with the increase in mass velocity and vapour quality [14].

## 1.2 **Electrohydrodynamics**

Electrohydrodynamics (EHD) involves the application of intense electric fields to fluids. In two phase flow, electrostatic body forces can be large enough to change the flow regimes in such way to enhance the heat transfer. This allows for the opportunity for making heat exchangers more effective and compact as well as intelligent.

This project will study the two-phase flow behaviour in tubular heat exchangers with the aim of understanding the influence of Electrohydrodynamics on local heat transfer coefficient.

Electrohydrodynamics (EHD) is the branch of thermal fluid science that deals with the interaction of high-voltage electric fields with fluids. This interaction induces electric body forces within the fluid, which can affect the two-phase flow, and therefore heat transfer and pressure drop [15] [16].

Heat transfer enhancement improves the performance of the heat exchanger and at the same time enables a considerable decrease in size, weight, volume, material and costs.

The field of EHD heat transfer enhancement has been continuously studied over the past 70 years. The earlier work was more concentrated on the enhancement of single-phase flow. In the last 30 years, many studies and researchers have shown a greater potential of EHD in enhancing two-phase heat transfer. [17]

EHD can be considered a very useful engineering technique for heat transfer enhancement since it is a non-mechanical, simple and offers an effective means of control of both the heat transfer and pressure drop. One of the major advantages of

EHD is that the heat transfer may be enhanced without a significant increase in pressure drop [16][18]. As such, EHD may allow for the production of highly compact and low cost heat exchangers with the possibility of solid state control.

A wide range of applications for EHD are reported in the literature e.g. pumping, single phase heat transfer, boiling, condensation, mixing, and liquid jets, (see Figure 1-4 and Figure 1-5) [19] [20] [21].


Figure 1-4. The mission patch for the planned test of the EHD pump aboard the International Space Station.(Source: WPI) [20]

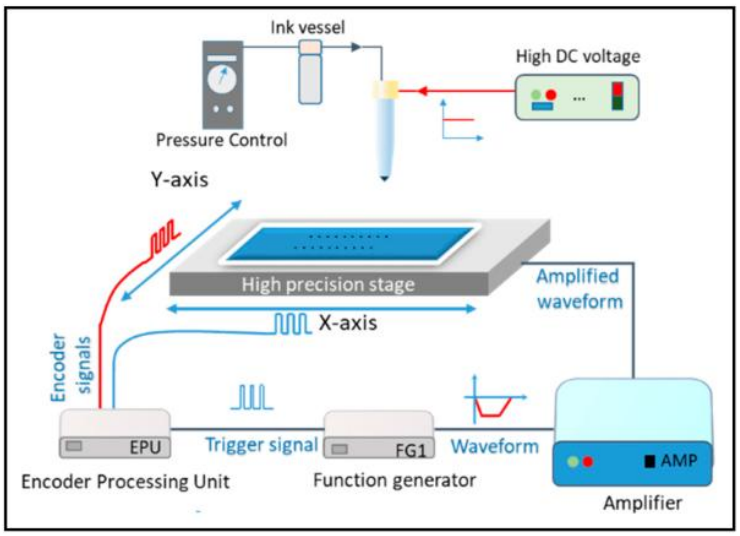


Figure 1-5. Schematics of the EHD printing systems with position synchronization [21]

The typical value of the current required to enhance the heat transfer associated with EHD is very low, resulting in very small power consumption comparing with other traditional technologies. This makes EHD an ideal method for heat transfer augmentation in microgravity [22].

## 1.3 **Scope and Objective**

The overarching objective of this research is to investigate vertical upflow boiling both with and without the effect of EHD. Specifically, a test facility will be constructed to allow the simultaneous observation of the vertical two phase flow and the measurement of the local heat transfer coefficient. Thus, the first sub-objective of this work is to study the flow regimes of vertical upflow boiling for varying heat and mass flux conditions. The results will be compared with existing flow regime maps which were developed for isothermal air-water systems or those developed in adiabatic viewing sections. In a similar way, the second sub-objective will involve the measurement of the heat transfer coefficient for vertical upflow boiling with the unique capacity to observe the flow regime where the measurements will be taken. Thus, the heat transfer will be related to changes in the flow boiling conditions for different heat and mass flux levels. Finally, the influence of EHD on the flow and heat transfer will be investigated. This will focus on the lower quality bubbly flow regime and the influence of high voltage magnitude and frequency on the two phase flow and heat transfer will be studied. Once again, the transparent yet diabatic test section will allow any changes in the heat transfer to be related to the flow dynamics.

.

# Chapter 2. Two Phase Flow

Multiphase flow is the simultaneous flow of two or more phases separated from each other by distinct interfaces. One common case of multiphase flow is two-phase flow, where at least one of the phases is a liquid, and the other is vapour or gas [23]

Two-phase flow has been applied to many fields because of its higher energy efficiency in comparison with single-phase flow, because of lower pumping power and higher heat transfer coefficients. Practical examples of gas-liquid flows take place in several applications such as: the flow of oil and gas in oil pipelines, the flow of steam and water in power plants and in steam-heating pipes and the flow of liquid and vapour refrigerants in the condensers and evaporators of refrigeration and air conditioning equipment.

In this work, the focus is on two-phase flows in which a liquid and vapour flow together in a straight tube, which is a very common scenario in heat transfer applications.

## 2.1 Basic definitions and terminology

This section defines the important parameters that are used to characterize the heat and mass transfer of two phase flows and is included here as they will be used throughout the manuscript.

The total mass flow rate ($\dot{m}$) is the sum of the mass flow rate of liquid phase ($\dot{m}_l$) and the vapour phase ($\dot{m}_v$ ):

$$\dot{m} = \dot{m}_l + \dot{m}_v \quad (1)$$

The total mass flux of the flow (G) is defined the total mass flow rate ($\dot{m}$) divided by the cross-sectional area of the flow (A),

$$G = \frac{\dot{m}}{A} \tag{2}$$

The quality (dryness fraction), x, is defined as the ratio of the mass flow rate of vapour phase ($\dot{m}_v$) to the total mass flow rate ($\dot{m}$),

$$x = \frac{\dot{m}_v}{\dot{m}} \tag{3}$$

The void fraction ($\alpha$) is defined here as the ratio of the cross-sectional area occupied by the vapour phase ($A_v$) to the total cross-sectional area (A) of the flow.

$$\alpha = \frac{A_v}{A} = 1 - \frac{A_l}{A} \tag{4}$$

The phase velocity is the volume flux divided by the cross-sectional area occupied by the phase.

$$u_v = \frac{\dot{V}_v}{A_v} = \frac{\dot{V}_v}{\alpha A} = \frac{\dot{m}_v}{\rho_v A_v} \tag{5}$$

$$u_l = \frac{\dot{V}_l}{A_l} = \frac{\dot{V}_l}{(1-\alpha)A} = \frac{\dot{m}_l}{\rho_l A_l} \tag{6}$$

The slip ratio is defined as the ratio of the vapour and liquid phase velocities,

$$S = \frac{V_v}{V_l} \tag{7}$$

$$S = \frac{x}{1-x}\frac{1-\alpha}{\alpha}\frac{\rho_l}{\rho_v} \tag{8}$$

The superficial liquid and vapour flux are defined as their velocities if they were to flow alone along the cross-section area of the tube.

$$j_l = \frac{G(1-x)}{\rho_l} \tag{9}$$

$$j_v = \frac{Gx}{\rho_v} \tag{10}$$

The Reynolds number for vapour and liquid are thus defined as:

$$Re_v = \frac{GD_h}{\mu_v}\frac{x}{\alpha} \tag{11}$$

$$Re_l = \frac{GD_h}{\mu_l}\frac{1-x}{1-\alpha} \tag{12}$$

The Froude number (Fr) represents the ratio of inertial forces to gravitational forces and is defined as:

$$Fr = \frac{u^2}{g\ D_h} \tag{13}$$

The Froude gas number for the vapour phase is defined as:

$$\mathrm{Fr_v} = \frac{\mathrm{x\ G}}{[\rho_\mathrm{v}(\rho_\mathrm{l} - \rho_\mathrm{v})\ g\ D_h]^{0.5}} \tag{14}$$

For the liquid phase, the Froude number can be expressed as:

$$Fr_l = \frac{G^2}{\rho_l^2 g\ D_h} \tag{15}$$

The Martinelli parameter, X, is a ratio of pressure drops of the single-phase flow terms and is defined as:

$$X = \left[\frac{(dp/dz)_l}{(dp/dz)_v}\right]^{1/2} \tag{16}$$

The Nusselt number (Nu) can be viewed as the dimensionless heat transfer coefficient. It represents the ratio of convective to conductive heat transfer across the boundary. It is defined as:

$$Nu = \frac{hD_h}{k} \tag{17}$$

The Masuda number ($M_d$), or dielectric Rayleigh number is defined as:

$$M_d = \frac{\varepsilon_\circ E_\circ^2 T_\circ (\partial \varepsilon_s / \partial T)_\rho L^2}{2\rho_\circ v^2} \tag{18}$$

Where $\varepsilon_\circ$ is the fluid permittivity, E is the electric field strength, $\rho$ is the fluid density and T is the fluid temperature, $\varepsilon_s$ dielectric constant.

It represents the relative strength of the electric field to that of viscosity and sometimes referred to as the Electric Rayleigh number.

### 2.1.1 Confinement number

The heat transfer and flow characteristics can be different over the ranges of millimeter to sub-millimeter size, and over the years, there has been much debate about what identifies a channel size as conventional or miniature. Mehedale et al. [24] and Kandlikar et al. [25] distinguish micro-channels from macro-channels based on the characteristics of channel size. Mehendale et al. [24] used the term meso-scale which is in between the micro and macro-scales whereas Kandlikar et al. [25] used the term mini-channel for a larger range, see Table 2-1

Table 2-1. Macro to micro-channel transition limits

| Channel | Mehendale et al. [24] | Kandlikar et al. [25] |
|---|---|---|
| | D | D |
| Micro-Channel | 1-100 μm | 10-200 μm |
| Meso-Channel | 100-1000 μm | |
| Mini-Channel | | 200 μm-3 mm |
| Macro-Channel | 1-6 mm | |
| Conventional Channel | > 6 mm | > 3 mm |

The Confinement Number, $C_o$, has been used for analysing the heat transfer associated with small channels, which helps enable the determination of the critical

size of the channel that defines the shift from isolated bubble regime to confined bubble regime and subsequently from large tubes to micro-channels based on physical criterion [26]. The Confinement Number was defined by Cornwell and Kew [23] in terms of the capillary number and the channel hydraulic diameter such that,

$$C_0 = \frac{\{\sigma/[g(\rho_l - \rho_g)]\}^{1/2}}{D_h} \tag{19}$$

Many studies of flow and heat transfer under a variety of conditions suggests that a broad general rule is that for $C_o > 0.5$, confined bubble flow occurs and the effects of confinement will be significant [27]. Ong and Thome [28] described a transition region between micro and macro scale flow behaviour, referred to as meso-scale, using $C_o$. It was found that this transition regime was present for $0.3 < C_o < 0.4$. Conventional unconfined channel flow is expected for $C_o < 0.3$.

In the case considered here, for the flow regime and heat transfer coefficient tests, the flow is in an 8 mm circular tube, which is classified as conventional macro-scale flow. For the EHD test where an electrode was inserted inside the tube, $D_h$ found 2.5 mm, which considered as a meso-scale channel.

## 2.2 **Flow Patterns and Flow Regimes**

Many types of liquid and vapour phase distributions can occur when two phase mixtures flow in a channel. This is commonly referred to as flow patterns or flow regimes. The type of flow pattern depends on the size and orientation of the flow channel, the difference between the vapour and liquid flow parameters, the gravitational forces acting on the flow, and the fluid properties.[29]

Many experiments have been carried out since the 1940's to visualize and record the various configurations in which gas and liquid may flow together [30], and the liquid-vapour distributions were classified by the observers into separate flow-regimes.

The flow regimes in vertical and inclined tubes are considerably different from those in horizontal tubes. The focus in this work is exclusively for the two phase flow regimes in horizontal and vertical tubes only.

### 2.2.1 Two-phase flow patterns in horizontal tubes

Since gravity acts perpendicularly to the flow direction in horizontal flow, the two-phase flow patterns are usually not axisymmetric and more complex than vertical two-phase flow[31]. Five distinct flow regimes were recognized in horizontal tubes by Bergelin and Gazley [30] in 1949. Five years later Baker [30] classified two additional flow regimes for horizontal flow. A list of the most typical flow regimes reported in the literature for condensing horizontal flow illustrated in Figure 2-1, collected by Dobson [32]. Although this classification is rather subjective, certain typical patterns have been observed by most researchers [30].

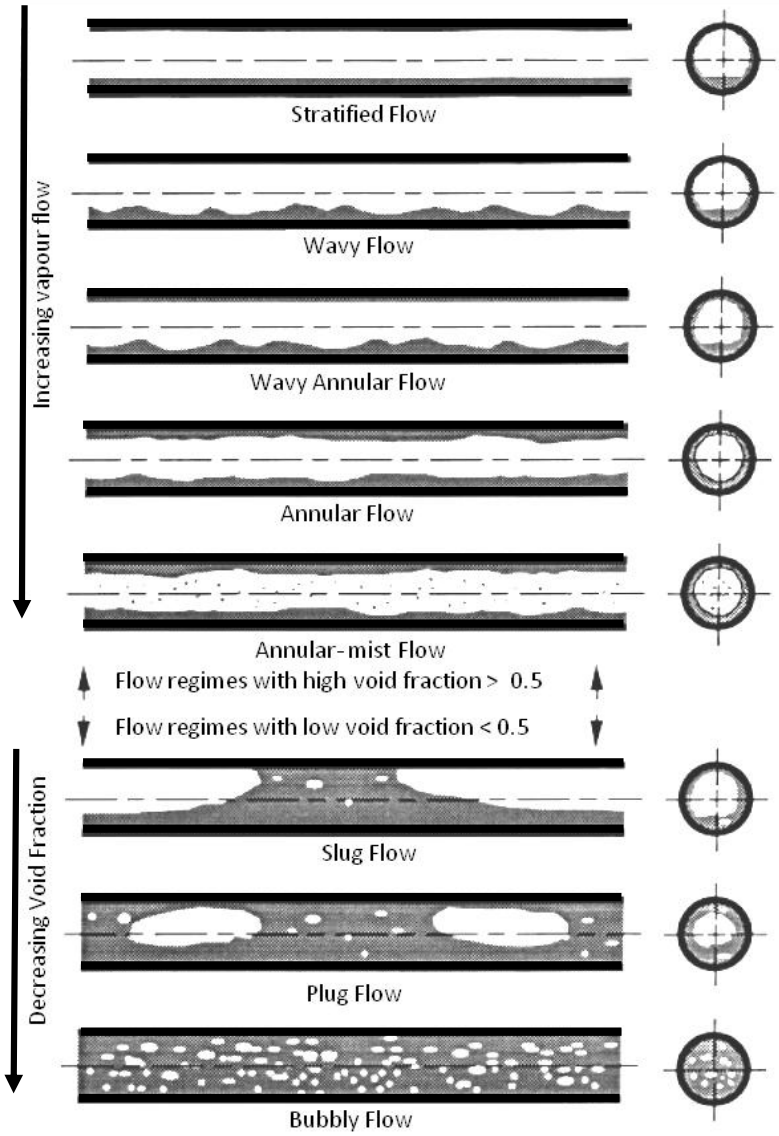


Figure 2-1. Flow regimes in horizontal, condensing two-phase flow [30]

From Figure 2-1 the flow regimes can be divided into two broad groups: in the top five regimes, the vapour flows as a continuous stream, in the bottom three types the vapour fragments are separated from each other by liquid. The flow regime is significantly influenced by the void fraction and the vapour flow rate. Generally, the vapour flow as a continuous stream if the void fractions is greater than 0.5.

At low vapour flow rate and high void fraction, the liquid flow becomes smooth and stratified. When the vapour flow rate is increased and moves much faster than the liquid, the shear causes agitation of the liquid-vapour interface, and the waves start to appear on the liquid-vapour interface.

As the vapour flow rate is increased further, the liquid starts to climb the side tube wall. When the tube wall is wetted completely by liquid, the flow pattern is described as annular flow, where a liquid layer flows along the wall and vapour flows in the core. Annular-mist flow takes place when a high vapour flow rates causes agitation of liquid at the interface, and this liquid becomes entrained in the vapour flow in the form of fine droplets.

In case of low void fraction, the vapour may cause rising columns of liquid to reach the top of the tube and break the continuity of vapour stream. These liquid columns are called a "slugs" and a flow of this pattern is called slug flow. Plug flow can be realized at lower void fractions, when the vapour becomes completely enclosed in the liquid in a form of elongated bubbles. Further lowering the void fraction results in smaller vapour bubbles travelling with the liquid stream, called bubbly flow [30].

### 2.2.2 Two-phase flow patterns in vertical tubes

When the flow is oriented upward in a vertical tube, gravity acts parallel to the flow resulting in notable differences in the two phase flow structures compared with the horizontal configuration. These are depicted in Figure 2-2 and are described as follow:

**Bubbly flow:** Small bubbles are dispersed as distinct substances in the liquid continuum flow. Distinctive features of this flow are moving and deformable of shapes but they are typically spherical and much smaller than the tube diameter, as shown in Figure 2-2.

**Slug Flow:** With the increase of the gas flow, the number of bubbles increases and become closer. At higher void fraction, the bubbles start to coalesce and form larger bubbles, taking the shape of a bullet, with a radial size of the tube diameter and a length up to two times the tube diameter. These large bubbles are commonly called Taylor bubbles and are separated from the wall by a thin film of liquid which may flow downward. They are separated from each other with a plug of liquid which may contain small bubbles.

**Churn Flow:** Churn flow is one of the least understood of gas-liquid flow regimes, and it appears only in vertical and near-vertical channels when there is a large gas fraction with a high velocity and small liquid fraction with low velocity. The flow regime is highly disturbed flow of gas and liquid and is distinguished by the presence of a very thick and unstable liquid film with the liquid often oscillating up and down. It is usually bounded by the slug and the annular flow regimes. Recent evidence suggests that Slug Flow is destabilized when the liquid film surrounding a Taylor bubble is flooded by the gas flowing upwards [33].

**Annular Flow:** With a higher gas velocity and a void fraction above 75-80%, the interfacial shear becomes dominant over gravity and the liquid is expelled from the centre of the tube and flows as a thin film on the channel wall, while the gas flows in the core of the tube. Annular flow can be pure or dispersed flow depending on the fraction of entrained small liquid droplets contained in the core gas flow.[34]

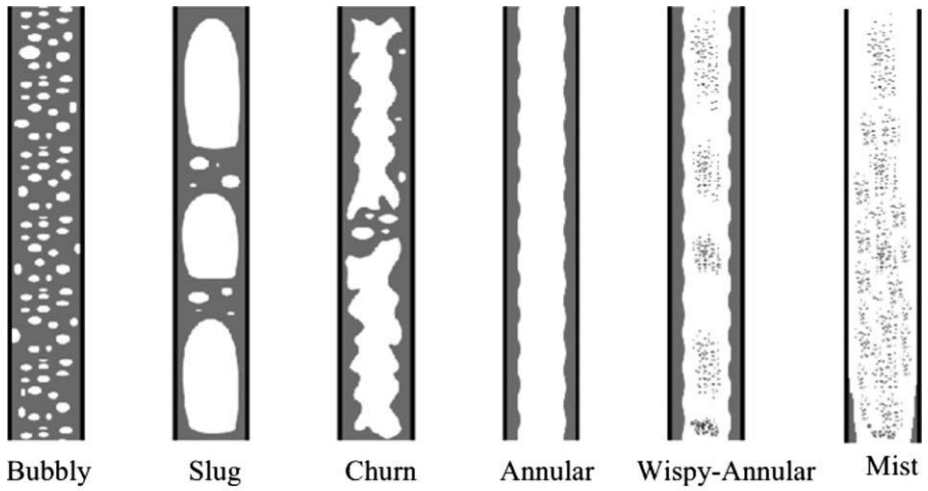


Figure 2-2. Schematic of flow patterns in vertical upward gas liquid flow [35]

**Wispy-Annular:** At relatively higher gas flow rates, the entrained droplet may form a coherent structure as clouds or wisps of fluid. This flow pattern was first identified by Bennett et al. [36], but not observed in many studies. [37]

**Mist flow:** At even higher gas flow rates, all the liquid is sheared from the wall and entrained as droplet in the core gas. The film thinned and becomes unstable and destroyed.

## 2.3 **Flow Regime Maps**

The observations of the flow regimes are usually plotted on a graph, the axes representing the flow rates of each phase flow, though in some instances the total mass flux of the two phases is represented on one axis and the other axis representing the mass fraction of the flow or vapour quality. Lines are incorporated between the various flow regimes on the graphs to represent the boundaries between each flow pattern to produce a "flow regime map".

In 1954, Baker correlated the flow regime to the volume flow rates of the vapour and the liquid and proposed one of the first flow regime maps as depicted in Figure 2-3.

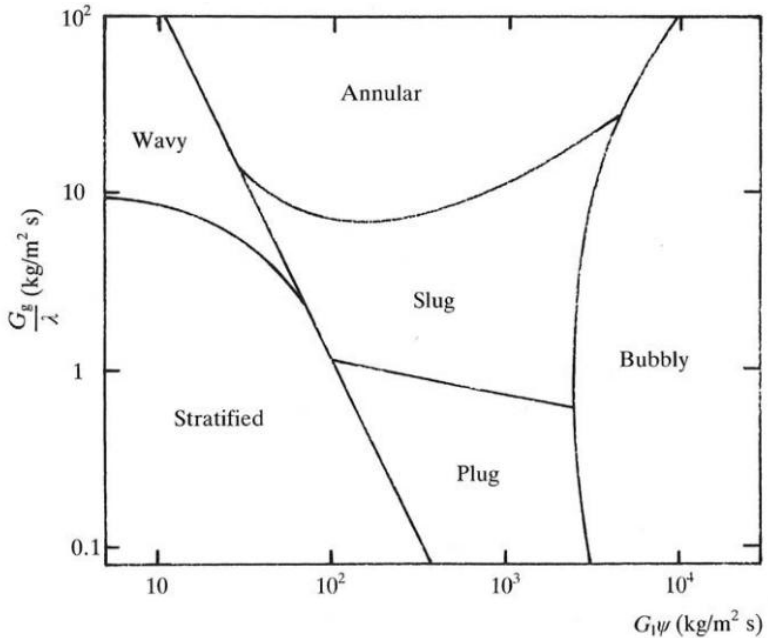


Figure 2-3. Baker flow map for horizontal tube [30]

The axes are defined in terms of $G_g/\lambda$ and $G_l\psi$, where the gas-phase parameter $\lambda$ is defined as:

$$\lambda = \left[\frac{\rho_g}{\rho_{air}}\frac{\rho_l}{\rho_{water}}\right]^{\frac{1}{2}} \tag{20}$$

The liquid-phase parameter $\psi$ is defined as:

$$\psi = \frac{\rho_{water}}{\rho}\left[\frac{\mu_l}{\mu_{water}}\left(\frac{\rho_{water}}{\rho_l}\right)^2\right]^{\frac{1}{3}} \tag{21}$$

Based on several studies and observations, Mandhane *et al.* [38] proposed the flow regime map shown in Figure 2-4. The flow pattern map coordinates are determined by the superficial liquid and vapour flux ($j_l$, $j_v$) (see Equations (9), (10)). The superficial velocity of the vapour $j_v$ represents the horizontal coordinate, the superficial velocity of the liquid $j_l$ represents the vertical coordinate. Figure 2-4 shows that at higher liquid flow rates, the flow has either slugs or bubbles and increasing the vapour superficial velocity results in an annular flow regime.

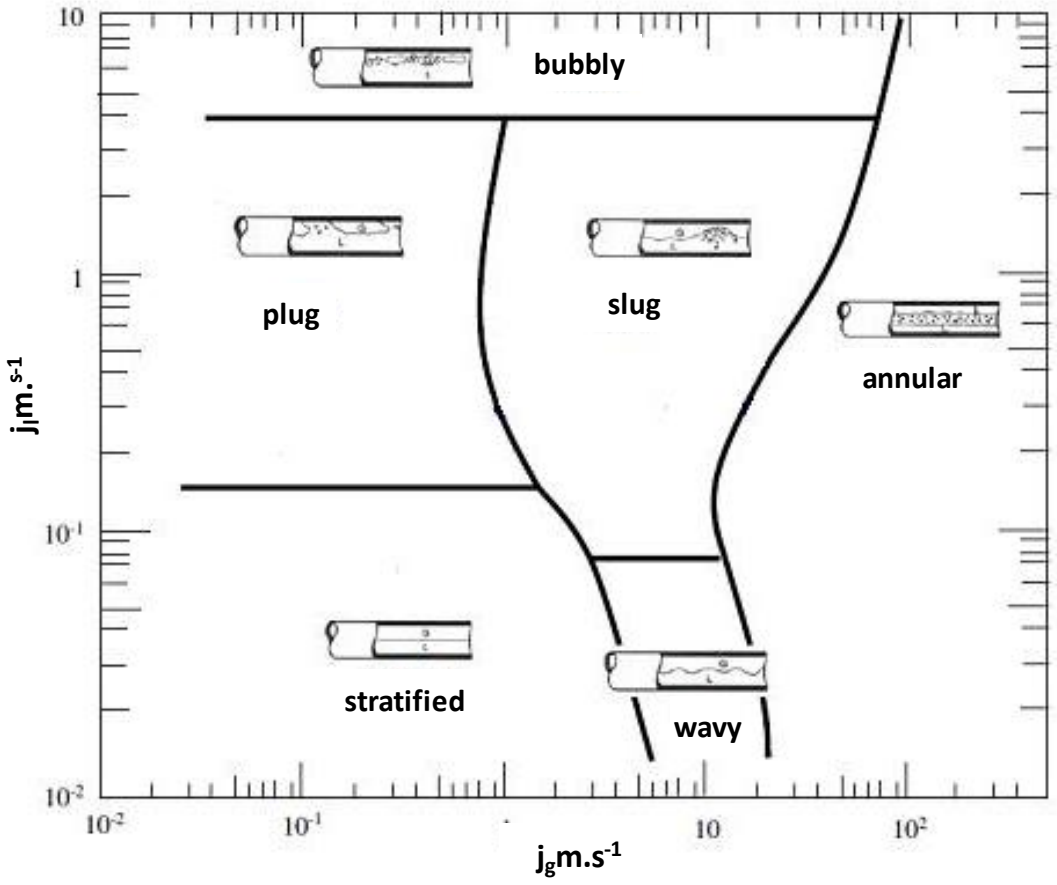


Figure 2-4. Flow pattern map for gas-liquid in horizontal pipes [38]

In practical applications a more general flow regime map is usually needed. These means that more data from a variety of fluids and a wider range of tube diameters must be included in the map. For this purpose, reasonable dimensionless groups have to be selected to represent these varying parameters.

Taitel and Duckler [39] suggest that in order to find appropriate dimensionless groups for the coordinates on flow regime maps, the mechanisms that lead to the flow regimes must be understood. They proposed four dimensionless groups to describe the flow regimes; the Martinelli parameter $X_{tt}$, the gas Froude number $Fr_G$, and new parameters K and T. Using these parameter they developed a three-part map shown in Figure 2-5, with parameter $Fr_G$ and X defined in Equations (14) and (22) respectively.

$$X_{tt} = \left(\frac{1-X}{X}\right)^{0.9} \left(\frac{\rho_v}{\rho_f}\right)^{0.5} \left(\frac{\mu_f}{\mu_v}\right)^{0.1} \tag{22}$$

Taitel and Duckler defined the K parameter as:

$$K = Fr_g Re_l^{0.5} \tag{23}$$

They also defined the parameter T as:

$$\mathrm{T} = \left[\frac{|(\mathrm{dp/dz})_\mathrm{l}|}{\left[\mathrm{g}(\rho_l - \rho_g)\right]^{0.5}}\right]^{0.5} \tag{24}$$

The pressure gradient $(\mathrm{dp/dz})_\mathrm{l}$ in equation (24) for the liquid phase is given by:

$$(\mathrm{dp/dz})_\mathrm{l} = -\frac{2 f_k \dot{m}_k^2}{\rho_k d_i} \tag{25}$$

The friction factor $f_k$ in the above equation depends on the flow Reynolds number. If Re <2000, the laminar flow calculation is used:

$$f_k = \frac{16}{Re_k} \tag{26}$$

If Re > 2000, the friction factor is calculated by the turbulent correlation,

$$f_k = \frac{0.079}{Re_k^{0.25}} \tag{27}$$

To determine the type of the flow using the Taitel and Duckler [39] map, first the X and $Fr_G$ are calculated and plotted on the top graph. If the coordinates (X, $Fr_G$) fall in annular flow area, then the type of flow is annular. If the coordinates (X, $Fr_G$) fall in the lower left area, then K is calculated and the flow regime is identified using the middle graph. If the coordinates (X, $Fr_G$) fall in the lower right area, then T is calculated and the flow regime identified using the bottom graph.

Though the Taitel and Duckler flow pattern maps were developed for adiabatic two-phase flows, they are often used with diabatic processes of evaporation or condensation.

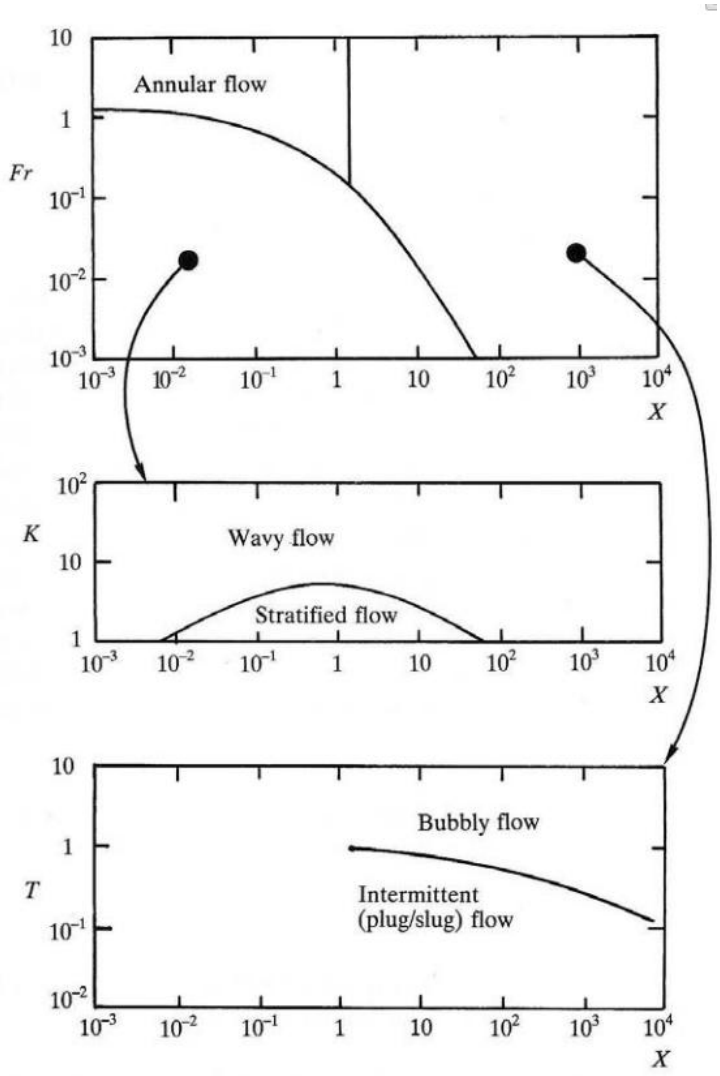


Figure 2-5. Taitel and Duckler [39] Two phase flow Pattern map for horizontal tube

### 2.3.1 Flow Pattern Map for Evaporation in Horizontal Tubes

#### 2.3.1.1 Kattan-Thome-Favrat [40] flow pattern map

For normal diameter tubes for both adiabatic and evaporating flows, Kattan, Thome and Favrat [40] proposed a modification of the Steiner [41] map. This flow pattern map includes the influences of heat flux and dryout on the flow pattern transition boundaries. The transition boundaries are a linear graph with mass velocity plotted versus gas or vapour fraction, which is more convenient to use compared to the log-log format of other maps (see Figure 2-6).

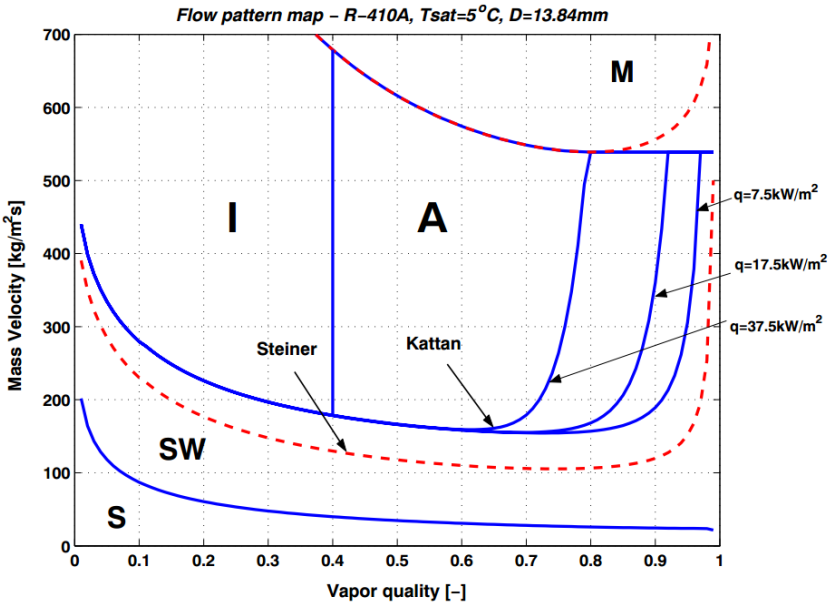


Figure 2-6. Kattan et al. [40], 23] flow pattern map (S : stratified, SW : stratified-Wavy, I : intermittent, A : annular, M : mist flow)

#### 2.3.1.2 Thome-El Hajal [43].

A more straightforward version of the Kattan, et al. [40] map was proposed by Thome and El Hajal [43] non-dimensional empirical exponents were added to include the effect of heat flux on the onset of dryout of the annular film (see Figure 2-7).

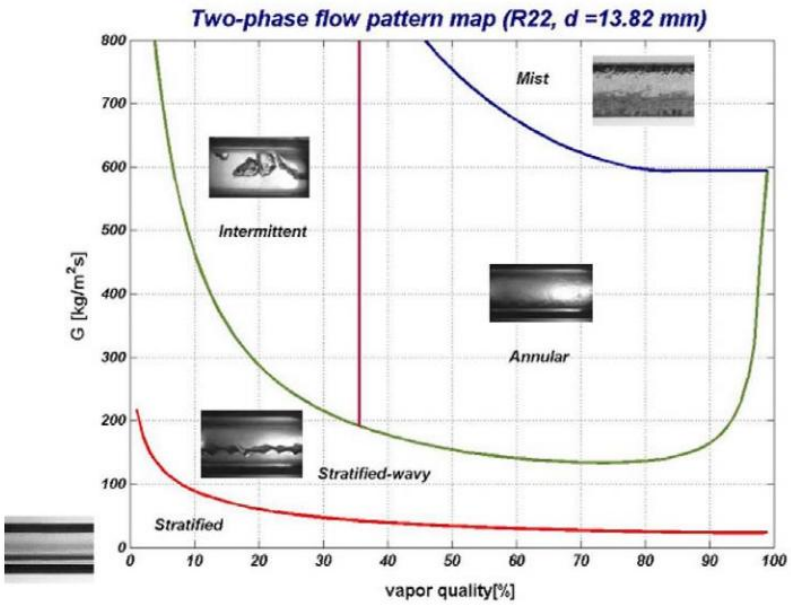


Figure 2-7. Thome-El Hajal [43] flow pattern map for refrigerant R-22

#### 2.3.1.3 Wojtan-Ursenbacher-Thome flow pattern map

Wojtan-Ursenbacher-Thome [44] developed a more recent version of the Kattan et al [40] flow map, based on dynamic void fraction measurement and their observation for mass fluxes between 70-200 kg/($m^2$ s) in a horizontal tube. The map includes the effect of heat flux on the transition to mist flow. They include some modification shown in Figure 2-8. The dashed lines correspond to dryout and mist flow transition curves.

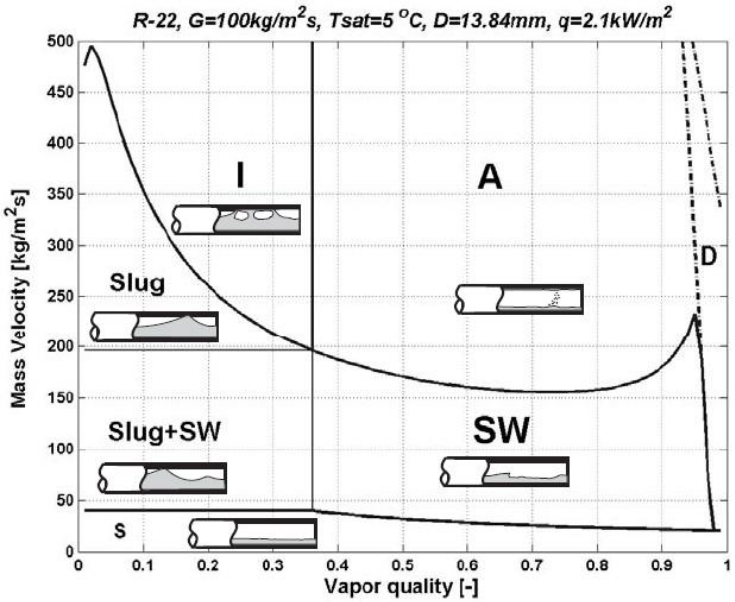


Figure 2-8. Wojtan-Ursenbacher-Thome [44] flow pattern map

### 2.3.2 Flow Pattern Map in Vertical Tubes

The Fair [45] flow map is one of the earliest adiabatic flow pattern maps available for vertical two phase flows. The vertical axis is the total mass flux of liquid and vapour, the horizontal axis represent Lockart-Martinelli parameter, Equation (23), and it divides the flow into four flow patterns, without a churn flow.

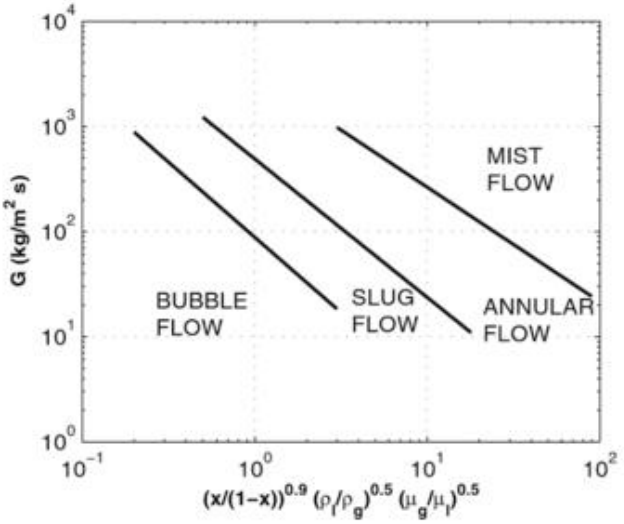


Figure 2-9. Two phase flow pattern map of Fair for vertical tubes [45]

Bennett et al. [46] [47] characterized the flow patterns based on the fluid vapour quality and mass flux, which is very convenient for evaporation processes. Their experiments were on steam/water at 35 and 70 bar in a 12.7 mm pipe, the heat flux was up to 1200 kW/m$^2$. The flow images were taken from an adiabatic glass section placed at the exit of the test section.

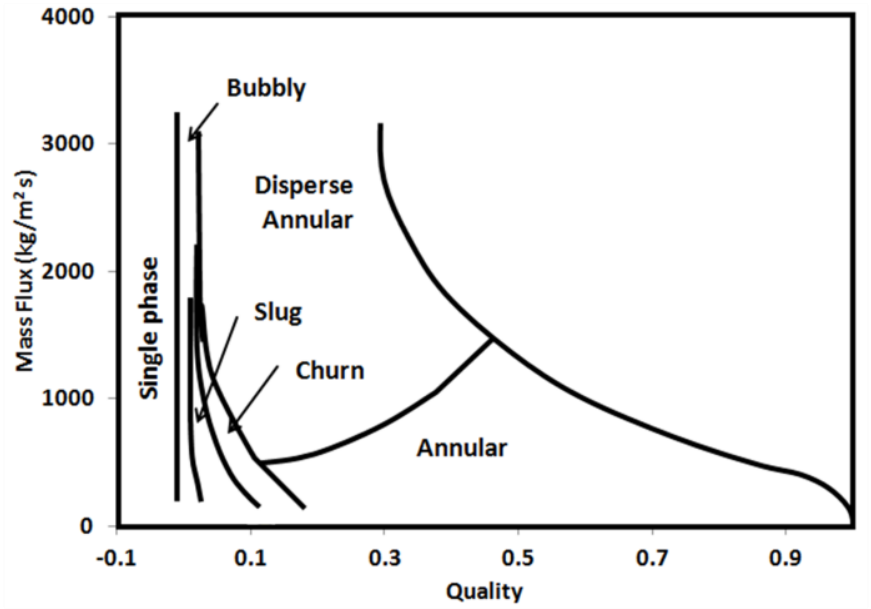


Figure 2-10. Bennett et al. [46] Flow pattern for steam-water flow in 12.7 mm bore tube at 6.89 MPa [46]

One of the more popular empirical flow-pattern maps for vertical upflow is shown in Figure 2-11, and was proposed by Hewitt and Roberts in 1969 [48]. On this map, the coordinates are the superficial momentum fluxes of the liquid and vapour phases. This map represent a wide range of experimental data for upward two-phase flow, which was carried out with air/water in an adiabatic 32 mm diameter pipe at 3 bar .

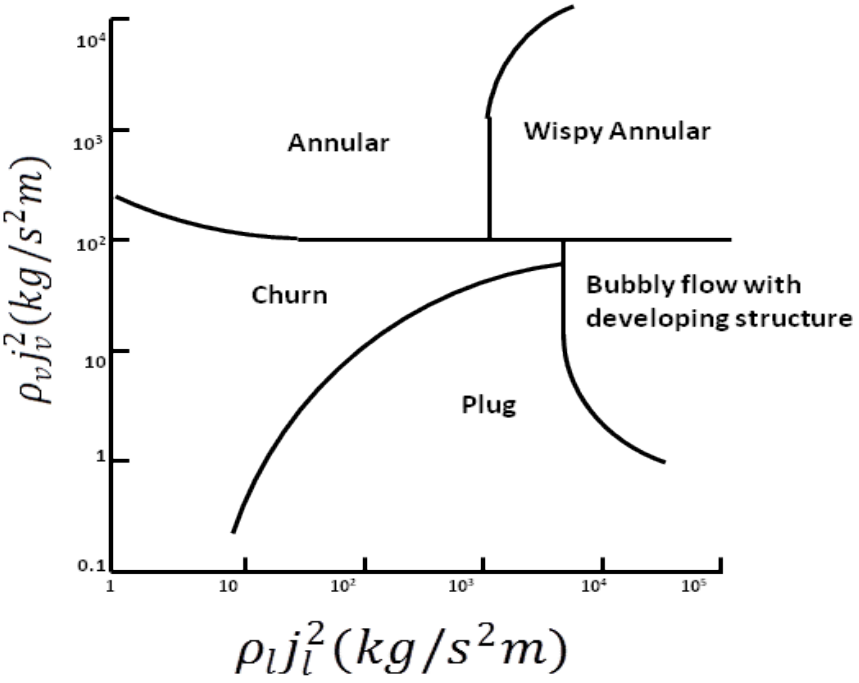


Figure 2-11. Vertical upward flow regime map of Hewitt and Roberts [48]

Another popular map is a semi-theoretically based map by Taitel et al. [49]. Some of the transitions have tube length and diameter dependence. The map is shown in Figure 2-13 for an air/water adiabatic system with a tube diameter of 72 mm and length of 1 meter. Taitel et al. [49] defined transition lines between flow regimes as follow [50]:

Bubbly flow to the slug flow regime transition:

$$J_l = 3.0\, J_g - 1.15 \left[\frac{g(\rho_l - \rho_v)\sigma}{\rho_l^2}\right]^{1/4} \tag{28}$$

Slug flow to churn flow transition:

$$J_l = -J_v - 0.025\sqrt{gD}\left(\frac{L}{D} - 8.93\right)^{1/4} \tag{29}$$

Churn to the annular flow transition:

$$J_v = 3.1 \left[\frac{g(\rho_l - \rho_v)\sigma}{\rho_l^2}\right]^{1/4} \tag{30}$$

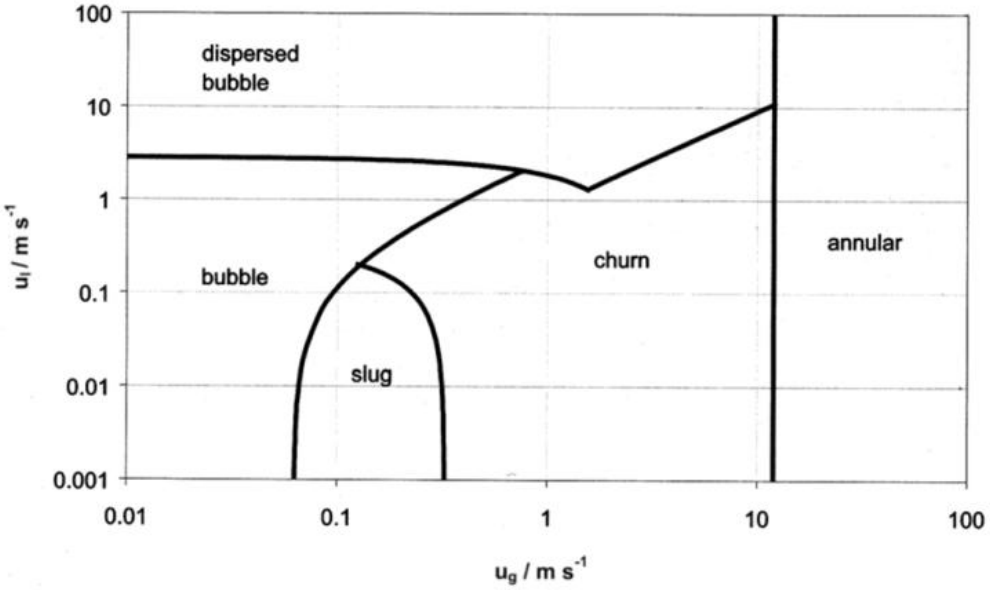


Figure 2-12. Taitel et al. (1980) flow pattern map for vertical flow [49]

Figure 2-13 shows a recent map for adiabatic flow of air/water in a 82.6 mm tube by Zhang et al. [51]. On this map, boundary lines are based on different objective criteria. The map is in reasonable agreement with the semi-theoretical map of Taitel et al [49] (Figure 2-12).

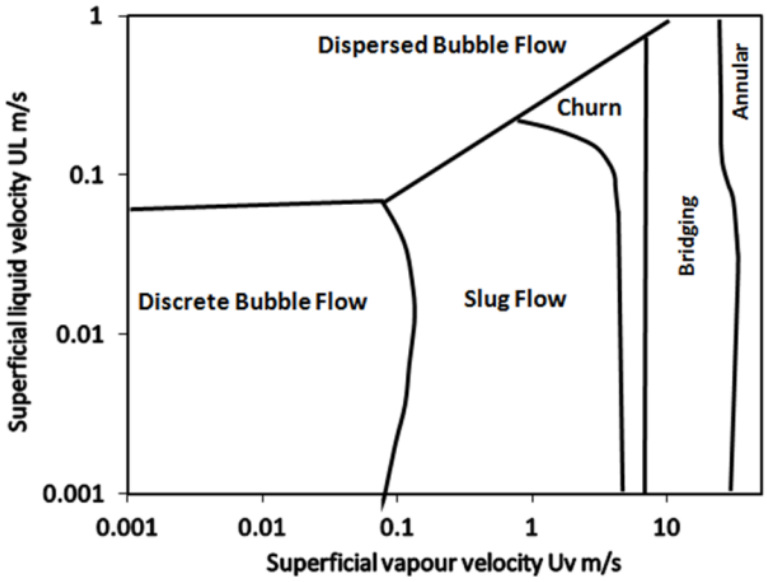


Figure 2-13. Flow pattern map for water/air in 82.6 mm diameter tube, by Zhang et al [51].

### 2.3.3 Effect of tube diameter on flow regime transitions

Ansari et al, [52] investigated the effect of tube diameter on the flow regime transitions for air/water adiabatic system. They found no significant influence on the bubbly-slug transition boundary by increasing the inner tube diameter, though the slug flow region shrinks considerably and the transition boundary from churn to annular pattern occurs at higher air superficial velocities as shown in Figure 2-14.

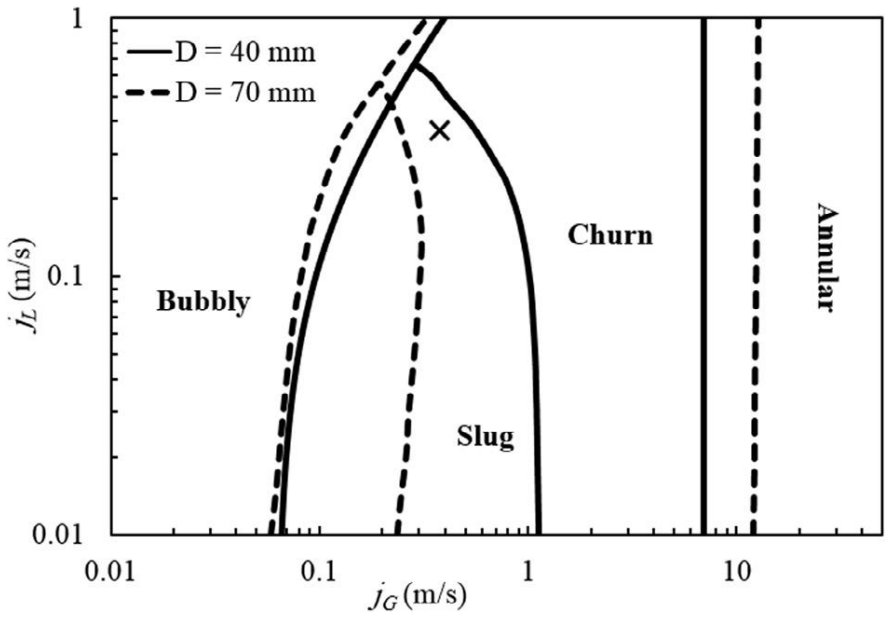


Figure 2-14. Flow pattern maps for upward gas–liquid two-phase flow vertical tubes (D 40 mm & 70 mm) [52]

Oya [53] investigated the adiabatic flow of air/fuel in a tubes of 6, 4, 2 mm diameter and found that the transition lines in the flow pattern maps were only affected slightly by the tube size both for vertical and horizontal flows.

Fukano and Kariyasaki [54] investigated an adiabatic air/water flow patterns in tubes of inner diameters from 1 to 9 mm, they concluded that the smaller the pipe inner diameter, the easier the formation of slugs.

Govier et al. [55] investigated the effect of tube diameter on upwards adiabatic vertical flow of air/water flow for diameters ranging from 16 to 63.5 mm. They found a small influence on the transition from the bubble to the slug flow pattern. However

the borders between slug and churn and between churn and annular flow pattern were affected considerably.

Most of the studies on flow patterns have dealt with adiabatic air-water flow, very limited data are available for other fluids and for diabatic process [56] [47].

### 2.3.4 Adiabatic and diabatic flow pattern maps

Kattan–Thome–Favrat [40] were one of the earliest researchers to develop convective boiling flow-pattern maps. They were developed under horizontal flow boiling conditions using five refrigerants (R-134a, R123, R402a, R404a, and R502) [35]. The flow regimes were identified from an adiabatic viewing window at the exit of the test section. They found that boiling flows differ from air/water type system. Their map covers a wide range of mass velocities and vapour qualities. The map is valid for both adiabatic and diabatic (evaporating) flows and includes the prediction of the onset of dryout at the top of the horizontal tube during evaporation as a function of heat flux and flow parameters [40].

Dukler and Taitel [50] indicated from their vapour/liquid experimental data that the flow regimes in flow boiling are different to that of adiabatic flow. This is not in agreement with other researchers, such as Frankum et al. [57], who concluded that the adiabatic flow pattern maps and associated correlations agree well with flow boiling results [57].

Huang et al. [58] investigated the flow boiling of water in a vertical rectangular channel and assessed the flow patterns form a viewing window at the exit of the test section. They noted that there was no slug flow regime, though this is possibly because of the relatively large dimension of the channel.

Huo et al. [59] obtained a vapour/liquid flow pattern map using R134a as the working fluid. For 10 bar operating pressure and tube diameter of 4.26 mm, they suggested that the reduction of the diameter was seen to shift the slug to churn and churn to annular transitions to higher values of gas velocity.

Celata et al. [60] used an optical probe to determine the flow-pattern for R12 inside a 2.3 m-long, 7.72 mm diameter heated tube at pressures of 12-27 bar. Albeit an intrusive measurement without direct observation of the flow pattern, this work does represent one of the only investigations where the flow regime is identified in the diabatic test section where the boiling is occurring. This is different to those which use visualisation techniques at an adiabatic viewing section downstream of the diabatic section. Their results were in a good agreement with the Weisman and Kang map developed in adiabatic, steady-state conditions.

Table 2-2. Adiabatic experimental studies for vertical flow pattern maps

| **Researcher** | **Diameter mm** | **Fluids** | **Adiabatic /Diabatic** | **Flow pattern Category** |
|---|---|---|---|---|
| **Fair [45]** | 25.4 | Air/water | Adiabatic | G − $1/X_{tt}$ |
| **Bennett et al. [46]** | 12.7 | Steam/water | Diabatic | G - x |
| **Hewitt and Roberts [48]** | 32 | Air/water<br>Steam/water | Adiabatic | $J_l^2\rho_L$- − $J_G^2\rho_G$ |
| **Taitel et al. [49]** | 20 | Gas-liquid t | Adiabatic | JL − Jg |
| **The Zhang et al. [51]** | 82.6 | Air / water | Adiabatic | |
| **Ansari et al. [52]** | 40- 70 | Air / water | Adiabatic | JL − Jg |
| **Rozenblit et al [61]** | 25 | Air / water | Adiabatic | JL − Jg |

Table 2-3. Vapour/liquid experimental studies for flow pattern maps

| Researcher | Diameter (mm) | Fluids | Orientation | Model |
|---|---|---|---|---|
| **Kattan–Thome–Favrat [40]** | 13.84 | R-410A | Horizontal | G – x |
| **R Revellin et al. [62]** | 0.509-0.790 | R-134a,R-245fa | Horizontal | G - x |
| **Huo et al. [59]** | 4.26, 2.01 | R134a | Vertical | JL − Jg |
| **Hatamipour et al [63].** | 9 Smooth and Microfin Tubes | R-134a | Horizontal | G - x, WeG −WeL |
| **Celata et al. [60]** | 7.72-mm | Freon 12 | Vertical | JL – Jg |

## 2.4 Summary of knowledge on flow patterns and regimes

Several flow pattern maps are available for predicting two-phase flow regimes in horizontal tubes, but most of them were developed based on air-water data and few were specifically developed for refrigerants. In order to overcome this shortcoming, some empirical factors were introduced to extrapolate these air-water maps to refrigerants. Another important characteristic is that most maps were developed for adiabatic conditions and then extrapolated to diabatic conditions. As it has been pointed out previously, the extrapolation procedure may not always produce reliable results. The original Kattan-Thome-Favrat [40] flow pattern map and their respective updates were developed specifically for refrigerants under vapour/liquid and gas/liquid conditions, overcoming the two drawbacks previously mentioned. Furthermore, the Wojtan-Ursenbacher-Thome version of the original Kattan-Thome-Favrat flow [40] pattern map includes the influences of heat flux and dryout on the flow pattern transition boundaries, providing a much more accurate prediction of the flow regimes for horizontal flow. The same has not yet been considered for vertical flows.

Most of the flow pattern maps available in the literature are for air/water flows and much fewer have been developed for vapour/liquid flows, thus there is incomplete knowledge of the flow regimes associated with convective boiling two phase flows. For the vapour/liquid flow maps that do exist, the diabatic (heated) test sections where the boiling is actually occurring are fabricated from metal due to heat transfer

requirements. The flow regimes are thus identified from adiabatic viewing windows at the heated section exit. The problem with this is that the flow regime and phase distributions in the adiabatic viewing section are not the same as that in the heated section, especially considering that bubbles which form, grow and depart from the heated surface do not appear in the adiabatic section. Thus, it can be said that the visualized flows for these investigations are not at all the same as those in the heated section, apart from possibly annular-type flow regimes. This makes any relation of the flow regimes with the heat transfer problematic since the actual phase distributions where the heat transfer is taking place is not observed. Another shortcoming in the literature is that there are comparatively few flow regime maps and associated research for vertical two phase flows compared with horizontal flows

The above discussion helps define the motivation for the first objective and contribution of the present work. Here, a new test facility has been designed and constructed which allows the direct observation of the two phase flow within a heated and transparent test section arranged in the vertical upflow configuration. The makes the current work unique in this field, as the flow patterns are examined in the actual diabatic and boiling conditions. Thus, the first objective of the present work is to contribute to the understanding vertical upflow convective boiling by measuring and identifying flow patterns under diabatic conditions for varying flow rates and heat fluxes for vertical upflow convective boiling. The flow regime results obtained under diabatic conditions are compared with several existing flow regime maps and conclusions and recommendations are made regarding their suitability for actual boiling scenarios.

## 2.5 Two Phase Flow and Heat Transfer

One of the many practical engineering applications of two phase flow is for heat transfer technology. From a heat exchanger design perspective, it is important to be able to predict the temperature of the wall of a boiling surface for a given heat flux or conversely to predict the wall heat flux for a known wall temperature. Fundamental to each of these is the ability to predict the convective boiling heat transfer coefficient. This section focuses on the published methodologies used to estimate the wall heat transfer coefficient for vertical flow convective boiling.

### 2.5.1 Regions of Heat Transfer

A subcooled liquid flow entering a vertical and uniformly heated tube with a known heat flux over its length can be considered as one of the simplest scenarios of forced convective boiling in a tube and is ideal for illustration purposes. For a given heat flux and mass flow rate the liquid eventually will evaporate completely provided the tube is long enough. Several flow regimes encountered over the length of heated tube are shown in Figure 2-15, specifically for the vertical flow orientation. The picture illustrates the temperature different and corresponding heat transfer regions.

**Region A (single-phase convection):** When the liquid enters the heated tube the temperature increases gradually up to the saturation temperature, while the wall temperature remains below the temperature required for nucleate boiling. For this conditions the heat transfer to the liquid is a single-phase convective heat transfer only [29].

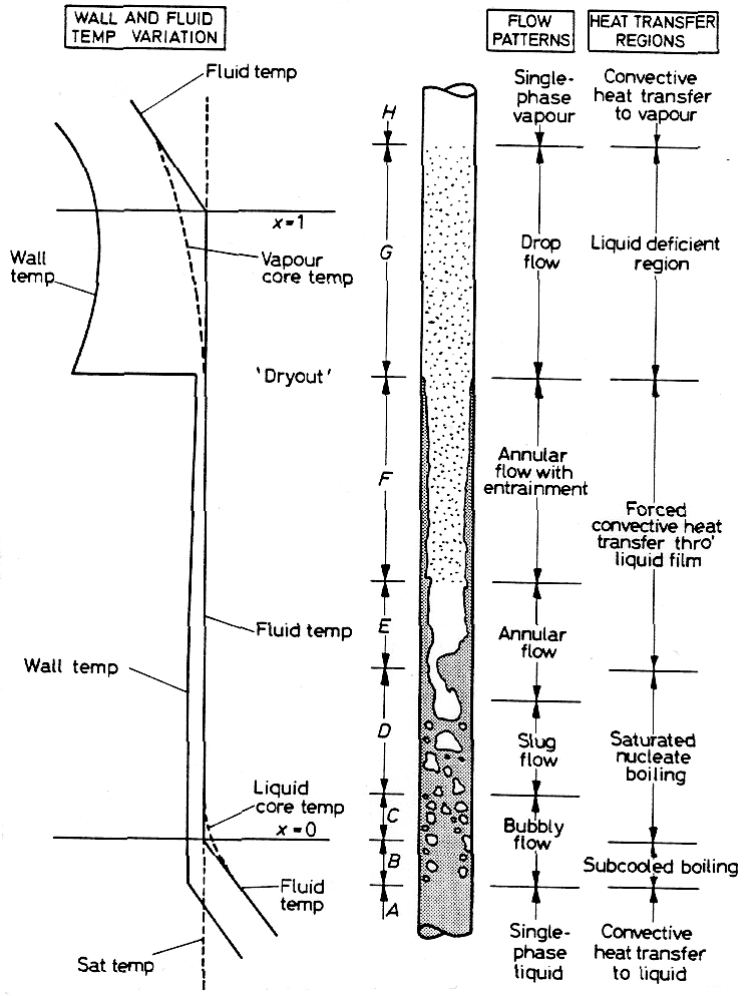


Figure 2-15. Forced convective boiling with qualitative temperature profile for a uniform heat flux boundary condition [31]

**Region B (subcooled nucleate boiling region):** At a certain length along the tube, the formation of vapour bubbles start to occur at the wall which is now superheated ($\Delta T_{sat}>0$) even though the bulk liquid may still be in a subcooled state ($\Delta T_{sub}>0$) [29]. Bubbles form, grow and detach from the heated surface and collapse in the subcooled bulk flow and this defines the first part (B) of the bubbly flow regime.

**Region C (saturated nucleate boiling region):** In this region the liquid reaches the saturation temperature and the transition between regions B and C is the point at which the thermodynamic quality is such that x=0. Bubbles grow and detach from the surface and are entrained into the bulk flow. This is the second part C of the bubbly regime.

**Regions D and E (the two-phase forced convective region of heat transfer):** As the quality increases, a point may be reached where the mechanism of heat transfer changes from a process of "pure boiling" to a process which includes "evaporation", and the flow pattern changes from bubbly or slug and churn flow to annular flow.

**Regions F:** In this region, the low thermal resistance of the thin liquid film may become sufficient to prevent the liquid, in contact with the wall, to be superheated to a temperature that allows bubble nucleation. This means the heat is removed more effectively from the wall by forced convection toward the liquid-vapour interface, which causes liquid to evaporate, without nucleation occurring.

**Region G (liquid deficient region):** When the liquid film evaporates completely, this called the critical heat flux (CHF) or dryout condition, and is accompanied by a rise in the wall temperature. For a constant heat flux, this condition may cause extreme wall temperature levels and is typically avoided in heat exchanger designs.

## 2.6 Flow boiling heat transfer correlation

While single-phase heat transfer correlations can handle the heat transfer for subcooled liquid and superheated vapour flows, the intermediate heat transfer mechanisms associated with flow boiling is complicated by phase change, phase interaction and fluid mixing and the single phase correlations are not applicable as they severely under predict the convective heat transfer coefficient. Furthermore, when a boiling conditions starts in a tube, bubbles are produced at certain nucleate sites whereas the rest of the surface of the tube remains in contact with the liquid. In this condition, the heat transfer mechanism can be a blend of single-phase convection nucleate boiling.

There are a limited number of correlations available in the literature for flow boiling of saturated liquids in the vertical flow orientation. Most of these consider the contribution from two heat transfer mechanisms: nucleate boiling ($h_{nb}$) and convective boiling ($h_{cb}$). In general, heat transfer models have been classified into three categories: superposition, asymptotic and enhancement models. In *superposition models* the two phase heat transfer coefficient is simply the sum of the nucleate

boiling and the convective boiling contributions. The well-known correlation of Chen [64], for example, is based on this model. In *asymptotic models* the largest value of the heat transfer coefficient of the two mechanisms dominants. This is achieved with asymptotic matching of the two terms such that:

$$h \quad = \sqrt[n]{(h_{nb})^n + (h_{cb})^n} \tag{31}$$

Where the exponent n equal to 2 in Wattelet et al. [65] correlation.

Shah [8] introduced the *enhancement model* which is based on the boiling enhancement over single phase heat transfer. In this model the single phase heat transfer coefficient is calculated and multiplied with the largest of three possible enhancement factors: nucleate boiling, bubble suppression or convective boiling. A similar enhancement approach is employed in the Kandlikar correlation [66].

### 2.6.1 Chen correlation [67]

Chen [64][68] proposed a widely used correlation for the overall heat transfer coefficient for convective boiling in vertical tubes. Chen's correlations [67] were formulated by predicting the nucleate boiling component of the heat transfer using the Forster and Zuber [69] pool boiling correlation and a suppression factor S. It offered a relatively simple additive form of nucleate boiling and convective terms [66]:

$$h_{tp} = h_l \mathrm{E} + h_{nb} \mathrm{S} \tag{32}$$

where

$$h_{\mathrm{nb}} = 0.00122 \left[ \frac{k_l^{0.79} C_{pl}^{0.45} \rho_l^{0.49}}{\sigma^{0.5} \mu_l^{0.29} h_{fg}^{0.24} \rho_v^{0.24}} \right] \Delta T_{sat}^{0.24} \Delta P_{sat}^{0.75} \tag{33}$$

The wall superheat is simply $\Delta T_{sat} = (T_{wall} - T_{sat})$ and $\Delta P_{sat} = (P_{wall} - P_{sat})$ where $P_{wall}$ is the saturation pressures of the fluid at the wall temperature and $P_{sat}$ is saturation pressure of the fluid. In Equation (32) the suppression factor is determined as;

$$S = \frac{1}{1 + 2.53 \times 10^{-6} Re_{TP}^{1.17}} \tag{34}$$

where the local two-phase Reynolds number, $Re_{TP}$ , is defined as:

$$Re_{TP} = Re_l E^{1.25} \tag{35}$$

The single phase convective term is calculated using the Dittus-Boelter [70] correlation whereas the enhancement factor, E, is based on the Lockhart Martinelli parameter such that;

$$E = \begin{cases} 1, & \frac{1}{X_{tt}} \leq 0.1 \\ 2.35\left(\frac{1}{X_{tt}} + 0.213\right)^{0.736}, & \frac{1}{X_{tt}} > 0.1 \end{cases} \tag{36}$$

where $X_{tt}$ is the Lockhart-Martinelli parameter defined as:

$$X_{tt} = \left(\frac{1-x}{x}\right)^{0.9} \left(\frac{\rho_g}{\rho_f}\right)^{0.5} \left(\frac{\mu_f}{\mu_g}\right)^{0.1} \tag{37}$$

The Chen correlation [40][39] can be used over the whole region of saturated nucleate boiling and two-phase forced convection regions and its use can be extended into the subcooled boiling region.

### 2.6.2 Shah correlation [71]

The Shah [71] correlation is possibly the most widely used correlation for the saturated two-phase flow nucleate boiling heat transfer in horizontal and vertical tubes [66] . The correlation aims to predict the two phase component of the heat transfer, though with a different general correlations that depend on the Boiling Number, *Bo*, and a dimensionless convection number, *C*o, which were posed to distinguish whether nucleate boiling (nb) or forced convective boiling (cb) influences were dominant. The larger value of $h_{nb}$ or $h_{cb}$ is then taken for $h_{tp}$. To the best of knowledge, this was the first correlation applicable to both horizontal and vertical tubes. It has been tested with a large database by many researchers with mostly satisfactory results [72].

Shah defined additional dimensionless parameter, N, in terms of:

$$N = \begin{cases} Co & for\ vertical\ tubes\ or\ horixontal\ tubes\ with\ Fr > 0.04 \\ 0.38\ CoFr^{-0.3} & for\ horizontal\ tubes\ with\ Fr \leq 0.04 \end{cases} \quad (38)$$

For vertical tubes at all values of the liquid Froude number, the dimensionless parameter $N = Co$, where,

$$Co = \left[\frac{1-x}{x}\right]^{0.8} \left[\frac{\rho_G}{\rho_L}\right]^{0.5} \quad (39)$$

The boiling number is,

$$Bo = \frac{q''}{Gh_{fg}} \quad (40)$$

and the convective boiling heat transfer coefficient, $h_{cb}$, is calculated as;

$$\frac{h_{cb}}{h_l} = \frac{1.8}{N^{0.8}} \quad (41)$$

Where $h_l$ is the liquid only heat transfer coefficient calculated from the Dittus-Boelter equation [70]. The nucleate boiling heat transfer coefficient is estimated based on the Table below:

Table 2-4. Nucleate boiling heat transfer coefficient correlations for the Shah correlation.

| | |
|---|---|
| $\frac{h_{nb}}{h_l} = 230\ Bo^{0.5}$ | N > 1.0Bo > 0.0003 |
| $\frac{h_{nb}}{h_l} = (1 + 46Bo^{0.5})$ | N > 1.0Bo< 0.0003 |
| $\frac{h_{nb}}{h_l} = F_s Bo^{0.5} \exp(2.74N - 0.1)$ | 1.0> N > 0.1 |
| $\frac{h_{nb}}{h_l} = F_s Bo^{0.5} \exp(2.74N - 0.15)$ | N < 0.1 |

In the above two equations, Shah's constant FS = 14.7 when Bo > 0.0011 and FS = 15.43 when Bo < 0.0011.

### 2.6.3 Gungor and Winterton [73]

Gungor and Winterton [73] proposed a modified correlation based on the Chen correlation [67] and chose the Cooper [74] pool boiling correlation for the nucleate boiling heat transfer coefficient such that;

$$h_{tp} = Eh_{\mathrm{l}} + Sh_{nb} \tag{42}$$

where,

$$h_{nb} = 55Pr^{0.12-0.4343\ln(R_p)} \times (-0.4343\ln(\mathrm{Pr}))^{-0.55} M^{-0.5} q^{"0.67} \tag{43}$$

Here, $h_L$ is calculated from the Dittus-Boelter equation [70] using the local liquid fraction of the flow. A two-phase convection multiplier, $E$, is a function of the Martinelli parameter and the heat flux via the Boiling Number;

$$E = 1 + 24000Bo^{1.16} + 1.37\left[\frac{1}{X_{tt}}\right]^{0.86} \tag{44}$$

where the Martinelli parameter, $X_{tt}$, is defined in Equation (22).

The boiling suppression factor $S$ is given as,

$$S = [1 + 0.00000115E^2 Re_L^{1.17}]^{-1} \tag{45}$$

with $Re_L$ based on mass fraction of liquid.

### 2.6.4 Gungor and Winterton [75]

Gungor and Winterton [75] soon after proposed a simpler version of their earlier correlation based only on convective boiling,

$$h_{tp} = E_{new} h_l \tag{46}$$

The updated two-phase convection multiplier $E_{new}$ was defined as,

$$E_{new} = 1 + 3000Bo^{0.86} + 1.12\left[\frac{x}{1-x}\right]^{0.75}\left[\frac{\rho_L}{\rho_v}\right]^{0.41} \quad (47)$$

The accuracy was found to be much better than the earlier correlation and this version has been recommended by Thome [76] as the better of the two when compared to flow boiling data obtained in his study.

### 2.6.5 Jung and Radermacher Correlation [77]

The correlation of Jung and Radermacher [77] is an additive model of the same type as the Chen correlation [67]. Unlike Shah's "greater of the two", it uses individual terms for convection and nucleate boiling [78] in the following form:

$$h_{tp} = Eh_l + Sh_{nb} \quad (48)$$

The nucleate boiling contribution calculated using Stephen and Abdelsalam's [79] nucleate pool boiling heat transfer correlation ($h_{nb}$) and a boiling suppression factor (S), which are defined in following equations:

$$h_{nb} = 207\frac{k_l}{D_b}\left(\frac{qD_b}{K_l T_{sat}}\right)^{0.745}\left(\frac{\rho_v}{\rho_l}\right)^{0.581} Pr_l^{0.533} \quad (49)$$

where

$$D_b = 0.0146\beta\left[\frac{2\sigma}{g(\rho_l - \rho_g)}\right]^{0.5} \quad (50)$$

$\beta$ represents the contact angle between the liquid-vapour interface and the solid surface and is taken as 35°. The term S is defined as,

$$S = 4048\, X_{tt}^{1.22} Bo^{1.13} \quad for \quad X_{tt} \leq 1 \quad (51)$$

$$S = 2 - 0.1\, X_{tt}^{-0.28} Bo^{-0.33} \; for \; 1 < X_{tt} \leq 5 \quad (52)$$

The convective contribution, modelled by the Dittus–Boelter equation [70],is corrected by the two-phase enhancement factor (E) which is given as:

$$E = 2.37\left(0.29 + \frac{1}{X_{tt}}\right)^{0.85} \quad (53)$$

### 2.6.6 Kandlikar correlation [66]

Kandlikar [66] has developed a correlation applicable to both horizontal and vertical channels. It uses the same correlating parameters as the Shah correlation [71] but also has a fluid specific multiplier for nucleate boiling. Values of this multiplier have been given for only 10 fluids [66].

For vertical flows, Kandlikar' s correlation estimates the value of the heat transfer coefficient as,

$$h_{tp} = h_l[C_1 Co^{C_2} + C_3 Bo^{C_4} F_K] \quad (54)$$

where $h_l$ is the heat transfer coefficient for single-phase flow calculated by Dittus-Boelter correlation [70], *Bo* is the Boiling Number and *C*o is the convection number, both given earlier. The values of the constants are for Co < 0:65; $C_1$ = 1.136; $C_2$ = -0.9; $C_3$ =667.2; $C_4$ = 0.7 and for Co > 0:65; $C_1$ = 0.6683; $C_2$ = - 0.2; $C_3$ =1058.0; $C_4$ = 0.7. The value of $F_K$ has been taken here as equal to 1.3, close to those of similar refrigerants [80].

### 2.6.7 The Wattelet et al. Correlation[65]

Wattelet et al. [65] proposed an asymptotic matching model proposed by Kutateladze [1961] to combine the nucleate boiling and convective boiling modes of heat transfer in the form [81];

$$h_{tp} = \left[h_{nb}^{2.5} + (ERh_l)^{2.5}\right]^{1/2.5} \quad (55)$$

where $h_{nb}$ is calculated using the Cooper pool boiling correlation corrected by a suppression factor, *S*, and the convective contribution, modelled by the Dittus–Boelter equation [70], corrected by enhancement factors *E* and *R*, which are determined as follows [78];

$$E = 1 + 1.925X_{tt}^{-0.83} \quad (56)$$

$$R = \begin{cases} 1.32\, Fr_l^{0.2} & for \quad Fr_l < 0.25 \\ 1 & for \quad Fr_l \geq 0.25 \end{cases} \tag{57}$$

where $Fr_l$ is Froude number for the liquid phase calculated as.

$$Fr_l = \mathrm{G}^2 / (\rho_l^2 \mathrm{g\, D}) \tag{58}$$

## 2.7 **Summary of knowledge on two Phase Flow and Heat Transfer**

Several correlations have been developed for predicting two-phase flow heat transfer coefficient in vertical channels. The empirical correlations differ in their formulation strategy as well as their numerical value under ostensibly the same conditions. Furthermore, these correlations have been developed by considering the average heat transfer of a test section. Within the test section the vapour quality can change considerably and thus the heat transfer mechanisms and flow regimes can also vary considerably over the tube length. Thus, these correlations do not give information regarding the heat transfer and how they relate to the flow regime. Further to this, similar to what was discussed earlier, the heated tests sections have been opaque which also adds to the problem associated with trying to understand the heat transfer in relation to the flow regime.

The second objective of the present investigation is to contribute to the understanding vertical upflow convective boiling by measuring the local heat transfer coefficient and taking advantage of the new transparent test section to relate the heat transfer with the observed flow regimes. The heat transfer results are then compared with the existing empirical correlations and conclusions and recommendations are made regarding their suitability.

# Chapter 3. Electrohydrodynamic Augmentation of Heat Transfer Coefficient

## 3.1 Electrohydrodynamic (EHD) Phenomena

EHD is the field of thermal fluid science that is concerned with the effect of electric field forces on fluids and fluid bodies. This interaction can create electric body forces which may induce motion and instabilities in the fluid medium. The strength of electric body forces ($f_e$) affecting the dielectric fluid in the presence of an electric field consists of three terms, which are expressed in equation (59) [82]:

$$f_e = \rho_e \bar{E} - \frac{1}{2} E^2 \nabla \varepsilon + \frac{1}{2} \nabla \left[ \rho E^2 \left( \frac{\delta \varepsilon}{\delta \rho} \right)_T \right] \quad (59)$$

where $\rho_e$ is the charge density, E is the electric field strength, $\varepsilon$ is the fluid permittivity, $\rho$ is the fluid density and T is the fluid temperature.

The forces resulting when an electric field is applied to a fluid medium can be classified into three component [83]:

- The electrophoretic force, also known as the Coulomb force, represented in the first term in Equation (59) acts on the free charge within the fluid. This force usually dominates for adiabatic single-phase flow under the application of direct current and depends on the polarity of the electric field.
- The dielectrophoretic force, represented in the second term in Equation (59) is a result of nonuniformity in permittivity of the fluid medium, which can be particularly strong in multiphase fluid systems due to the large difference between the permittivity between the different phases. This means that the dielectrophoretic force can have a significant influence on the flow and heat

transfer if two phases exist, such as in convective boiling and condensation. On the contrary, this force is weaker than the electrophoretic force for adiabatic single-phase flow.

- The electrostrictive force occurs due to variations of the permittivity with changing density and temperature [84] [85].

Depending on fluid condition, the three components of the EHD force can significantly affect the fluid. In convective boiling, all three forces can be present, though the dielectrophoretic force is generally expected to dominate [82].

## 3.2 Electrohydrodynamic Heat Transfer Augmentation for Horizontal Two-phase Flow

Over the past three decades, there have been many studies on the topic of EHD augmentation of heat transfer in two-phase flow. The research involved the influence of DC and AC electric fields on the flow and heat transfer augmentation for both boiling and condensation [17]. The EHD technique creates a dynamic electric field to alter the flow regime creating increased mixing of the flow and/or phases and improved wetting of the heat transfer surface [18]. In the literature, the horizontal flow configuration has been predominantly studied and most of our knowledge of EHD heat and mass transfer for two phase flows is based on horizontal flow boiling. As a result, this section is focussed on the current understanding of EHD augmented two phase flow, though it is carefully noted that it is for the horizontal flow orientation and not necessarily valid for vertical flow systems.

### 3.2.1 Effect of DC Applied Voltage on Heat Transfer Coefficient

Experimental data and theoretical models have shown clear evidence that the EHD forces can generate significant enhancement of convective boiling and condensation heat transfer coefficients [86] [35]. The magnitude of heat transfer enhancement depends upon the electric field strength relative to the rate of the axial momentum flux of the fluid [82]. For example, an experimental investigation of Sadek et al. [83] using R134a as the working fluid revealed that the effect of increasing the EHD voltage for fixed mass flux, heat flux, and inlet quality can improve the overall heat transfer coefficient up to 3.4 folds. The main results of this study are depicted in

Figure 3-1 and show a parabolic type increase in the heat transfer coefficient with increased applied DC voltage.

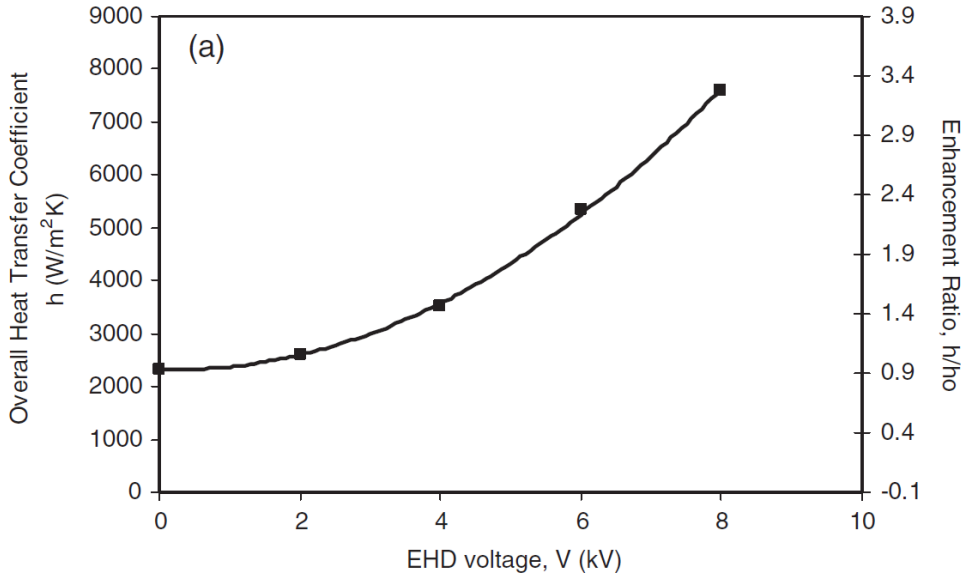


Figure 3-1. The Effect of varying the varying applied voltage on the heat transfer coefficient at G = 83.4 kg/(m$^2$ s), q" = 10.2 kW/m$^2$ and $x_{in}$ = 66% with R134a [83]

Others [87] [15] [88] have found similar trends regarding applied electric field strength and heat transfer enhancement, though they will differ somewhat depending on the nature of the experiments.

### 3.2.2 Effect of DC Applied Voltage on Pressure Drop Penalty

The applied voltage influences the phase distribution and subsequently increases the pressure drop penalty [88]. The increase in the pressure drop depends on how significant the EHD force components are with respect to the fluid momentum rate, since it is related to the degree of phase redistribution [18]. The pressure drop increases more at the lower mass flux and lower inlet quality [86].

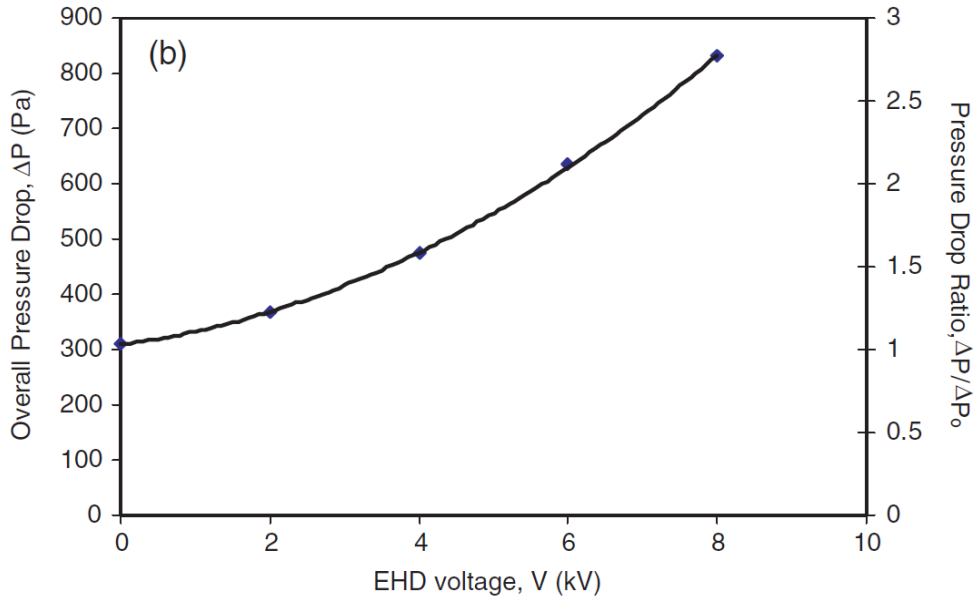


Figure 3-2. Effect of varying the varying applied voltage on the pressure drop at G = 83.4 kg/($m^2$ s), q"= 10.2 kW/ $m^2$, $x_{in}$ = 66% [83]

Many researchers [87] [89] [83] indicated that the application of an EHD voltage increases the pressure drop across the tested section, similar to that depicted Figure 3-2 [83]. Thus, as with most heat transfer enhancement techniques, the enhancement comes at a cost. However, compared with other techniques such as turbulators and surface extensions, the pressure drop penalty associated with EHD is less. Furthermore, these 'fixed' enhancement techniques do not offer the possibility of dynamic feedback control of the heat transfer, and EHD does [87] [85].

### 3.2.3 Mass flux effect on EHD augmentation

In general, the heat transfer coefficient increases with increase of mass flux, but the augmentation of EHD decreases. Cotton et al. [86] fixed the heat flux at 11 kW/$m^2$ and inlet refrigerant quality at 80 % and showed a maximum enhancement of heat transfer coefficient at lower mass fluxes (70-120 kg/($m^2$ s)), but they found limited evidence of enhancement with the application of EHD beyond 200 kg/($m^2$ s) as shown

in Figure 3-3

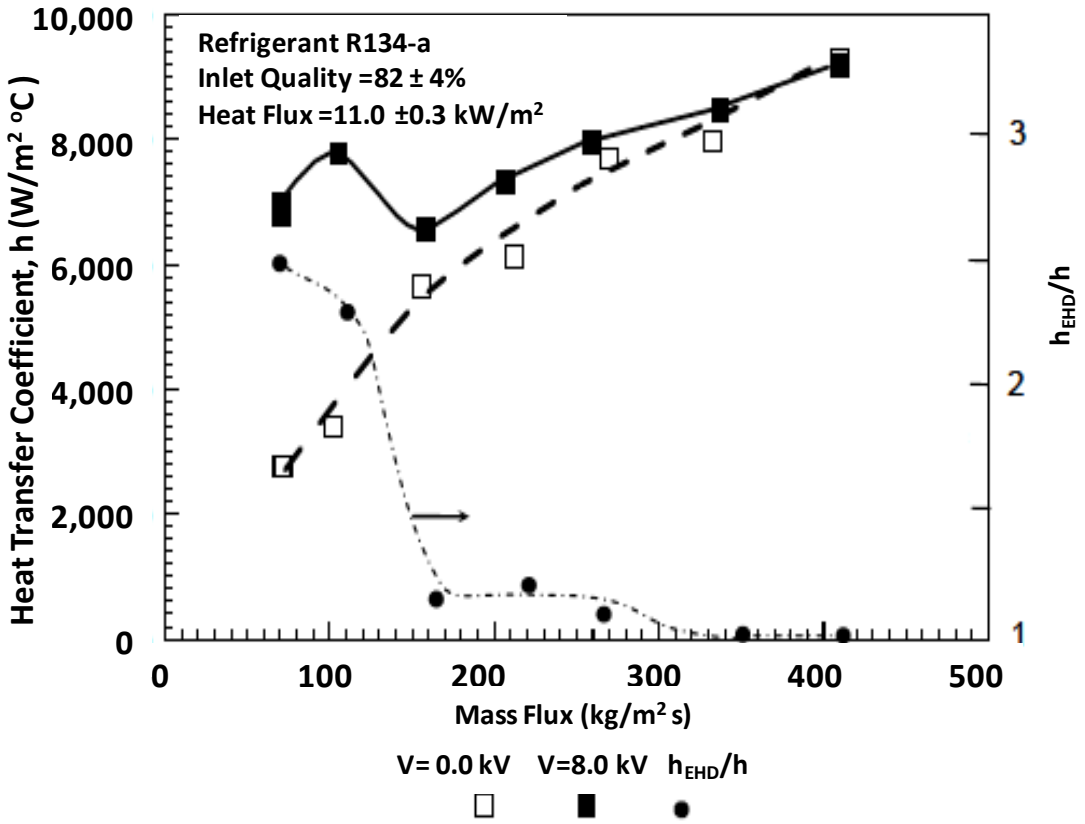


Figure 3-3.

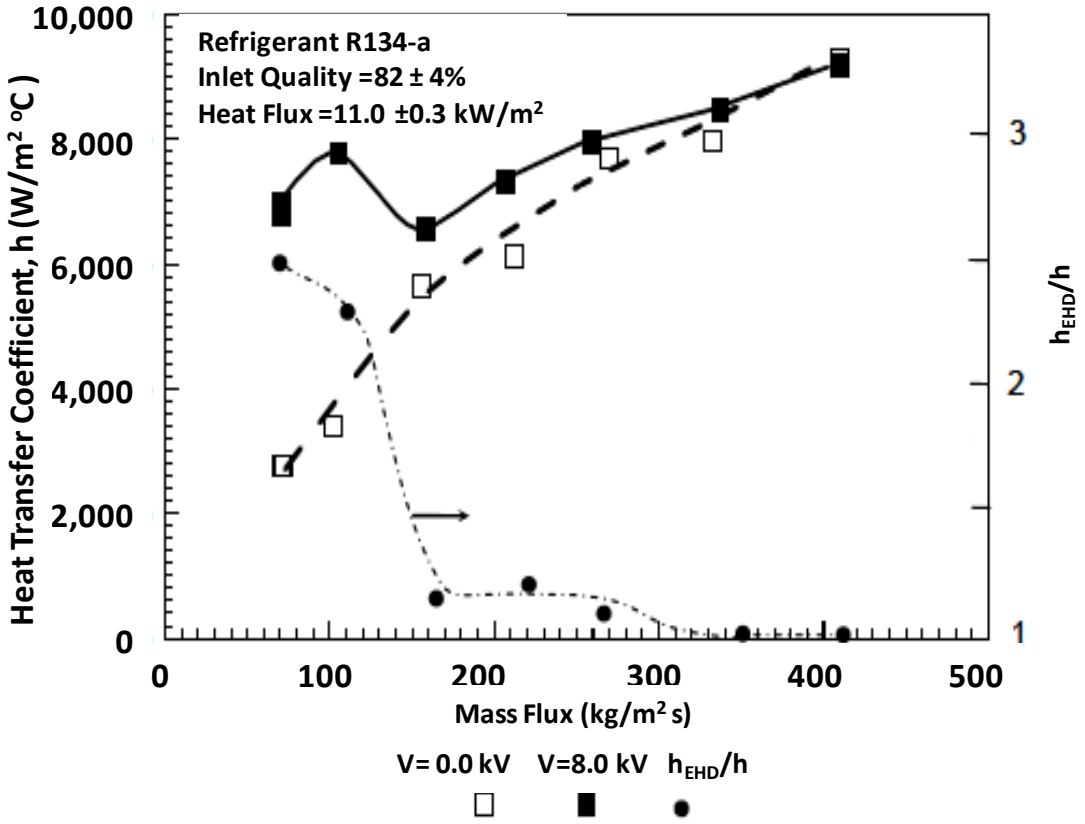


Figure 3-3. The effect of mass flux on the average condensation heat transfer coefficients, for applied voltages of 0 kV and 8 kV DC [86].

Ng, et al. [90] also confirmed that the EHD is most effective at a lower mass flux, due to the lower liquid–vapour shear. They noticed that the difference between 5 and 15 kV on the heat transfer enhancement and pressure drop penalty is not as large when the mass flux is high.

In another experiment, Cotton et al. [18] found significant increases in the Nusselt number, up to (3-fold) for the lowest flow rate (Re = 3500) with a similar increase in the overall pressure drop. In contrast, the heat transfer enhancement is lower for the higher mass fluxes.

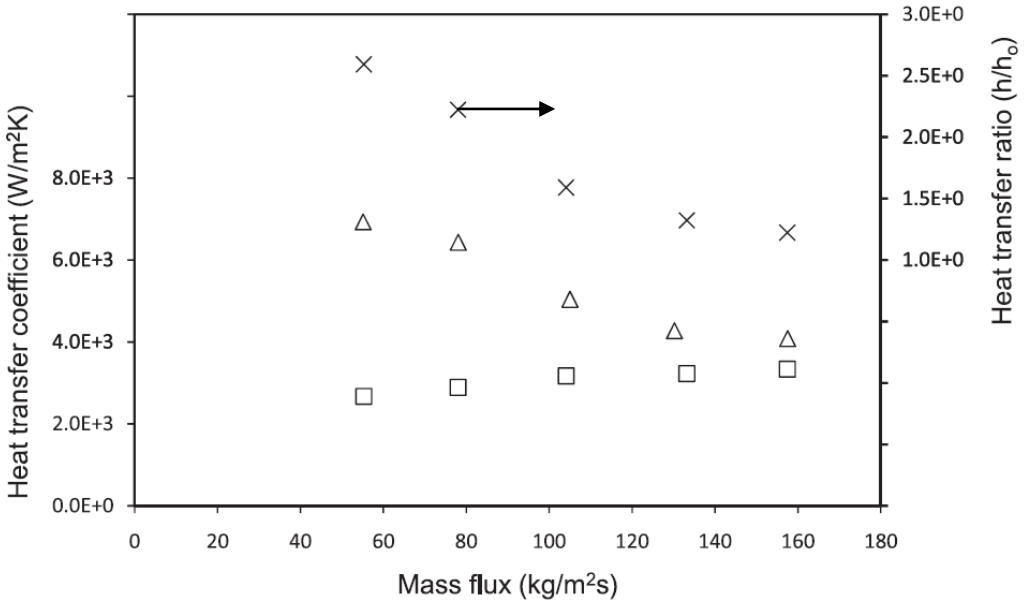


Figure 3-4. The effect of mass flux on heat transfer, □ 0 kV, Δ EHD 8 kV, q" = 5.7 kW/m$^2$, $x_{avg}$ = 45% [6]

Sadek et al. [16] plotted heat transfer coefficient and the heat transfer enhancement ratio for different mass fluxes at a fixed average quality of 45% with applied voltage of 8 kV DC and without EHD, as shown in Figure 3-4. The heat transfer ratio, which is defined as the ratio of the heat transfer coefficient with applied voltage to that without applied voltage, decreases from the maximum ratio ($h/h_o$ = 2.8) at the lowest mass flux of (G = 55 kg/(m$^2$ s)) to 1.2 at a mass flux of 156 kg/(m$^2$ s). These results indicate that EHD forces must be considered in relation to inertial forces when heat transfer enhancement is the goal.

In order to determine the voltage range and extent to which EHD forces are capable of influencing the flow and heat transfer, Cotton et al. [88] considered two dimensionless groups ($E_{hd}/Re^2$) and ($M_d/Re^2$) as a function of the current and applied voltage as shown in Figure 3-5 and Figure 3-6, respectively. The EHD number or conductive Rayleigh number $E_{hd}$ represents the relative strength of the electrophoretic force to the viscous force [91]. The EHD number is defined as:

$$E_{hd} = \frac{I_o L^3}{\rho_o \, v_o^2 \, \mu_c \, A} \tag{60}$$

where $I_o$, L, A, $\rho_o$, $\nu_o$, and $\mu_c$ are the time averaged discharge current, characteristic length, cross sectional area, density of the fluid, kinematic viscosity of the fluid and ion mobility of the fluid ($m^2/V{\cdot}s$) respectively.

The Masuda number represents a ratio of the dielectrophoretic force to the viscous force [91]. The Masuda number or dielectric Rayleigh number $M_d$ defined as:

$$M_d = \frac{\varepsilon_\circ E_o^2 T_o (\partial \varepsilon_s / \partial T)_\rho L^2}{2\rho_o \nu^2} \tag{61}$$

Where $\varepsilon_\circ$ is the permittivity of free space and $E_o$ is the reference electric field.

The shaded regions in Figure 3-5 and Figure 3-6 represent the conditions where both effects of electric field induced flow and forced convection forces can be expected to be of influence on the flow. The ratios ($E_{hd}/Re^2$) ≥ 0.1 and ($M_d/Re^2$) ≥ 0.1 define the minimum condition where an influence of the electric field on the flow of liquid in the channel may be expected.

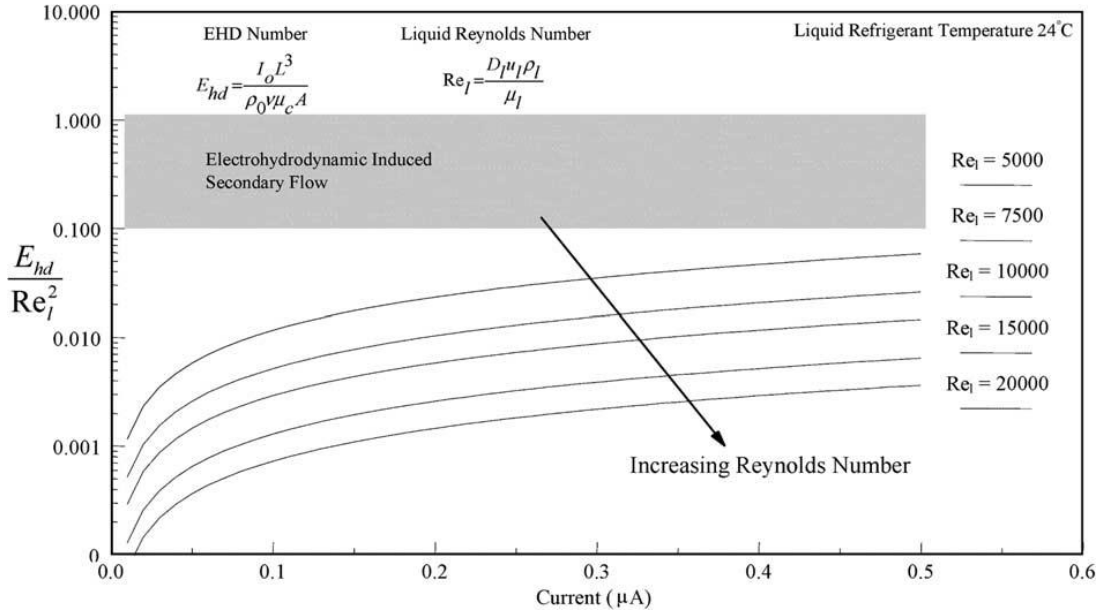


Figure 3-5. The relationship between $E_{hd}/Re_l^2$ ratio as a function of current at 24 ˚C [88]

Figure 3-5 shows that for their experiments with R134a, the electrophoretic influence on the two phase flow would not likely be influencial on flow and heat transfer augmentation. However, Figure 3-6 shows that the dielectrophoretic EHD effect

increases with increased voltage and decreases with Reynolds number. The dimensionless ratio ($M_d/Re_l^2$) indicates that the dielectrophoretic effect will be influential when the applied voltage is greater than about 6.0 kV and the Reynolds number Re < 5000. Figure 3-6 also suggests that EHD will not have a significant effect on the flow for the regions of Re > 20,000. The flow condition in these regions will be determined only by inertial forces and the flow redistribution due to electrohydrodynamic forces is unlikely and confirms the observations discussed earlier.

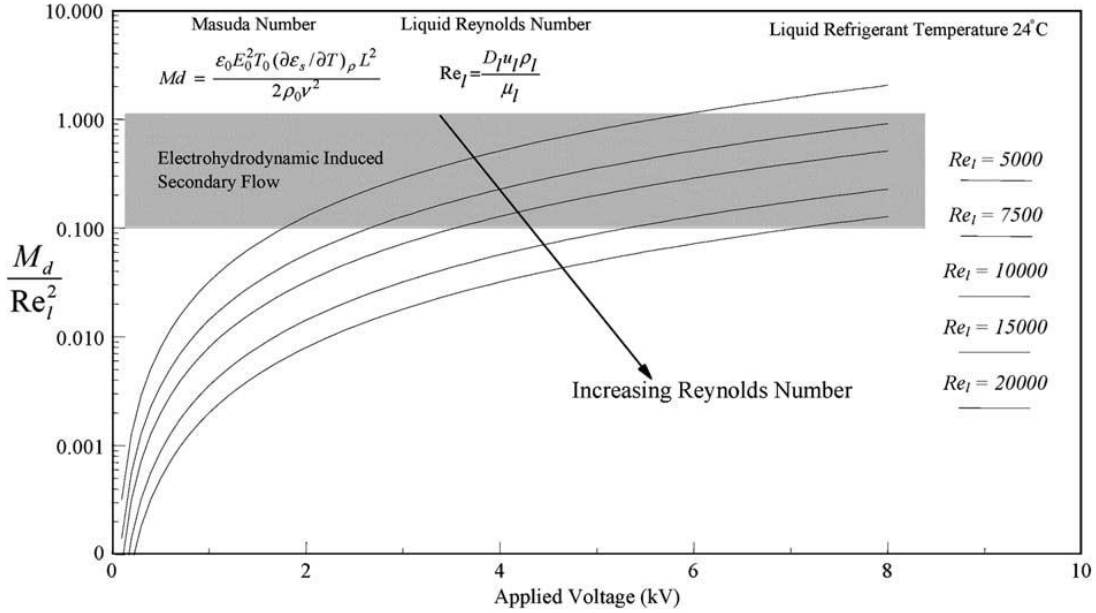


Figure 3-6. Experimental relationship between the ($M_d/Re_l^2$) ratio as a function of applied voltage at 24 ˚C [88]

Sadek et al. [16] confirm that when the ratio ($M_d/Re_l^2$) decreased due to the increase of Reynolds number, which is a function of mass flux, the augmentation and the heat transfer ratio ($h_{EHD}/h_o$) decreased as shown in Figure 3-7.

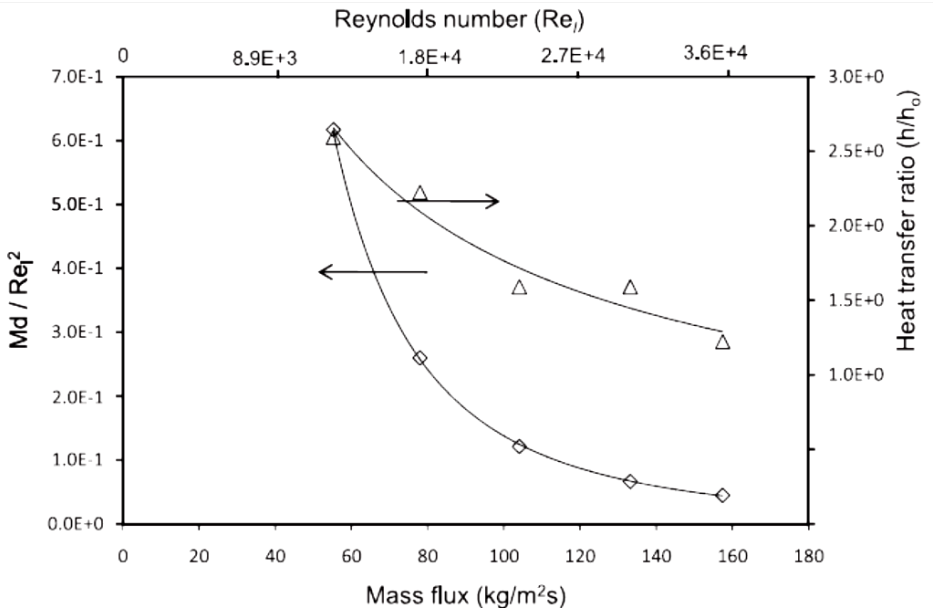


Figure 3-7. The effect of mass flux on ◊ ($M_d/Re_l^2$), and Δ ($h_{EHD}/h_o$) at (8 kV), q"= 5.7 kW/m$^2$ and $x_{avg}$ = 45% [16]

More recently, McGranaghan and Robinson [15] showed that the EHD forces considerably influenced the flow regimes for boiling of HFE7000 in the horizontal configuration, and these flow regimes offer notable improvement of the heat transfer once the EHD forces became of the same order of magnitude as the inertial ones, as given by $Md/Re^2 \sim 1$.

### 3.2.4 Quality effect on EHD augmentation

Cotton et al. [86] studied the effect of the electric field for different vapour qualities and noted that the electric field is more dominant for lower average test section quality regions ($x_{avg}$ < 30%). For the range of 45% ≤ $x_{in}$ ≤ 65% the enhancement increases from 2.3-fold to a peak of 3-fold and the effect begins to diminish at qualities above $x_{in}$ > 65%, see Figure 3-8. It was also noted that the pressure drop penalty decreased for higher inlet qualities [86].

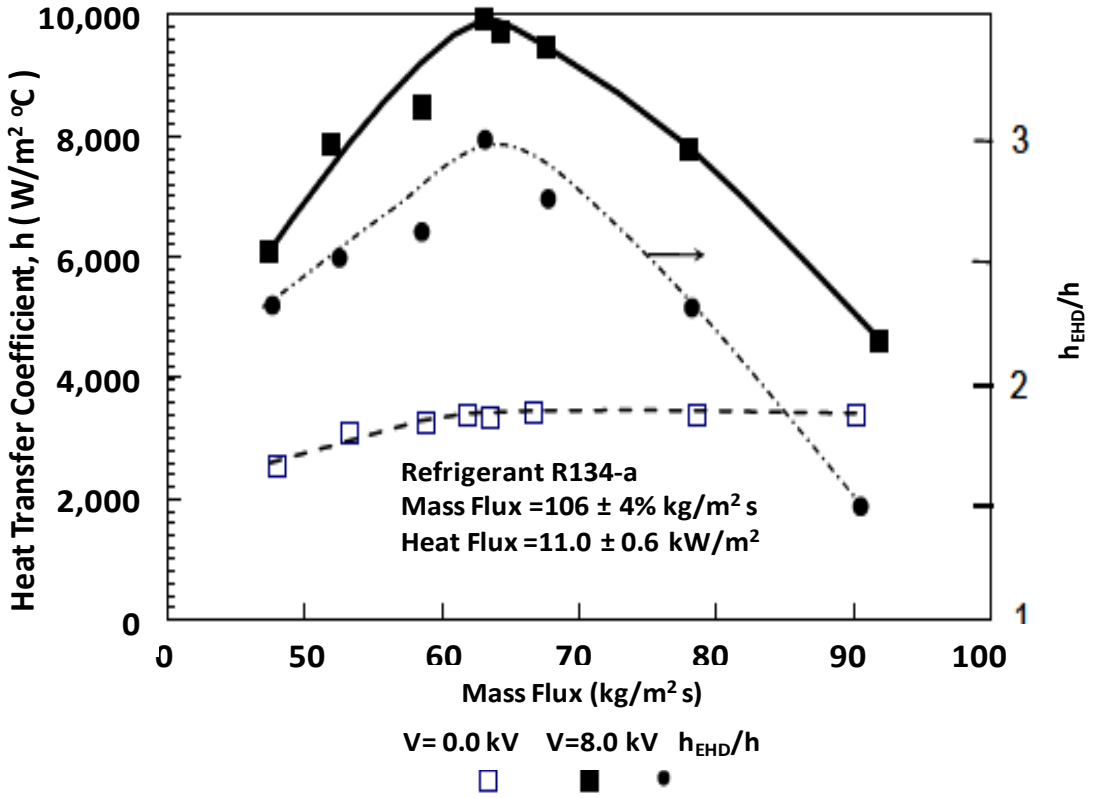


Figure 3-8. The effect of inlet quality on condensation heat transfer coefficients and, for applied voltages of 0 kV and 8 kV DC [86]

Bryan [82] investigated the effect of the change in quality on the EHD forces the impact on heat transfer and pressure drop for 0, 5, 15 kV. The results are shown in Figure 3-9, which illustrates that the heat transfer coefficient increases as quality increases at 0 kV. Applying 5 kV causes a small increase in the heat transfer coefficient and the pressure drop, up to x = 44%, above which the heat transfer starts being suppressed, though the pressure drop still increases. At 15 kV, an increase in the heat transfer coefficient is 170% at lower quality (x = 0.13) with an increase in the pressure drop of one order of magnitude. Conversely, at higher quality (x = 0.68), the EHD force suppresses the heat transfer by 125% while generating over 40% increase in pressure drop.

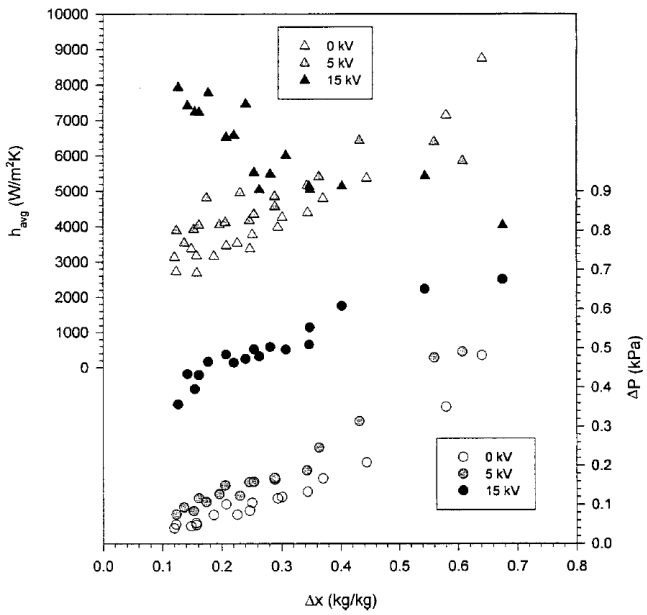


Figure 3-9. Heat transfer coefficient and pressure drop versus change in quality at $G_{avg}$=99.9 kg/(m$^2$ s) and $T_{sat}$ at 4.9°C [82]

### 3.2.5 Flow Regime Effect on EHD Augmentation

Cotton et al. [88] stated that the degree of augmentation depends strongly on the initial flow pattern, and the phase redistribution increases the pressure drop with an augmentation or suppression of heat transfer. When the flow redistribution causes wetting of an originally dry surface of the tube or thins the thermal boundary layer, vaporization and heat transfer enhancement occurred. They concluded that the flow regime determines the enhancement of convective boiling. For example, Cotton et al. found evidence that the flow regime may change from stratified wavy flow to annular flow with the application of 10 kV [92] causing notable augmentation of heat transfer and presser drop.

The Sadek et al. experiments [83] also provide evidence that the EHD forces are strong enough to extract sufficient liquid from the liquid stratum at the bottom region of the tube to cause flow regime transition from stratified flow to annular flow. When the interfacial electric body force extracts the liquid from the bottom stratum towards the vapour core, it results in a phase redistribution with a resultant increase in heat transfer [16].

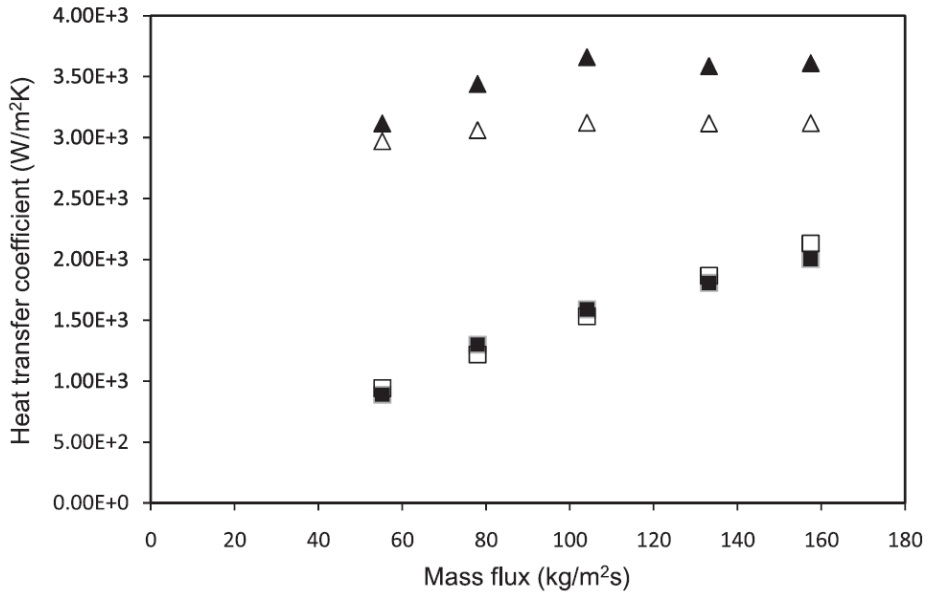


Figure 3-10. Heat transfer coefficient without EHD forces for ■ experimental-bottom, ▲ experimental-top, □ model-bottom, Δ model-top [16]

Sadek et al. [16] suggested that the heat transfer coefficient is influenced by the film thicknesses, which is a function of mass flux and gravity. Therefore, the bottom and the top of tube are affected differently, as shown in Figure 3-10. When the mass flux is less than 100 kg/($m^2$ s), increasing the mass flux increases the vapour shear, leading to thinner film thickness and therefore higher heat transfer coefficients. At mass fluxes greater than 100 kg/($m^2$ s), the thickening of the film due to the liquid being swept from the bottom stratum towards the top and sides of the tube offsets the thinning due to the vapour shear and therefore the heat transfer remains nearly constant. For mass fluxes greater than approximately 130 kg/($m^2$ s), the effect of EHD on the top heat transfer is negligible and causes enhancement only for the bottom [16].

### 3.2.6 Electrode Design Effect on EHD Augmentation

Bryan et al. [93] stated that the electrode design affects the EHD enhancement and suggest that the electrodes must be properly designed with respect to the quality, flow regime, heat flux, and mass flux ranges. Nangle-Smith experimental data [94] also provided evidence that for each specific electrode design an optimum EHD enhancement occurs for a given quality, flow regime, heat flux, and mass flux. Regardless, the concentric rod electrode is the most studied electrode configuration.

### 3.2.7 Effect of AC Electric Field on EHD Augmentation

Recent experiments have shown that the application of pulse voltages provides a wider range of heat transfer and pressure drop augmentation compared to an applied DC voltage. [95]. Cotton et al. [18] found considerably improved heat transfer enhancement when applying a high voltage, with the overall enhancement with 12.4 kV applied voltage being approximately 3-fold, compared with the field-free case. The local heat transfer enhancements exceeded 4-fold near the outlet of the channel (see Figure 3-11). However, the enhancement was a function of the applied voltage and frequency, as shown in Figure 3-11.

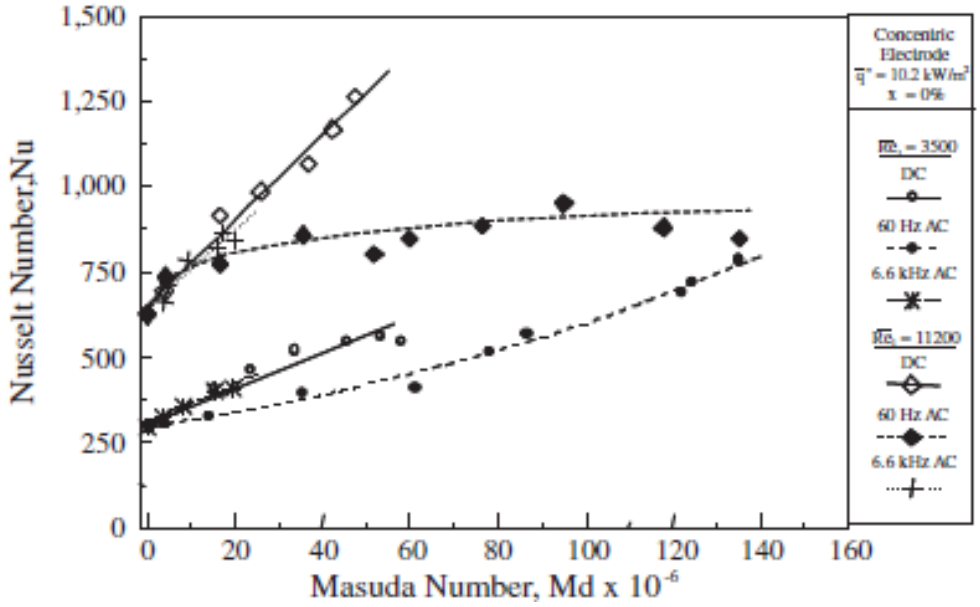


Figure 3-11. The Effect of the DC and AC Masuda numbers on the average Nusselt number [18]

Sadek, et. al. [95] experimented with a near sinusoidal 62.5 Hz AC applied voltage and showed that the heat transfer and pressure drop trends change considerably as compared to the DC conditions.

### 3.2.8 Effect of Low Frequency Applied Voltages Range

Sadek et al. [96], [97] noted that for the low frequency range of (4 Hz ≤ f ≤ 10 Hz), the two-phase flow was able to respond to the repeated on/off action of the applied square wave signals. Figure 3-12 shows that the increasing of the frequency in this

range increases the heat transfer. They elucidate that this is due to the amount of liquid extracted from the bottom stratum to the vapour core.

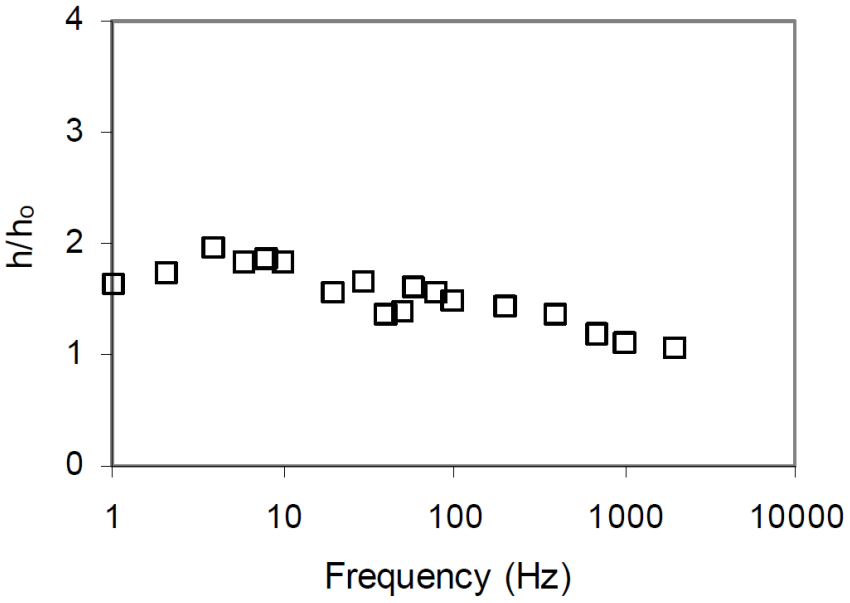


Figure 3-12. Effect of frequency (Hz) on heat transfer enhancement ratio. Measurements taken for square a wave between 0kV and 8 kV and constant mass flux of G= 55 kg/($m^2$ s), inlet quality (x= 45%) and outlet quality (x=30%) [96]

Later, Sadek et al. [95] found that for the low pulse repetition rate range, increasing the pulse repetition rate increases heat transfer and pressure drop, with the latter shown in Figure 3-13. The two-phase flow in this region responds to the induced EHD forces, and liquid is extracted from the bottom stratum to the centre electrode and then pushed radial outwards. Increasing the pulse repetition rate in this range increases the repetition of the extraction cycle and therefore increases heat transfer and pressure drop, see Figure 3-12 and Figure 3-13.

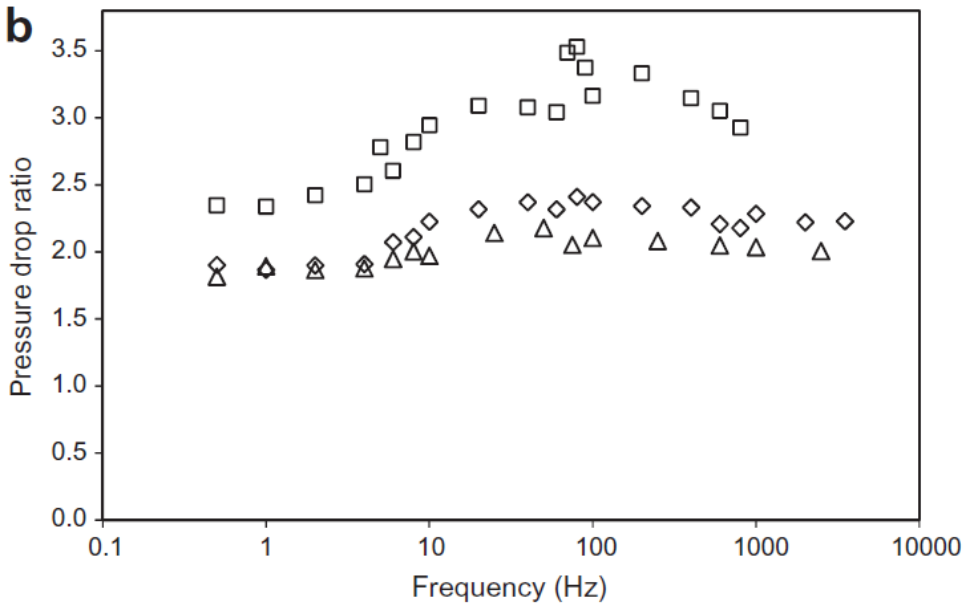


Figure 3-13. Effect of pulse repetition rate on pressure drop ratio □ G = 57 kg/(m$^2$ s, ◇ G = 100 kg/(m$^2$ s, △ G = 150 kg/(m$^2$ s) [95]

### 3.2.9 Effect of Intermediate Frequency Applied Voltages Range

In the intermediate range of frequencies (10 Hz ≤ f ≤ 100 Hz), the time period of the applied signals was less than the time needed to complete the extraction cycle, and only the liquid-vapour interactions below the electrode were observed. Increasing the frequency decreases the time available for liquid extraction and therefore decreases heat transfer enhancement. Increasing the frequency in this range increases the intensity of the liquid-electrode interactions and therefore increases the pressure drop as well [96] [97].

Sadek et al. [95] also observed that in the intermediate range of pulse repetition rate, liquid droplets were able to respond to the applied voltage and therefore increasing the pulse repetition rate increases the frequency of the liquid droplet oscillations. It was concluded that this increase of pulse repetition rate increases the pressure drop but decreases heat transfer augmentation, as shown in Figure 3-14.

Cotton et al. [18] noted that at 60 Hz the heat transfer results are consistently lower than that of DC. This is due to the short duration of applied voltage, which was not enough to extract the liquid from the stratified layer, resulting in a thicker stratified layer at the bottom of the tube, see Figure 3-11.

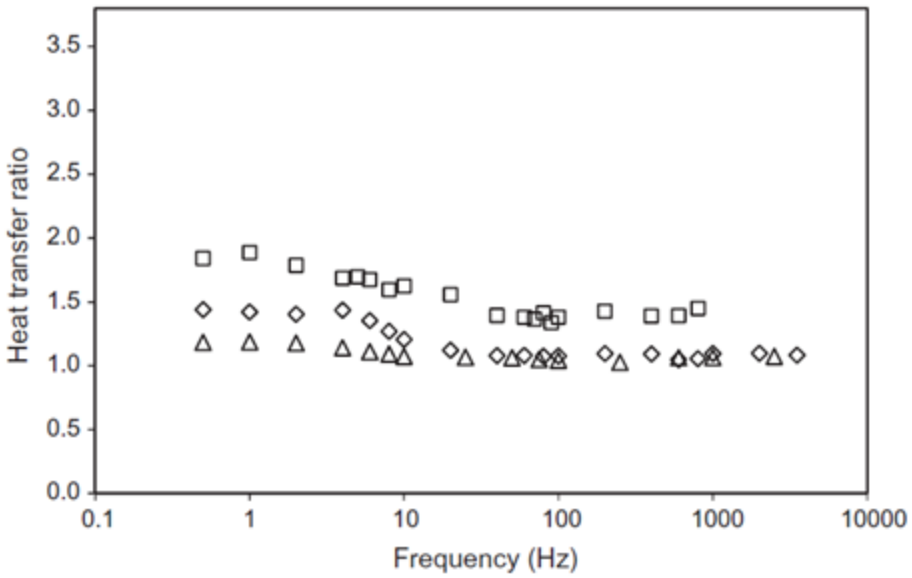


Figure 3-14. Effect of pulse repetition rate on heat transfer ratio. □ G = 57 kg/(m$^2$ s, ◇ G = 100 kg/(m$^2$ s, △ G = 150 kg/(m$^2$ s) [95]

### 3.2.10 Effect of High Frequency Applied Voltages Range

In the high-frequency range (f ≥ 100 Hz), the liquid vapour interactions are less dynamic compared to the lower frequency range. This is mainly because the fluid medium cannot respond to the high frequency of the applied signals and no change in the two-phase flow regime was observed. The flow regimes approach those for the DC case and both heat transfer and pressure drop decreased with an increase of frequency [96] [97].

Sadek et al. [95] confirmed that for pulse repetition rates greater than 100 Hz, the liquid droplets cannot completely respond to the applied voltage and the amplitude of the liquid droplet oscillations decreases with an increase of pulse repetition rate. The response continues to decrease until there is no significant effect of the pulse repetition rate on the two-phase flow patterns at 400 Hz. They concluded that for high pulse repetition rate range, the heat transfer and pressure drop decrease until the two-phase flow patterns resemble that for an applied DC voltage case.

The Cotton et al. [18] expriemental results show a similarity between the DC and the 6.6 kHz AC applied voltage as shown Figure 3-15, and they have a higher augmentation then the 60 Hz case (see Figure 3-11).

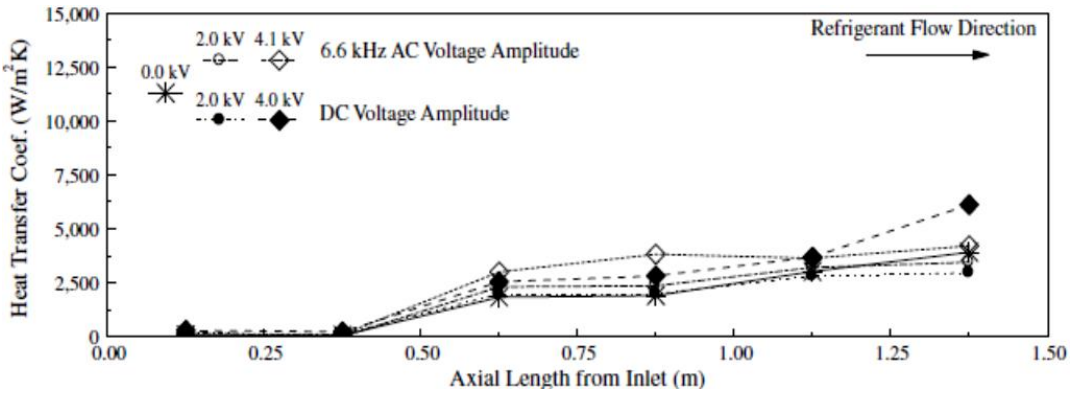


Figure 3-15. Local Heat Transfer Coefficients along the Top Portion of the Tube [18]

### 3.2.11 Effect of EHD Signal Duty Cycle on HT Performance

A duty cycle is the percentage of one period in which a signal is active. Sadek et al. [95] performed many experiment for duty cycles of 25%, 50% and 75%, for applied pulse voltage of 8 kV at pulse repetition rates in the range of 0.5 Hz–1.5 kHz. Three mass fluxes of 55,100, and 150 kg/($m^2$ s)were tested with an average vapour quality of 45%. Sadek concluded that the heat transfer enhancement increased with the increase in the duty cycle as shown in Figure 3-16.

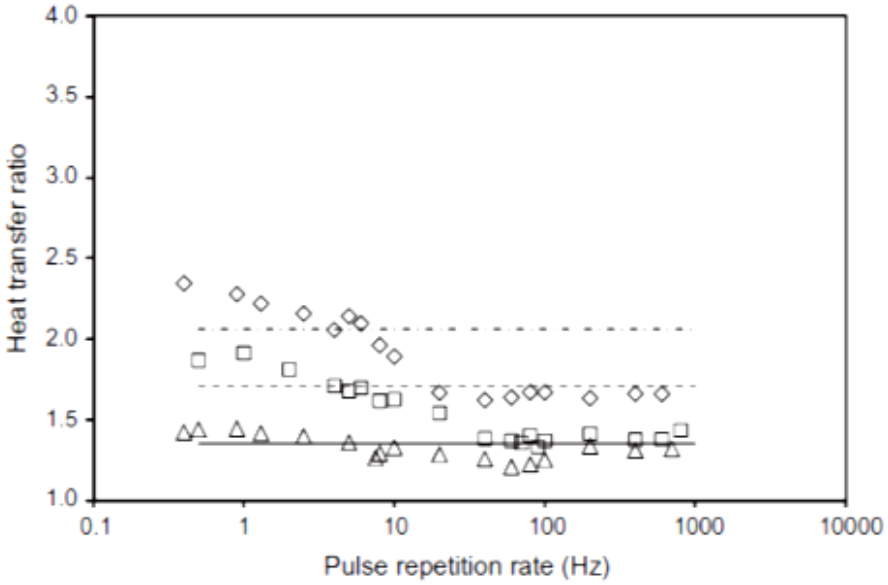


Figure 3-16. The effect of pulse repetition rate on heat transfer, △ 25%, □ 50%, ◇ 75% duty cycle, q" = 5.7 kW/$m^2$ and $x_{avg}$ = 45% [95]

Ng et al. [90] noted that enhancement increases with the duty cycle for all mass fluxes, to approximately 2.7-fold at mass fluxes of 45–55 kg/($m^2$ s) and 1.2-fold at a mass flux of 110 kg/($m^2$ s), as shown in Figure 3-17.

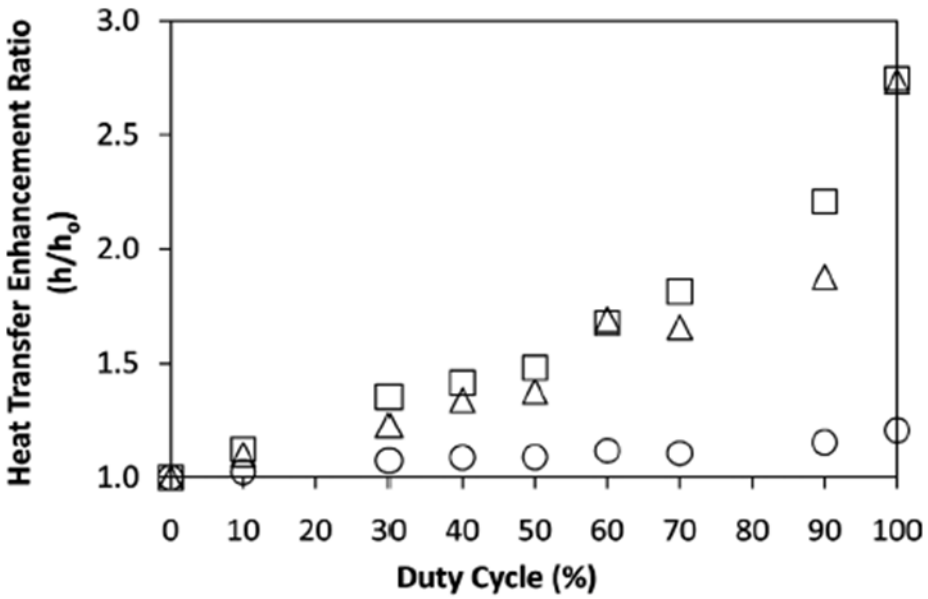


Figure 3-17. Effect of duty cycle on heat transfer enhancement ratio. Pulse width 58 ms, $x_{avg}$ 50%, G of Δ45, □55, and ○ 110 kg/($m^2$ s) [90]

The augmentation of heat transfer and pressure drop increases with duty cycle, which are a measure of the overall voltage applied per pulse cycle [90]. The fraction of time at which the two-phase flow is subjected to EHD at the 75 % duty cycle is greater than that for the 25 % and 50% duty cycles and the amount of liquid extraction from the bottom stratum is greater and this results in better heat transfer enhancement [98].

### 3.2.12 Effect of EHD Signal Modulation on HT Performance

Ng, et al [90] investigated the augmentation of heat transfer and pressure drop for three different pulse widths (29, 58, and 115 ms) using an 8 kV pulse width modulated (PWM) signal with duty cycles ranging from 0% to 100% at mass flux of 45, 55, and 110 kg/($m^2$ s). They concluded that the enhancement of heat transfer and pressure drop increased with pulse width. Higher pulse widths sustain the EHD flow structures for a longer time period, which results in a greater effective voltage applied to the flow. An increase in the effective voltage is expected to increase the heat transfer because it is a measure of the overall voltage applied per pulse cycle

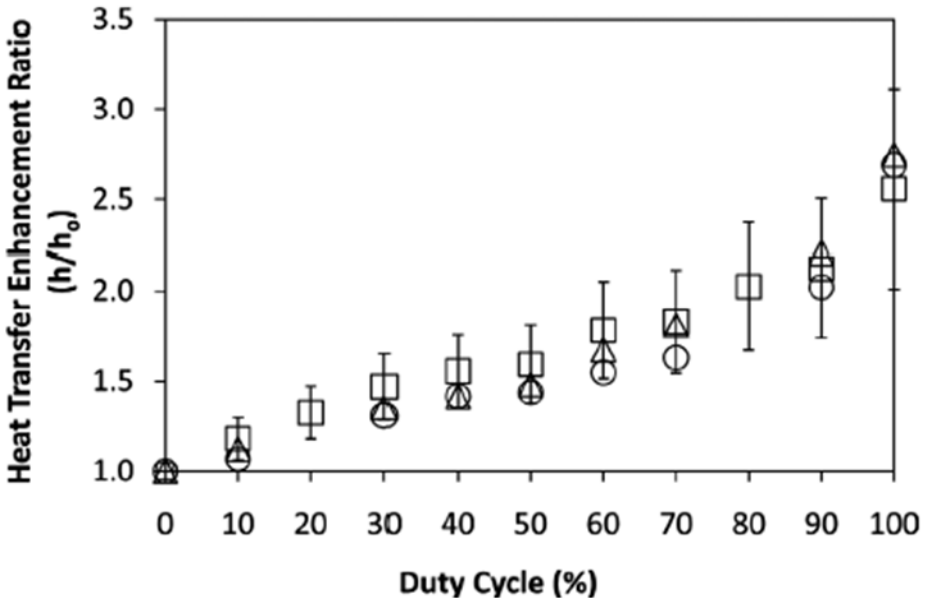


Figure 3-18. Effect of duty cycle on the heat transfer enhancement ratio for a mass flux of 55 kg/(m$^2$ s), $x_{av}$ of 50% and pulse width of ○ 29, Δ58, and □ 115 ms

### 3.2.13 Effect of EHD Signal Polarity on HT Performance

Nangle-Smith et al. [94] studied initially stratified flow and revealed that the negative voltages tend to wet the upper heat transfer surface more than positive voltages. This may occur due to the Coulomb (electrophoretic) force acting in the same direction as the polarisation forces (dielectrophoretic & electrorestrictive) once the liquid surrounds the electrode. Figure 3-19 shows that negative DC voltages can increase the heat transfer coefficient by up to 300%. Therefore, the negative polarity waveforms enhance convective boiling heat transfer more than positive polarity waveforms for a stratified wavy flow pattern.

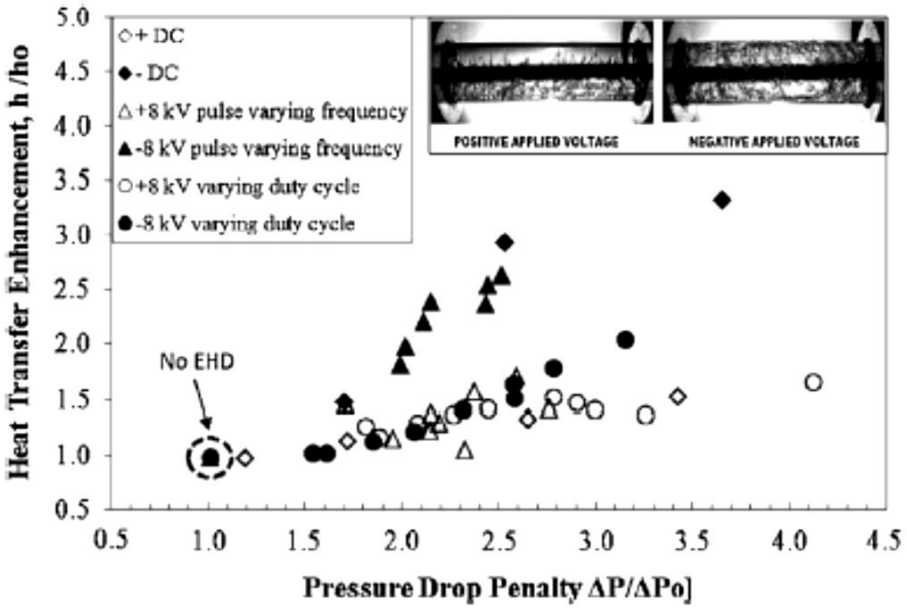


Figure 3-19. Heat transfer enhancement versus pressure drop penalty for EHD waveform parametric study. G = 60 kg/($m^2$ s, $x_{av}$= 40%, q" = 7.5 kW/$m^2$[94]

### 3.2.14 Feed back control of Heat Transfer using EHD

The Cotton et al. [86] experimental study revealed that the EHD is a simple and effective means of control of both the heat transfer and pressure drop of a heat exchanger. The condensation experimental results show that the average heat transfer coefficients and pressure drop can be modulated by as much as 3-fold through application of AC as opposed to DC voltages. The pressure drop and heat transfer can be independently changed, which is a not possible in traditional passive heat exchangers. The differences are attributed to an oscillatory flow pattern, likely due to the continuous transition between flow regimes caused by the approximate "on/off" electric field applied under an AC voltage.

McGranaghan et al. [87] implemented a PID control program to the test section, and were able to maintain heat exchanger heat transfer at a set point within satisfactory limits in a reasonable response time.

Sadek et al. [95] concluded that the main advantage of AC applied voltage is that it provides a wider range of heat transfer and pressure drop augmentation compared with DC. This can be controlled by manipulating the pulse repetition rate and the duty cycle of the applied pulse voltage. This makes the system more amenable to control, which is not the case if using either DC voltages or passive heat transfer techniques.

Nangle-Smith et al. [94] determined that the EHD augmentation is a fast responding method of load control, for convective boiling heat exchangers and requires less additional power. The Nangle-Smith experiments show that the suggested EHD based controller can regulate subject to ±25% deviation in thermal load variations from the designed steady state load condition. This EHD control does not change the flow rate or the flow quality significantly from that of the original field free set point. Nangle-Smith concluded that a high voltage, negative polarity DC waveforms can be used as a low power, fast responding method of load control in convective boiling systems.

### 3.2.15 EHD Mechanisms

While there is agreement in the literature that EHD presents a promising active technique for heat transfer enhancement, there is an incomplete understanding of how the high voltage electric fields affect the heat transfer mechanisms [95].

Cotton et al. [92] found that the maximum electric field strength is near the electrode region, and the EHD force attracts the liquid towards the higher electric field strength and forces the vapour bubbles to the lower electric field strength; the tube wall in their design. They suggested that the phase mixing created by this additional EHD body forces on the bubbles and the liquid extraction phenomena dominates the mechanisms of flow augmentation and hence the subsequent heat transfer enhancement. In these instances, the polarization forces are dominant.

Bryan et al. [93] emphasised that the primary mechanism of the EHD force density results from the local change in permittivity between the liquid and vapour. They illustrate that the EHD force enhances the heat transfer by thinning and/or destabilizing the liquid layer. Depending on the mass flux and the EHD force, it can thin the liquid layer to a point of removing it which may drastically reduce the heat transfer, especially at low mass fluxes and high heat fluxes.

The Cotton, et al. [99] theoretical approach and analytic calculations revealed that if the flow is annular, the electric field strength increases with increased film thickness. They found that for liquid levels below the electrode; an attractive force draws the liquid upwards against gravity, and when combined with the suction pressure due to the vapour velocity, this leads to an early transition to intermittent or annular flow if

the flow was initially stratified. As the liquid level increases and contacts the electrode, the electric field resembles that of a single-phase liquid, consequently there is unlikely to be significant vertical forces acting across the vapour-liquid interface. This distribution is expected to yield an attractive force that draws the liquid near the tube wall towards the electrode. When the liquid level is above the electrode, the field strength is expected to create an attractive force in the vertical direction, against gravity [99].

Cotton et al. [88] noted that the thinner liquid layer increases the heat transfer coefficient along the bottom surface which in turn decreases the wall superheat, but does not vary significantly along the tube length, as the bottom surface is continuously wetted along its entire length. Conversely, the top surface superheat changes significantly along the length of the test section which implies an axial variation of the flow regime. As the applied voltage level is increased, the interfacial electric force increases, attracting the liquid towards the upper part of the channel, wetting the upper portions of the channel that were previously dry. This increases the heat transfer coefficient along the top surface which accounts for the decreases in the wall superheat.

The Sadek et al. [83] work agrees with the above hypothesis, that the effect of increasing the applied voltage level is a progressive decrease in the bottom liquid layer thickness with an associated decrease in the wall temperature and increase in heat transfer coefficient and pressure drop.

The Sadek et al. [16] experimental results compared to the predictions of the conventional heat transfer models show that the liquid extraction causes an increase in heat transfer due to the change in the mode of heat transfer at the bottom of the tube from convective condensation to film condensation.

## 3.3 EHD Condensation Heat Transfer Augmentation in a Vertical Two-phase flow

The studies of the effect EHD on the condensation heat transfer in vertically orientated tubes showed that the electric field had a significant effect on the increase of the condensation heat transfer coefficient [100] [101] [102] [103]. Velkoff and

Miller [104] improved the condensation heat transfer of Freon-113 in a vertical copper tube by 1.5-fold. Didkovsky et al. [101] experiments achieved a 20-fold increase in the heat transfer coefficient using EHD. Further to this, many correlations have been proposed to estimate the condensation heat transfer coefficient using EHD on the outside and inside of vertical tubes. [105] [106] [107].

In terms of the mechanisms responsible for the heat transfer augmentation, Cheung et al. [108] showed that the heat transfer was enhanced by the removal of the condensate through EHD induced liquid extraction and dispersion phenomena. Velkoff and Miller [104] explained the enhancement in terms of the reduction of the film thickness caused by spraying of condensate into the vapour phase and by formation of transverse waves. Bologa et al. [102] showed that the condensation heat transfer enhancement in an electric field was caused by interface deformation and by the associated effect of phase equilibrium displacement

## 3.4 EHD Boiling Heat Transfer Augmentation in a Vertical Two-Phase Flow

Only little work has been found in the literature concerning the EHD in boiling heat transfer for vertical heat exchangers [17].

Yamashita et al. [109] experimentally studied EHD enhancement of vertical falling film evaporation heat transfer of R-123 and its long-term effect on heat exchangers. They concluded that EHD enhancement utilized two electrohydrodynamic phenomenon: surface granulation by a nearly uniform electric field and extracting the liquid by a non-uniform electric field. Liu et al. [110] studied the effect of the electrode polarity on EHD enhancement of boiling heat transfer in a vertical tube using R-123 as working fluid. They found that the positive high-voltage gave much greater enhancements and requires lower average electric field strength to obtain a higher enhancement than the negative high voltage. They obtained the maximum enhancement factor of 2.1 at heat flux of 1.5 $kW/m^2$.

## 3.5 Summary of knowledge on electrohydrodynamic augmentation of heat transfer coefficient

This chapter was aimed to give an understanding of the field of electrohydrodynamic (EHD) augmented two phase flow and heat transfer; describing the theories, terminology and introducing flow regimes and flow mapping. It then covered the relevant parameters that may affect the augmentation of the heat transfer coefficient and the pressure drop in the two phase flow system subject to EHD augmentation.

The main reason for a certain amount of ambiguity in most of the previous EHD augmented two phase flow research is that the heated sections were predominantly metal to facilitate the heat to transfer to or from the fluid. Hence, there is no direct visualization of the flow within the diabatic test section, and the observation was usually through a window at test section exit. Otherwise, flow regimes were hypothesised based on measurements, such as the wall temperature. In addition, only the average overall heat transfer coefficients were typically measured, because water jackets were generally used as heat source or sink.

Recently, McGranaghan [87] [15] overcame the visualization problem by introducing a test section made of a sapphire tube, which allows for optical access to the flow and allows for local or average heat transfer measurements at the same time. Additionally, he deposited a transparent conductive layer of Indium Tin Oxide (ITO) on the outside surface of the sapphire tube. This ITO conductive layer is connected to an electric power supply to work as source of heat and is also connected to the high voltage ground to generate the electric field.

Like most previous studies, McGranaghan et al. [87] [15] designed their test rig to facilitate the measurement of heat transfer augmentation and pressure drop in a horizontal flow boiling configuration. They categorized results into three distinct zones: at low voltages up to 3 kV, thermal gains and pressure drop increased moderately, while at medium voltages between 4 and 7 kV, thermal gains increased more sharply, as did the pressure drop. After 7 kV, the level of increase in thermal performance and pressure drop began to diminish. They concluded also that the heat transfer enhancement is largest at the entrance of the test section where the quality is

the lowest and reaches 7.2-fold locally at an applied voltage of 8 kV, as shown in Figure 3-20. At the exit region the enhancement decreases to 2.4-fold due to the lower level of the bottom stratified layer, making it more difficult for the EHD effect to redistribute liquid to the top surface. They concluded also that the bottom surface enhancement reached 4-fold at 8 kV and does not depend strongly on the local quality as the bottom surface is continuously wetted.

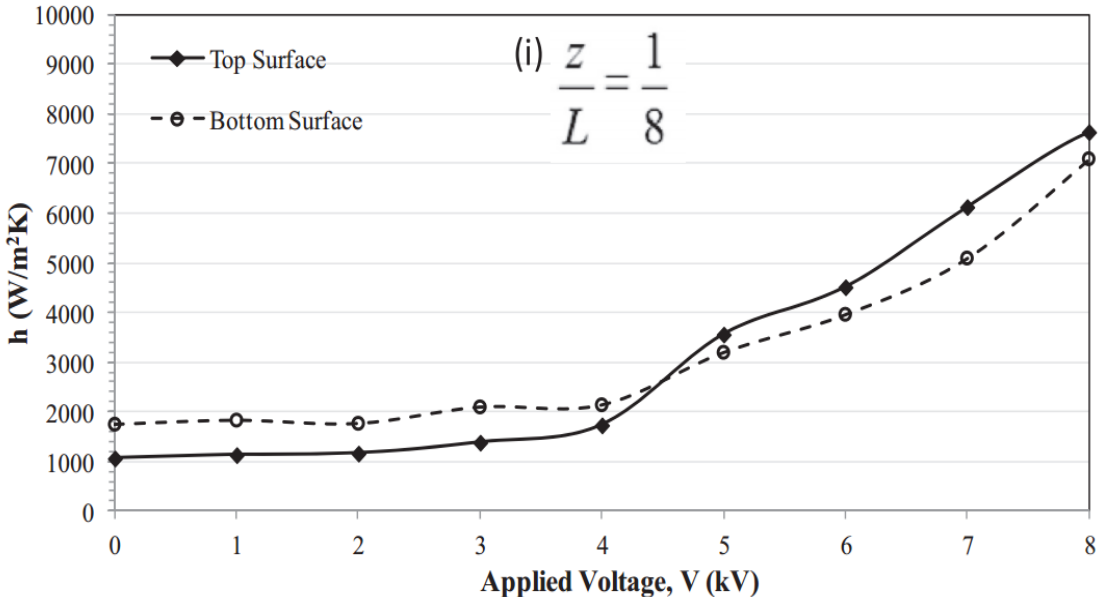


Figure 3-20. Heat transfer coefficient profiles at the entrance of the tube, G = 100 kg/(m$^2$ s), q"= 12.4 kW/m$^2$, P = 1 atm

The previous research almost entirely involves the investigation of EHD augmented horizontal two phase flow and all are performed in terrestrial gravity. Because of this, gravity is a dominant force that acts perpendicular to the flow, and due to the large density difference between the vapour and liquid phases, results in generally non-symmetric flow regimes i.e. predominantly stratified-type flows. The discussions above tend to revolve around the interaction of the stratified liquid layer and the electric field as a result of liquid extraction, due to polarization forces which tend to be a dominant for these types of flows. However, these flow regimes do not exist in vertical flow configurations and it is thus not possible to extrapolate the findings to the vertical orientation. Also, there is a growing interest in utilizing EHD in microgravity-based heat exchanger systems. Of course the stratified-type flow regimes will not exist in this scenario either. As a result we have little knowledge of EHD for flow regime types that exist in vertical and/or microgravity flows.

Thus, there is a clear gap in knowledge with regard to the influence of EHD for two phase flows which are not dominated by gravity. In particular, in a homogeneous bubbly flow, the EHD interaction with the flow and phases will be completely different to the horizontal terrestrial case where liquid extraction from a stratified layer tends to dominate.

The third major objective of the present investigation is to investigate and contribute to knowledge of EHD augmentation of vertical two phase flow. Using the new transparent and heated test section and local heat transfer measurements, the work will focus on vertical upflow and low to moderate vapour qualities and heat fluxes. In this way the work will focus on the EHD augmentation of homogeneous bubbly flows and heat transfer with particular focus on how EHD interacts with bubbles when AC waveforms and voltage magnitudes are varied. By eliminating the dominant mechanism of liquid extraction that overshadows other influences, it is hoped that this contribution will be relevant for both vertical terrestrial heat exchanger configurations as well as two phase heat exchangers in microgravity.

# Chapter 4. Experimental Apparatus and Methodology

## 4.1 Experimental Apparatus

The first version of the two phase flow loop was designed and constructed for horizontal flow EHD experiments by McGranaghan (2013) [87]. With this system as a starting point, it was redesigned and rebuilt to facilitate thermal and hydraulic measurements (temperature, flow, heat input, and pressure drop) for a vertical tube in convective flow boiling mode. In particular, a new test section was designed that can facilitate a high-voltage electric field to the flow from a concentric electrode, and observe the flow patterns through the test section and relate them with the physical measurements results in order to assess the effect of EHD on two phase flow heat transfer augmentation for vertical upflow.

The novelty of the apparatus stems from the transparent test section, which provides direct visual access to the flowing fluid. The test section is ohmically heated via an ITO coating deposited on a sapphire tube. Importantly, sapphire is thermally conductive and optically transparent. EHD is induced within the working fluid by an electrode concentrically fixed into the sapphire tube and connected to a high voltage power supply, with the ITO coating on the tube as the other electrode.

A schematic of the test facility is shown in Figure 4-1. It consists of a primary closed stainless steel piping flow circuit charged with HFE7000 as the working fluid and an instrumented transparent test section for measurement and observation of convective boiling. The secondary flow loop circulates chilled water to condense the working fluid.

HFE 7000 (methylperfluoropropylether) is a new-generation heat transfer fluids with a low global warming potential intended to replace traditional chlorofluorocarbons (CFC) type refrigerants, manufactured by 3M Corp. A key factor in its selection was its boiling temperature of 35°C at 1 bar, which allows for low saturation temperature experimentation at low gauge pressures (see Table 4-1), which allows the rig to operate at a low pressure differential to atmosphere, thus the high pressure compressor and sealing arrangements are not needed. Furthermore, the low boiling temperature reduces heat losses from the heated test section and HFE7000 has a high electrical permittivity which is ideal for EHD experimentation.

Table 4-1. Properties of HFE7000 @ 25°C (from 3M Corp) [111]

| | | |
|---|---|---|
| Molecular Weight | 200 | g/mol |
| Freeze Point | -122.5 | °C |
| Boiling Point | 34 | °C |
| Liquid Density | 1400 | $kg/m^3$ |
| Kinematic Viscosity | 0.32 | $mm^2/s$ |
| Kinematic Viscosity @-80°C | 2 | $mm^2/s$ |
| Kinematic Viscosity @-120°C | 17 | $mm^2/s$ |
| Coefficient of Expansion | 0.00219 | $K^{-1}$ |
| Critical Density | 553 | $kg/m^3$ |
| Critical Pressure | 2.48 | MPa |
| Critical Temperature | 165 | °C |
| Permittivity (Dielectric Constant) | 7.4 | - |
| Dielectric Strength | ~40 | kV |
| Latent Heat of Vaporization | 142 | kJ/kg |
| Solubility of water in fluid | ~60 | ppmw |
| Solubility of air in fluid | ~35 | vol % |
| Specific Heat | 1300 | J/(kg K) |
| Surface Tension | 0.0124 | N/m |
| Thermal Conductivity | 0.075 | W/(m K) |
| Vapor Pressure | 64.6 | kPa |
| Volume Resistivity | 1.08 | ohm-m |

### 4.1.1 The Primary Loop

The main components in this primary loop are the pump, electrical heater, test section, condenser and pressure control vessel.

The working fluid is circulated with a pump through the electric pre-heater, the test section and the condenser. As depicted in Figure 4-1, the refrigerant flows through a filter/dryer (Carly DCY164) before it enters a closed gear pump (Micropump type GN-N23). The pump circuit also features a bypass and is coupled to a 3 phase variable speed motor to control the mass flux. The flow rate is then measured by a Titan Instruments 945 turbine flowmeter that can measure flows ranging from 0.2 to 4.5 L/min with an accuracy within ±3%.

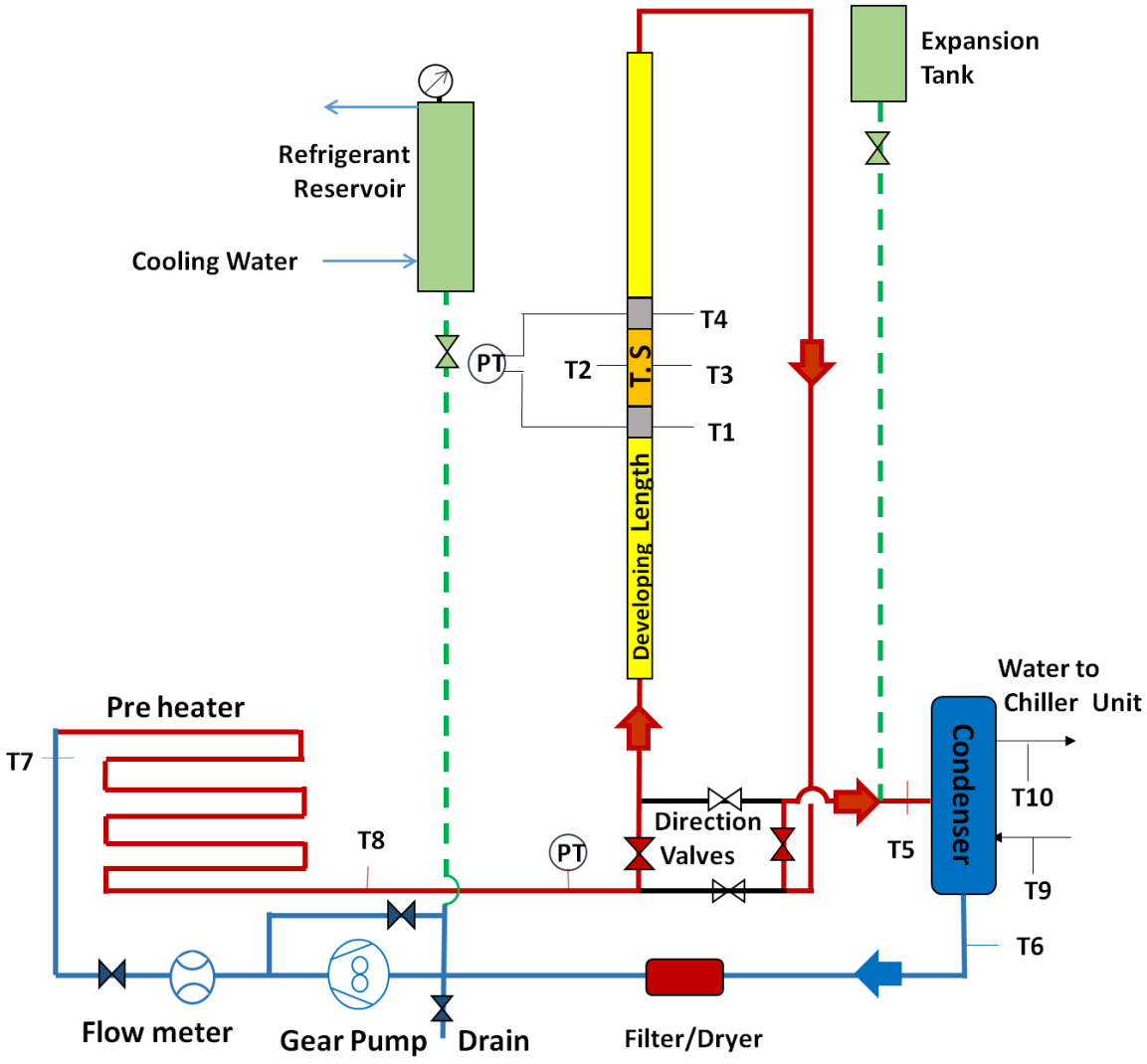


Figure 4-1. Schematic representation of the rig

The flow enters the pre-heater which is a 1.27 cm outside diameter electrically heated steel tube of overall length of 2.95 m that is bent into a serpentine configuration. The somewhat long section ensures that sufficient heat can be transferred to the working fluid at low to moderate heat fluxes, well below the critical heat flux. The electrical current flows in the tube wall, and the tube resistance facilitates Joule heating of the tube which is transferred to the fluid. The entire preheater is wrapped in sufficient insulation that heat losses to the ambient are negligible. The pre-heater is connected to the main flow loop with dielectric fittings see Figure 4-2 (SWAGELOK SS-8-DE-6). The range of power required and the power supply specification are listed in Appendix A. An Agilent Technologies System power supply (N5742A DC) was selected and connected to the tube ends and used to control the outlet thermodynamic state of the working fluid which is then routed to the test section.

Figure 4-2. New pre heater design

It is important to keep the thermodynamic quality of the working fluid within the preheater low enough that the risk of local dryout and “hot spots” forming on the steel tube surface is mitigated. The constant heat flux of the electric power coupled with a vapour barrier may cause high temperatures to occur on the heater surface and cause degradation of the fluid, as the maximum heat flux of 18 W/cm$^2$ is specified by 3M [54] for HFC 7000. For the experiments considered here, the fluid exit was slightly subcooled such that the fluid was in a liquid state throughout the test section.

With the fluid in a liquid state, the quantity of heat transferred from the pre heater to the working fluid can be calculated from the sensible energy change across the heater section, using the measured flow rate and working fluid inlet and outlet temperature difference, as logged by two calibrated type T thermocouples. The heat gained is given by the expression:

$$Q_{pre} = \dot{m}_{refr} C_{prefr} (T_8 - T_7) \tag{62}$$

An electrical connection is provided to measure the voltage and supplied to the electrical pre heater in order to perform an energy balance. It can also be used to estimate the exit enthalpy, and thus quality, for cases when the exit is a two phase flow. The electrical heat supplied is simply calculated as;

$$Q_{pre} = V_{pre} \times I_{pre} \tag{63}$$

A 0-10 bar electronic pressure transmitter (Bourdon Sedeme type E7-13) measures the fluid system pressure ($P_{in}$) at the exit of pre heater. For single phase flow, the pressure and associated temperature measurement at the exit is sufficient to determine the fluid thermodynamic state. If two phase flow is desired at the exit, the thermodynamic state can be determined with knowledge of the heat supplied to the working fluid.

As shown in Figure 4-5, the working fluid is routed from the pre-heater to the test section where it is forced upward through a 400 mm long developing length of 8 mm ID glass tubing before entering the main heated test section. Glass was used in order to visualize the inlet flow regime. For the cases studied here where the flow is slightly subcooled, the transparent developing length was used to ensure no bubbles were entering the test section. During testing, the section was wrapped in insulation to reduce heat losses to the ambient.

On exiting the test section, which will be discussed later, the working fluid continues flowing upward through another 400 mm length of glass tube, identical to the lower developing length section. At the top of the test section the refrigerant exits the glass tube through a machined fitting with an exit port machined with a $135^o$ angle to

reduce the elbow pressure effect that would occur with an abrupt right angle fitting see Figure 4-3.

As there is an elevation change from the test section inlet to the test section level, another pressure transmitter (Omega PX4201) was installed to record the pressure ($P_{exit}$) exiting the test section. This pressure reading allows a correction of the quality to be re-calculated as the two-phase fluid exits the test-section.

The working fluid is condensed in a compact plate heat exchanger supplied with cold water from a temperature controlled chiller unit (Thermo Scientific Accel 250 LC).

All the piping and equipment are contained within a framework constructed of modular aluminium profile bar (Bosch Rexroth) which allows for flexibility and modification. Most of the joints in the primary and cooling loops are Swagelok fittings except for some threaded joints which were sealed with epoxy adhesive. The main sapphire tube test section pressure sealing were fabricated in-house and tested satisfactorily to 2 bar, where the normal rig operating pressures range between 1.2-1.6 bar.

For the purpose of redesigning the system, the rig is required to be drained often. A drainage tap at the bottom of the rig is thus used for this purpose, see Figure 4-1. The refrigerant is collected in a clean bottle for reuse. Fresh refrigerant was used for the final tests.

To fill the rig with refrigerant, the rig is first vacuumed up to ~ -100 kPa through the refrigerant reservoir to remove air from the system. A flexible pipe, connected to the drain is immersed in refrigerant bottle, the valve opened slowly and the refrigerant allowed to flow into the rig up to the test section.

Preliminary tests found that air was still inside the system, and the following degassing procedures was carried out; the reservoir is connected to a tank was charged with a vacuum; the rig is operated and the vent valve slowly opened and the gas is collected at the reservoir vessel; the vacuum tank valve is slowly opened to allow the collected gas to carry over to the vacuum tank; the valve is closed and the

system run again allowing gas to reach the top of the system; the gas is vented off to the vacuum tank. It takes several charges of vacuum and recovery to get the rig to an acceptable working state. Once achieved, one charge every few days is sufficient to keep the rig gas free.

### 4.1.2 Test Section

The test section consists of a developing length, an electrically grounded transparent sapphire tube with a concentric electrode held in polypropylene supports, pressure taps and accompanying thermocouples.

In previous studies involving two-phase flow and EHD, the test section materials were typically fabricated from stainless steel or other metal [5, 8, 9, 11, 12, 28-30, 61, 68, 76, 77]. While this satisfied the engineering considerations of strength, corrosion resistance, electrical grounding (for EHD), electrical conductivity (for resistance heating) and high thermal conductivity, they have the disadvantage that flow regimes could not be observed directly over the heated length and had to be inferred from thermocouple measurements in the test section wall, utilising void fraction measurement by capacitive means or by using exit adiabatic glass viewing sections. As a result, the flow regimes are either hypothesized from measurements or are from what has been observed in adiabatic conditions. To the best of knowledge, there do not exist any flow regime maps that have been developed from direct visualization of diabatic vertical flow boiling. Similarly, heat transfer studies do not exist for vertical flow boiling where direct observation of the flow regime is available to correlate with the heat transfer behaviour. In other studies, transparent sections have been used with thin electrically conductive layers to afford Ohmic heating, but suffered from the drawback of limited heat flux capacity (e.g., [13]) due to burnout. The traditional solution is to provide a viewing section outside of the heat exchanger (e.g., [38]) but this remained separate from the main heat transfer area under study and is not representative of the boiling physics where the heat transfer is taking place. A test section fabricated from glass was investigated for the current study, but modelling showed that the low thermal conductivity of 1-1.5 W/m.K inhibited the effective heat transfer to the working fluid, resulting in excessive temperatures and significant heat transfer losses to the environment. Modern ceramics were then investigated and

aluminium oxide ($Al_2O_3$), or sapphire, was found to be available in various form, with acceptably high transparency (up to 86% in the visible spectrum) and with a thermal conductivity bettering that of stainless steel (25 W/mK versus 15 W/mK). In the investigation being described, use of a custom ordered transparent sapphire tube supplied by Cradley Crystals, Nizhny Novgorod, Russia was used. The tube was then coated with a 600 nm of Indium Tin Oxide (ITO) to allow for resistive heating of the outer tube wall, as well as the low voltage potential of creating the electric field. This thus allowed for the simultaneous measurement of the heat transfer while permitting visualisation of the entire flow field.

The first element of the test section is a developing length of glass tubing of outer diameter 10 mm, inner diameter 8mm and length of 400 mm (50 diameters) to allow the flow to fully develop before entry to the sapphire heated test section.

The test section is a 120 mm long transparent sapphire tube of 10 mm OD and 8 mm ID supported in two machined polypropylene supports (Figure 4-3), which are in turn securely bolted to the test section frame and connected to the glass tubes from the other ends as shown in Figure 4-3. Importantly, the polypropylene supports are designed in such a way that there is a smooth transition between the sapphire section and the upper and lower glass sections to minimise unwanted disturbances in the flow due to the transition joints. The polypropylene supports also contain ports to allow for a differential pressure measurement to be made across the test section as well as thermocouples for the fluid temperature measurement.

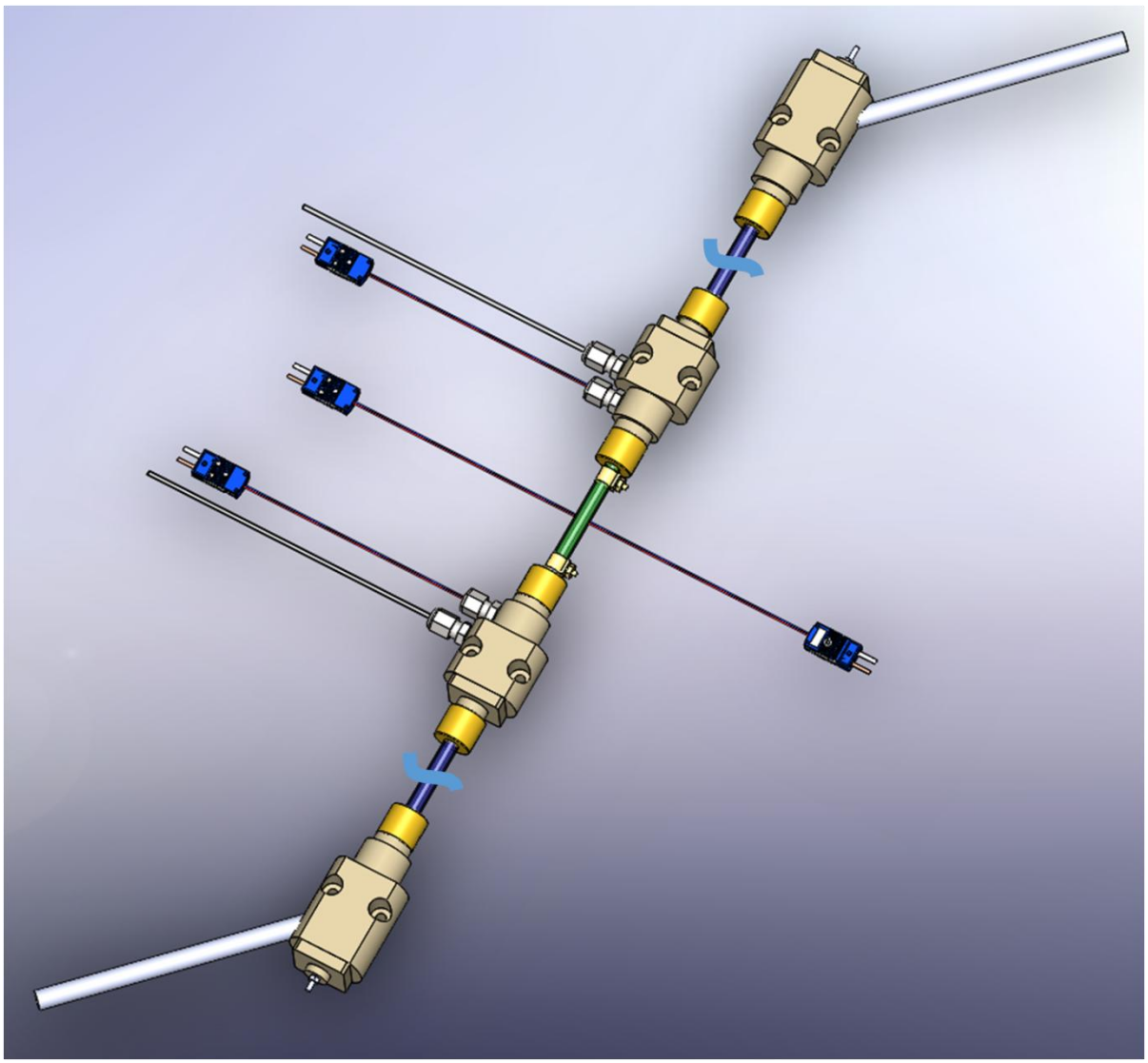

Figure 4-3. Test section 3D diagram

Polypropylene was chosen over other polymers for its balance of good electrical insulation qualities and chemical resistance to HFE7000. A complete guide to the choosing of polypropylene is given in Appendix B.

The sealing of the sapphire tube in the support is accomplished by a butyl rubber O-ring compressed by a threaded brass gland against the polypropylene support (see Figure 4-4).

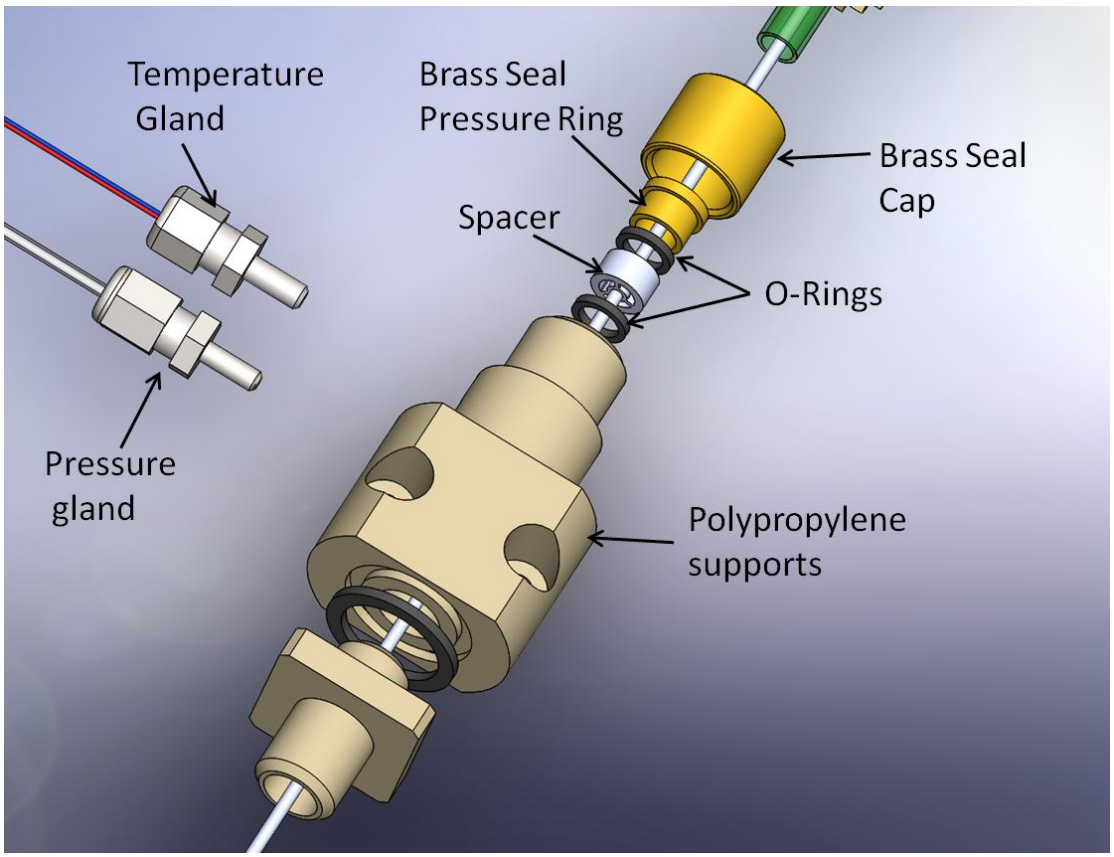


Figure 4-4. Polypropylene supports, O-rings seal and seal cap

An electrically conductive thin layer of indium tin oxide (ITO) of thickness 600 nm was deposited around the outer circumference so as to provide the electrical ground for high voltage EHD tests as well as supplying heat to the working fluid by resistive heating facilitating boiling of the working fluid. The latent heat absorbed by the working fluid changes the thermodynamic quality, and hence the flow regime varied along the test section.

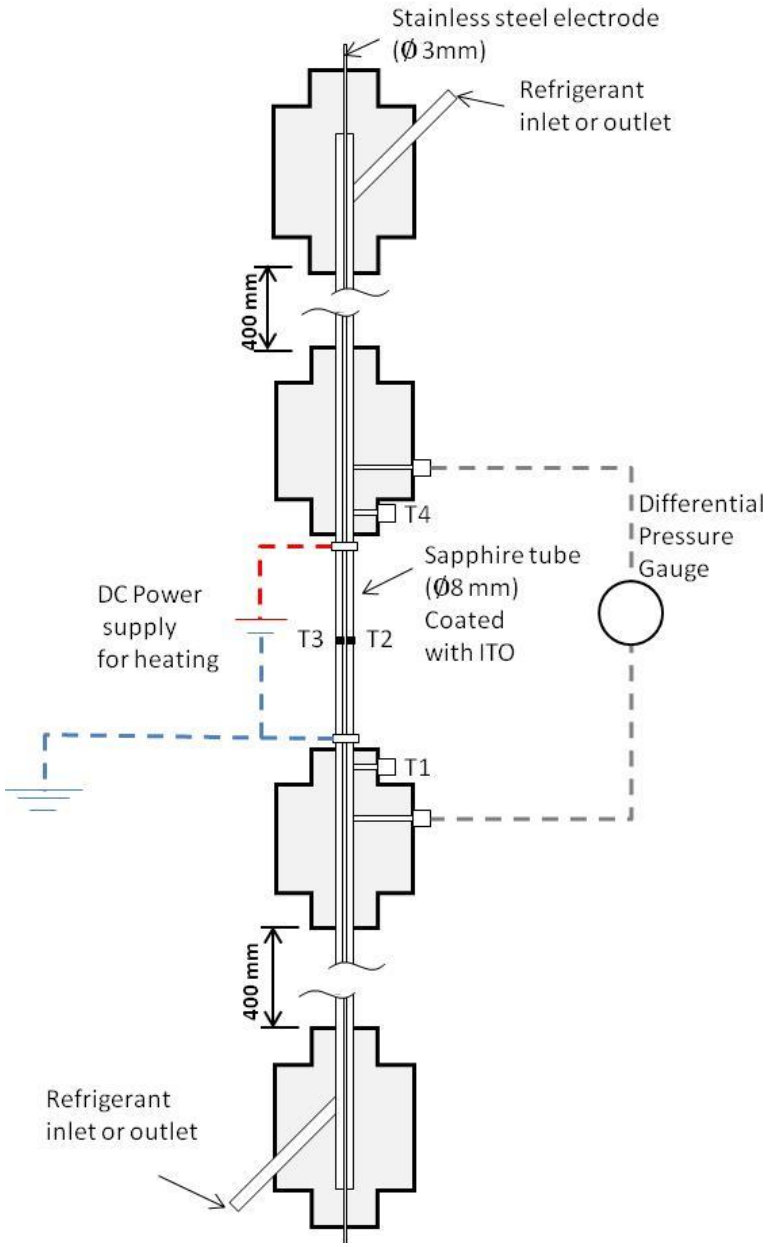


Figure 4-5. Schematic representation of the test section

The sapphire tube has two pockets, one left and one right, 0.5mm diameter by 0.5mm deep drilled into the tube wall at the middle of tube length where embedded type T miniature thermocouples (Omega type TMQSS-020(G)-6) are placed to record the wall temperature. The thermocouples are thermally insulated by a polyethylene sleeve to protect against axial thermal conduction, after which the tip is potted into the 0.5 mm deep pocket by a small amount of temperature resistant epoxy adhesive, as shown in Figure 4-7.

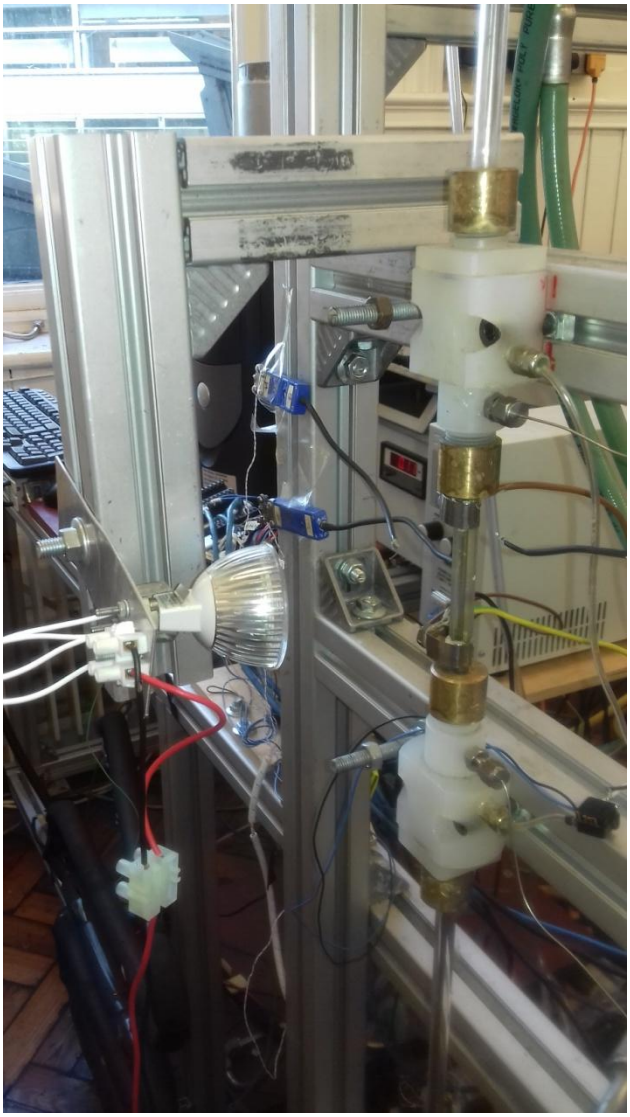

Figure 4-6. Test section showing developing length, sapphire tube and polypropylene support pieces

The pressure drop across the sapphire test section is measured by a Taylor DP504T 0-70 mbar differential pressure sensor; the pressure tappings can be seen in Figure 4-7. The thermocouple sealing and pressure compression sealing glands are shown in Figure 4-7.

Figure 4-7. Type-T thermocouple with sealing gland

The ITO coated tube is heated ohmically when electricity flows through the coating and this heat conducts across the sapphire to the working fluid. Due to the relatively high thermal conductivity of sapphire (~25 W/mK), the tube itself offers a very low thermal resistance which results in a low temperature drop across the tube and thus low ITO temperatures for a given heat flux. This reduces heat transfer to the ambient surroundings to negligible levels considering the low boiling temperature of HFE7000. Power to the ITO is supplied by EA-PS 8360-10 T EA ELEKTRO-AUTOMATIK power supply. Similar transparent ohmic heaters are already in use in similar flow boiling studies by Colin [81] and Ohta [13] who use an ITO layer on sapphire and a gold film on glass respectively. Regardless, this is a relatively new measurement technique for two phase flow research and vertical upflow boiling has not been considered in the literature.

The heating was accomplished by a ITO coating of 600 nm thickness which also functioned as the EHD ground, but also permitted sufficient current flow to allow electrical heating. The test section with the ITO coating conductivity of 10 Ω/sq led to

a total resistance of roughly 32Ω (see Equation (64)) permitting ohmic heating at lower voltages of around 100 V.

$$R = R_s \frac{L}{W} \tag{64}$$

where $R_s$ is the sheet resistance in (Ω/sq), L and W are length and width of the sheet respectively.

The current is provided via terminal clamps affixed to a ring of conductive adhesive forming annular bus bars at each end of the tube, see Figure 4-8.

Figure 4-8. Test section, conductive clamps and thermocouples position

In practice, the maximum current was around 1.6 A and the maximum voltage was regulated at around 70 V so as to provide about 110 W heat input into the refrigerant at the highest heat flux. An electrical schematic of the test section is shown in Figure 4-11.

### 4.1.3 The Electrode and High Voltage Supply

To apply the EHD forces across the flowing dielectric fluid, a circular stainless steel rod of 3 mm diameter and 1300 mm length runs concentrically along the inside of the of the test section. For flow continuity, the rod ran the entire length of the developing and exit glass tubes as well. The rod acted as a high voltage electrode and created an annulus with a 2.5 mm gap thickness to test the effects of moderate confinement, as may be encountered in tube-and-shell-heat exchangers. Two tripod support pieces locate the electrode concentrically within the polypropylene (Figure 4-9) and prevented excessive oscillations of the electrode inside the tube induced by the EHD and fluid forces. These spacers are inserted at the two ends of sapphire tube, see Figure 4-4.

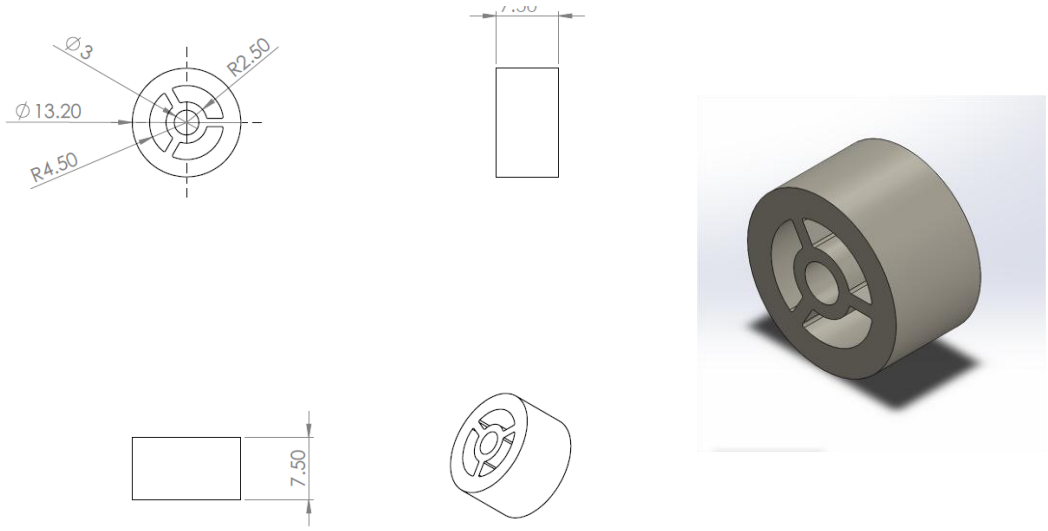


Figure 4-9. Tripod spacers support

The electrode is threaded at the each end to permit tensioning of the electrode and secure attachment of the high voltage connection at one end.

As mentioned, a thin layer of indium tin oxide (ITO) with a thickness of 600 nm and a conductivity of 10 Ω/sq was deposited around the entire outer circumference providing a ground for the high voltage and allows for adequate visualization of the two phase flow. The transmissibility of the ITO coating is given in Appendix C. A ring of high silver content adhesive provides electrical continuity to the ITO coating. A steel clamp affixed to the annular adhesive ring completes the grounding via a wire to the rig frame (see Figure 4-10).

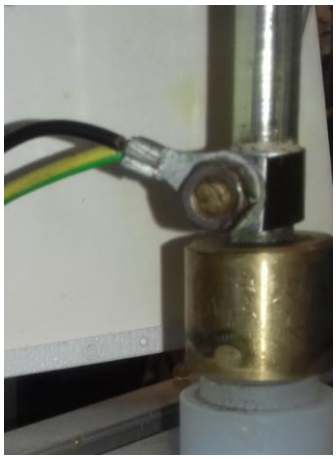

Figure 4-10. Conductive clamp

A Matsusada AMT series 0-10 kV high voltage amplifier supplied the high voltage to the electrode. A TG 1006 function generator delivers the primary signals of amplitude and frequency to the amplifier. The high voltage amplifier features current and voltage monitor outputs which can be used to record actual current and voltage parameters of the high voltage waveforms.

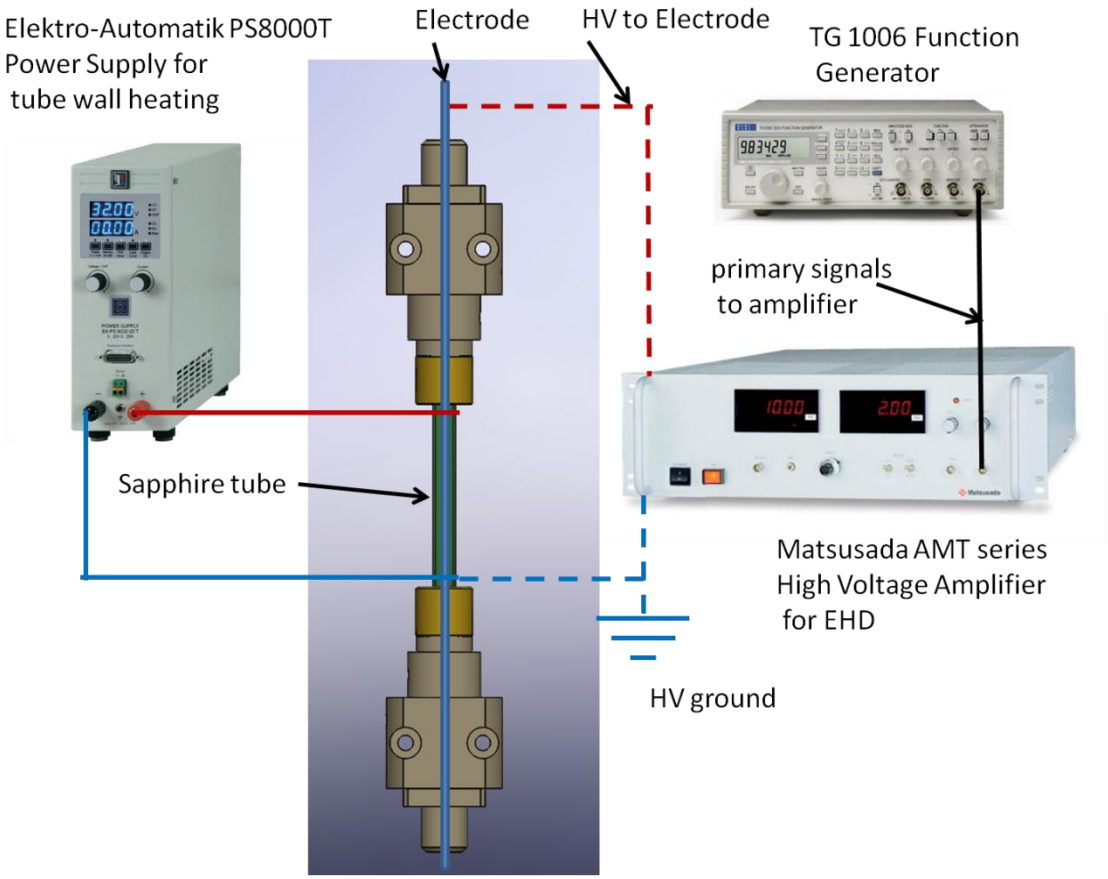


Figure 4-11. Electrical schematic of the test section

The fluid temperatures are measured at various locations in the loop using seven Type T thermocouples, 150 mm long and 1.5 mm diameter as depicted in Figure 4-1. A further two type T thermocouples were imbedded into 0.5 mm deep pockets machined into the wall of the sapphire tube to measure the wall temperature half way along the length of the tube see Figure 4-12.

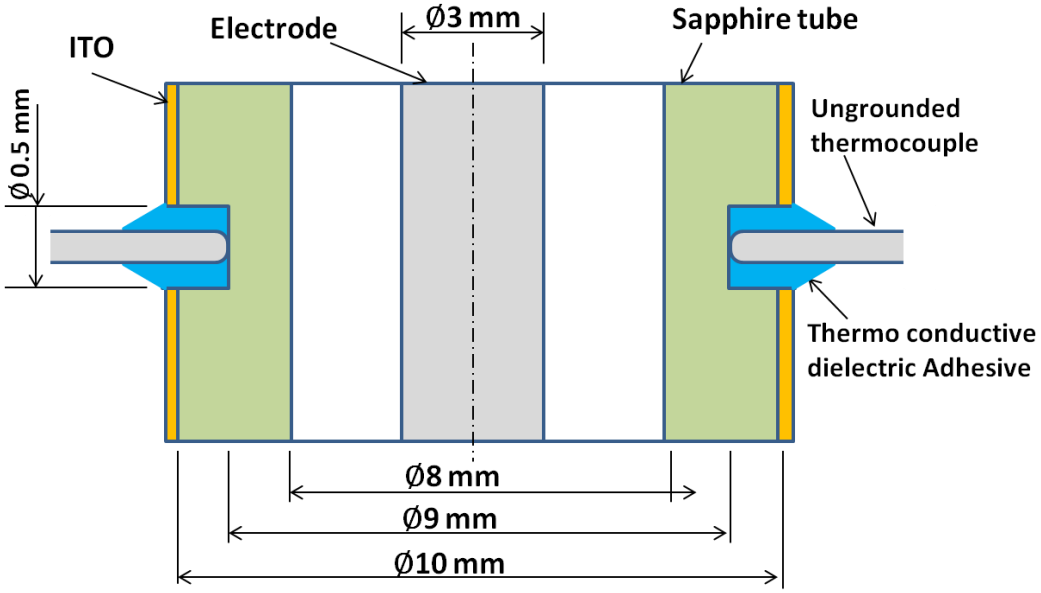


Figure 4-12 Two ungrounded T type thermocouple imbedded into into the wall of the sapphire tube

Two flow meters were used; one turbine type 0 - 4.5 L/min (Titan Instruments 945) was used for the refrigerant in the main loop and a turbine type (Gems FT-110, 1-10 L/min) was used for the water flow rate in the chillers loop.

To measure the pressure drop across the test section, a differential pressure transducer (Taylor DP 504T) was used.

### 4.1.4 The Cooling Loop

After the two-phase working fluid leaves the test section, the mixture enters a compact plate heat exchanger (up to 52 kW) where it is condensed by a stream of cooling water pumped from a controlled chiller unit (Grant RC1400G). The cooling water flow rate is regulated by a gate valve and bypass. T-type thermocouples monitor the water temperatures at the condenser inlet and outlet, and again at the working fluid inlet and outlet. The heat extracted from the working fluid balances that gained by the condensing water stream. The heat transferred to the cooling water in the condenser is calculated as,

$$Q_{con} = \dot{m}_{water} C_{water} (T_{10} - T_9) \tag{65}$$

### 4.1.5 Expansion Tank and Refrigerant Reservoir

An expansion vessel, shown schematically in Figure 4-1, is fitted before the condenser in the primary loop to mitigate pressure fluctuation and maintain the system at a steady thermodynamic state. A stainless steel reservoir, fitted with a cooling water jacket, is also connected to the system prior to the pump. The cooling jacket maintains the pressure inside the vessel to one that is lower than the rig operating pressure to aid in the removal of non-condensable gas, and allows for safe venting of excess pressure at any time.

The system pressure is monitored manually by means of the electronic pressure transmitters (Bourdon Sedeme type E7-13). In addition, the vessel is connected at all times to an external vacuum vessel, allowing a vent if rig pressure were to increase to high levels. This external vacuum vessel also allows the system to be scavenged of air or non-condensable gases (NCGs) from bleed locations at the test section exit and from the top of the reservoir vessel. Any refrigerant liquid carried over during purging of NCG settles in the bottom of the vessel and can be recovered via a drain valve. After draining refrigerant from the vessel, a vacuum pump is used separately to replenish the vacuum in the external vessel, thus keeping refrigerant losses to a minimum.

Various ancillary valves on the loop allow for flow pressure control, removal of non-condensable gas and drainage.

## 4.2 ITO Coated Sapphire Tube

While it is believed that this is one of the first times that this type of novel test section has ever been used, which incorporates thermal conductivity, an electrical ground, and all the while allowing full visual access to the flow, there are a number of characteristics that made the test section differ from conventional metallic test sections. These are briefly considered in the next sub-sections.

### 4.2.1 Thermal Conductivity Considerations of the Sapphire Tube

Sapphire thermal conductivity is as around 25 W/(m K) (see Appendix F) depending on manufacturing method, individual suppliers etc. The relative importance of

convection heat transfer to the fluid or conduction through the tube wall is measured by Biot number (Bi), and it is defined as:

$$\mathrm{Bi} = \frac{\mathrm{R_{cond}}}{\mathrm{R_{conv}}} = \frac{\mathrm{h}L}{\mathrm{k}} \tag{66}$$

where h is the convective heat transfer coefficient on the inside of the tube, L is the characteristic length, in this case the sapphire tube thickness, and k is the thermal conductivity of the sapphire tube wall. The Biot number values smaller than 0.1 means that the heat conduction across the tube material is much less restricted than the heat convection to the fluid, and temperature gradients are negligible across its thickness.

The Biot number for the tube in the radial direction was found to be less than 0.1 for boiling conditions, see Figure 4-13, which means that the conduction resistance is very small and the convective process is the dominant resistance in the thermal network circuit. Given the low Biot number of the tube, the temperature through the tube wall in the radial direction can be assumed uniform.

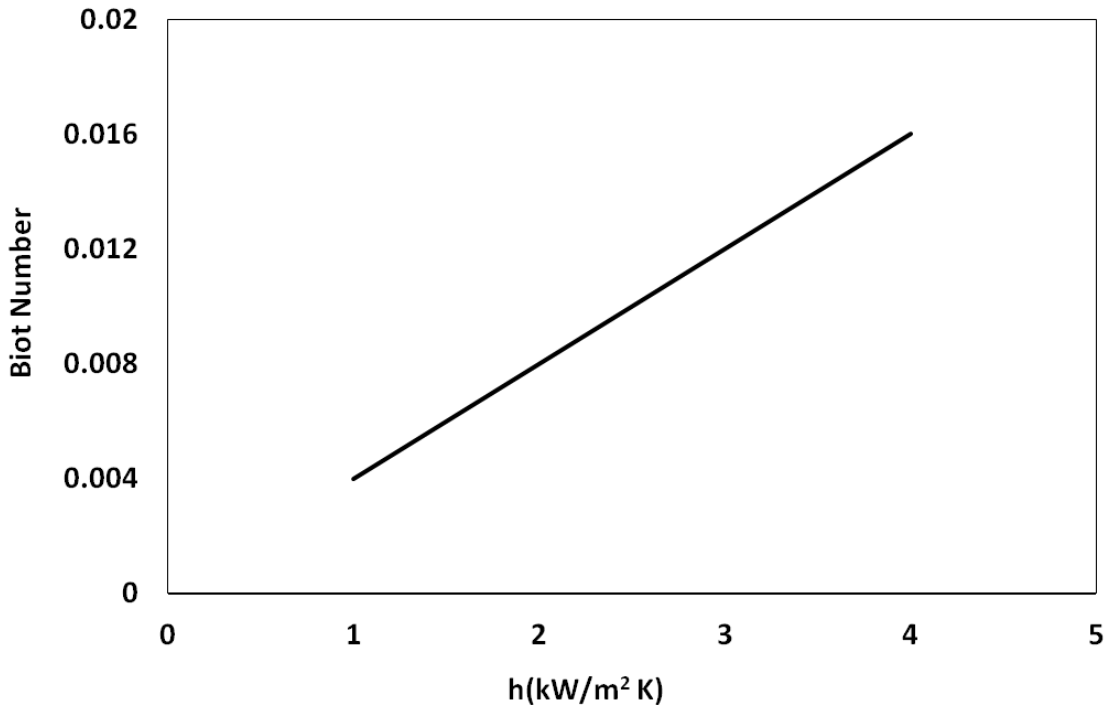


Figure 4-13. Biot Number for boiling conditions

### 4.2.2 Surface Finish of the Tube.

The sapphire tube was supplied by TYDEX “as grown” by Stepanov method (analogue of EFG process, see Appendix F). It was drawing from a molten pool of aluminium oxide (Al2O3). This method is fast and relatively inexpensive but dimensional accuracy can vary. The tube was not ground or polished though was glassy and smooth. Although these would have improved optical properties of the tube, very smooth surfaces are not ideal for boiling and there much be a trade-off between flow visualization and boiling surface quality.

The sapphire tube surface roughness was tested by a 3D optical White Light Profilometer (WLI). The results shows surface roughness of about 0.2 µm, with patches that can be up to 0.7 µm, see Figure 4-14 . This is ideal since machined metallic surfaces have surface roughness typically in this range [112].

The tube has some undulation and a slight bow of around 0.5 mm along its length. Some glassy undulations or ribs were also visibly noticeable on the tube. The surface of the sapphire tube may be somewhat different from an equivalent metallic tube, especially in relation to wetting characteristics and the ability of the tube to create nucleation sites, especially since HFE7000 is a highly wetting fluid. This may cause a large overshoot in superheat for the Onset of Nucleate Boiling (ONB) and thus boiling hysteresis. However, the fairly rough surface should provide adequate nucleation sites once boiling has commenced.

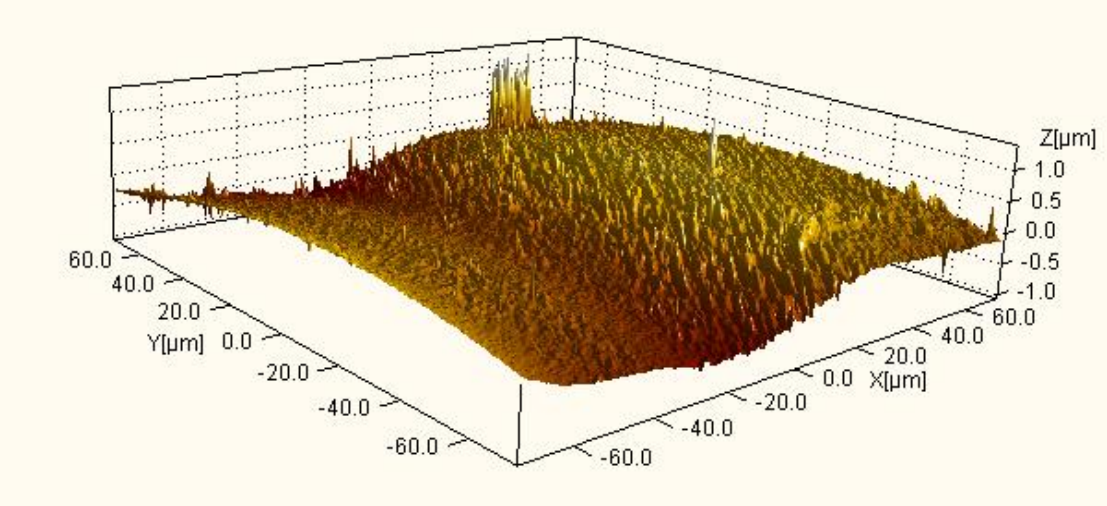


Figure 4-14. WLI image of the sapphire tube

### 4.2.3 Variation in thickness of the ITO coating thickness.

One of the major issues which may affect the whole boiling process is the non-homogeneous distribution of the ITO coating and possible non-uniform heat flux. Measurement of the ITO coating thickness is not possible, however, while Diamond Coatings Ltd. gives assurances of an evenly distributed coating over the tube. IR images of the heated tube tend to confirm this and, regardless, any small variations in the heat flux on the outer tube will be evened out at the inner surface due to heat spreading within the tube wall.

### 4.2.4 Data acquisition

The data acquisition system consisted of one National Instruments Compact DAQ 9172 8-slot chassis unit with several types of modules used depending on the

measurement taken (see

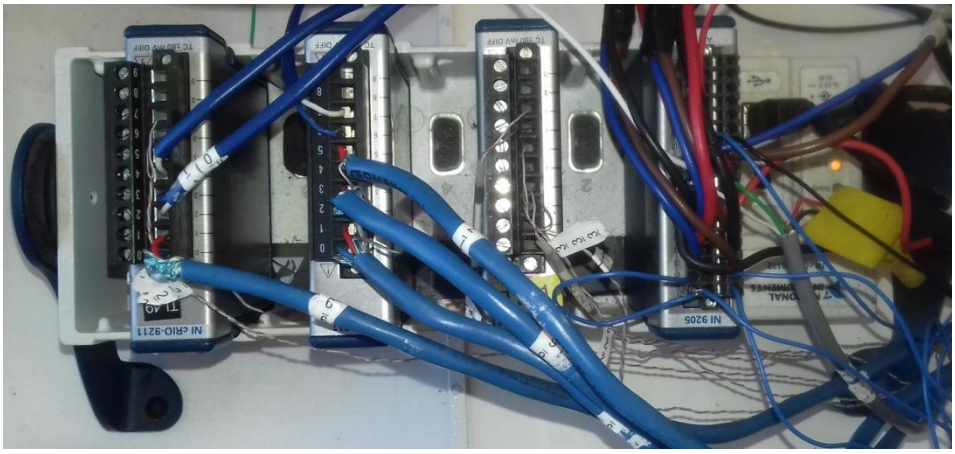

Figure 4-15). Three NI9211 4-channels thermocouple modules which have an accuracy of 0.07°C over the entire range were used for test section embedded T-type thermocouples and the remainder of the T-type thermocouples throughout the facility. The NI9211 modules featured integral cold junction compensation circuitry. One NI9205 module with an accuracy of ±200 mV over a range of ±10 V [113] was used for the high level analogue signals such as pressure, flow meters output and power measurements for the heater, the pre-heater and the high voltage monitoring.

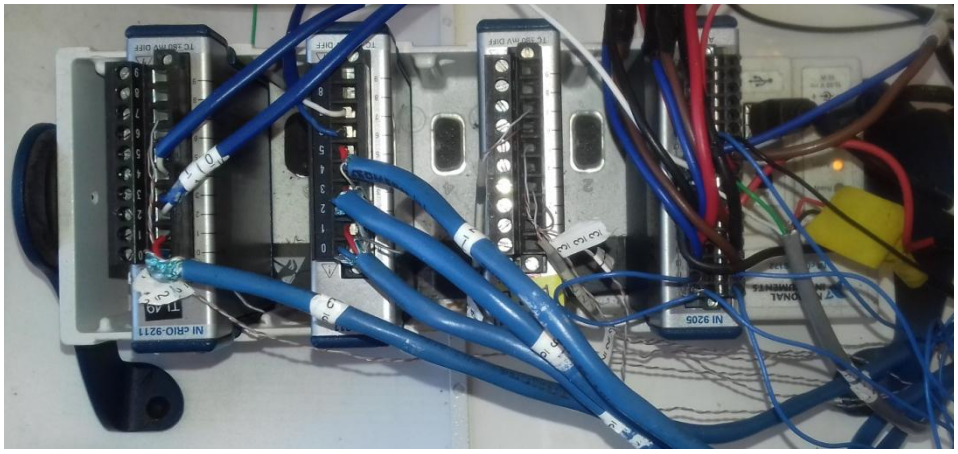

Figure 4-15. Data logging hardware

An Omega HCTB-3020 thermal bath calibrator was used to calibrate all thermocouple inputs against a reference 4-wire thermistor (type General Electric ES-215) accurate to 0.01°C and HP 34401A multimeter.

Temperature, pressure and flow were measured directly from instruments, while other fluid properties which vary with state are calculated indirectly from polynomials generated from look-up tables in Excel.

The water circuit was open and nominally at atmospheric pressure therefore the properties are calculated at the measured temperature and the influence of pressure was neglected. The HFE7000 working fluid was flowing within a closed loop and subjected to phase change, pressure and temperature variation. Variations of fluid properties such as density, viscosity, specific heat and latent heat were considered as functions of temperature by generating respective polynomial curve fits from look-up tables supplied by 3M Corp, see Appendix D. These polynomials were input into the Labview to enabled computation of water and HFE7000 properties. Table 4-2 shows a list of calculated properties, see Appendix D.

Table 4-2. Summary of Fluid Properties Determined from Temperature and pressure

| **Fluid** | **Property** | **Data Source** |
|---|---|---|
| **Water** | $\rho$ | NIST [83] |
| | $\mu$ | NIST |
| | $C_p$ | Rogers and Mayhew[82] |
| **HFE7000** | $\rho$ | 3M Corp |
| | $C_p$ | 3M |
| | $h_f$ | 3M |
| | $h_{fg}$ | 3M |

A program to display and collect data was developed using Labview®. The front panel of the programme shows the rig in schematic form with all measured parameters, see Figure 4-16. The program collected data at a frequency of 10Hz and saved data for 10 second when required, this was employed when the rig achieved steady state for heat transfer measurements.

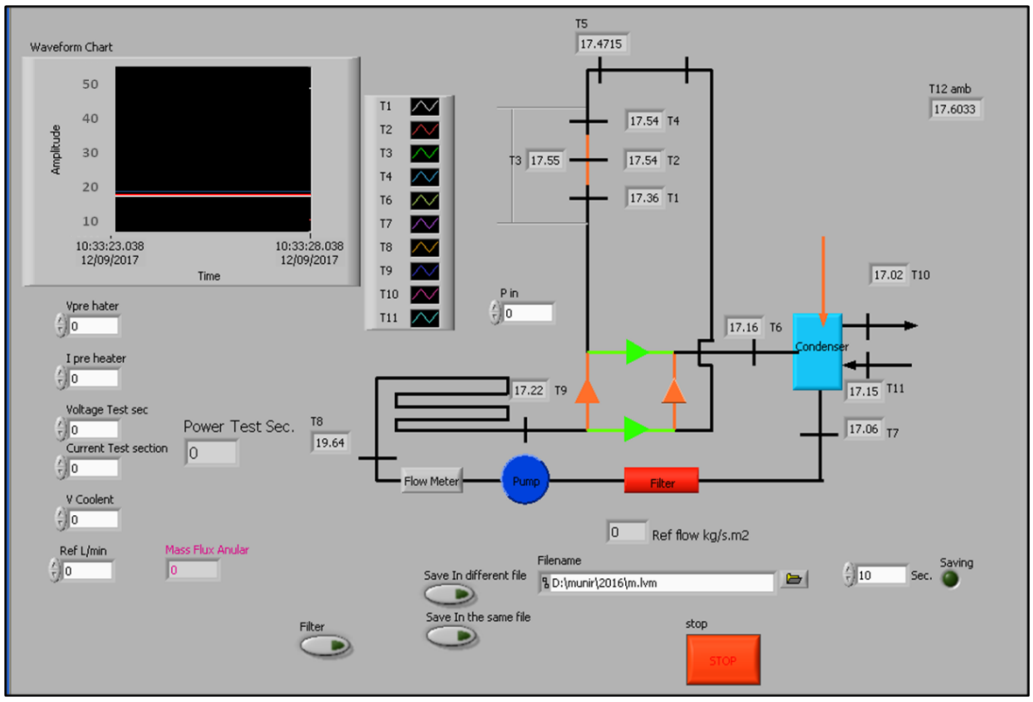


Figure 4-16. Front panel of Labview® data acquisition program

## 4.3 **High Speed Imaging System**

A black and white high-speed (HotShot 1280 cc) (NAC Image Technology) camera with its associated software was used for high speed videography of the two phase flow through the transparent ITO-sapphire test section for each experiment.

LED cluster lamps (Fawoo LH-03) of 240 lumens provides a backlighting for the test region of the sapphire tube. Images were recorded at a shutter speed of 1000 f/s in order to capture rapid vapour and liquid movements caused by the flow or EHD force.

The camera field of view is 280 x 1072 pixels and the acquisition frequency is 1000 images per second. The spatial resolution of the images is 53.3 pixels/mm. The field of view is such that the entire 120 mm heated section could be viewed and recorded.

One second worth of data were recorded and stored as videos for each test point, which include 1000 frames for later analysis. Most important videos can be viewed using QR codes in various location though this thesis.

## 4.4 Experimental procedure

There were three series of experiments carried out in this investigation. The main parameters of interest in this research are the fluid mass flow rate, the heat flux and the EHD voltage magnitude and frequency.

In the first test series the mass flux was varied (50 kg/($m^2$ s), 100 kg/($m^2$ s), 200 kg/($m^2$ s) and the heating power was increased incrementally nearly to the CHF, and boiling curve and heat transfer coefficient was plotted vs the heat flux and flow maps were plotted for different thermodynamic quality.

In the second test series the mass flux was again fixed at G=100 kg/($m^2$ s) for all tests, the heat flux was set for low and high flux, the EHD voltage was set at 8 kV and the EHD frequency was varied from 1 Hz to 1000 Hz.

For test series one, the aim is to investigate local heat transfer coefficients at the midpoint of the tube. While this allowed measurement of the heat transfer coefficients at the imbedded thermocouple location, this test section has the shortcoming of not providing an overall heat transfer coefficient.

In test series two the main focus was on the influence of EHD and thus the heat flux across the test section was fixed. This was achieved by adjusting the electric power across the test section so that 110 W of heat was transferred to the refrigerant for all tests. This power setting was chosen as it was sufficient to achieve fully developed boiling though was safely below CHF.

The experiments were performed by setting the working fluid flow rate and the thermodynamic state at the inlet of the heated test section by adjusting the pump and pre-heater settings respectively. In this work the inlet thermodynamic state was set with a nominal subcooling of 2$^{o}$C to approximate saturated inlet conditions. The small degree of subcooling was required to ensure single phase flow at the inlet. Subsequent to this, heat to the ITO was initiated and the heat flux then increased in increments, keeping all other parameters constant, and allowing the system to stabilize at each heat flux setting before recording of data. The results are presented in the form of boiling curves, heat transfer coefficients and flow regime maps. Due to the damaging

effect of excessive temperature on the ITO heater, the maximum heat flux tested was kept safely below CHF to avoid burnout and destruction of the heater element.

Many parameters have to be regulated to specific set points in certain order to obtain the desired output and to avoid any damage to the rig; these can be accomplished by following the steps below:

- Set the HFE7000 mass flux by adjusting the pump speed.
- Adjust inlet quality of working fluid by controlling the electrical input to the pre-heater.
- Monitor and regulate pressure, mass flux and allow the system to reach steady state.
- Set the electrical heating of the sapphire tube by adjusting the electric power to the heater.
- Regulate the condenser mass flow and temperature, to ensure complete condensation of the refrigerant.
- When conditions are near steady state, apply EHD voltage to the electrode and allow to re-stabilise
- Acquire averaged data once steady state is achieved, usually after 20-40.
- Observe flow regime through transparent test section, acquire high speed videos.
- Acquire high speed measured data to record transient behaviour.
- Process data and photos.
- Repeat procedure for next test parameter.

### 4.4.1 Experimentally Measured Parameters and Test Conditions

This section explains how the experimental measurements were collated to calculate the heat transfer coefficients in the test sections under both field-free and EHD conditions. Experimental parameters which were key variables in the tests are summarised in Table 4-3, and all experimental measurements are listed in Table 4-4.

Table 4-3. Summary of Experimental Conditions in Test Section

| **Parameter** | **HFE7000** |
|---|---|
| Test Series one | |
| Mass Flux | (50 kg/($m^2$ s), 100 kg/($m^2$ s), 200 kg/($m^2$ s) |
| Heat Flux | 0- 60 W/$m^2$ |
| Pressure | 1.2 bar (abs) |
| Inlet Quality | 0 % |
| High Voltage | 0 kV |
| Test Series two | |
| Mass Flux | 100 kg/($m^2$ s) |
| Heat Flux | 6 kW/$m^2$ |
| Pressure | 1.2 bar |
| High Voltage | 0, 2, 4, 6, 8 kV |
| HV Frequency | 100 Hz |
| Test Series three | |
| Mass Flux | 100 kg/($m^2$ s) |
| Heat Flux | 6, 16 kW/$m^2$ |
| Pressure | 1.2 bar |
| High Voltage | 10 kV |
| HV Frequency | 0, 1, 60, 100, 500, 1000 Hz |

Table 4-4. Experimental Measurements

| Reference | Property | Unit | Location |
|---|---|---|---|
| T1 | Temperature | °C | Test section inlet |
| T2 | Temperature | °C | Middle of sapphire tube |
| T3 | Temperature | °C | Middle of sapphire tube |
| T4 | Temperature | °C | Test section exit |
| T5 | Temperature | °C | Condenser entry, refrigerant |
| T6 | Temperature | °C | Condenser exit, refrigerant |
| T7 | Temperature | °C | Pre heater entry, refrigerant |
| T8 | Temperature | °C | Pre heater exit, refrigerant |
| T9 | Temperature | °C | Condenser entry, water |
| T10 | Temperature | °C | Condenser exit, water |
| T11 | Temperature | °C | Ambient temperature |
| P Diff | Pressure | mbar | Differential pressure across test section |
| Pin | Pressure | bar | Pressure at Pre heater exit |
| Pout | Pressure | bar | Pressure at Test Section exit |
| $I_{pre}$ | Current | A | Current to pre heater |
| $V_{pre}$ | Voltage | V | voltage to pre heater |
| $I_{Test}$ | Current | A | Current to test section |
| $V_{Test}$ | Voltage | V | voltage to test section |
| $I_{amp}$ | Current | A | Current from high voltage amplifier |
| $V_{amp}$ | Voltage | V | voltage from high voltage amplifier |
| $\dot{m}_{ref}$ | Flow rate | kg/sec | Mass flow rate of refrigerant |
| $\dot{m}_{water}$ | Flow rate | kg/sec | Mass flow rate of coolant |

The Reynolds numbers of the working fluid in the sapphire test section ($Re_{refr}$) is calculated from the single phase liquid flow rates and flow areas, such that,

$$Re_{refr} = \frac{\dot{m}_{refr} D_h}{A_i \mu_{refr}} \quad (67)$$

Where $D_h$ is the hydraulic diameter which in the case of annular tube $D_h = D_o - D_i$. Subscripts refr refer to working fluid and $A_i$ is the sapphire tube/electrode annular cross sectional area.

## 4.5 Data Reduction

### 4.5.1 Heat Transfer Coefficient

The parameters required to calculate the local heat transfer coefficient are the saturation temperature of the refrigerant ($T_{sat}$), the tube wall temperature ($T_{wall}$ measured at the outside tube wall using the imbedded thermocouples) and the surface heat flux at the inner wall. With the electrical heating set an approximately constant heat flux is imposed at each point on the tube surface. Thus, knowing the power supply potential difference (V) and the current (I) through the ITO coating, the total heat transfer can be calculated simply by:

$$Q_{add} = V \times I \tag{68}$$

In order to determine the quantity of heat transferred to the refrigerant, the heat loss between the external surface and the ambient air has to be subtracted from the heat, supplied;

$$q = q_{total} - q_{loss} \tag{69}$$

The heat loss consists of natural convection, and to a lesser extent radiation, to the ambient surroundings. To quantify the heat losses an experiment was conducted to obtain the value of the effective convection-radiation heat transfer coefficient ($h_o$). The system was evacuated so that heat transfer was only to the ambient and the test section incrementally heated and a simple correlation for $h_o$ could be estimated from the resulting heat flux – temperature difference curve (see Appendix E). In this way, the heat losses during boiling experiments can be estimated through the expression,

$$q_{loss} = h_o A_o (T_{wall} - T_\infty) \tag{70}$$

where $T_w$-$T_\infty$ is the wall to ambient temperature difference and $A_o$ is the tube outer surface area.

Based on the above, the heat flux to the refrigerant can be estimated as:

$$q^{"} = \frac{VI - h_o A_o (T_w - T_\infty)}{A_i} \tag{71}$$

where $A_i$ is the inner surface area. Thus the boiling heat transfer coefficient can be estimated as follow:

$$h = \frac{q''}{\Delta T_{sat}} \tag{72}$$

where $\Delta T_{sat}$ is the wall superheat $T_w$-$T_{sat}$. Here it is appropriate to use $T_{sat}$ as the heat sink temperature since the measurement is taken at the mid-point of the heated test section where, for boiling conditions, the fluid is no longer subcooled as will be discussed later.

### 4.5.2 Vapour Quality

The vapour quality is an important parameter in prescribing the mechanisms of heat transfer for convective boiling, as is evidenced by the fact that it is a parameter used in many predictive correlations for the heat transfer coefficient. It is also a fundamental parameter used in predicting the flow regimes using established flow regime maps.

An energy balance on the heated test section is given as;

$$VI = \dot{m}_{refr} C_p (\Delta T_{sub}) + \dot{m}_{refr} x_t h_{fg} + Q_{loss} \tag{73}$$

The expression illustrates that a portion of the electrical heat supplied to the ITO coating is transferred to the working fluid and some is lost to the ambient surroundings. The portion of the heat transferred to the working fluid can be segmented into that which increases the sensible heat of the slightly subcooled inlet liquid to saturation after which the heat is converted to latent heat by increasing the vapour quality. Rearranging the above expression, the vapour quality at the exit can be determined as;

$$x_t = \frac{VI - Q_{loss} - \dot{m}_{refr} C_p (\Delta T_{sub})}{\dot{m}_{refr} h_{fg}} \tag{74}$$

Since the inlet thermodynamic state is very close to saturation, the average quality is approximately that of the halfway point of the test section i.e. $0.5x_t$.

## 4.6 Instrumentation Accuracy and Experimental Uncertainty

The uncertainty of the experimental results can be estimated by the method outlined by Kline and McClintock [114]. If a result R is a function of the independent variables $x_1$, $x_2$, $x_3$, $x_n$;

$$R = f(x_1, x_2, x_3, .. x_n) \tag{75}$$

Let $\sigma_R$ be the uncertainty in the result and $\sigma_{x1}, \sigma_{x2}, \sigma_{x3}, .. \sigma_{xn}$ be the uncertainties in the independent variables. Then the uncertainty in the result is given as:

$$\sigma_R = \sqrt{\left(\frac{\partial R}{\partial x_1}\sigma_{x1}\right)^2 + \left(\frac{\partial R}{\partial x_2}\sigma_{x2}\right)^2 + \left(\frac{\partial R}{\partial x_3}\sigma_{x3}\right)^2 + \left(\frac{\partial R}{\partial x_n}\sigma_{xn}\right)^2} \tag{76}$$

The relative uncertainty defined as the uncertainty of the result divided by the value of the result.

$$U_R = \frac{\sigma_R}{R} \tag{77}$$

### 4.6.1 Uncertainty of the heat applied to the test section ($Q_{test}$)

From equation (71) q" is a function of:

$$q" = f(L_t, V, I, L) \tag{78}$$

From equation (76) the absolute uncertainty is given by:

$$\sigma_{q"} = \sqrt{\left(\frac{\partial q"}{\partial L_t}\sigma_{Lt}\right)^2 + \left(\frac{\partial q"}{\partial V}\sigma_V\right)^2 + \left(\frac{\partial q"}{\partial_I}\sigma_I\right)^2 + \left(\frac{\partial q"}{\partial L}\sigma_L\right)^2} \tag{79}$$

$$\sigma_{q"} = \sqrt{\left(\frac{VI}{L}\sigma_{Lt}\right)^2 + \left(\frac{L_t I}{L}\sigma_V\right)^2 + \left(\frac{L_t V}{L}\sigma_I\right)^2 + \left(-\frac{L_t VI}{L^2}\sigma_L\right)^2} \tag{80}$$

The relative uncertainty defined as:

$$U_R = \frac{\sigma_R}{R} = \frac{L}{L_t VI}\sqrt{\left(\frac{VI}{L}\sigma_{Lt}\right)^2 + \left(\frac{L_t I}{L}\sigma_V\right)^2 + \left(\frac{L_t V}{L}\sigma_I\right)^2 + \left(-\frac{L_t VI}{L^2}\sigma_L\right)^2} \quad (81)$$

$$U_{q"} = \frac{\sigma_{q"}}{q"} = \sqrt{\left(\frac{\sigma_{Lt}}{L_t}\right)^2 + \left(\frac{\sigma_V}{V}\right)^2 + \left(\frac{\sigma_I}{I}\right)^2 + (-\sigma_L)^2} \quad (82)$$

### 4.6.2 Uncertainty of the Local Heat Transfer Coefficient

From equation (72) local heat transfer coefficient is a function in;

$$h = f(q", A, T_{wall}, T_{sat}) \quad (83)$$

From equation (76) the uncertainty of heat transfer coefficient can determined from:

$$\sigma_h = \sqrt{\left(\frac{\partial h}{\partial q}\sigma_q\right)^2 + \left(\frac{\partial h}{\partial A}\sigma_A\right)^2 + \left(\frac{\partial h}{\partial T_{wall}}\sigma_{T_{wall}}\right)^2 + \left(\frac{\partial h}{\partial T_{sat}}\sigma_{T_{sat}}\right)^2} \quad (84)$$

$$\sigma_h = \sqrt{\begin{matrix}\left(\frac{1}{A\,(T_{wall}-T_{sat})}\sigma_q\right)^2 + \left(-\frac{q}{A^2\,(T_{wall}-T_{sat})}\sigma_A\right)^2 \\ + \left(-\frac{q}{A\,(T_{wall}-T_{sat})^2}\sigma_{T_{wall}}\right)^2 + \left(\frac{q}{A\,(T_{wall}-T_{sat})^2}\sigma_{T_{sat}}\right)^2\end{matrix}} \quad (85)$$

$$U_h = \frac{\sigma_h}{h}$$

$$= \frac{A\,(T_{wall}-T_{sat})}{q}\sqrt{\begin{matrix}\left(\frac{1}{A\,(T_{wall}-T_{sat})}\sigma_q\right)^2 + \left(-\frac{q}{A^2\,(T_{wall}-T_{sat})}\sigma_A\right)^2 \\ + \left(-\frac{q}{A\,(T_{wall}-T_{sat})^2}\sigma_{T_{wall,i}}\right)^2 + \left(\frac{q}{A\,(T_{wall}-T_{sat})^2}\sigma_{T_{sat}}\right)^2\end{matrix}} \quad (86)$$

$$U_h = \sqrt{\left(\frac{\sigma_q}{q}\right)^2 + \left(\frac{\sigma_A}{A}\right)^2 + \left(\frac{\sigma_{T_{wall}}}{(T_{wall}-T_{sat})}\right)^2 + \left(\frac{\sigma_{T_{sat}}}{(T_{wall}-T_{sat})}\right)^2} \quad (87)$$

$$U_h = \sqrt{{U_{q"}}^2 + {U_A}^2 + \left(\frac{\sigma_{T_{wall}}}{(T_{wall}-T_{sat})}\right)^2 + \left(\frac{\sigma_{T_{sat}}}{(T_{wall}-T_{sat})}\right)^2} \quad (88)$$

### 4.6.3 Accuracy of instrumentations

Table 4-5 lists the accuracy of each instrument on the experiment facility.

Table 4-5. Accuracy of instrumentation.

| Measurement | Device | Absolute Uncertainty | Relative Uncertainty |
|---|---|---|---|
| Temperature | Type T thermocouples (omega) | 0.1 Calibrated | @ 1 °C ±10%<br>@ 10 °C ±1% |
| Refrigerant flow rate | Titan Instruments Type 945 | | ±3.0% |
| Water flow rate | Gems FT-110, 1-10 L/min | | ±3.0% |
| Pressure gauge | Omega 1-3 bar | | ±0.25% |
| Diff pressure gauge | Taylor DP 504t | | ±0.2% |
| Voltage to preheater | Matrix MX22 Multimeter | | ±1% |
| Current to preheater | Matrix MX22 Multimeter | | ±0.25% |

### 4.6.4 Experimental Uncertainty

The relative uncertainty of the heat added to the test section, $U_{Q_{sec}}$, can be calculated from Equation (82);

Table 4-6. The relative uncertainty in heat transfer

| $V_{sec}$ | $I_{sec}$ | $L_t$ | $\sigma_{Lt}$ | $\sigma_{Vsec}$ | $\Sigma_{Isec}$ | $\sigma_L$ | $U_{Qsec}$ |
|---|---|---|---|---|---|---|---|
| **190** | 0.8 | 20 | 0.01 | 0.01 | 0.025 | 0.01 | 0.0328 |

The relative uncertainty in the heat transfer coefficient $U_{hi}$ can determined from Equation (88). The relative uncertainty $U_A$ first needs to be calculated;

$$A = \frac{\pi}{4} d^2 \tag{89}$$

From (76)

$$\sigma_A = 2 * \frac{\pi}{4d}\sigma_d \tag{90}$$

From (77)

$$\mathrm{U_A} = \frac{2\sigma_d}{d} \tag{91}$$

Table 4-7. The relative uncertainty in the heat transfer coefficient

| **d** | $\sigma_{\mathbf{d}}$ | **A** | $\mathbf{U_A}$ | $\mathrm{T_{wall}}$ | $\mathrm{T_{sat}}$ | $\sigma_{\mathbf{Twall}}$ | $\sigma_{\mathbf{Tsat}}$ | $\mathbf{U_{hi}}$ |
|---|---|---|---|---|---|---|---|---|
| **0.08** | 0.001 | 0.005 | 0.025 | 32 | 30 | 0.01 | 0.01 | 0.0588 |

## 4.7 **Energy Balances**

The results of a series of energy balances commissioning tests were performed on preheater and the condenser to ensure the correctness of the instrumentation and are described below.

Figure 4-17 shows a plot of the energy balance of the electric pre heater heat exchanger. $Q_{Pre}$ represents the electric power added to the preheater which is determined by product of current and voltage (VI) and $Q_{refr1}$ is the working fluid energy gain which determined by:

$$Q_{refr1} = \dot{m}_{refr} C_{refr} (T_{sat} - T_9) \quad (92)$$

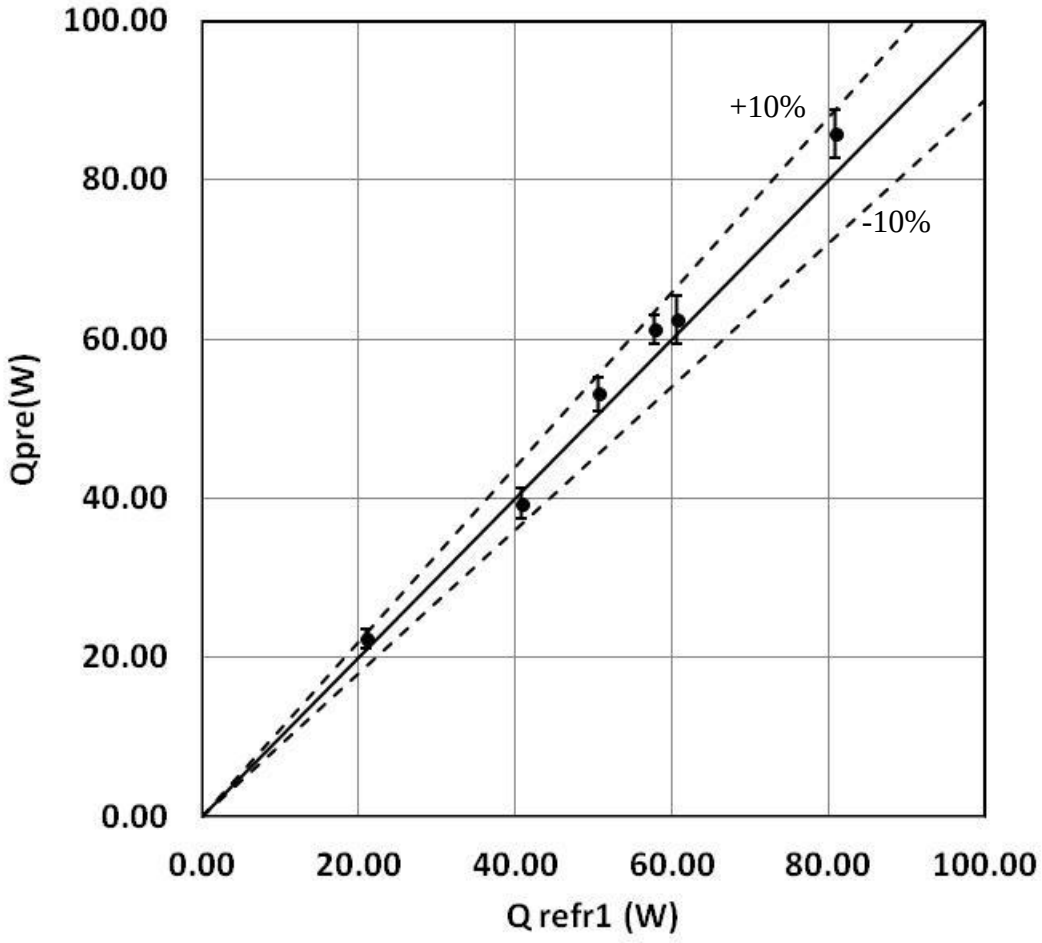


Figure 4-17. Energy balance on the preheater

The plot displays acceptable agreement over a range of input power.

Figure 4-18 plots the energy balance across each fluid stream for single phase flow in the condenser. $Q_{refr2}$ represents the working fluid energy loss across the heat exchanger and $Q_{cond}$ is the water side energy gain, and both are described as:

$$Q_{refr2} = \dot{m}_{refr} C_{prefr} (T_{12} - T_{13}) \quad (93)$$

$$Q_{cond} = \dot{m}_{water} C_{pwater} (T_{14} - T_{15}) \quad (94)$$

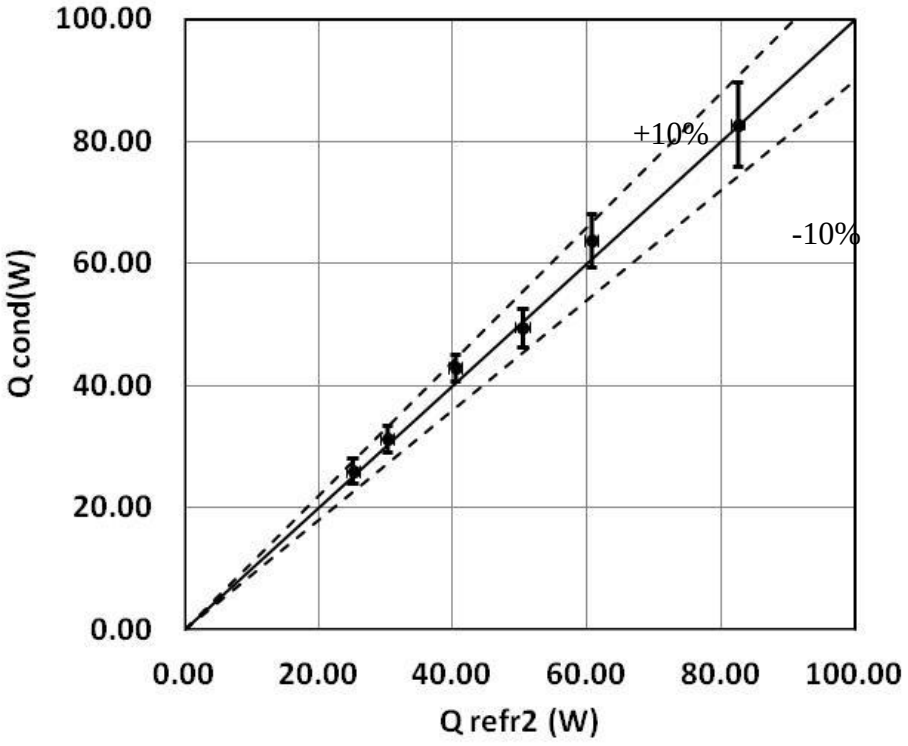


Figure 4-18. Condenser energy balance

The graph again displays good agreement over power input levels at various heat loads.

To lessen the uncertainty associated with the thermocouple measurements it is very important to ensure that the temperature differences on the water side are kept as large as possible since the thermocouple errors lead to greater uncertainty with lower temperature differences which may lead to unacceptably error on the derived parameter. To achieve this, the flow rates were adjusted in order to maintain a sufficiently large ΔT. This is achieved by implementing a bypass between the chiller inlet and outlet.

# Chapter 5. Flow Visualization and HTC Correlation under Field Free Conditions

The test section described above is unique as it allows the simultaneous measurement of the local heat transfer coefficient and visualization of the local flow regime whilst allowing the mass flux, heat flux and local thermodynamic quality to be varied. Visualization of flow regimes under diabatic conditions is very rare in the published literature and to the best of knowledge this is the first study to consider vertical upward two phase flow and heat transfer. In fact, this may be the first study that characterizes flow regimes under diabatic boundary conditions [115]. Since there exist several flow regime maps developed with adiabatic boundary conditions, the first contribution of this work is aimed at verifying their correctness under diabatic conditions, and if necessary, offering a new map for this condition. In a similar manner, many heat transfer coefficient correlations exist for vertical upflow convective boiling, though none exist with local observation of the flow regime. Thus, the second contribution is to evaluate the accuracy and correctness of existing correlations and, if necessary, offer a new correlation for vertical upflow boiling.

## 5.1 Flow Visualization

The high speed camera enables visualization of flow patterns for various mass and heat fluxes through the transparent ITO-sapphire heated test section. Three main flow patterns have been observed under different mass and heat fluxes: bubbly flow, bubbly-slug flow and churn flow. Figure 5-2 shows still images for a mass flux of 100 kg/($m^2$ s) and heat fluxes between 8.4 kW/$m^2$ to 59.3 kW/$m^2$. Figure 5-3 shows cartoons of the flow regimes as interpreted from the corresponding video footage. Figure 5-4 shows still images of the flow at a mid-range heat flux of 36 kW/$m^2$ for flow rates ranging between 50-300 kg/($m^2$ s).

Identifying flow regimes is somewhat subjective. In this study it is complicated by the fact there is significant nucleate boiling on the tube wall which obscures the central region of the flow, which is not the case for adiabatic flow visualization sections. For this study the following was used to identify the various flow regimes.

*Bubbly Flow*: Bubbly flow was identified as the flow pattern where discrete spherical-type bubbles occupied the flow region. This could include regions where some bubble coalescence has occurred, but the resulting coalesced bubble is still the structure of a bubble. Examples are given below.

*Slug Flow*: Slug flow was identified by the existence of large vapour structures that were of the approximate size of half the tube diameter or larger and were not spherical. Slugs were discrete vapour structures and the flow was still predominantly vertical.

*Churn Flow*: Churn flow was identified by a vapour core that did not contain structured slugs. The flow included horizontal motion (transverse to the flow direction) and chaotic mixing of the phases.

Figure 5-1 shows close-up examples of the different flow regimes and how they are identified.

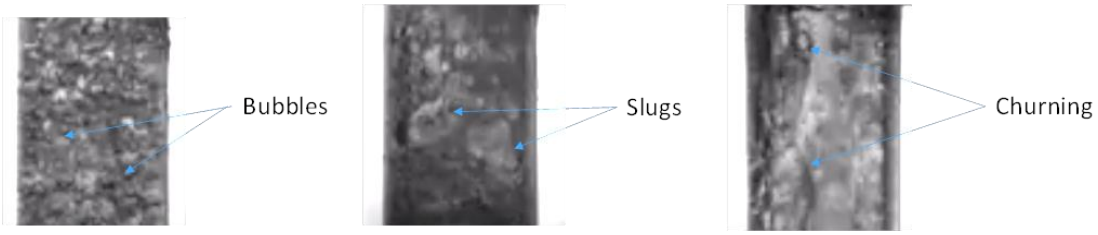


Figure 5-1. Different flow regimes and how they are identified

Figure 5-2 (a) shows the flow regime just subsequent to the Onset of Nucleate Boiling (ONB), where it is clear that it is the bubbly flow regime, as would be expected. Here the bubbles nucleate, grow and detach on the heated wall, with some sliding along the wall and some entering the bulk flow. In the lower region the bubbles remain fairly

isolated, though moving upward the bubble density increases and some bubble coalescence is observed. As the heat flux increases, Figure 5-2 (b) shows that more nucleation sites have become active. This, together with the observation that the frequency of bubble departure size increases, results in more notable bubble coalescence in the core of the flow, though the flow regime is still bubbly flow. With further increase in heat flux the vapour generation rate increases to the extent that the coalescence phenomenon leads to the formation of vapour slugs, though there is still significant nucleate boiling at the tube wall. This is identified here as a bubbly-slug flow regime. Though this is difficult to identify with the still image due to the high density of bubbles near the wall, they are identifiable from the high speed images and are illustrated in the associated cartoon for clarity (See Figure 5-2 (c) (d)). Churn flows occur when the heat flux and vapour generation rate is high enough to destabilize the slugs, causing them to break apart resulting in a chaotic flow regime with significant mixing and stirring of the phases (See Figure 5-2 (e)). As above, these are difficult to identify with still image so the cartoon in Figure 5-3 is included as an impression of the high speed video.

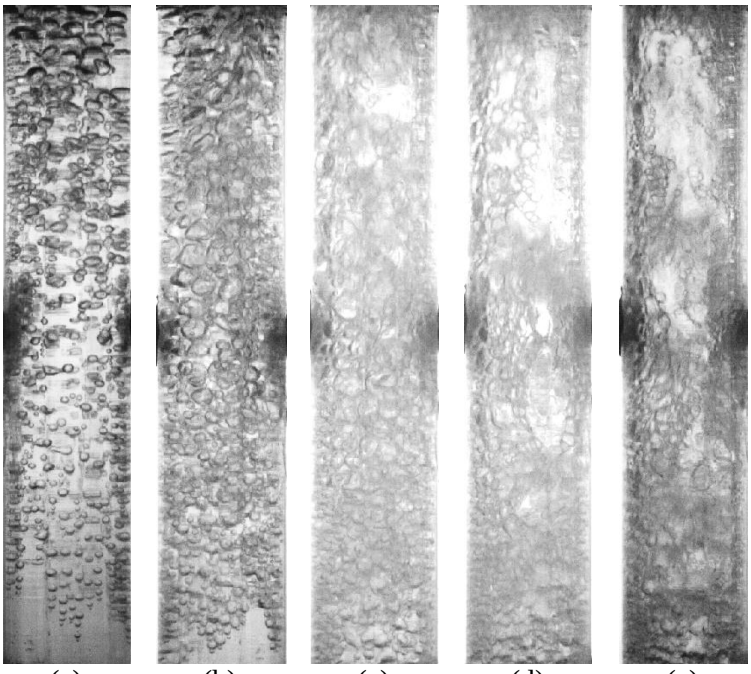


Figure 5-2. Flow visualisation at 100 kg/($m^2$ s)and different heat flux (a) 8.8 (kW/$m^2$) (b) 20.29 (kW/$m^2$) (c) 35.66 (kW/$m^2$) (d) 51.44 (kW/$m^2$) (e) 61.69 (kW/$m^2$)

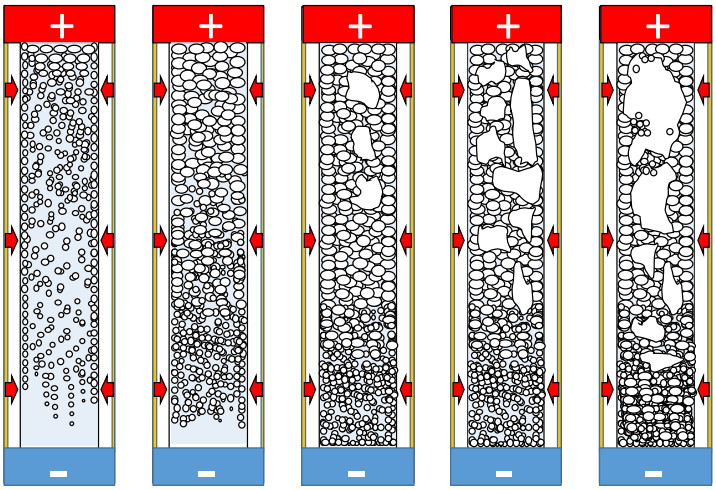


Figure 5-3. Flow regime cartoon (a) Partial nucleate boiling(b) fully bubbly flow (c) Slug flow (d) Churn flow (e) Transitional to annular flow

To illustrate the influence of mass flux, Figure 5-4 shows a comparison of the different mass fluxes (50, 150, 300 kg/($m^2$ s), under the same heat flux of 36 kW/$m^2$. At the lowest mass flux of 50 kg/($m^2$ s) the flow regime is bubbly near the entrance, slug in the mid region and transitions to churn flow at the top half of the tube (see Figure 5-4 (a)). For the 150 kg/($m^2$ s) it is clear that the bubbly-slug flow transition occurs higher up in the tube and churn flow does not appear in the upper region (see Figure 5-4 (b)). For the highest mass flux of 300 kg/($m^2$ s) the flow is bubbly across the whole test section (see Figure 5-4 (c)).

Since the fluid is saturated and the heat flux is the same for each case, it can be said that the vapour production rate is the same. However, this is not the only factor that determines the flow regime since it is clear that the mass flow rate influences the flow regime distribution in the test section. At highest flow rate (Figure 5-4Figure 5-3 (c)) the bubbles generated and detached from the wall are observed to move faster due to the higher flow rate. The higher vertical velocity of the bubbles tends to reduce the occurrence of bubble coalescence so that there is a fairly uniform distribution of small bubbles in the core of the flow, which results in bubbly flow from entrance to exit even though the quality has increased. On the other hand, for the lowest flow rate, the slower moving bubbles interact with one another and tend to coalesces and form initially bigger bubbles which, as the quality continues to increase, coalesce to form

slugs. Further along, these slugs merge which opens the core of the flow to high velocity vapour causing aggressive phase interaction resulting in churn flow.

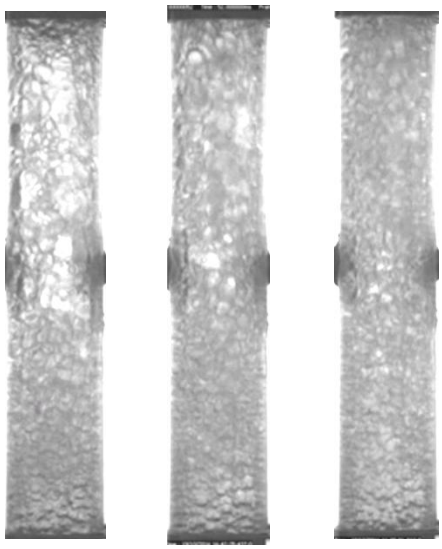

(a) (b) (c)

Figure 5-4. Flow visualisation at $q^{//}$=36 kW/m$^2$ for different mass fluxes (a) 50 kg/(m$^2$ s)(b) 150 kg/(m$^2$ s) (c) 300 kg/(m$^2$ s)

## 5.2 **Comparison to existing flow pattern maps**

Two-phase flow pattern observations are presented in the form of flow pattern maps. The experimental flow regimes are compared to seven existing flow pattern maps available in the literature. From flow boiling visualization three distinct two-phase flow patterns have been observed: bubbly flow, slug flow, churn flow. The annular flow has not been reached, as the heat flux was limited to avoid the burning of coating on the outer surface of the tube.

The observed flow-pattern data for the HFE-7000 vapour-liquid two-phase flow are compared in Table 5-1, against the different empirical theoretical flow-pattern maps. The table shows the number of experimental data points for each flow regime counted in each region on the predicted flow map along with the percentage of the data points

correctly predicted. This method was used by Frankum et al. [57] as a quantitative method to determine the accuracy of flow pattern maps.

Table 5-1 shows that the Bennett et al. [35] flow map is the best prediction flow map for the experiment conditions, it has predicted 80% of data points. The second best flow map is Zhang et al. [51] with 60 % of data points were correctly determined.

Table 5-1. Observed Flow-Pattern Data Against Predicted Flow Pattern Flow-Pattern Maps.

| | | **Observed -Pattern** | | | |
|---|---|---|---|---|---|
| **Model** | **Predicted Pattern** | Bubbly | Slug | Churn | % Correct |
| **Bennett [35]** | Bubbly | 14 | 3 | | |
| | Slug | 1 | 8 | 2 | 80.0 |
| | Churn | | | 2 | |
| | Annular | | | | |
| **Fair [45]** | Bubbly | 10 | 11 | 1 | |
| | Slug | | | 3 | 40.0 |
| | Churn | | | | |
| | Annular | | | | |
| **Zhang [51]** | Bubbly | 6 | | | |
| | Slug | 7 | 11 | 4 | 60.7 |
| | Churn | | | | |
| | Annular | | | | |
| **Taitel [49]** | Bubbly | 3 | | | |
| | Slug | 5 | 2 | | 32.1 |
| | Churn | 5 | 9 | 4 | |
| | Annular | | | | |
| **Hewitt [48]** | Bubbly | 3 | | | |
| | Slug | 6 | 2 | | 17.2 |
| | Churn | 5 | 9 | 4 | |
| | Annular | | | | |
| **Ansari [52]** | Bubbly | | | | |
| | Slug | 8 | 2 | | 23.1 |
| | Churn | 5 | 7 | 4 | |
| | Annular | | | | |

### 5.2.1 Comparison of G -1/$X_{tt}$ flow pattern map with Fair [45]

Experimental data plotted in terms of mass flux and Martinelli parameters and compared to Fair [45] flow map as shown in Figure 5-7.

The experimental test results are plotted the on Fair [45] flow pattern map as shown in Figure 5-5. The transition for different flow pattern can be observed clearly from this figure. As the inverse of the Martinelli parameter ($1/X_{tt}$) increases the Fair map predicts that the transition lines of the mass flux decreases in a linear fashion in logarithmic coordinates. It is evident that the experimental data points follow a very similar trend though (i) there is no churn flow on the Fair map, which is likely grouped with the slug flow, and (ii) the Fair transition lines are shifted to the right of the data from this work. It is this concluded that the Fair map not suitable for diabatic convective boiling conditions since Table 5-1 shows that it only predicts 40% of data points, and the majority of the data being in the bubble-flow region.

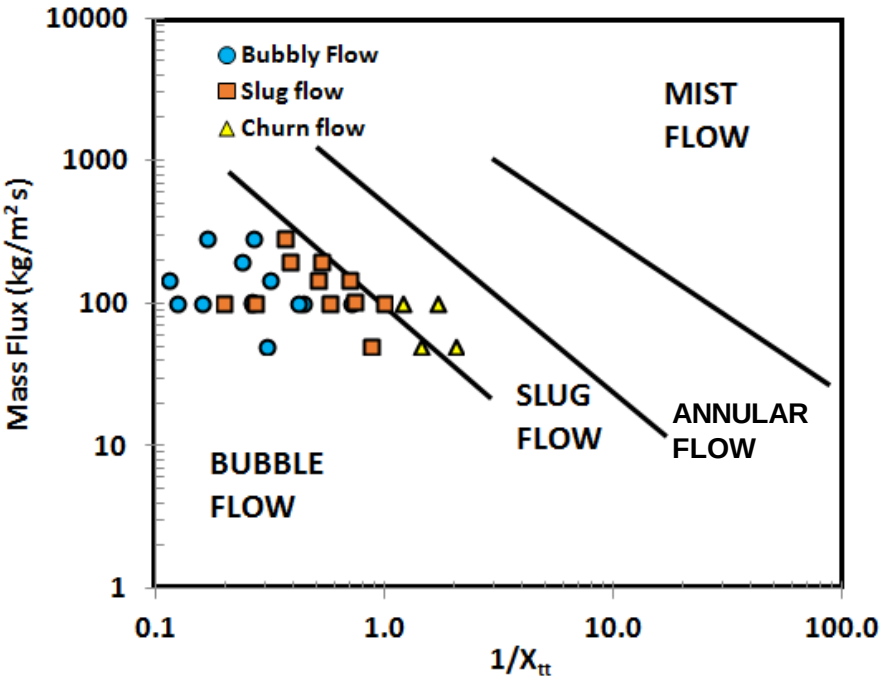


Figure 5-5. Comparison of G -1/$X_{tt}$ flow pattern map with Fair [26].

### 5.2.2 Comparison of G-x flow pattern map with Bennett et al. [35]

Bennett et al. [35] proposed the G –x based flow pattern depicts in Figure 5-6 As it is shown, it is plotted in linear Cartesian coordinates and includes a specific Churn flow regime region. The dashed portion of the transitions lines are extrapolations of those provided by Bennett et al. [35] which were not originally depicted for the lower mass fluxes.

The experimental data results are plotted on Bennett et al. [35] flow map as shown in Figure 5-6. The transition from the bubbly to slug and from slug to churn can be observed clearly from this figure and tends to follow the same trend.

In general all the predicted flow regime regions occur over a relatively small quality range and this is also true for the measured diabatic data points of this investigation. Also, as quality increases the Bennett et al. [35] flow map predicts that the transition lines decrease, as represented by the mass flux, and this is also true for the diabatic measurements of this work. It is noted that the agreement between the Bennett et al. bubbly-to-slug transition and the diabatic measurements is very good suggesting that the mass flux – quality relationship is important in defining this regime transition. The transition from slug to churn flow regimes is also reasonable, though the Bennett et al. transition lines tend to predict the transition at slightly higher qualities, and this may be a difference due to the difference between the adiabatic and diabatic conditions tested, or simply due to the subjective nature of visual identification of flow regimes. Regardless, the Bennett et al. [35] flow map was able to predict the three flow regime, with small overlap, with about 80% of data point of this work in the correct flow regime region. The Bennett et al. [35] flow map appears to be the most suitable flow pattern map of all those investigated, though higher heat fluxes will have to be tested to confirm the churn-to-annular transition.

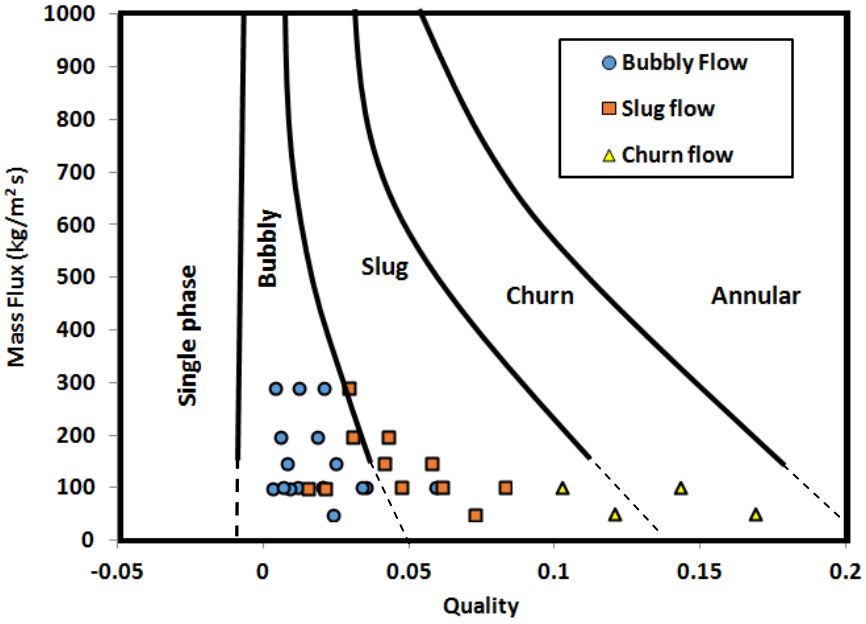


Figure 5-6. Comparison of G-x flow pattern map with Bennett et al. [44]

### 5.2.3 Comparison of $\rho_l J_l^2$- $\rho_g J_g^2$ flow pattern map with Hewitt and Roberts [48]

Experimental data plotted in terms of the superficial momentum fluxes of the liquid, $\rho_l J_l^2$, and vapour $\rho_v J_v^2$ phases and compared to Hewitt and Roberts [48] flow map is shown in Figure 5-7. Predicted map shows a more complex series of flow regime transitions and includes a distinct the Wispy Annular regime. The measured data points of this work are identified by the mass flux which tend to be almost vertical (almost constant $\rho_l J_l^2$) for a given mass flux setting. Increasing heat flux causes the increase in the $\rho_v J_v^2$ parameter for a given mass flux, which in comparison with the Bennet et al. flow map would be associated with an increase in quality.

Figure 5-7 shows that there is a large discrepancy between the predicted adiabatic flow pattern map of Hewitt and Roberts [48] flow and the present diabatic experiment. Notably, the slug (plug) and churn flows are very poorly predicted with them lying in the Annular-type regime, which in fact was not reached in these experiments suggesting that this transition line occurs at much higher $\rho_v J_v^2$ for diabatic upward two phase flow. The only regime that seems to be reasonably

predicted is the bubbly flow regime. Since only ~17% of the measured data is predicted by this map it is deemed unsuitable for diabatic upward two phase flow.

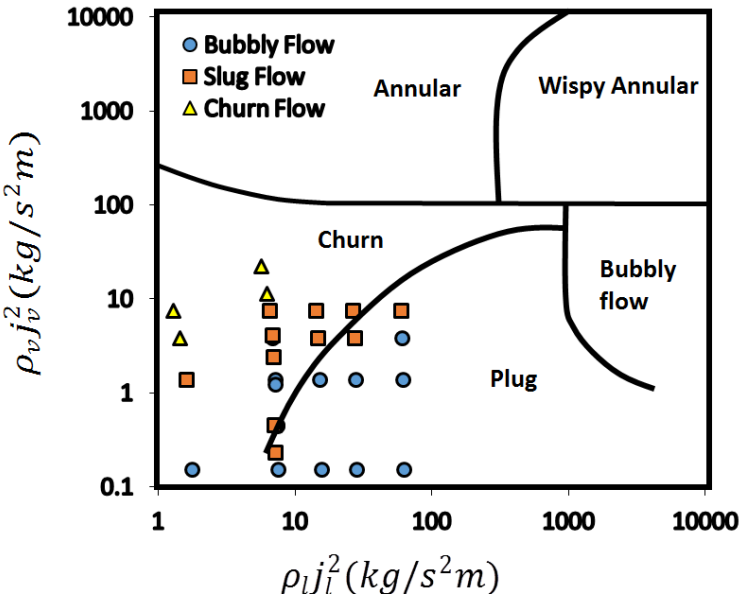


Figure 5-7. Comparison of $\rho_l J_l^2$- $\rho_g J_g^2$ flow pattern map Hewitt and Roberts [48]

### 5.2.4 Comparison of $J_L$- $J_g$ flow pattern map with Taitel et al. [49], Zhang et al. [51], Ansari et al. [52] and Rozenblit et al. [61]

For the evaporating flow cases considered here, as the heat flux increases so does the quality and the superficial gas velocity and this occurs with a with a proportionately small reduction of the liquid superficial velocity. This will occur in conjunction with a change in the boiling dynamics and subsequent transitions through different flow regimes. In this section the experimental data is plotted in terms of the superficial vapour and liquid velocities ($J_L$- $J_g$) and compared to Taitel et al. [49], Zhang et al. [51], Ansari et.al [52] and Rozenblit et al [61] flow regime maps. These flow maps all have a similar general layout, with an initial bubbly flow regime that extends from low to moderate superficial vapour velocities. A domed shaped slug flow regime then exists over a mid-range of superficial velocities that is bordered by bubbly flow and churn flow with an apex that transitions to bubbly-type flow. At higher superficial velocities the slug flow transitions to the churn flow regime and then annular flow. In general, considering the discussion in the previous section, the transitions are in qualitative agreement with the observations made here because the superficial

velocity increases with imposed heat flux and this was observed to cause the flow regime transitions. Thus, the main difference between these different flow regime maps is primarily the location of the transition lines, and these would tend to depend on the experimental facility and working fluids used. It is again noted that none of these maps were developed for the case where the flow pattern is observed where boiling is taking place.

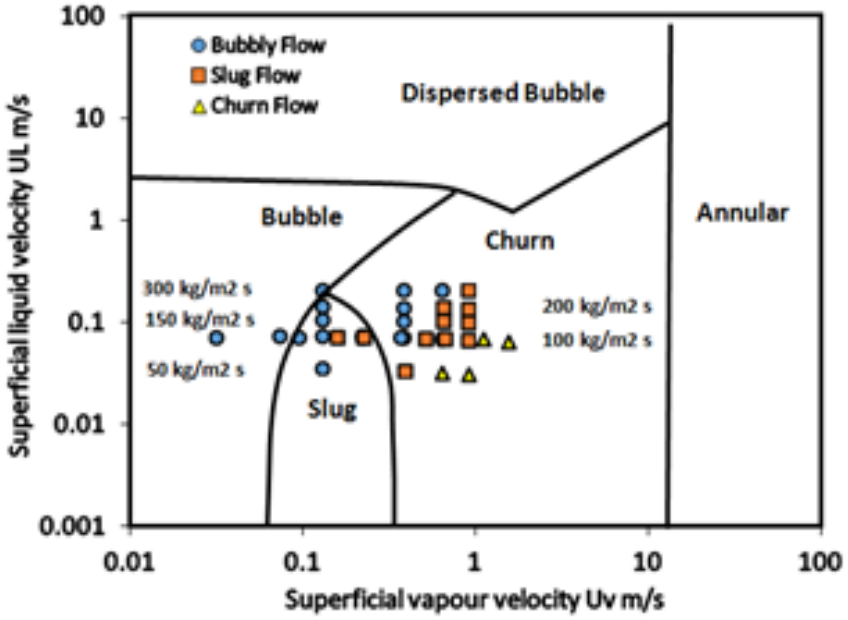


Figure 5-8 Comparison of $J_L$- $J_g$ flow pattern map with air/water Taitel et al. [49] map

The Taitel et al. [49] flow map shown in Figure 5-8 was developed for their air/water data and shows generally poor agreement with the current data. The domed slug flow regime tends to be of generally the correct form and height but is positioned at low superficial velocities. Even though it is able to predict all the churn flow data, only a small portion of the bubbly and slug flows are predicted. In general, the proposed transition borders should be shifted to higher superficial velocities.

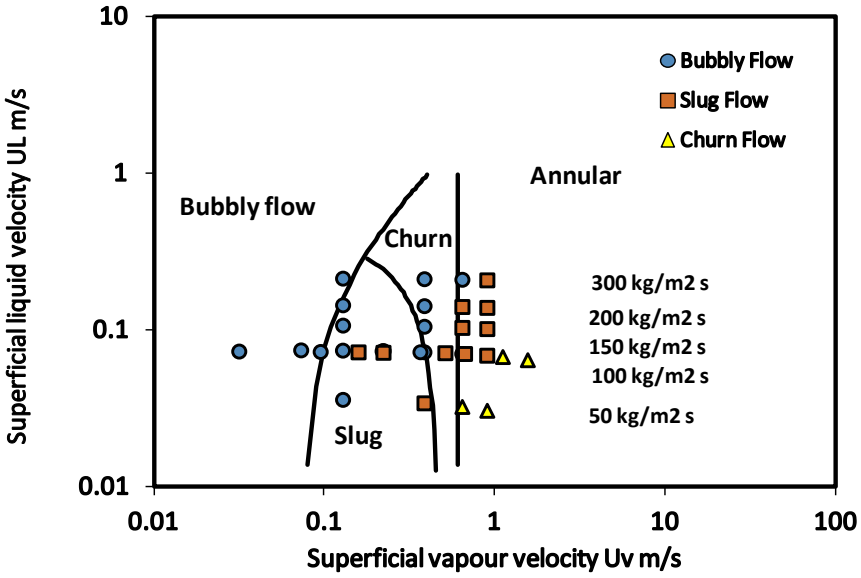


Figure 5-9. Comparison of $J_L$- $J_g$ flow pattern map with calculated air/water Taitel et al. [49] map

Figure 5-9 is constructed using the mathematical transition formula suggested by Taitel et al. [49], Equations (28) (29) ,(30) and using the fluid HFE-7000 properties and tube dimensions. The transient lines are similar for those of the air/water map in Figure 5-8 except the churn to annular transient line is shifted to lower superficial vapour velocities. In general it does not improve the agreement with the current data.

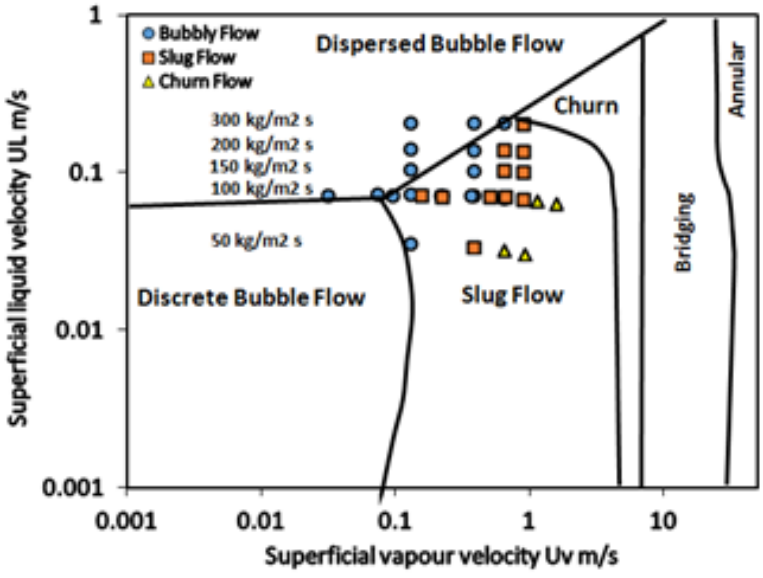


Figure 5-10. Comparison of $J_L$- $J_g$ flow pattern map with Zhang et al. [51]

The Zhang et al. [51] flow map is shown in Figure 5-10. It differs from the previous map as it has a much lower transition superficial liquid velocity between discrete and differentiates between churn and bridging flow regimes. Dispersed bubbly flow i.e. when bubbles rise as vertical columns liquid down-flowing between the bubble columns, has not been observed here for the diabatic boiling so may only be a regime specific to adiabatic air/water –type flows. Regardless, the flow map also shows relatively good agreement with experimental bubbly and slug data, though the churn flow transition is at notably high superficial vapour velocity. In general it does a better job at predicting the current data than the Taitel et al. flow map.

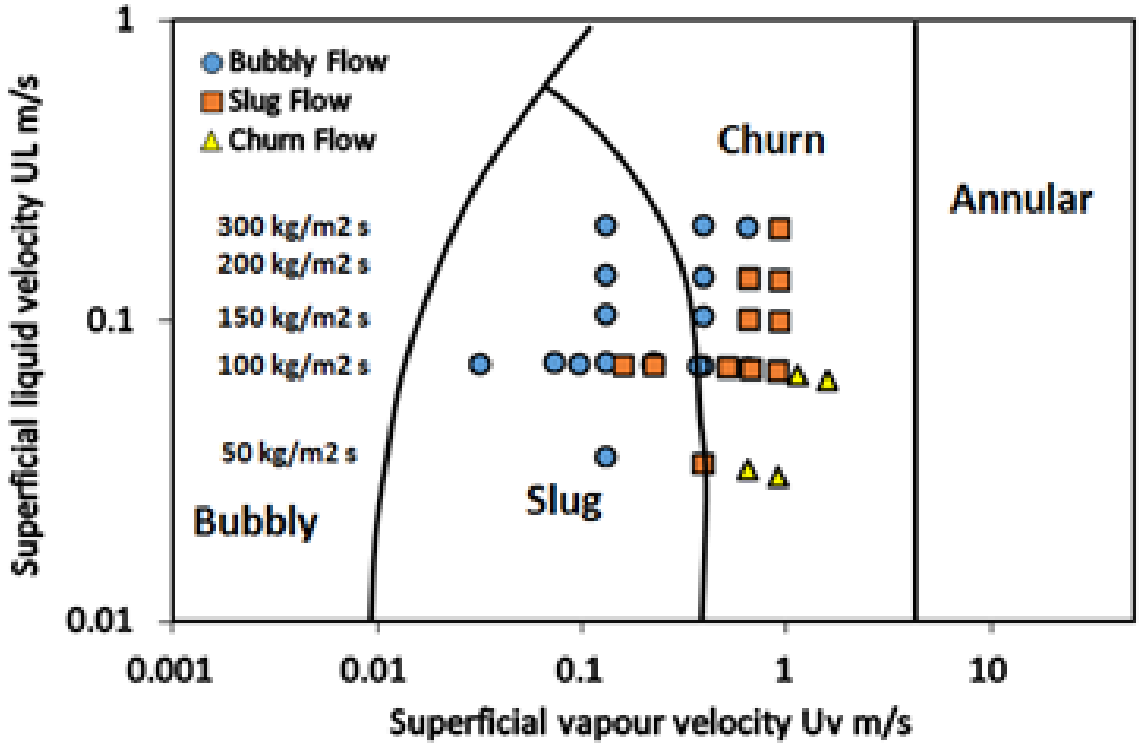


Figure 5-11. Comparison of $J_L$- $J_g$ flow pattern map with Ansari et al. [52]

The Ansari et.al [52] flow map is shown in Figure 5-11 and is very similar in form to the Taitel at al. map except that the bubbly-slug flow transition occurs at much lower superficial velocities. In general this makes its predictive capability worse than that of Taitel et al.

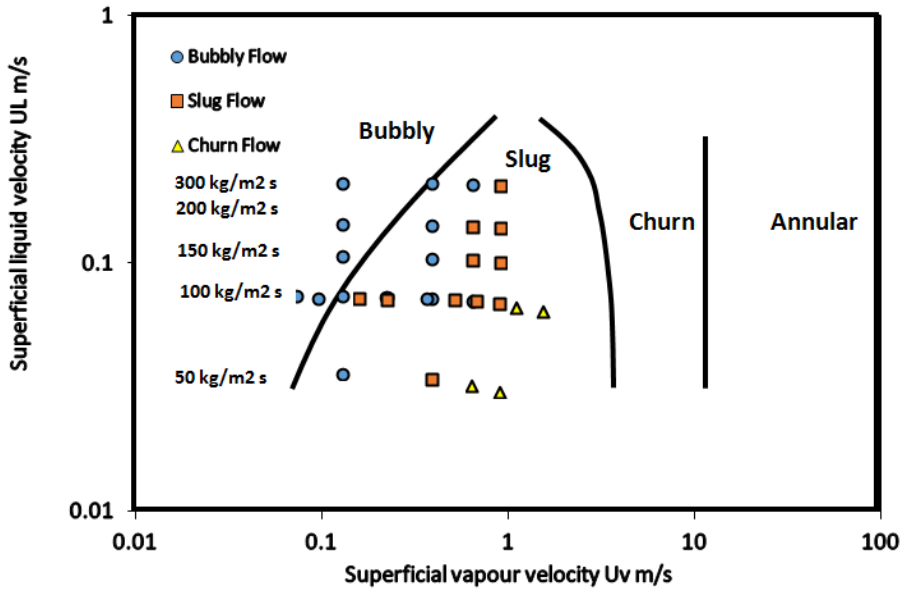


Figure 5-12. Comparison of $J_L$- $J_g$ flow pattern map with Rozenblit et al. [61]

The Rozenblit et al. [61] flow map is shown in Figure 5-12. Again it is similar to the Taitel et al. flow map though shows a less steep transition line for bubbly-slug flow. Although this transition line seems to occur at too low superficial velocities, the sloped trend tends to be consistent with the present data. Consistent with the other flow maps, the slug-churn flow transition is predicted at higher superficial velocities compared with the present data.

### 5.2.5 Conclusions

Experimental investigation of upward vertical flow boiling for HFE 7000 has been performed in a tubular heat exchanger. Three distinct flow patterns have been observed: bubbly flow, slug flow and churn flow. The experimental flow regimes are compared to seven existing maps for vertical two phase flows available in the literature. The Bennett et al. [44] flow map was determined to be the most reliable for the experimental conditions tested in this work with ~80% of the flow regimes correctly predicted. The flow maps developed for adiabatic flows using the superficial liquid and vapour velocities poorly predicted the present data.

Although the seven flow maps used to compare with the present results were developed for vertical upward flow, there are large discrepancies in most of them and the main reason can be summarised as follows;

- The flow regime identification in this work was for boiling under diabatic wall conditions where the bubble production and distribution are significantly different to those of adiabatic conditions, especially to those where the gas fraction is injected into the liquid to create the two phase flow opposed to boiling
- Because of the vapour bubble generation at the wall, the void fraction distribution is not even in the tube cross section nor along its length. This would affect the bubble coalescence and phase interactions and should affect the nature of the flow regimes and transitions between them.
- The existence of temperature gradients within the working fluid in the direction of channel height, and, the temperature gradient between the bulk and near-tube-wall fluid may lower the viscosity and reduce the wall shear stress, affecting the local turbulence that may cause bubbles to either coalesce or remain dispersed.
- The low pressure of the flow allows the bubbles to expand and coalesce much easier.

## 5.3 **Heat Transfer under Field Free Conditions**

A boiling curve plots the imposed wall heat flux versus the superheat of the heated wall and is depicted in Figure 5-13. As the figure shows, there are three distinct regions identified by the slope of the $q''$ vs $\Delta T_{sup}$ curve. At the beginning, under slightly subcooled conditions, while increasing the heat flux the mechanism of heat transfer is single-phase forced convection, identified in Figure 5-13 as Region 1. Further increase in the heat flux results in an increased wall superheat that is sufficient to initiate bubble nucleation and the system enters the bubbly flow regime, shown as Region 2 in the boiling curve Figure 5-13 shows, the initiation of nucleate boiling causes the heated surface temperature to drop significantly as the surface becomes highly populated with nucleation sites. This reduction in superheat shows clear evidence of the enhanced heat transfer mechanisms associated with the presence of the bubbles. Notably, the slope of the boiling curve increases significantly indicating a much higher heat transfer coefficient (HTC) for bubbly flow (Region 2). With further

increase in the heat flux the vapour generation rate is high enough to cause bubble coalescence in the core of the flow and the flow transitions to the slug flow regime, as described in the last section. With regard to the heat transfer, the boiling curve shows a clear change in slope when this flow regime transition occurs signifying a change in the mechanisms of heat transfer in Region 3, which here is improved over that of the bubbly flow regime. Entering the churn flow regime (Region 4) does not show a significant change in the slope of the boiling curve.

Figure 5-14 plots the heat transfer coefficient with respect to increasing heat flux. Initially, the figure shows a constant heat transfer coefficient with the increase of heat flux up to about 9 $kW/m^2$, and this is representative of single phase liquid flow prior to ONB (Region 1). The constant heat transfer coefficient trend is expected for single phase flow as it primarily depends only on the Reynolds number and is insensitive to the heat flux, apart from some possible small changes due to fluid property variations with temperature which would be within the experimental uncertainty of these experiments.

Single-phase forced convection heat transfer calculated using Dittus-Boelter and Gnielinski correlation yields a HTC value which is not too different from experimental data see Figure 5-14

Figure 5-14 illustrates the dramatic increase of heat transfer coefficient subsequent to the ONB and the beginning of the bubbly flow regime (Region 2), as it jumps from A to B with about a 300% increase in heat transfer coefficient with a small increment in the heat flux. The difference in measured wall superheat between just prior to and just subsequent to boiling incipience is known as the temperature overshoot. In this experiment the overshoot was about 22 ºC, which is large due to the relatively smooth sapphire surface and the highly wetting properties of HFE 7000 which tends to flood potential nucleation sites. It should be noted that when the heat flux was lowered in increments, nucleate boiling could be maintained down to a wall superheats as small as 1 K illustrating the boiling hysteresis effect.

Figure 5-17 (a) shows the bubbly flow regime that occurs just subsequent to ONB. At the previous heat flux setting the flow was single phase until, at the ONB heat flux,

one or more nucleation events occurred which subsequently populate most of the surface with active sites. It is an extremely rapid event and is believed to be due to one or a few nucleation sites activating which seeds neighbouring sites resulting in the cascading sequence of nucleation site seeding until the surface is covered.

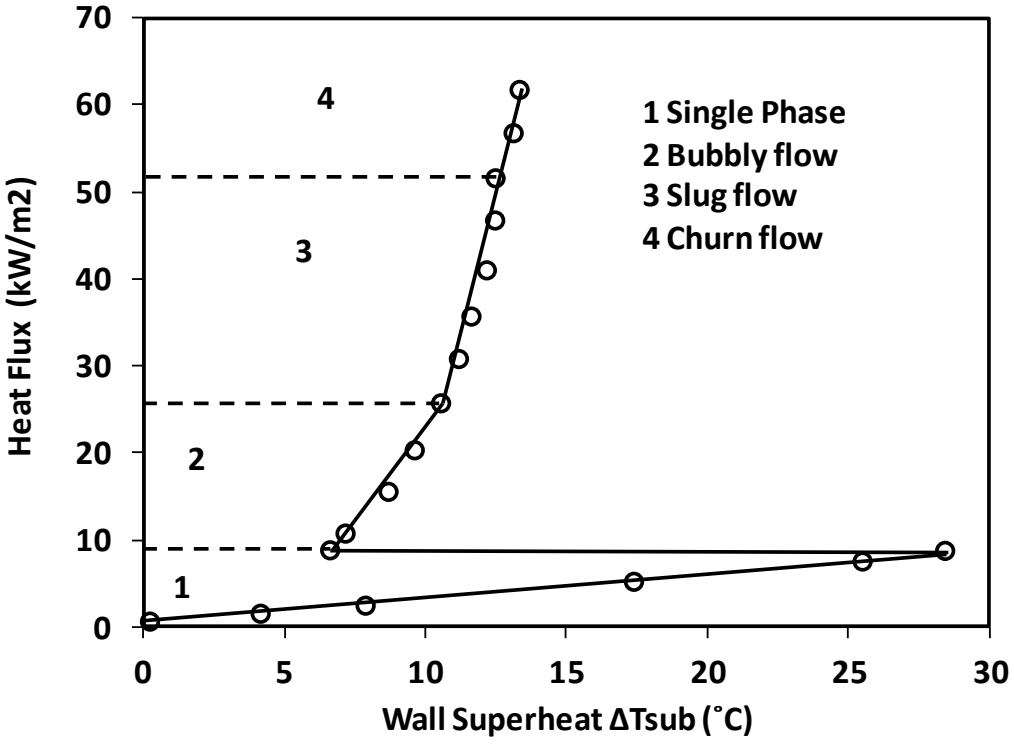


Figure 5-13. Boiling curve at 100 kg/(m$^2$ s) , $\Delta T_{sub}$=2°C

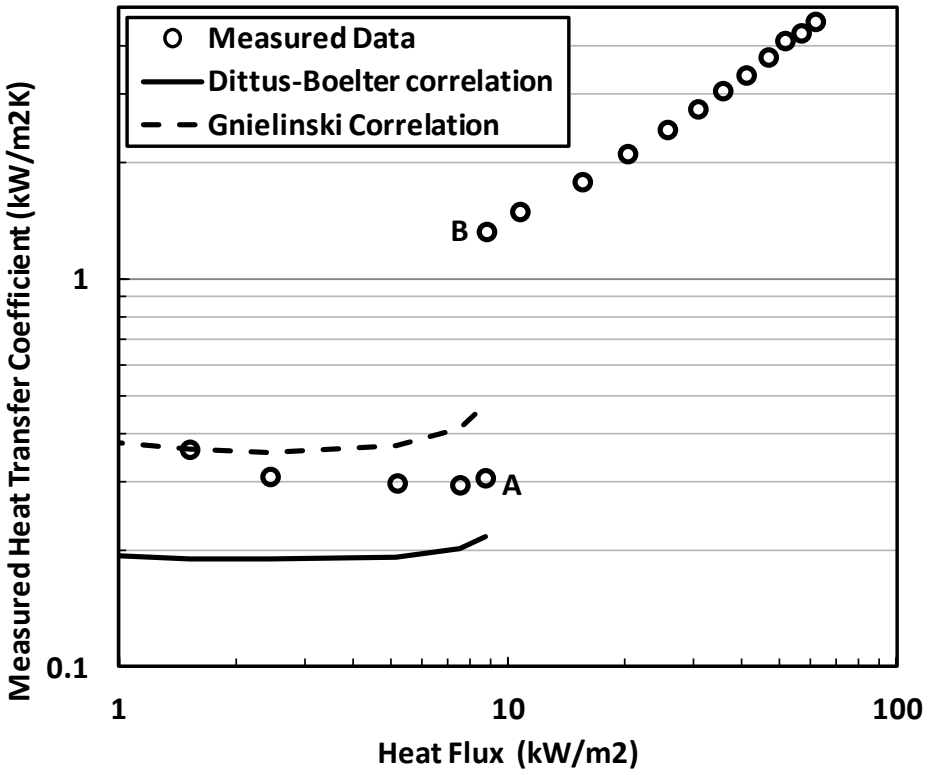


Figure 5-14. Heat transfer coefficient versus heat flux at 100 kg/($m^2$ s), $\Delta T_{sub}$=2°C

Increasing the heat flux beyond the ONB, the high speed videos show that continuously more nucleation sites are activated Figure 5-2 ((a) to (e)) and the bubble frequency and departure size increase. This is depicted in Figure 5-3 (b). Compared to single phase flow, where the increase in heat flux increases the temperature of the liquid phase, here the increased heat flux increases the vapour generation rate and the local quality. As Figure 5-13 shows, compared with single phase flow, only small increases in the wall superheat occur for like increases in heat flux (Region 2). Also, Figure 5-14 shows that the heat transfer coefficient increases with increasing heat flux indicating that the heat transfer mechanisms improve with increase in the vapour generation rate, so the increase in the bubble activity is responsible for escalating the heat transfer coefficient and this is qualitatively consistent with the observation made from the high speed videos. After ONB the HTC increases with a power law of $h \alpha q''^{2.8}$. This cubic relationship illustrated that the presence of the bubbles improves the effectiveness of the heat transfer, and the escalation in the heat transfer coefficient is initially due to the increasing nucleation site density, bubble frequency and departure size of the bubbles as the heat flux increases.

As discussed in the previous section, increasing the heat flux for a fixed total mass flow rate causes the vapour quality and superficial vapour velocity to increase, with minor influence on the liquid superficial velocity. The increased vapour generation rate becomes large enough that bubbles coalesce forming vapour slugs within the core flow signifying the transition from bubbly flow to slug flow. The high speed videos show that the slug flow regime has much more rigorous mixing of the phases and the slugs interact with the bubbles growing at the wall. Figure 5-13 shows a fairly rapid change in slope at between 20 & 30 $kW/m^2$ which coincides with the observed transition from bubbly to slug flow. Thus, from the visualization of the diabatic two phase flow afforded by this apparatus, the escalation in the heat transfer coefficient is here shown to be due to a flow regime transition which changes the mechanisms of heat transfer at the wall. The data also suggests that the transition from slug to churn flow does not have a measurable influence on the heat transfer mechanisms.

Figure 5-15 (a) and (b) shows the boiling curves for three different mass fluxes (50

kg/(m$^2$ s), 100 kg/(m$^2$ s), 150 kg/(m$^2$ s)), the figure show the heat transfer coefficient is direct function of heat flux, and it is insensitive to the mass flux, which suggests that the dominant heat transfer mechanisms are associated with the local bubble activity opposed to convective influences, which is consistent with earlier boiling studies [116] [117] [118]. This will be discussed in a later section when the data is

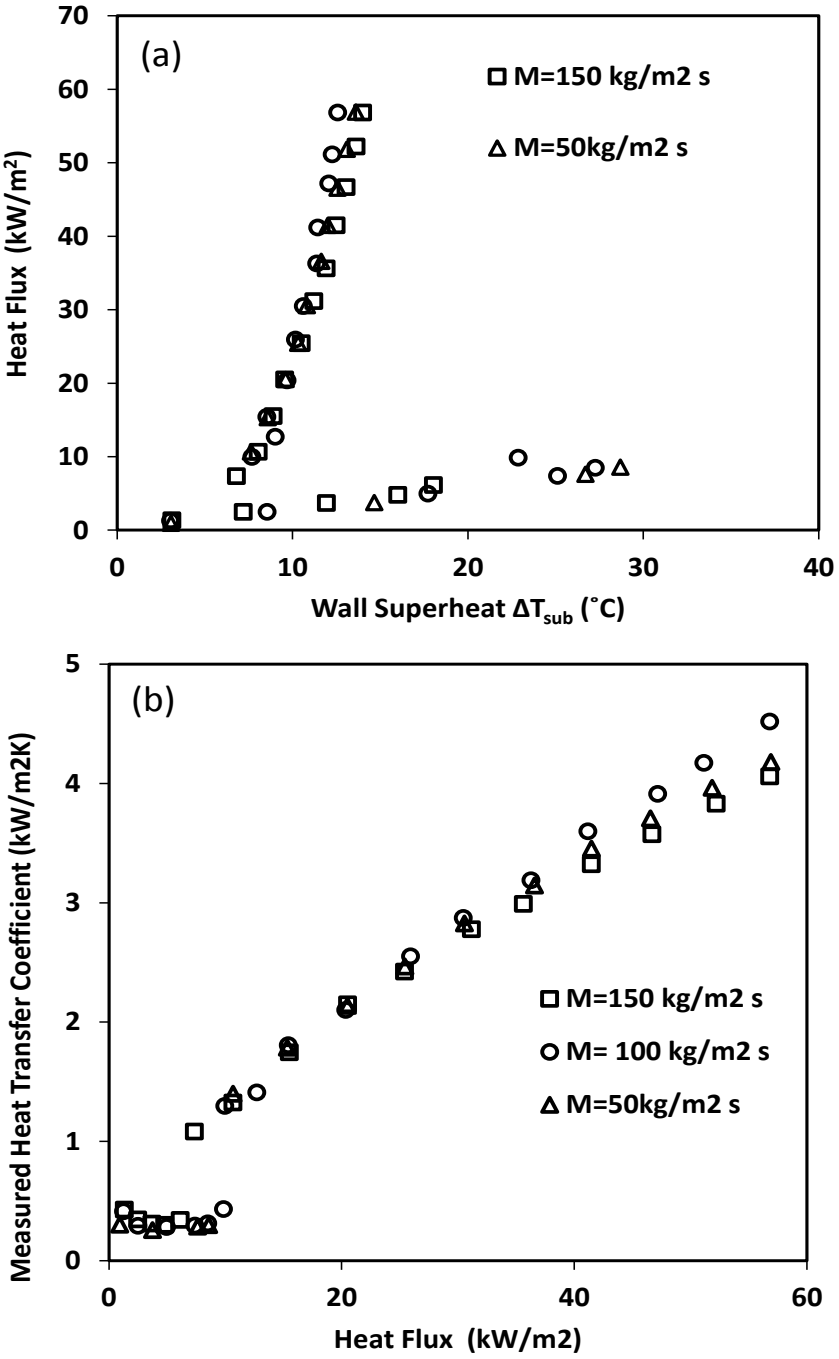


compared with existing vertical flow boiling heat transfer correlations.

Figure 5-15. Heat transfer coefficient vs heat flux for two different mass fluxes.

## 5.4 **Confinement**

As one of the research objectives is to study the EHD enhancement on the heat transfer coefficient, therefore a stainless steel road of 3 mm has been inserted through the test section tube to create an electric field between across the refrigerant. The inside tube diameter is 8 mm resulting in gap of 2.5 mm between the road and the inside wall. An obvious question with regard to EHD enhanced heat transfer is whether the presence of the tube itself influences the heat transfer, and thus a study was performed to address this.

The presence of the electrode can cause a confinement effect that changes the boiling dynamics and associated heat transfer. In the extreme cases, for example, boiling in a microchannel, where the effective channel size is smaller than the effective bubble size is considerably different that a large pipe where the bubbles are free to depart and be carried with the free stream. To distinguish between confined and unconfined flows, the Confinement Number was introduced by Cornwell and Kew [23] (see equation (19)). The term d in the equation determined as hydraulic diameter, which for an annulus is;

$$D_h = (D_o - D_i)/2 \tag{95}$$

The confinement number $C_o$=0.39 for this annular test section. The general rule is that $C_o$<0.3 will be an unconfined flow and cases where $C_o$>0.5 will be confined, with 0.3 < $C_o$ < 0.4 representing a transition regime [28] Clearly $C_o$ for this study lies within the range where possible confinement effects may be present.

Comparisons between heat flux and heat transfer coefficient in the open tube ‘circular’ flow and in the annular flow are shown in Figure 5-16. Figure 5-16 (a) shows the comparison at lower Reynolds number 2100, and Figure 5-16 (b) shows the comparison at higher Reynolds number 3050. In order to match the Reynolds numbers of the two scenarios the flow rate was adjusted. Regardless, the comparisons show no change in the HTC upon inserting the electrode.

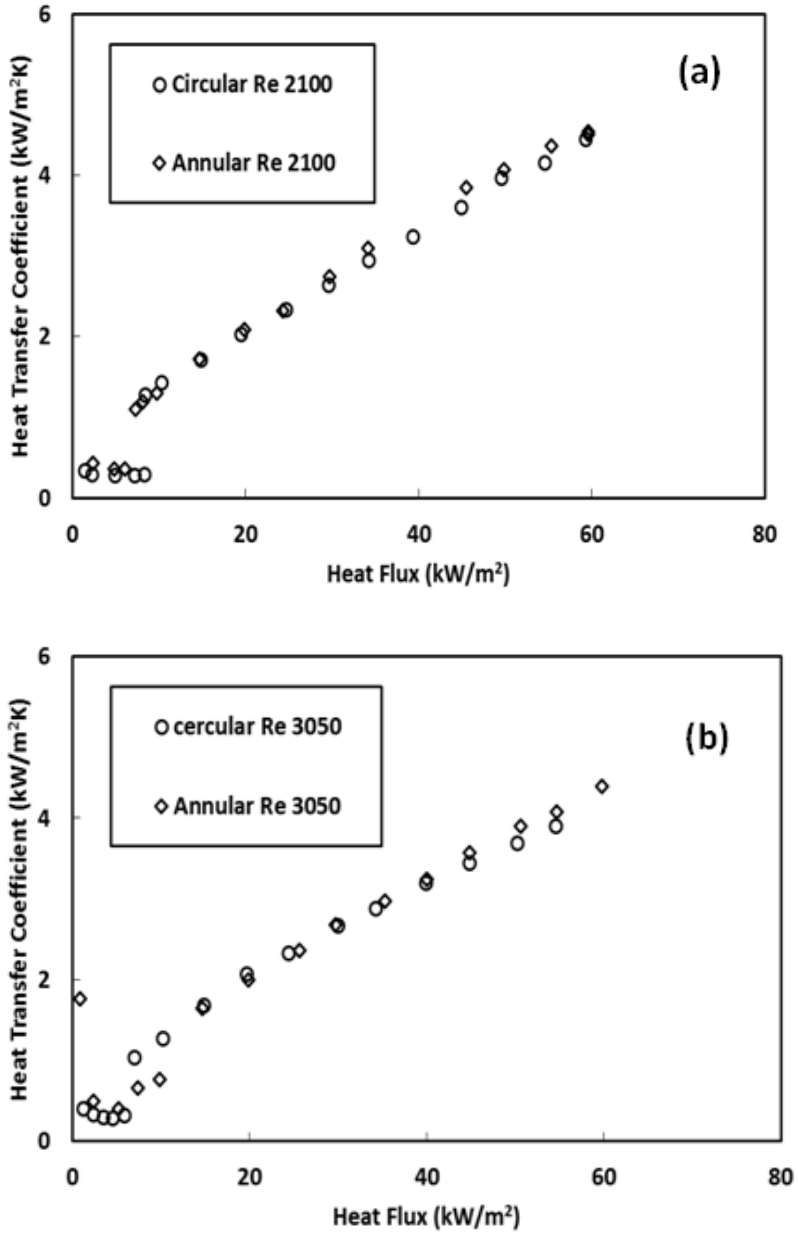


Figure 5-16. Compare between the circular flow and the annular flow (a) Re =2100, (b) Re=3050

Figure 5-17 shows a visual comparison between circular flow and annular flow channels for varying heat flux, and thus different overall flow regimes. Figure 5-17 (a&b) shows that at the lower heat flux the bubbles are fairly sparse and small enough that any the tube does not appear to be interfering with the bubbles at the tube wall. The same can generally be said about the slug (Figure 5-17 (c&d)) and churn (Figure 5-17 (e&f)) flow regimes that occur at the higher heat fluxes.

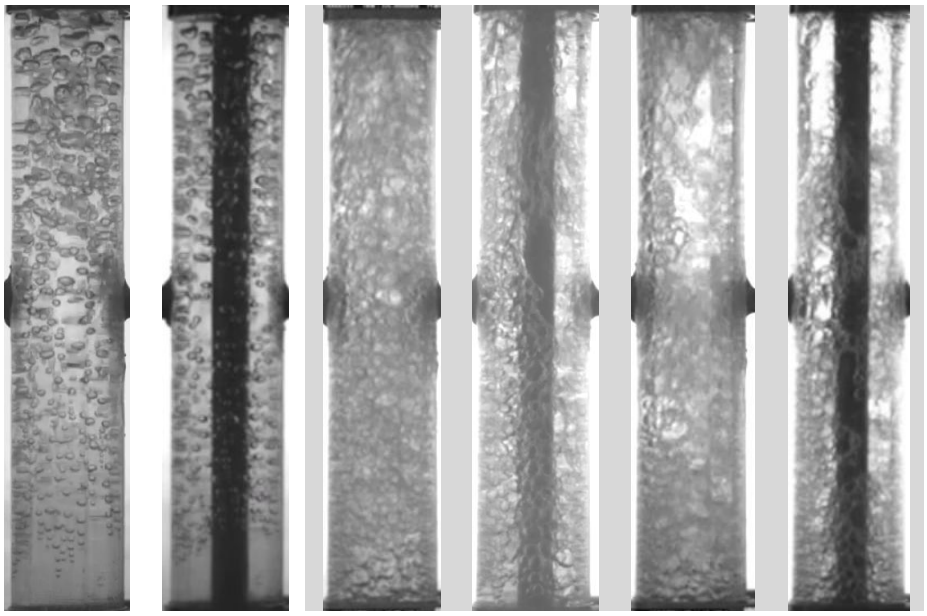

(a) (b) (c) (d) (e) (f)

Figure 5-17. (a), (b) 100 kg/(m$^2$ s), 10 kW/m$^2$ (c), (d) 150 kg/(m$^2$ s), 35 kW/m$^2$,(e) , (f)100 kg/(m$^2$ s), 60 kW/m$^2$ [(a), (c), (e) unconfined flow, (b), (d), (f) semi-confined flow]

## 5.5 **Evaluate boiling convective heat transfer correlation with experimental data**

Seven different flow boiling heat transfer coefficient prediction correlations for vertical flow boiling were discussed earlier and are summarized in Table 5-2 and subsequently evaluated against the experimental results in this section. The prediction deviations between the experimental and predicted values from each correlation are listed in Table 5-2, where the MRD is the mean relative deviation (a negative MRD indicates that the correlation under predict the HTC), the MAD is the mean absolute deviation and the (RMS) root mean square of deviation and are defined as follows:

$$MAD = \frac{1}{n}\sum \left|\left(h_{exp} - h_{pre}\right)/h_{exp}\right| \times 100\% \tag{96}$$

$$\text{MRD} = \frac{1}{n}\sum \left(h_{exp} - h_{pre}\right)/h_{exp} \times 100\% \tag{97}$$

$$\text{RMS} = \sqrt{\frac{1}{n}\sum\left[\left(h_{exp} - h_{pre}\right)/h_{exp}\right]^2} \times 100\% \quad (98)$$

Table 5-2. Comparison between experimental data and correlation predictions.

| | Correlations | MRD | MAD | RMS |
|---|---|---|---|---|
| **1** | Wattelet et al [65] | 21% | 21% | 21% |
| **2** | Shah [71] | -19% | 21% | 26% |
| **3** | Gungor & Winterton [75] | 33% | 33% | 34% |
| **4** | Kandlikar correlation [66] | 35% | 46% | 51% |
| **5** | Gungor & Winterton [73] | 108% | 108% | 110% |
| **6** | Chen [67] | 251% | 251% | 277% |
| **7** | Jung & Radermacher [77] | 260% | 260% | 456% |

Table 5-2 shows that the Shah [71] and Wattelet et al. [65] correlations have given the best agreement with the measured data. The negative MRD indicates that the second correlations under predict the HTC, while the last four correlations over predict HTC, and quite significantly.

The Chen correlation [67] has been found to over predict the HTC with a high MAD of 251 %, see Table 5-2. Furthermore, this correlation seems very sensitive to mass flux, as clear in Figure 5-18, which does not agree with the experimental measurements of this investigation.

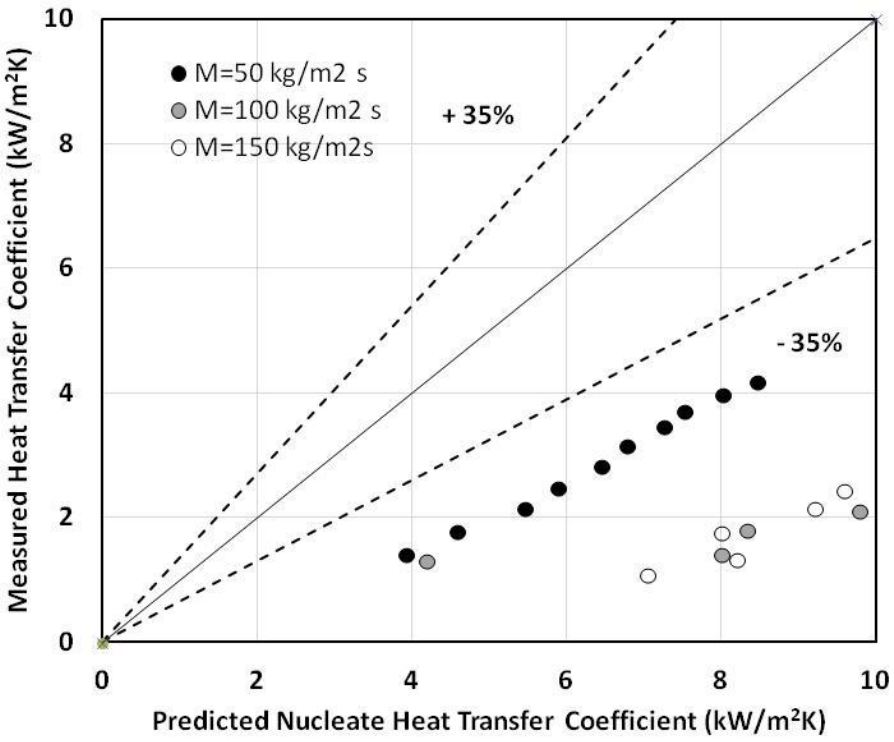


Figure 5-18. Measured HTC vs Chen correlation [67]

The Shah correlation [71] predicts the convective boiling HTC using four different general correlations that depend on the Boiling number, *Bo*, and a dimensionless convection number, $C_{o,}$, such that the larger value of $h_{nb}$ or $h_{cb}$ is then taken for $h_{tp}$. This procedure of separating the regions causes a discontinuity in predicted HTC, and this has been noted from many researchers [66]. This has been avoided here by using only the first equation in Table 2-4 for all test regions, which eliminated the discontinuity and slightly under predicts the HTC. The MAD and RMS are found to be 21% and 26 % respectively which is considered as acceptable agreement with measured data. The MRD is -19% which illustrates that this correlation consistently under-predicts the experimental data. However, Figure 5-19 does show that this correlation is sensitive to mass flux.

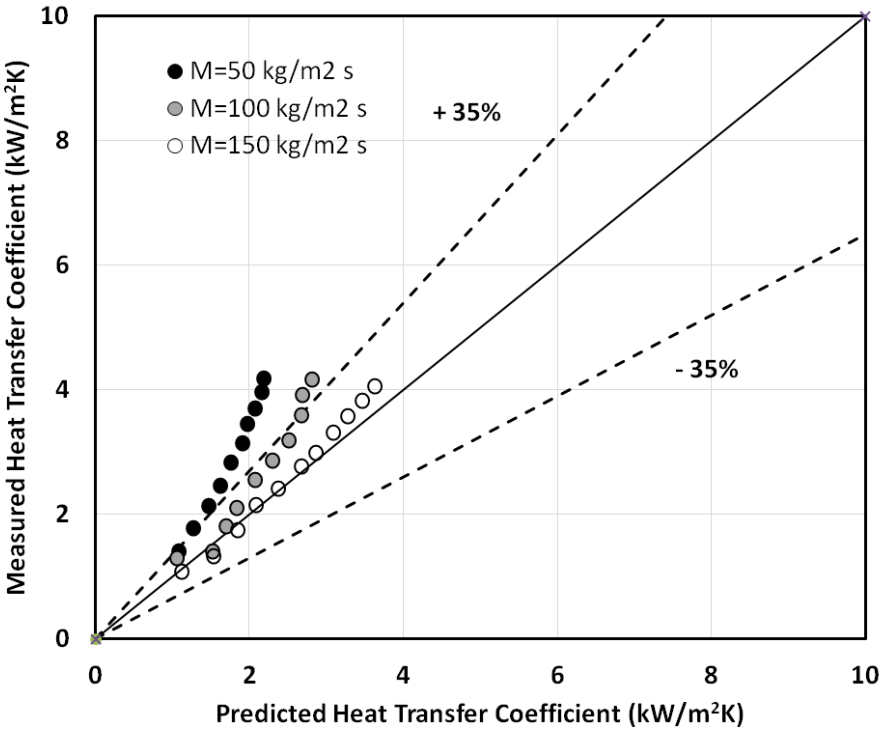


Figure 5-19. Measured HTC vs Shah correlation [71]

The Gungor and Winterton [73] correlation significantly over predict the measured HTC, with MAD, MRD and RMS of ~108 %, as seen in Figure 5-20. This correlation incorporates Cooper correlation to predict the nucleate HTC. Cooper correlation is very sensitive to surface roughness. Here the default roughness of 0.1 μm which is close to the 0.2 μm roughness measured on the outside of the tube, though the inside could be rougher or smoother but could not be measured. A significant reduction in the roughness would have to be imposed to improve the agreement with the measurements. Furthermore, although not largely sensitive to flow rate, the correlation predicts an increase in heat transfer coefficient with decreasing flow rate which is counter intuitive.

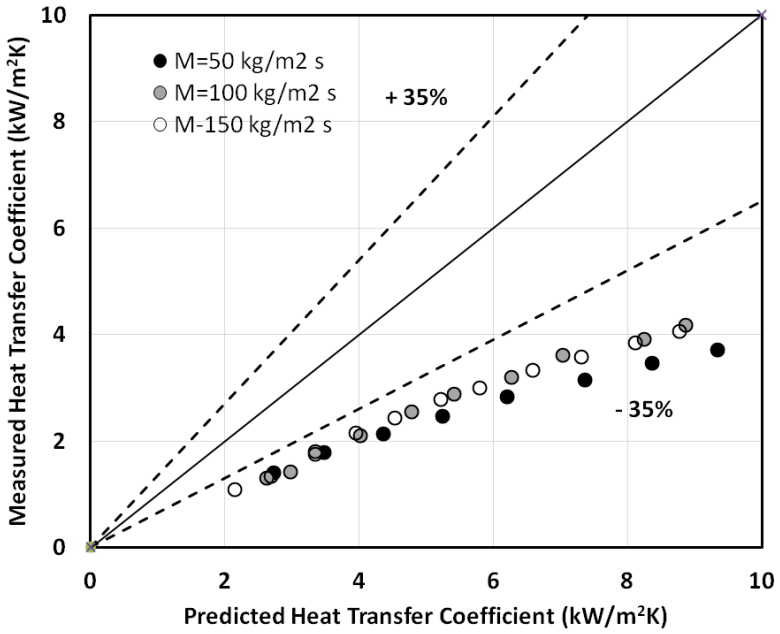


Figure 5-20. Measured HTC vs Gungor & Winterton [73]

The Wattelet et al. correlation [65] correlations also uses Cooper correlation to predict the nucleate HTC. Figure 5-21 shows the result using the default surface roughness of 0.1 μm and good agreement with the measurements is found, with MAD, MRD and RMS of 21% which is reasonable for a two phase flow correlation. It is noted that the correlation is not sensitive to flow rate for the range tested which agrees with the measured trend.

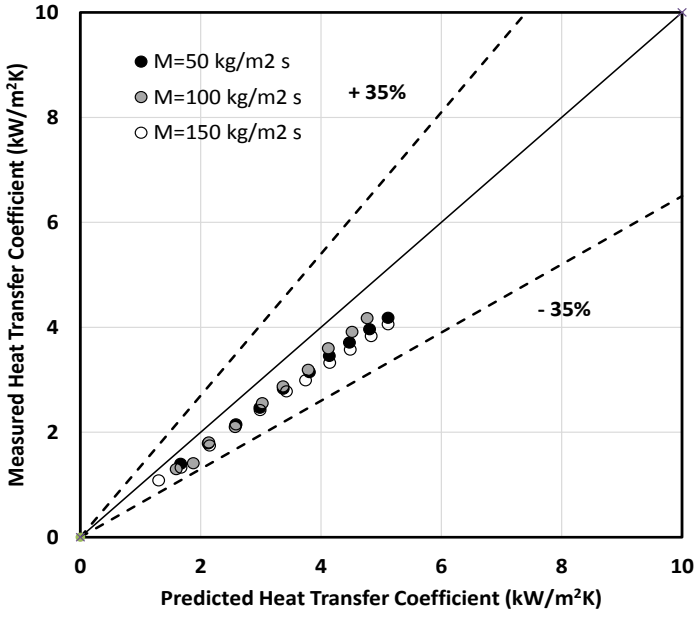


Figure 5-21. Measured HTC vs Wattelet et al. correlation [65]

Jung & Radermacher Correlation[77] over predict the HTC at lower quality, at higher quality it suffer from discontinuity as shown in Figure 5-22. The suppression factor depends on the Martinelli parameter ($X_{tt}$), which is a function of vapour quality, when the quality changes from 0.08 to 0.1 the $X_{tt}$ changes from 1.01 to 0.84, and the suppression factor calculation method changes from Equation (51) to Equation (52) which occur an increases of 6.1 times, this causes a jump of predicted HTC as shown in Figure 5-22. This correlation is insensitive to flow rate for the most of tested range which agrees with the measured trend.

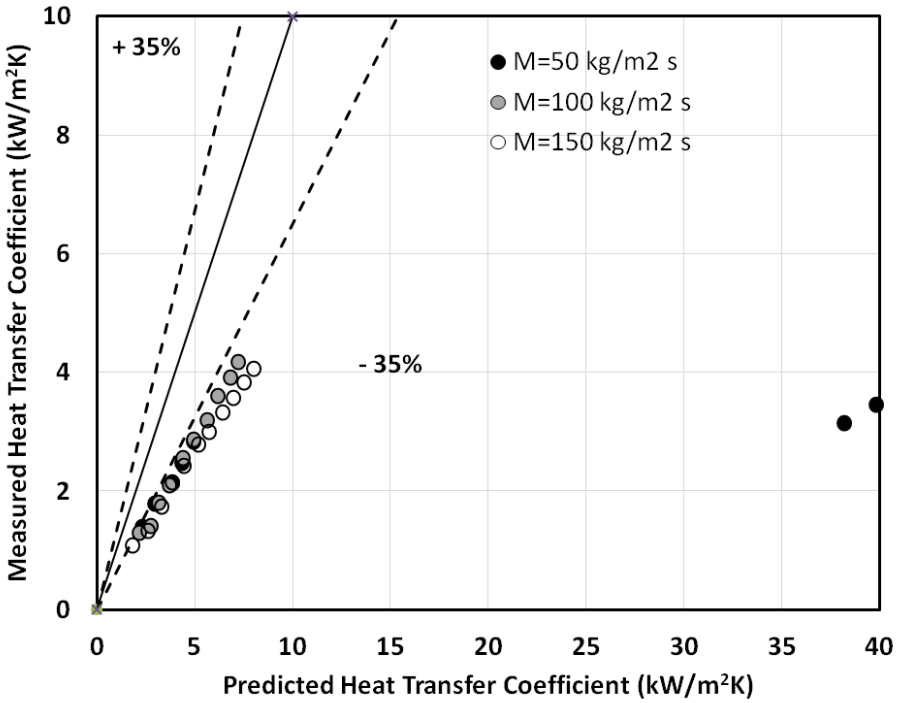


Figure 5-22. Measured HTC vs Jung & Radermacher [77]

The updated Gungor & Winterton [75] correlation shows quite good agreement with the measured data as shown in Figure 5-23. Here the MAD and RMS are 33, which can be considered acceptable agreement for an empirical boiling correlation. The MRD is quite high, at 34%, as the data as there is an almost over predictions as shown in Table 5-2. Although there is some sensitivity to flow rate, it is not severe.

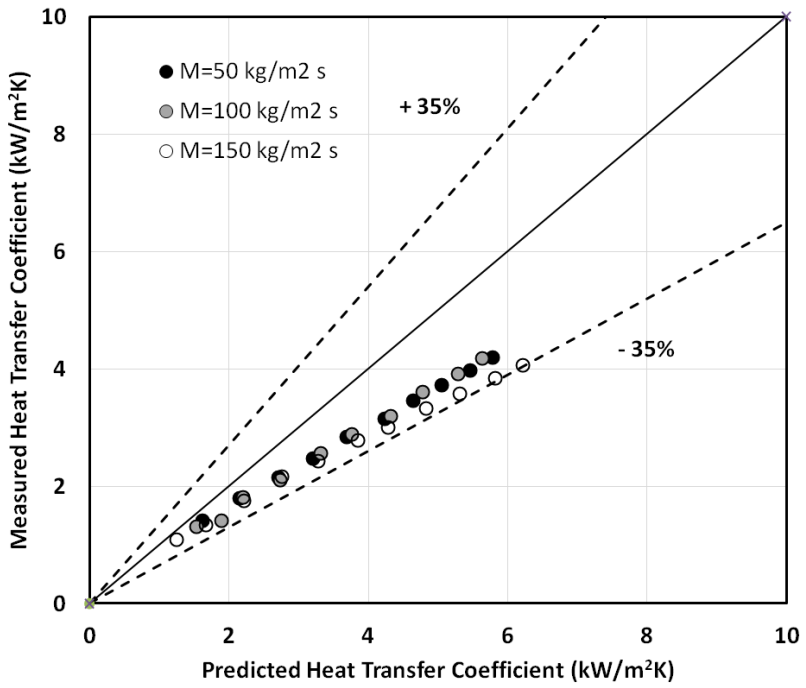


Figure 5-23. Measured HTC vs Gungor & Winterton [75]

Kandlikar correlation [66] gives a good agreement with the measured data MAD 46 %, but it also suffer from discontinuity as shown in Figure 5-24.

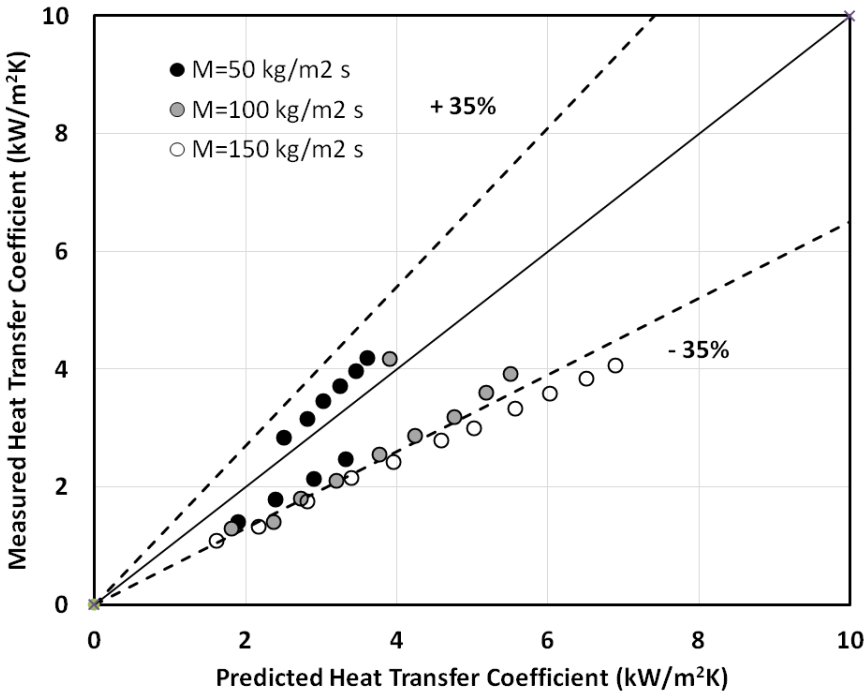


Figure 5-24. Measured HTC vs Kandlikar [66]

To investigate the effect of mass flux on the prediction correlations, the intercept and slop for the prediction data for each mass flux has been calculated, and then the averaged was determined along with the STD from the mean. This gives a sense of the sensitivity of the correlation to flow rate and is plotted in Figure 5-25 shows, where the line is the average data and the mean STD is the error bars. For the example case here the Shah correlation [71] and Wattelet et al. [65] correlations were considered. Figure 5-25 shows a large sensitivity of the Shah correlation to mass flux, while Wattelet et al. correlation does show a minor sensitivity, which is more consistent with the experimental. This also confirmed by considering the mean STD, which was 46 % for Shah correlation and only 11% for Wattelet et al. correlation, which indicates to the insensitivity of Wattelet et al correlation to mass flux change.

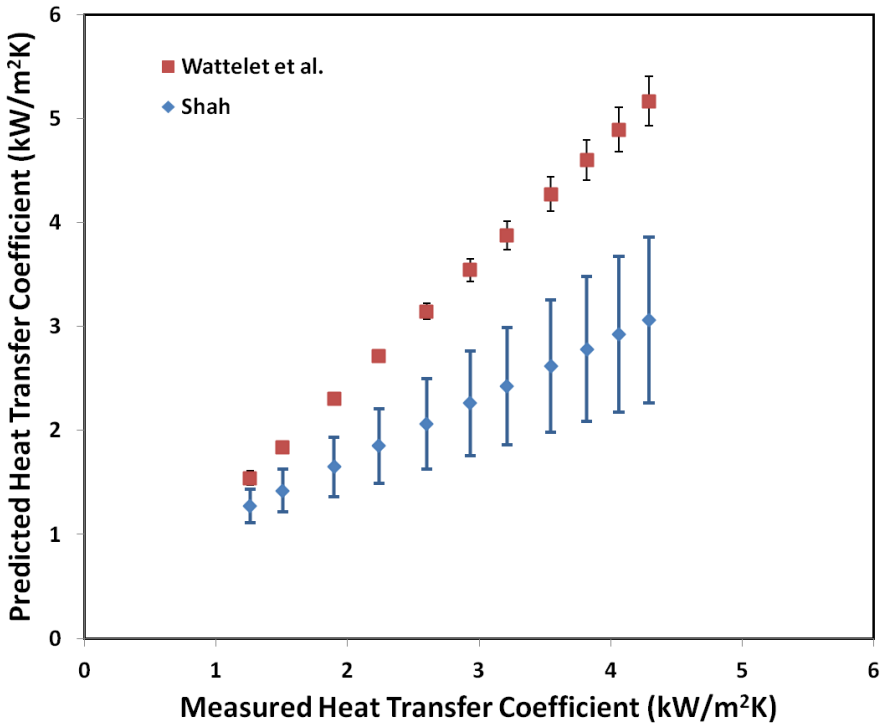


Figure 5-25. Measured data vs Wattelet et al. [65] and Shah [71] errors

## 5.6 **Pool boiling Cooper correlation**

The result above suggests strongly that, for the range of parameters tested, convective effects are not dominant and the boiling dynamics dominate the heat transfer. Thus, one may expect that a pool boiling-type correlation would give reasonable predictions of the heat transfer and of course not be sensitive to the flow rate. To this end, the

Cooper pool boiling correlation, which is the one used in the Wattelet et al. correlation, was also compared with measured data and this is shown in Figure 5-26. The figure shows that there is quite good agreement with this straight forward correlation, and is in fact the best performing correlation of all those considered above. In fact, there is growing evidence, including flow boiling in channels [119] and jet impingement boiling [120] [121], including a wide range of fluids, that tend to show not only the same insensitivity to flow rate, but that the Cooper correlation does an excellent job at predicting the experimental data.

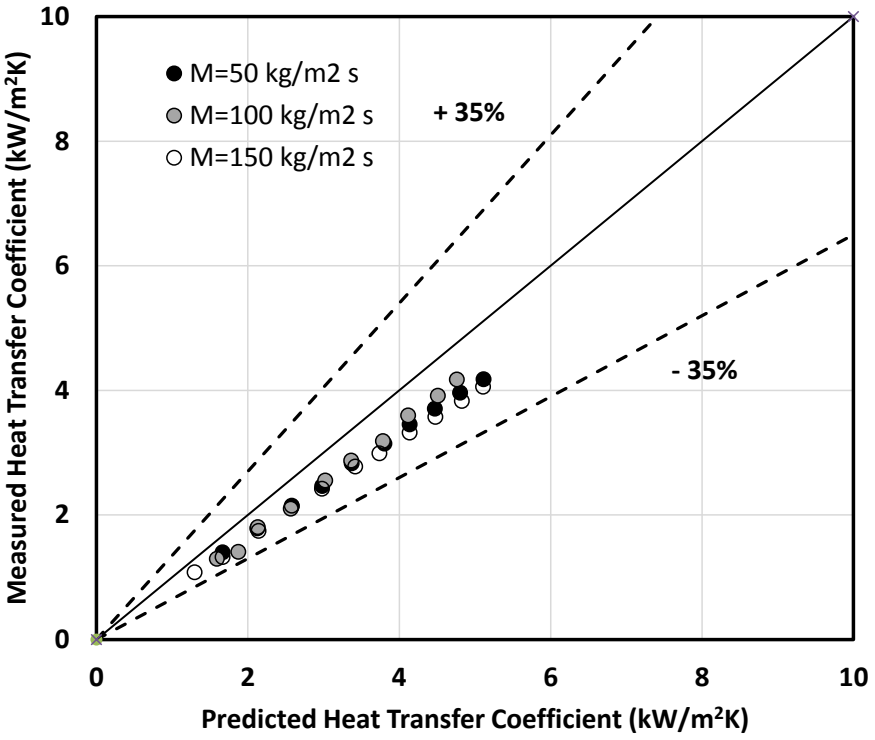


Figure 5-26. Measured HTC vs Cooper correlation

So when boiling starts the heat transfer is dominated by the bubble dynamics and the mechanisms of heat transfer are basically the same as pool boiling. Thus the Cooper correlation can be used for flow boiling when not enough data is available. As it's easy to use and seems to be very accurate across a broad range of flow boiling configurations, including a wide range of fluids.

## 5.7 **Conclusions**

An experimental investigation of upward vertical flow boiling for HFE 7000 has been performed in a circular and annular heat exchanger. To the best of knowledge this is one of the first studies that obtained local heat transfer data together with full visual access to determine the associated flow regime at the measurement location. Results shows that the heat transfer coefficient is a very strong function of imposed heat flux, which is evidence to suggest that the dominant heat transfer mechanisms are associated with the local bubble activity opposed to convective influences. In particular the boiling dictates the flow regime and an interesting result is that the boiling heat transfer coefficient asymptotically matches a linear line for nucleate boiling at lower heat fluxes and a higher slope linear line at higher heat fluxes for the more rigorous slug and churn flow regimes. The inflection region was observed to occur at the transition from bubbly flow to slug flow.

Tests were performed to study the influence of mass flux between 50-150 kg/($m^2$ s) as well as semi-confinement. The measurements showed no significant influence of these parameters.

The experimental boiling heat transfer data for HFE 7000 were then compared against seven predictions correlations for vertical upflow convective boiling. Each correlation has a unique behaviour in predicting the experimental results as each accounted for the influence of convection and boiling on the overall heat transfer in different ways. The results demonstrate good agreements between experimental data and the prediction of the Wattelet et al. correlation [65] with MRD, MAD, and RMS of 21%. The Shah [71] and Gungor & Winterton [75] correlations show acceptable agreements, while the Kandlikar [66] correlation predicted result that are outside of what can be considered acceptable. The Gungor & Winterton [73], Chen correlation [67] and Jung & Radermacher [77] correlations display a largest deviation and must be used with caution. The end result was that correlations that showed the least sensitivity to flow rate and used the Cooper pool boiling correlation were the most accurate.

Finally, the Cooper pool boiling correlation was tested against the experimental measurements and, consistent with some earlier and more recent published studies, the correlation did a very good job at predicting the vertical upflow convective boiling data for the range of parameters tested. This result tends to support the conclusion that the nucleate boiling activity at the heated surface is the dominant mechanism of heat transfer for the cases studied.

# Chapter 6. EHD enhancement of Heat Transfer

The objective of these experiments is to determine the EHD enhancement of heat transfer during upflow convective boiling in the vertical annulus with increasing heat flux, applied electric field strength and AC frequency. This section discusses the thermal-hydraulic results obtained from the instrumented sapphire test section which was electrically heated via a thin conductive coating of ITO on its outer surface. In this test section, the measured wall temperature varied due to changing electrical heating power and the flow regime inside the tube. The heat exchanger test section implements a uniform electrical heating of the tube wall enabling an accurate method of calculating the local heat transfer coefficient, and being transparent, allows flow visualisation so that one is able to link the observed flow regime with local heat transfer.

It should be noted that this is the first investigation ever performed which is capable of measuring the local wall heat transfer coefficients while under EHD conditions, and with full visual access to the flow regimes, for vertical upflow convective boiling. Since the flow regime transition is the main cause of the enhancement of heat transfer according to many studies, this study will offer new insight into the influence of EHD on the behaviour of flow boiling of dielectric fluids by taking high speed videos of the flow. To this end, the high speed camera was set at 1000f/s and used to record videos of the entire test section images at different applied voltages, different AC frequencies, and different heat fluxes.

Many parameters can be varied in this experimental apparatus which can lead to an unrealistically large number of tests unless a focussed programme is planned in advance. Previous work of McGranaghan [15] and Cotton [83] for horizontal EHD augmented flow boiling were used as a first filter to select certain parameters. For example, a mass flux of 100 kg/($m^2$ s)was shown in these studies to be sufficiently large to be inertially dominated in the field-free condition, though not being so high that EHD effects would be overshadowed. Besides this, they showed that the influence of EHD reduces at approximately $Re^{-2}$ whereas the pressure drop penalty increases at approximately $Re^2$ so that increased flow rates are not desirable since they result in a large penalty for moderate enhancement. Both of these studies focussed on

an applied AC frequency of ~100 Hz AC, and had shown good enhancement in horizontal two phase flow, so this frequency was selected here as the baseline voltage frequency. To be consistent with the previous section, a nearly saturated inlet thermodynamic state, that is a subcooling of 2 K, was selected for all experiments. Table 6-1 summarizes the test matrix of the experimental programme. Finally, it was also decided to focus on the lower quality bubbly flow regime since, as discussed earlier, it is the least effective flow regime in terms of heat transfer and is thus the regime most requiring enhancement.

Table 6-1. Varied Parameters for each test

| Test | q" (kW/m$^2$) | Voltage kV | Frequency Hz |
|---|---|---|---|
| **1** | 4-60 | 0 | NA |
| **2** | 6 | 0-8 | 100 |
| **3** | 16 | 0-8 | 100 |
| **4** | 6 | 10 | 0-1000 |
| **5** | 16 | 10 | 0-1000 |

In the next sections, the heat transfer coefficient (HTC) was evaluated under free field conditions and under EHD conditions. With EHD conditions, the HTC was examined for different voltage magnitudes and AC frequencies. Flow regimes were visualized using high speed videography in order to attempt to better understand the effect of EHD on the flow regime and its resulting influence on the heat transfer.

## 6.1 Heat Transfer under Field Free Conditions

To evaluate the enhancement of HTC under EHD conditions, a free field test was first conducted to use as reference case. Prior to this test the rig was disassembled as it was found that the electrode had shifted due to a faulty spacer and was causing premature arching. The test rig was drained and the test section reassembled with new spacers added at the inlet and outlet to ensure the electrode was centred and the brass pressure seal rings were replaced with one fabricated from plastic to avoid arching.

In this baseline experiment the heat transfer coefficient (HTC) at the mid-section of the test section under field-free conditions was calculated. As mentioned above, the refrigerant mass flux, G, was adjusted to 100 kg/($m^2$ s) and, consistent with earlier tests, the inlet subcooling was adjusted to 2 K by tuning the preheater power. The electric power input to the test section was increased until the Onset of Nucleate Boiling (ONB) which occurred at ~4 kW/$m^2$, and subsequently increased in increment up to ~60 kW/$m^2$. Again, the wall temperatures were recorded by thermocouples inset into the sapphire tube walls at the midpoint of the test section. The local heat transfer coefficient was determined as discussed in Chapter 4.

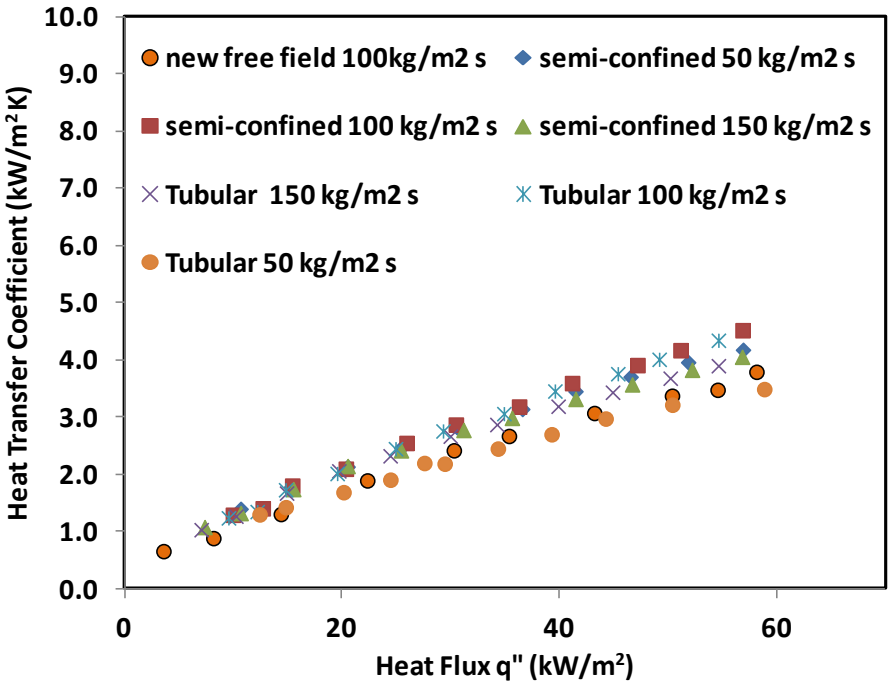


Figure 6-1. Free field boiling heat transfer coefficients vs heat flux. Retest for G=100 kg/($m^2$ s). Tubular

Figure 6-1 shows that the heat transfer coefficients vs heat flux for the pre-EHD retest together with all of the boiling data from the previous tests. These results compare well with previous results, even after dismantling and reassembling the test section and making minor modifications. This further instils confidence of the measured and calculated experiment results and experimental procedure.

Figure 6-2 shows still images of the field-free fully developed bubbly flow regimes at 6 kW/m$^2$ and 16 kW/m$^2$ heat fluxes and these will be used as base case visualizations to compare the forthcoming results with EHD enhancement for different voltage magnitudes and AC frequencies.

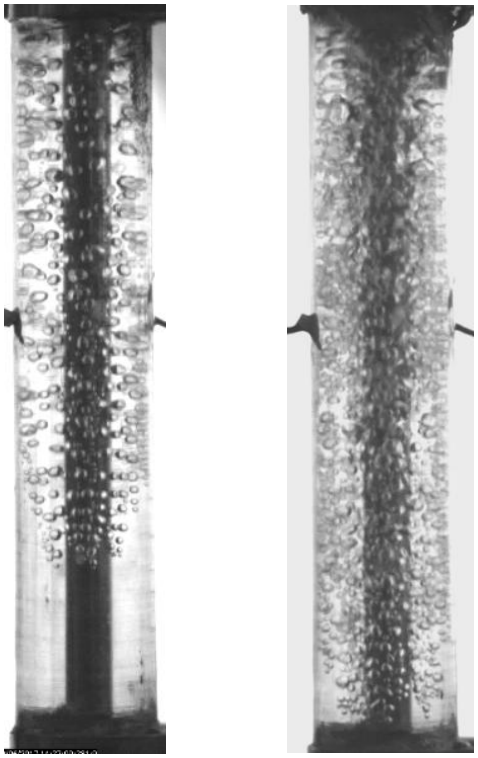

(a) (b)

Figure 6-2. Field free flow regime a (a) 6 kW/m$^2$ (b) 16 kW/m$^2$

## 6.2 **AC EHD Augmentation**

In the first set of experiments a low heat flux setting of $q^{//}$=6 kW/m$^2$ was applied and the peak-to-peak voltage was increased from 0 to 10 kV in 2 kV increments at a fixed frequency of 100 Hz. Figure 6-3 shows influence of applied voltage magnitude on the HTC. As it is shown, the HTC increases monotonically with voltage, starting at from 1.23 kW/(m$^2$ K) at 0 kV to 2.2 kW/(m$^2$ K) at 8 kV AC EHD voltage, which gives maximum enhancement of 1.78.

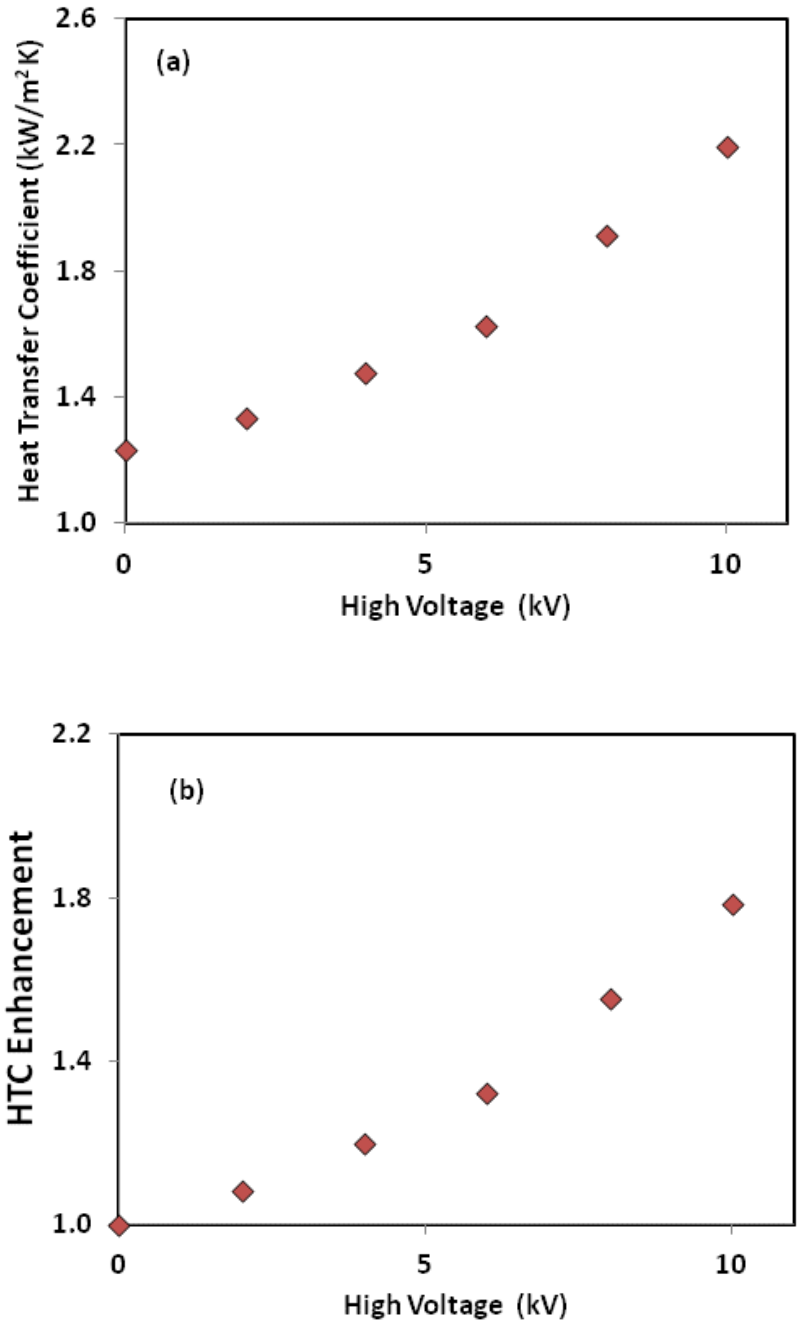


Figure 6-3. HTC and the enhancement at G=100 kg/(m$^2$ s), $q^{//}$=6 kW/m$^2$ and V=0- 8 $kV_{p-p}$ @100 Hz (a) HTC vs voltage magnitude, (b) HTC enhancement vs voltage magnitude

Another experiments were conducted with frequency of 100 Hz, the EHD voltage was applied incrementally from 0 to 10 kV, mass flux was fixed at 100 kg/(m$^2$ s), though at a higher heat flux of 16 kW/m$^2$. The results shown in Figure 6-4 show that the HTC increase with applied voltage magnitude is initially small, though escalates after 6 kV.

The HTC increased from about 2.2 kW/(m$^2$ K) for the field free case to 3.3 kW/m$^2$ at 10 kV, with an associated enhancement of up to 1.55.

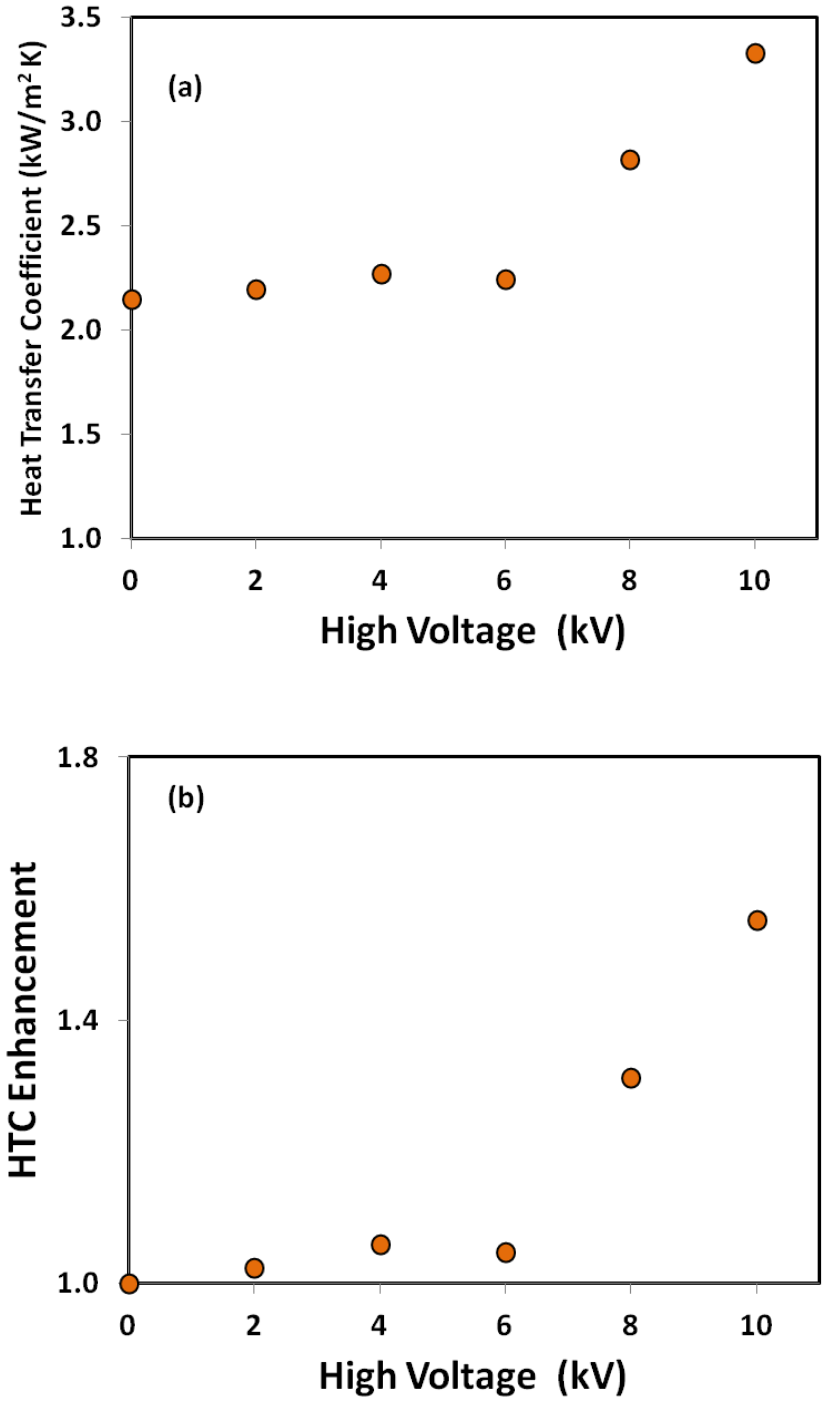


Figure 6-4. HTC and the enhancement at G=100 kg/(m$^2$ s), $q''$=16 kW/m$^2$ and V=0- 10 $kV_{p-p}$ @100 Hz (a) HTC vs voltage magnitude, (b) HTC enhancement vs voltage magnitude

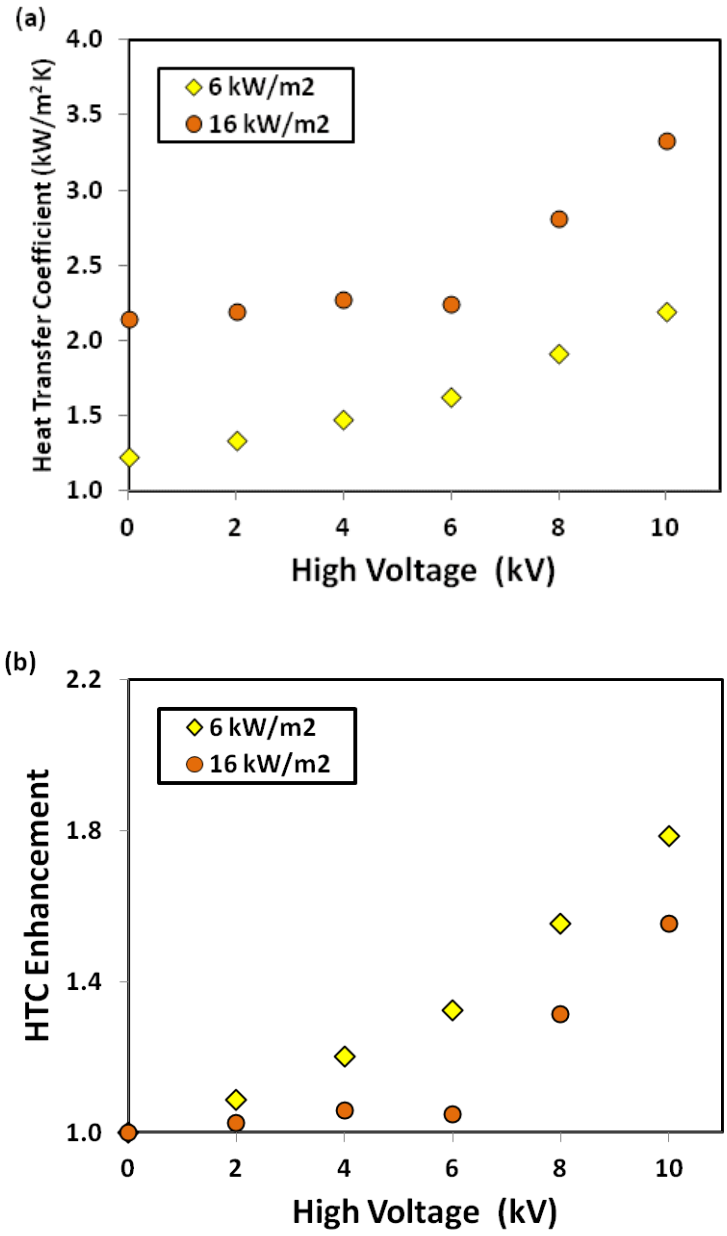


Figure 6-5 (a) shows a higher HTC with higher heat flux, which is due to the increase of nucleate site density and bubble frequency as explained in Chapter 5.

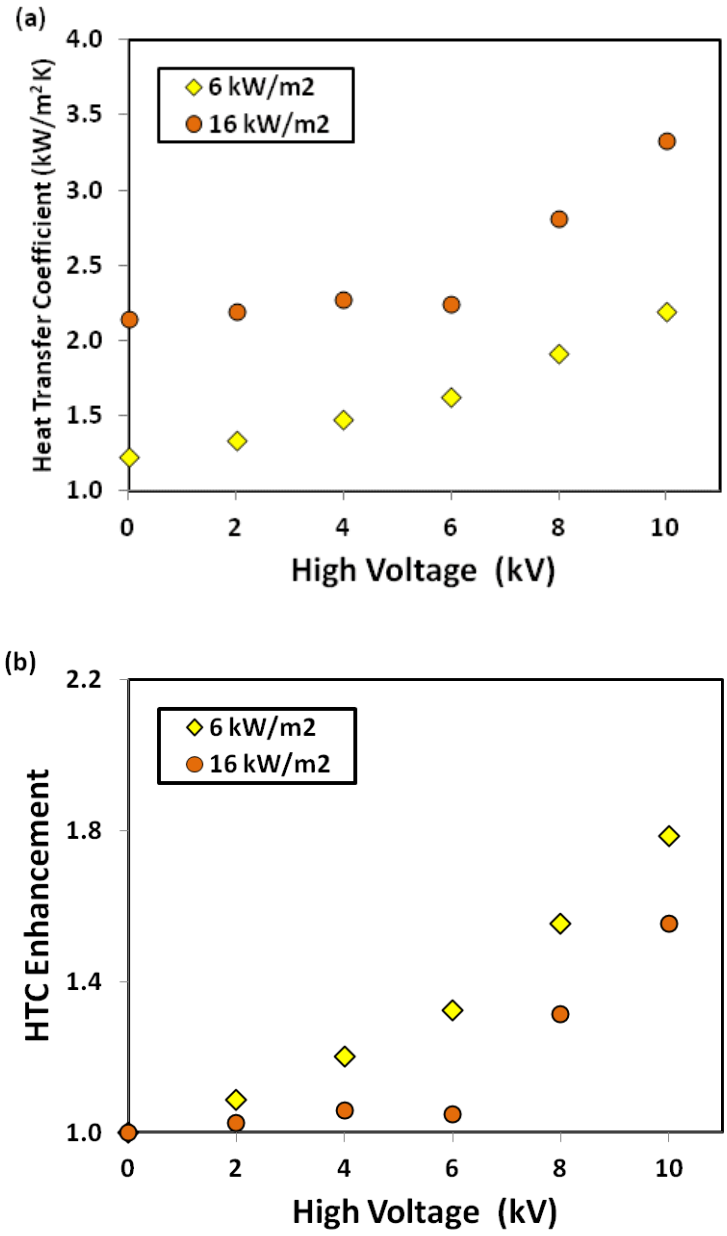


Figure 6-5(b) shows a general increasing enhancement with applied voltage magnitude for both heat fluxes, though the enhancement for lower heat flux is more notable at lower voltages from 2 kV. After about 6 kV the enhancement increases at the same rate for both lower and higher heat flux cases.

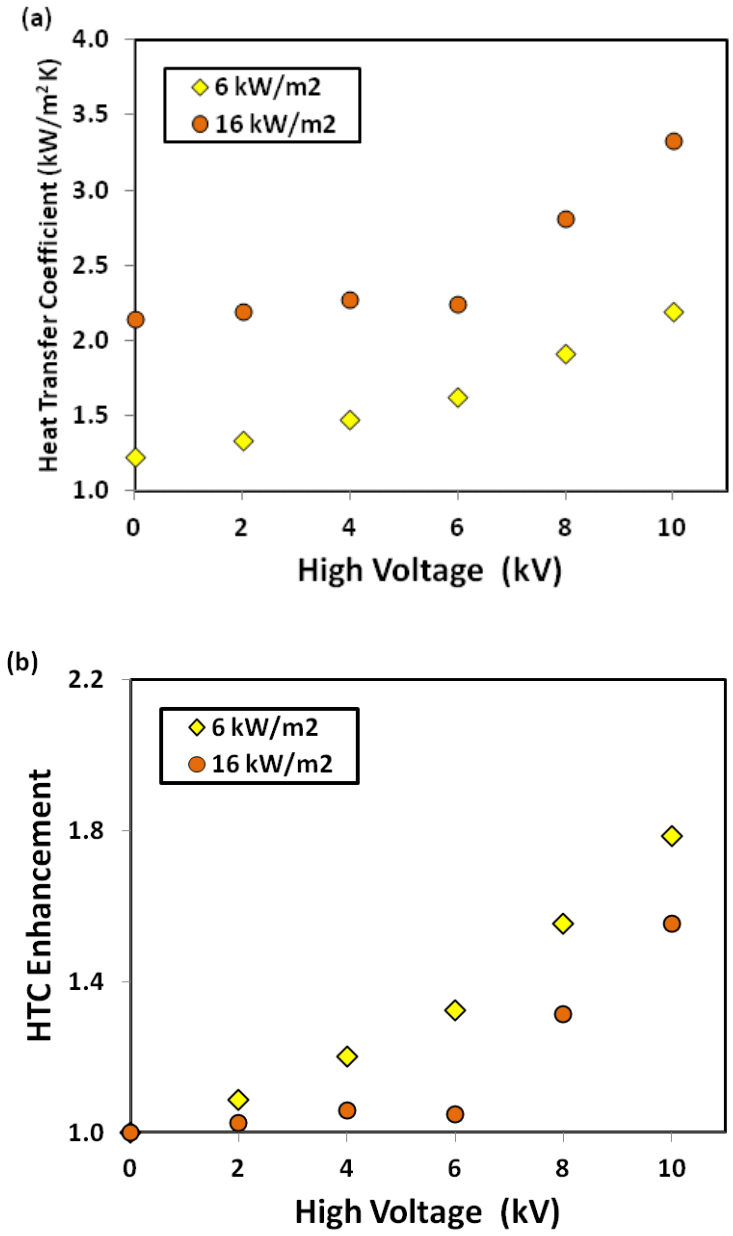


Figure 6-5. HTC and the enhancement at G=100 kg/ ($m^2$ s), $q''$=6 kW/$m^2$ and 16 kW/$m^2$ and V=0- 10 $kV_{p-p}$ @100 Hz (a) HTC vs voltage magnitude, (b) HTC enhancement vs voltage magnitude

Figure 6-6 shows the flow regimes observed along the test section under high and low heat fluxes for the field free and 100 Hz AC electric field conditions at 8 kV. The images show a clear difference between the field free and EHD flow regimes as well as a difference of applied heat flux for both cases. However, this is a dynamic process and, apart from showing a qualitative difference, the still images do not provide enough information to understand the mechanisms that may cause the observed

enhancement. This will be discussed in the next section for the high heat flux case, were it is understood that the same applies for the lower heat flux though the bubble generation rate and nucleation site density is lower resulting in lower HTCs for the low heat flux case.

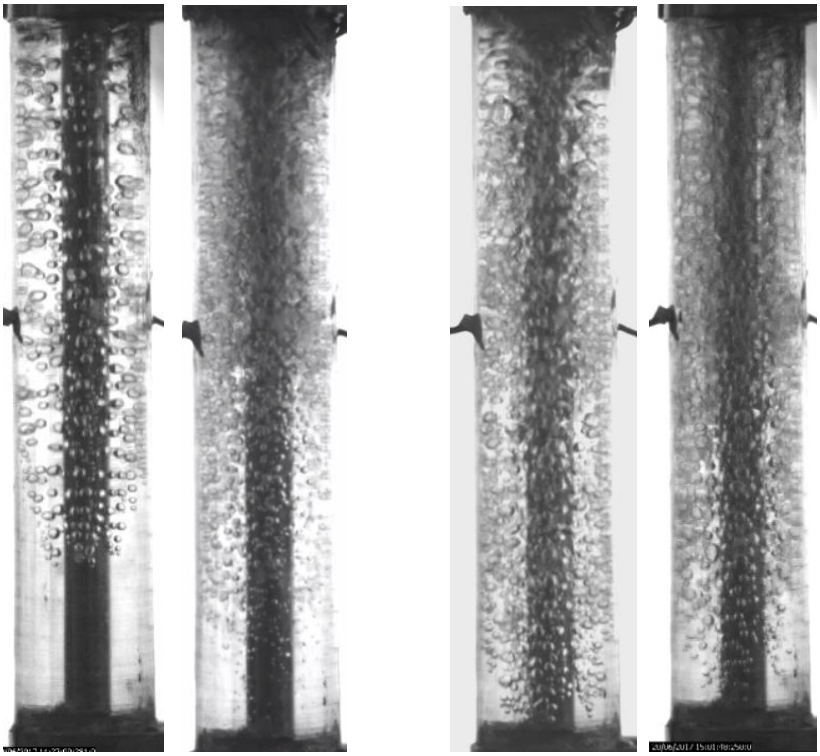

**(a)** (b)

Figure 6-6. Flow visualization for 0 kV (left) and 8 kV (right) at 100Hz, (a) 6 kW/m$^2$ (b) 16 kW/m$^2$

### 6.2.1 Influence of 100 Hz EHD on flow regimes and heat transfer

Figure 6-7 shows the flow regimes observed along the test section under AC electric field conditions for $V_{p-p}$= 0-8 kV for the $q''$~ 16 kW/m$^2$ tests. One of the most striking observations is that, compared with the field free and low voltage cases in Figure 6-7 (a) and (b), there is an observable drop in the nucleation site density at the high applied voltages, Figure 6-7 (d) and (e). This drop in the number of nucleation sites is consistent with the fact that the wall superheat becomes lower as the HTC is increased for the same applied heat flux, but is at the same time not consistent with the notion that bubble growth and departure at the wall is the dominant heat transfer mechanism. Another general observation is that the size of the bubbles in the core of the flow

appear to be smaller. This would also be consistent with bubble growth from a surface with lower superheat.

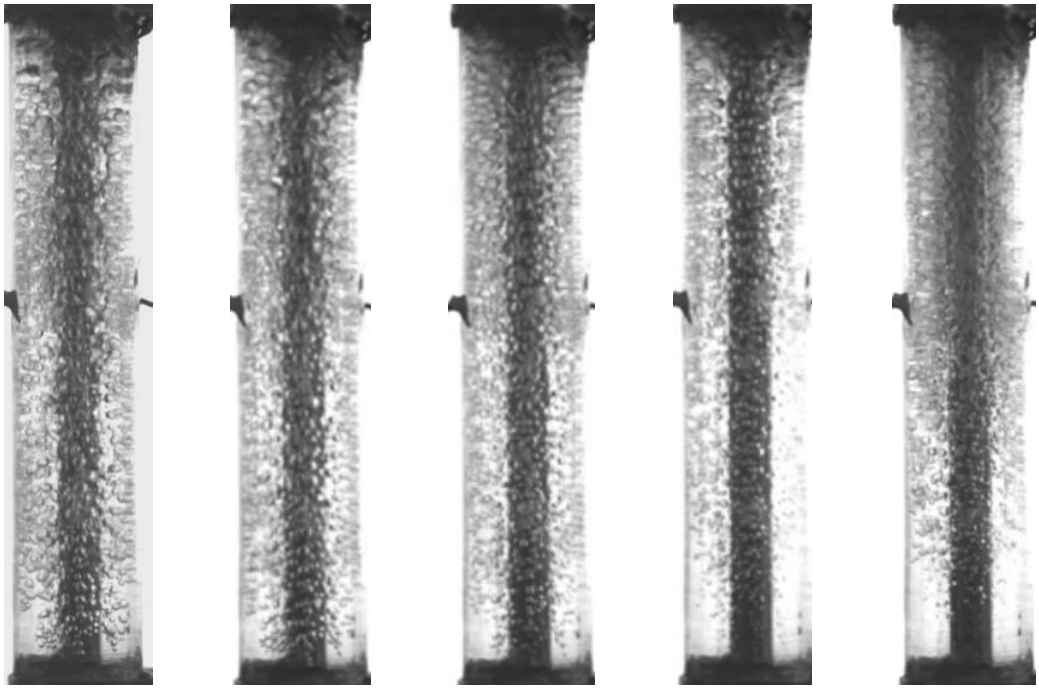

(a) (b) (c) (d) (e)

Figure 6-7. Observed flow regimes at different EHD voltage G=100 kg/(m$^2$ s), $q''$= 16 kW/m$^2$, f=100 Hz, V=0-8 kV AC (a) 0 kV (b) 2 kV (c) 4 kV (d) 6 kV (e) 8 kV

These observations are highlighted in Figure 6-8 which shows a close up of bottom section of flow regime (a) at 0 kV and (b) at 8 kV. Bubble sizes were roughly measured under free field and 8 kV 100 Hz conditions relative to the tube outer diameter (10 mm) as shown in Figure 6-8. Under free field condition Figure 6-8 (a) the bubbles sizes in the core of the flow range between 0.5 mm and 1 mm. At 8 kV 100 Hz condition, the average bubble in the core flow does not exceed ~0.5 mm. It is also clear that the void fraction is considerably less of the 8 kV case.

The lower nucleation site density and the smaller bubble sizes are evidence that the EHD forces are acting on the bubbles growing at the wall as well as the detached bubbles in core of the flow in such a way that the heat transfer is enhanced, and these will now be discussed by considering the high speed videos.

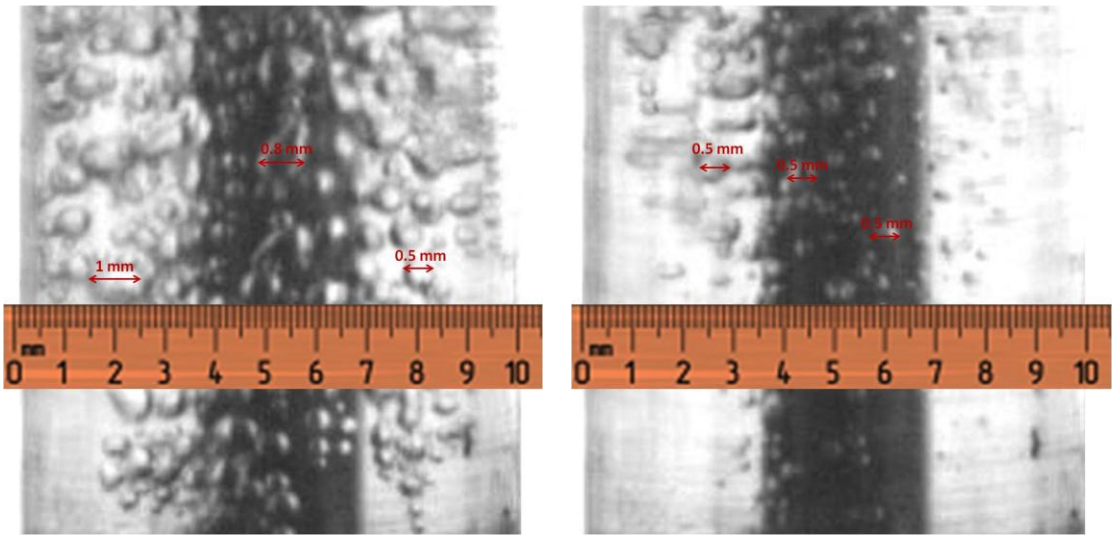


(a) (b)

Figure 6-8. Bubble size (a) under free field condition (b) under 8 kV for G=100 kg/(m$^2$ s), q$^{//}$= 16 kW/m$^2$, f=100 Hz

### 6.2.2 Bubble generation at the wall

For the purpose of understanding the influence of EHD on the bubble dynamics, the bubble growth time was investigated for both free field and EHD field conditions. Here a specific nucleation site that was active for both cases was chosen, though the trend observed was found to be general for most of the bubbles in the viewing section.

Figure 6-9 shows still images of a section of the test section for field free case along with the nucleation site being observed. Here, 10 bubbles were generated in 30 ms which results in a bubble frequency of about 333 Hz (one bubble every 3 ms), and this was about the order for other bubbles in the viewing frame. For the 10 bubbles observed, the average growth time i.e. the time from nucleation to departure, was 3.5 ms and the approximate departure diameter was 0.45 mm.

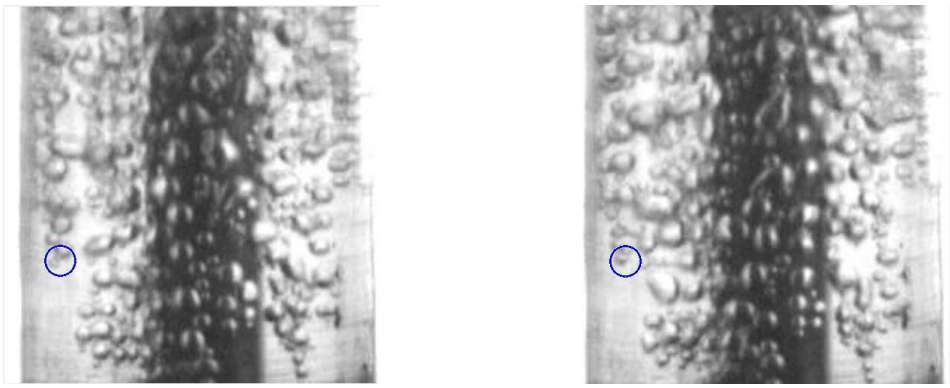

(a) (b)

Figure 6-9. Bubble growth time under free field condition $q''$= 16 kW/m$^2$ (a) 0 second Frame 1 (b) 30 ms Frame 30

The same procedure as above was used to calculate a bubble growth time under 8 kV and 100 Hz (Figure 6-10). At this frequency, three cycles of the AC field will occur in the 30 ms observation frame. Here, 5 bubbles were generated in 30 ms at the same site, which is half the frequency of the field free case i.e. one bubble every 6 ms. For the 5 bubbles observed, the average growth time i.e. the time from nucleation to departure, was 3.6 ms and the approximate departure diameter was 0.32 mm.

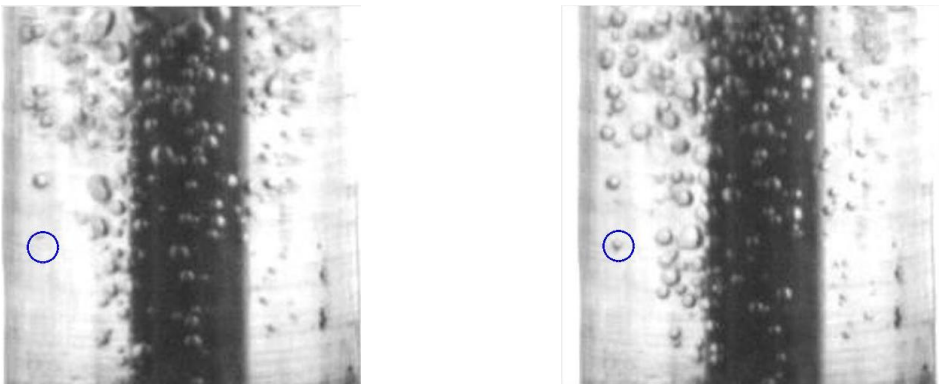

(a) (b)

Figure 6-10. Bubble growth time under 8 kV 100 Hz (a) Frame at 0 ms (b) Frame 30 at 30 ms

Thus, under the influence of EHD, the boiling at the wall is such that smaller bubbles of lower frequency are generated. For individual bubble events, the growth time of the bubbles with EHD is shorter which means the waiting time is longer. These, in

combination with the observation that the nucleation site density is lower, are counter to what would be expected for enhanced heat transfer. This suggests that bubble generation activity at the wall is not the reason for enhancement of heat transfer coefficient and that another mechanism must be responsible.

### 6.2.3 Bubble motion in the core flow

The most important observation of flow regime under AC high voltage is the bubble zigzagging motion due to the EHD forces. The bubbles under EHD force are observed to alternately move inward towards the electrode and then outwards towards the tube wall while and the same time moving upward with the main flow. This result in a zigzag flow path and an example is traced in Figure 6-11, noting that all of the bubbles were following this type of trajectory.

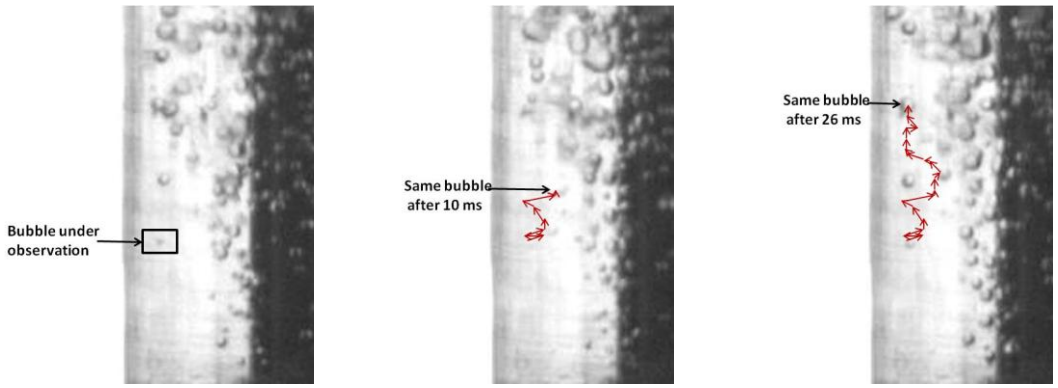


Figure 6-11. Bubbles Zigzagging under EHD forces

This zigzag bubble motion depicted in Figure 6-11 is the most notable difference in the bubble dynamics compared with the field free case and is the mechanism responsible for the HTC enhancement. The main observations from the high speed videos are:

1. There is an attractive force on the bubbles that pulls them towards the electrode. This causes early detachment of the bubbles and accounts for the observation of lower growth time and smaller departure bubble sizes.

2. Departed bubbles in the core flow are attracted to the electrode but do not reach the electrode because of the change of electric field polarity

3. Upon the change in polarity the bubbles then change direction and are forced back towards the wall.

4. This movement continues until the bubble leaves the test section or coalesces with other bubble e.g. Figure 6-11 (c).

Thus, compared with the field free case where the bubble growth activity at the wall is the main mechanism of boiling heat transfer, EHD forces cause the detached bubbles to zigzag in the wall region and this movement interrupts the thermal boundary layer at the wall causing enhanced mixing and thus improved heat transfer. Thus the bubbles in the core are responsible for enhanced cooling and this effect causes a lower wall temperature which also accounts for the lower nucleation site density with EHD.

As discussed earlier, most of the EHD enhanced research has been performed for relatively low mass flux horizontal flow boiling. From this work the general consensus is that the polarization forces, in particular the dielectrophoretic force, is dominant [122] [123]. This is likely the case for horizontal flows since they are predominantly stratified or annular type flows and the liquid extraction mechanism of phase redistribution is so strong that is overshadows any other EHD mechanisms. This is verified by the researchers observing that the EHD-events occurred at double the applied AC voltage, since the polarization forces are proportional to $E^2$ and thus respond in an on-off manner to the AC electric field. In the vertical flow case here, there is no stratification and thus there is no liquid extraction mechanism. In its absence, only the interaction of the electric field with the bubbles is left. The important observation that results is that the bubbles are alternately pulled and pushed to/from the electrode. Observing the bubbles from the high speed videos, this occurs at the frequency of the applied AC voltage, here 100 Hz. The fact that the bubbles are pulled towards the electrode, and this is in the opposite direction of the polarization forces, and that they are both attracted and repelled from the electrode is strong evidence that the electrophoretic force is not only present, but is dominant in the vertical flows considered here, especially considering that this force is proportional to

*E* and, unlike the polarization forces, is sensitive to polarity. Thus, there is in fact charge in this flow and this charge induces strong electrophoretic forces on the bubbles which then act to enhance the heat transfer.

## 6.3 **Influence of applied voltage frequency for low heat flux**

In this section the influence of applied voltage frequency will be discussed, first for the low heat flux cases of $q''$= 6 kW/m$^2$ and then later for the $q''$= 16 kW/m$^2$ tests. These will be considered for a mass flux of G=100 kg/(m$^2$ s), applied voltage magnitude of V= 10 kV$_{p-p}$, and the AC frequencies of 1, 10, 60, 100, 500, 1000 Hz.

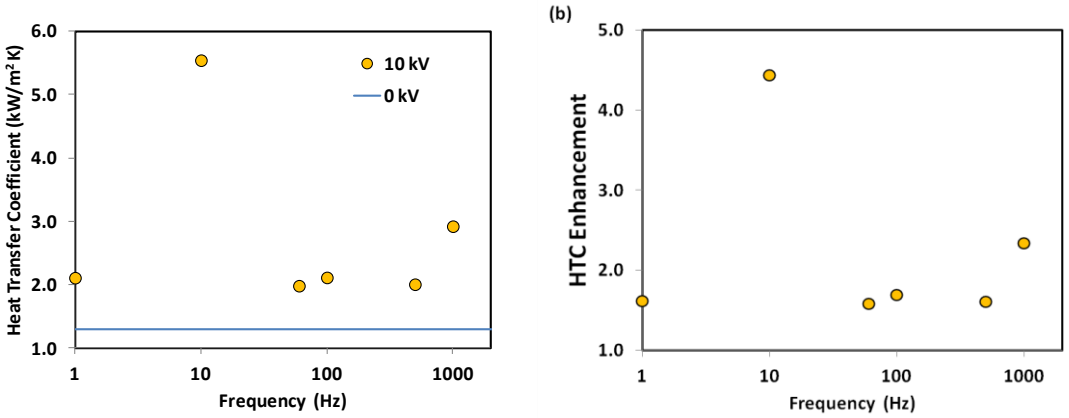


Figure 6-12. (a) HTC vs the frequency, (b) HTC enhancement vs frequency for G=100 kg/(m$^2$ s), $q''$=6 kW/m$^2$, V=10 kV$_{p-p}$ and f=1 - 1000 Hz

Figure 6-12 shows the HTC and HTC enhancement with respect to increasing applied voltage frequency. The results show that at 1 Hz there is an enhancement of about 1.6-fold that increases substantially to a notable peak in the HTC of about 5.8 kW/m$^2$ and the maximum enhancement of 4.4 at 10 Hz which then reduces to the region of 1.6 –fold enhancement at the higher frequencies up to 1000 Hz. HTC.

To better understand the mechanism(s) for heat transfer enhancement, the flow regime of the 10Hz case is studied together with the frequencies on either side of the peak i.e. 1Hz and 60 Hz. These are shown in the still photographs in Figure 6-13, which are taken at the end of the bubble attraction to the electrode phase for each case. Figure 6-13 (a) shows the bubble attraction at 1 Hz, where the bubbles are seen to be drawn all the way to the electrode and constructs a wavy/ churn type of vapor layer, which

may be considered here as an inverted annular flow on the electrode. Figure 6-13 (b) shows the bubble attraction at 10 Hz, where the bubbles tend to form a mist-type vapor cloud around the electrode. Figure 6-13 (c) shows that for the 60 Hz case the bubbles have moved towards the electrode away from the wall, but not enough to reach the electrode, as is observed in the other lower frequency cases. Each case will now be considered in more detail.

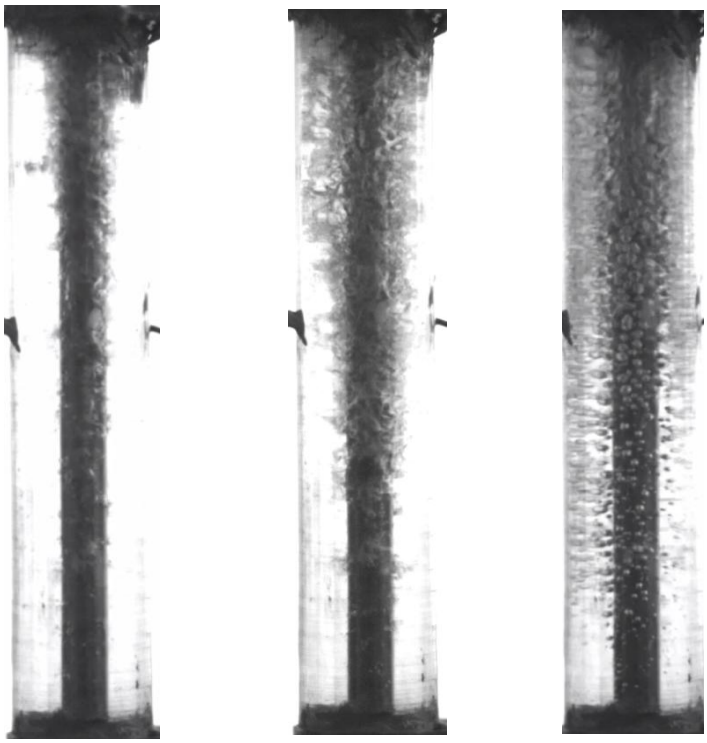

(a) (b) (c)

Figure 6-13. Over all test section images G=100 kg/($m^2$ s), $q^{//}$=6 kW/$m^2$ , V=10 $kV_{p-p}$
(a) 1 Hz (b) 10 Hz (c) 60 Hz

### 6.3.1 Flow regime at 1 Hz

Figure 6-14 shows the cycle of flow regimes created with respect to the 1 Hz and 10 kV applied AC voltage across the flow. The base flow is in the bubbly regime as discussed earlier, and thus the heat transfer would be expected to be that associated with the bubbly flow regime at this lower hat flux. However, when the AC high voltage is applied, a transient process occurs, which here has been segmented into four distinct phase redistribution processes which will be discussed below.

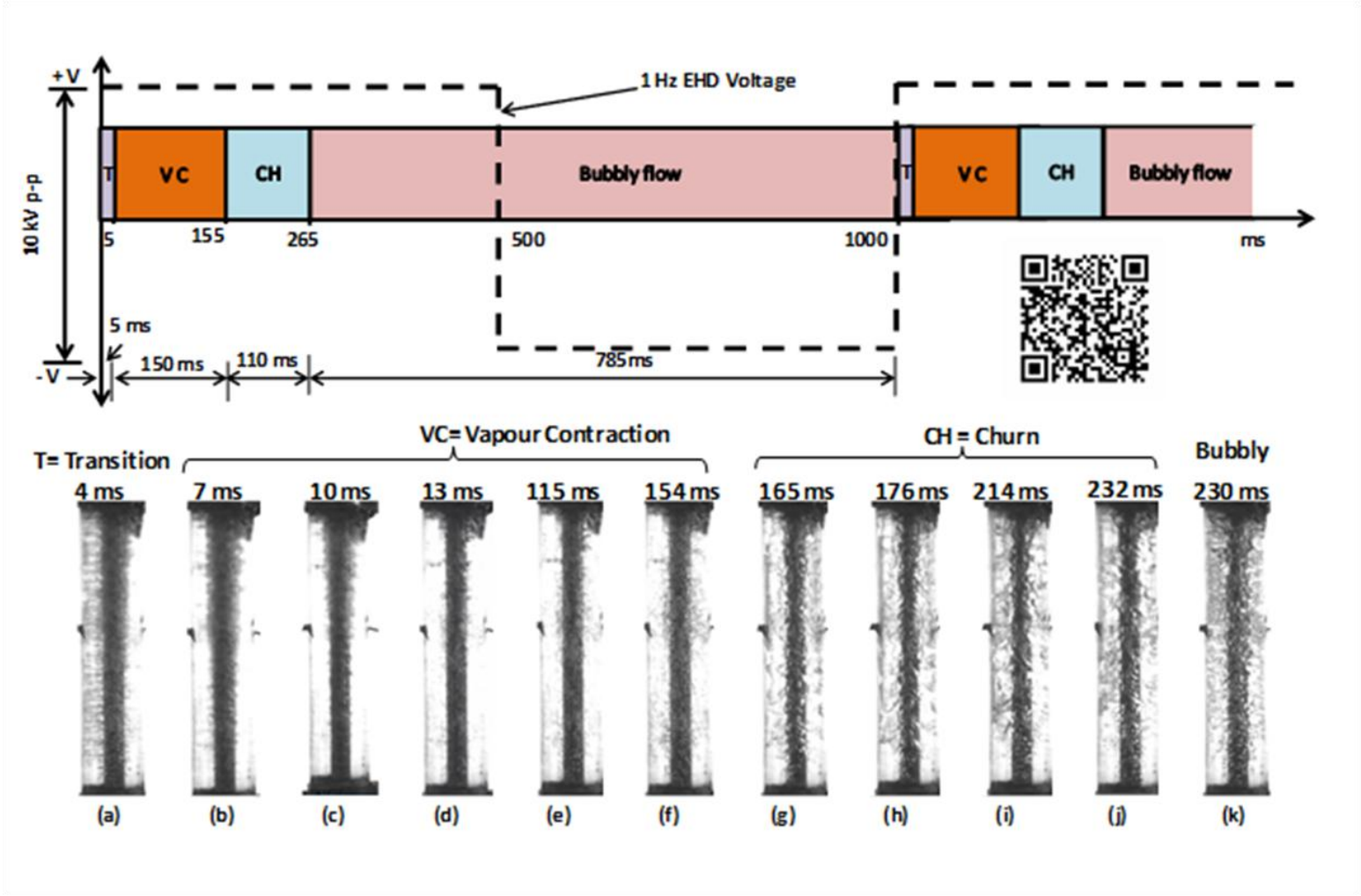


Figure 6-14. Voltage and flow regime cycles for G=100 kg/($m^2$ s), $q''$=6 kW/$m^2$ , V=10 $kV_{p-p}$ at 1 Hz.

*Transition Phase (T):* When the high voltage switches to +10 kV the bubbles are acted on by the electric field in such a way that they are attracted to the electrode. Remembering that the polarization forces act in such a way as to repel the bubbles from the electrode, this opposite affect is evidence that the bubbles are charged and are thus attracted to the positive electrode by the stronger electrophoretic force. Referring to Figure 6-15, the mechanism responsible for this is charge injection into the fluid from the wall which accumulate on the bubble surface. The now negatively charged bubbles are then attracted to the positive electrode by the electrophoretic (Coulomb) force causing them to move across the flow towards the electrode. Referring to Figure 6-14 (a) and (b) the transition phase is quite short, lasting only about 5 ms before the bulk of the vapour has all reached the electrode. It would be expected that this sweeping of the bubbles away from the wall region would cause improved heat transfer, and this is evident from the observation that there is no bubble nucleation at the wall for some time after the transition phase.

*Vapour Contraction Phase (VC)*: The VC phase, depicted in Figure 6-14 (b) to (f) is characterized by the vapour being held-up at the electrode, which itself is still in the +10kV phase of the AC cycle. The vapour forms a wavy/ churn type of vapor layer, which may be considered here as an inverted annular type flow on the electrode. Moving in time from Figure 6-14 (b) to (e), the constricted vapour around the electrode VM in the bottom half of the test section remains tightly bound around the electrode though over time it is observed that bubbles are entrained from the vapour layer (e.g. Figure 6-14 (d)) which move upward with the flow though stay near the electrode. This vapour contraction phase lasts about 150 ms and as Figure 6-14 shows there are no bubbles generated at the wall until about 40 ms into this phase, though they are few, small in size and not vigorous.

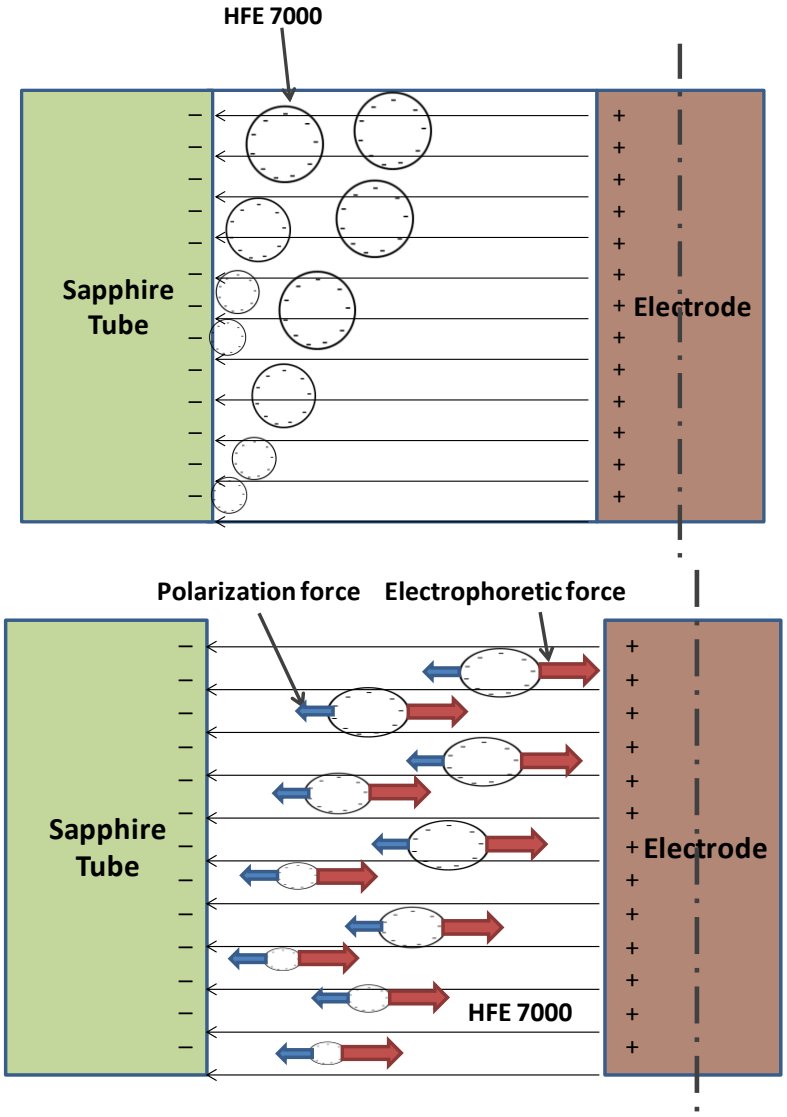


Figure 6-15. Schematic of Transition (T) phase where charge injection from the wall into the fluid negatively charges the bubbles (top) causing them to be attracted to the positive electrode (bottom)

The interaction of EHD with the phases is very complex during the VC phase and one can only hypothesize about the EHD action based on what has been observed in the videos. Here it is thought that the contraction of the vapour around the electrode has two main effects. First, it draws the negative charge to the electrode resulting in a discharge phase and thus weakening of the electrophoretic force which is keeping the vapour tight to the electrode, as sketched in Figure 6-16. As the electrophoretic force weakens there is a likely still polarization force pulling inward and these together with the shear of the flowing liquid cause instabilities which makes the interface very wavy and entrains bubbles into the flow, reducing the volume of vapour against the surface. At some point the pull of the polarization force and the shear instabilities cause the

vapour film to collapse, expelling the vapour back into the core of the flow, which starts the next phase.

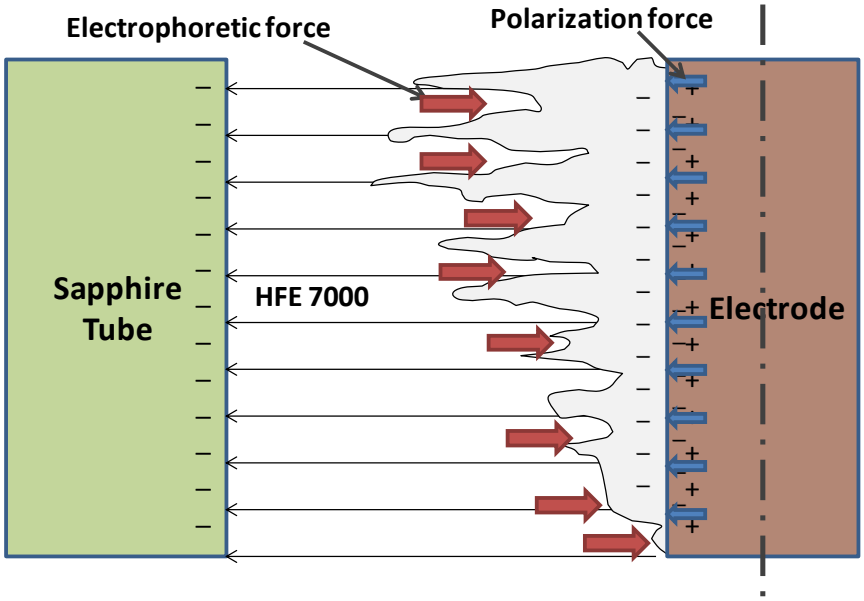


Figure 6-16. Schematic of Vapour Contraction (VC) phase where all of the vapour has been attracted to the electrode and is held there as it discharges

*Churn Phase (CH)*: The VC phase, depicted in Figure 6-14 (g) to (j) is characterized by the discharged vapour being expelled from the electrode into the bulk flow. Since they are discharged and the voltage is still in the +10kV phase of the AC cycle, the bubbles are acted on by the dielectrophoretic force, pushing them towards the wall. In the videos, this appears as a rather sudden event, where the nearly bare (from vapour) wall is suddenly re-washed with vapour. As shown in Figure 6-14 and sketched in Figure 6-17, the resulting flow regime is an aggressive churn flow. As seen in the last chapter, the churn flow regime has much better heat transfer characteristics than the bubble flow regime due to the more aggressive mixing of the phases at the wall. The CH phase lasts about 100 ms and as it diminishes, bubbly flow develops starting from the lower section of the tube and working its way upward until the entire flow regime is reset to the original baseline bubbly flow regime.

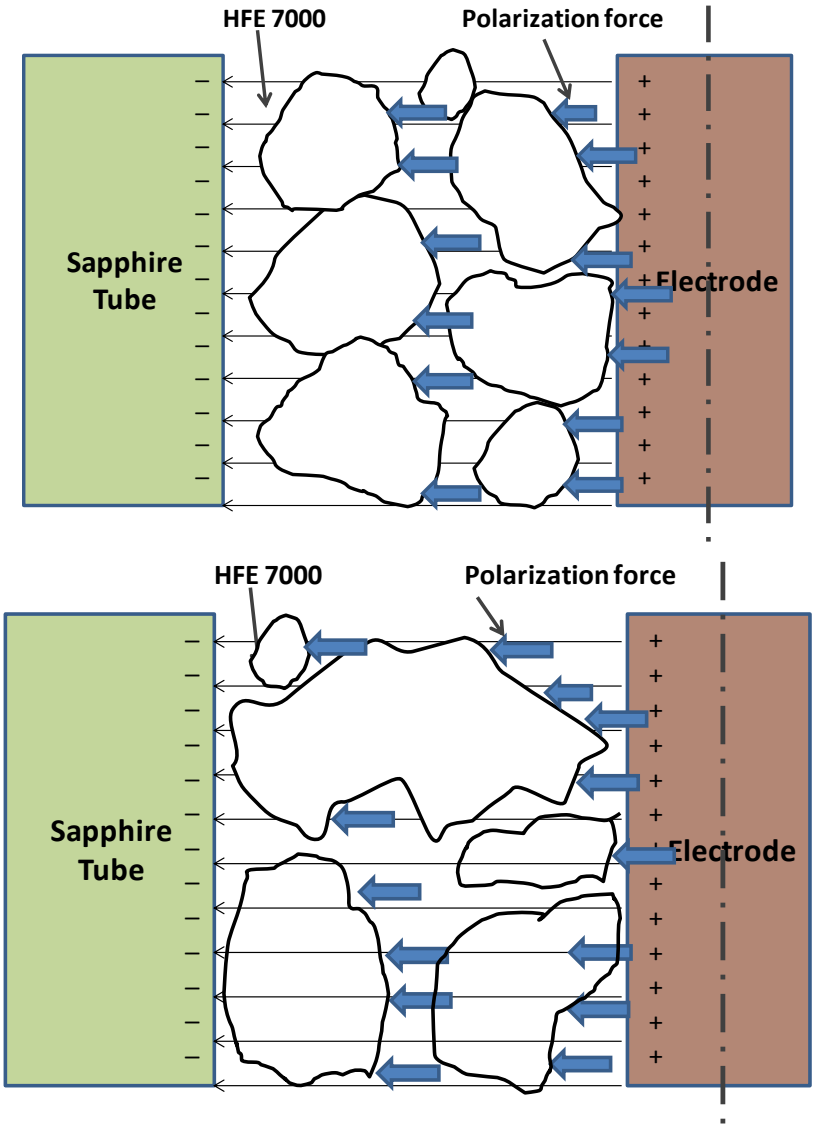


Figure 6-17. Schematic of Churn (VC) phase where the discharged vapour has been forced back into the bulk flow and is acted on by the dielectrophoretic force pushing it towards the wall (top) causing a well-mixed churn flow (bottom)

*Bubbly Phase*: The bubbly flow regime was detailed in the last chapter so will not be detailed here. However, as depicted in Figure 6-14 it is important to note that this regime begins about halfway through the +10 kV phase of the AC cycle and lasts through the -10 kV phase right up until the beginning of the next voltage cycle, when the entire cycle is then repeated.

Flow regimes are well known to dictate the effective boiling heat transfer coefficient. Generally, the more aggressive the mixing of the phases near the wall, the higher the heat transfer coefficient. In the case considered here enhancement, 3 flow regimes

occur in each AC cycle, each of them with different heat transfer characteristics and each of them lasting for a different period of time. The percentage of time in each regime is of course important with regard to time averaged heat transfer coefficient considering the cycle is repeated continuously.

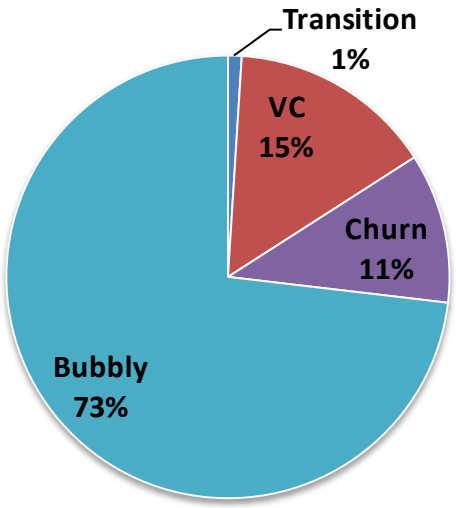


Figure 6-18. Percentage time for each flow regime at 1 Hz, 10 kV $_{p\text{-}p}$

Figure 6-18 shows the percentage of time for each flow regime in the 1 Hz frequency cycle. The transition phase takes about 1% of the cycle time, which is a small portion of the period. However, the rapid movement of bubbles towards the electrode will cause significant mixing of the flow and disrupt the heat boundary layer at the wall resulting in enhanced cooling. The vapour contraction (VC) phase occurs next and lasts for 15 % of the total period. Here the vapour is held on the electrode and this can be considered a transient conduction phase where the thermal boundary layer is re-established and the wall temperature recovers, and this should improve heat transfer. The repelling of the vapour from the electrode to the wall and the resulting well mixed churn flow that results would have associated with it much enhanced heat transfer, as discussed in Chapter 5 where it can be about 3 times higher than bubbly flow. This phase lasts for about 8 % of the total AV voltage period. About 75 % of the voltage cycle time is associated with the baseline bubbly flow regime, which would be the lowest in terms of the HTC. Based on these observations, one would expect that the 1 Hz frequency would show enhanced heat transfer, but because so much of the time is in the bubbly flow regime one would not expect the enhancement to be

excessive. Referring to Figure 6-12 (b) this is in fact the case, where a 1.6 fold enhancement is measured.

What is important about these observations is that the heat transfer should be improved by adjusting the voltage frequency to reduce or eliminate the time spent in the bubbly regime, and this is discussed next.

### 6.3.2 Flow regime at 10 Hz

Figure 6-19 shows the flow regimes under 10 Hz 10 $kV_{p-p}$ applied voltage. As in the 1 Hz case, when EHD force comes to effect at the initiation of +10 kV, the bubbles become charged and move towards the electrode, this being the transition (T) phase, which lasts about 5 ms ( Figure 6-19 (a)). The vapour contraction (VC) phase again follows with the vapour held against the electrode. Unlike the 1 Hz case, this only lasts about 15 ms which is notably shorter. The reason for this is unclear though may be due to the frequency affecting the free charge in the fluid in such a way that the discharging of the vapour to the point that the dielectrophoretic force becomes strong enough to collapse the vapour film and then push the resulting bubbles back to the wall. This requires further research. Regardless when, the vapour is finally pushed back to the wall starting the churn regime. Figure 6-14 shows this regime for the 1 Hz case this regime lasted ~110 ms and during the final stage, bubbly flow was re-establishing. The same is observed here for the 10 Hz case, and is evident in Figure 6-19 (h), though more clear in the high speed videos which can be watched using QR Code printed on Figure 6-19. The important thing here is that for the 10 Hz frequency, the flow never returns to the original free field-type bubbly flow regime which should retain a state of enhanced heat transfer for the entire period of the AC applied voltage.

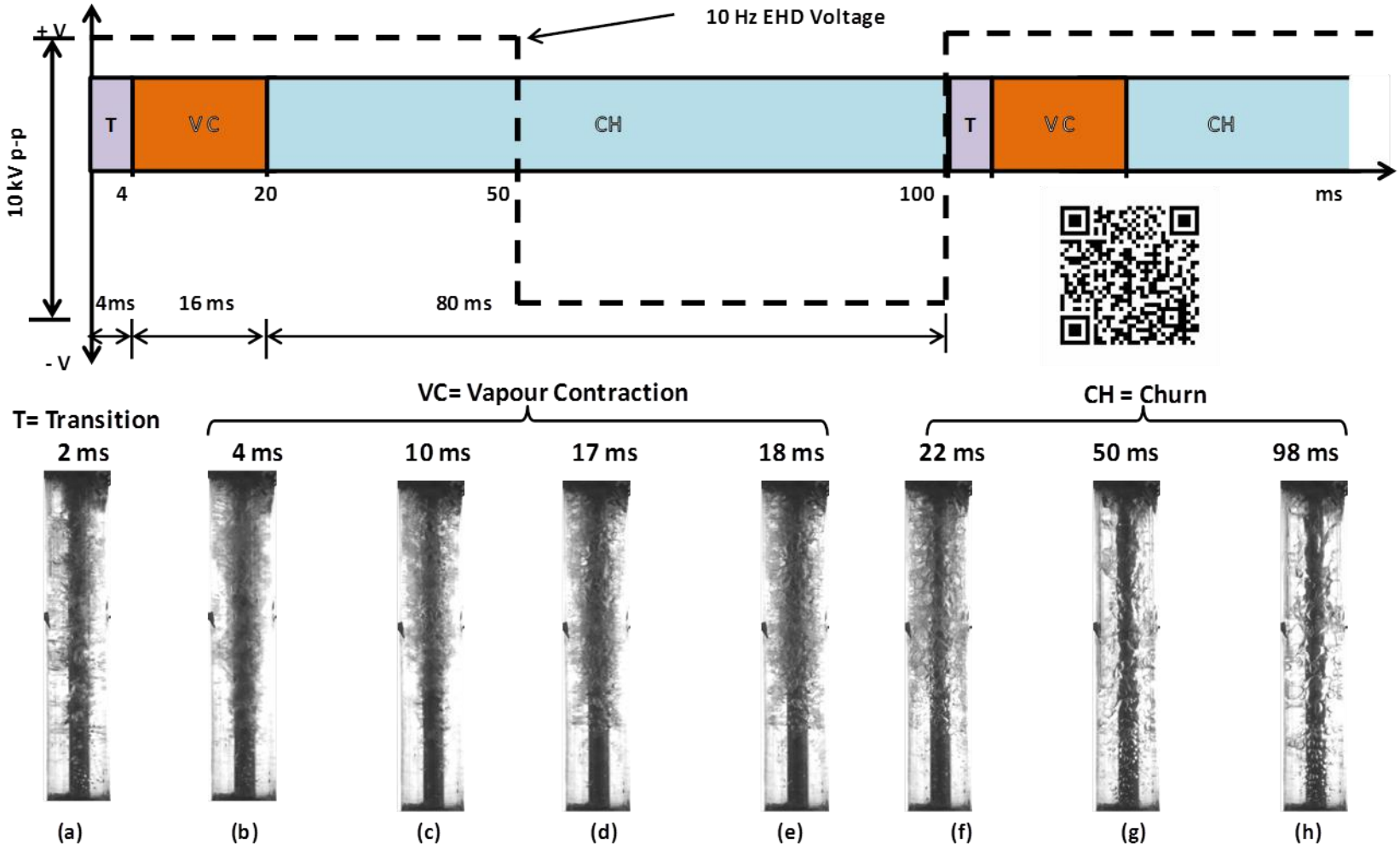


Figure 6-19. Voltage and flow regime cycles for G=100 kg/($m^2$ s), $q^{//}$=6 kW/$m^2$ , V=10 $kV_{p-p}$ at 10 Hz

This cycle of flow regime repeated once with every AC high voltage cycle, which is 100 ms. The transition phase takes only about 4 % of the cycle time, which may be insignificant as a flow regime, but as mentioned earlier causes enhanced cooling due to disrupting the thermal boundary layer which recovers during the vapour contraction (VC) phase, and this occurs at a frequency that is 10 times faster than the 1 Hz. The VC phase lasts about 16 % of total cycle. This is the phase where the vapour is held to the electrode and little to no nucleation is observed at the heated wall. Although lasting a relatively short period of time the T and VC phases are important because the next phase in the cycle, the churn phase (CH) would not occur if they were not part of the cycle. When the discharged vapour is forced back to the wall, longer lasting and likely much higher HTC churn flow that results lasts for about 80 % of the cycle. Although the baseline bubbly flow regime is just beginning to be established at the 100 ms mark, the next high voltage cycle begins setting the system into the next T-VC-CH cycle. This, the lower heat transfer bubbly flow regime is avoided and the heat transfer is dominated by churn flow. It is noted in the previous chapter that the HTC associated with the churn flow regime was in the region of 4 to 4.5 kW/(m$^2$ K) which agrees fairly well with the measured HTC of about 5.5 kW/(m$^2$ K) for this 10 Hz EHD case.

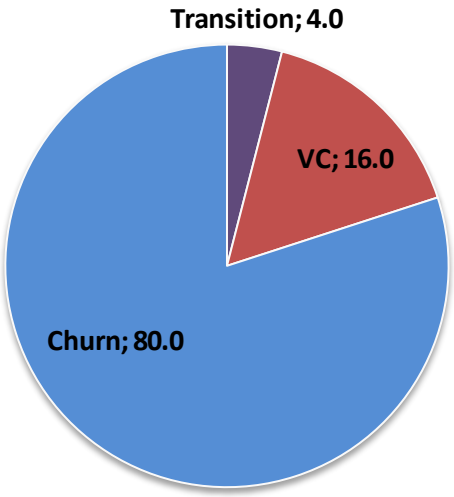


Figure 6-20. Percentage time for each flow regime at 10 Hz, 10 kV $_{p\text{-}p}$

### 6.3.3 Flow regime at 60 Hz

Figure 6-21 shows the flow regimes and events timeline under 60 Hz 10 $kV_{p-p}$ electric field. The case here is not fundamentally different to that discusses in Section 6.2. When +10 kV occurs the charged bubbles move toward the electrode because they are acted upon by the electrophoretic force. However, because of the higher frequency, the +10 kV is only 'on' for about 8 ms and this is not enough time for the full vapour contraction event to occur i.e. the bubbles do no form a vapour film around the electrode. When -10 kV occurs, the bubbles are pushed back into the core and towards the wall and the flow is bubbly. Thus, the bubbles zigzag at the frequency of the electric field and, as discussed earlier, disturb the fluid in the wall region causing enhanced mixing and thus improved heat transfer. However, as Figure 6-12 shows, this is not as effective as the 10 Hz which is dominated by the churn-type flow regime.

Figure 6-22 shows the percentage of time occupied by each regime in the test section at 60 Hz. As it is shown, about half of the period is Transition (T) with bubbles pulled quickly towards the electrode, and the other half is Bubbly flow, with the bubbles pushed mildly back into the core an towards the wall. As mention, insufficient time exists for the full vapour contraction (VC) phase and subsequently the rigorous churn flow could not be established either.

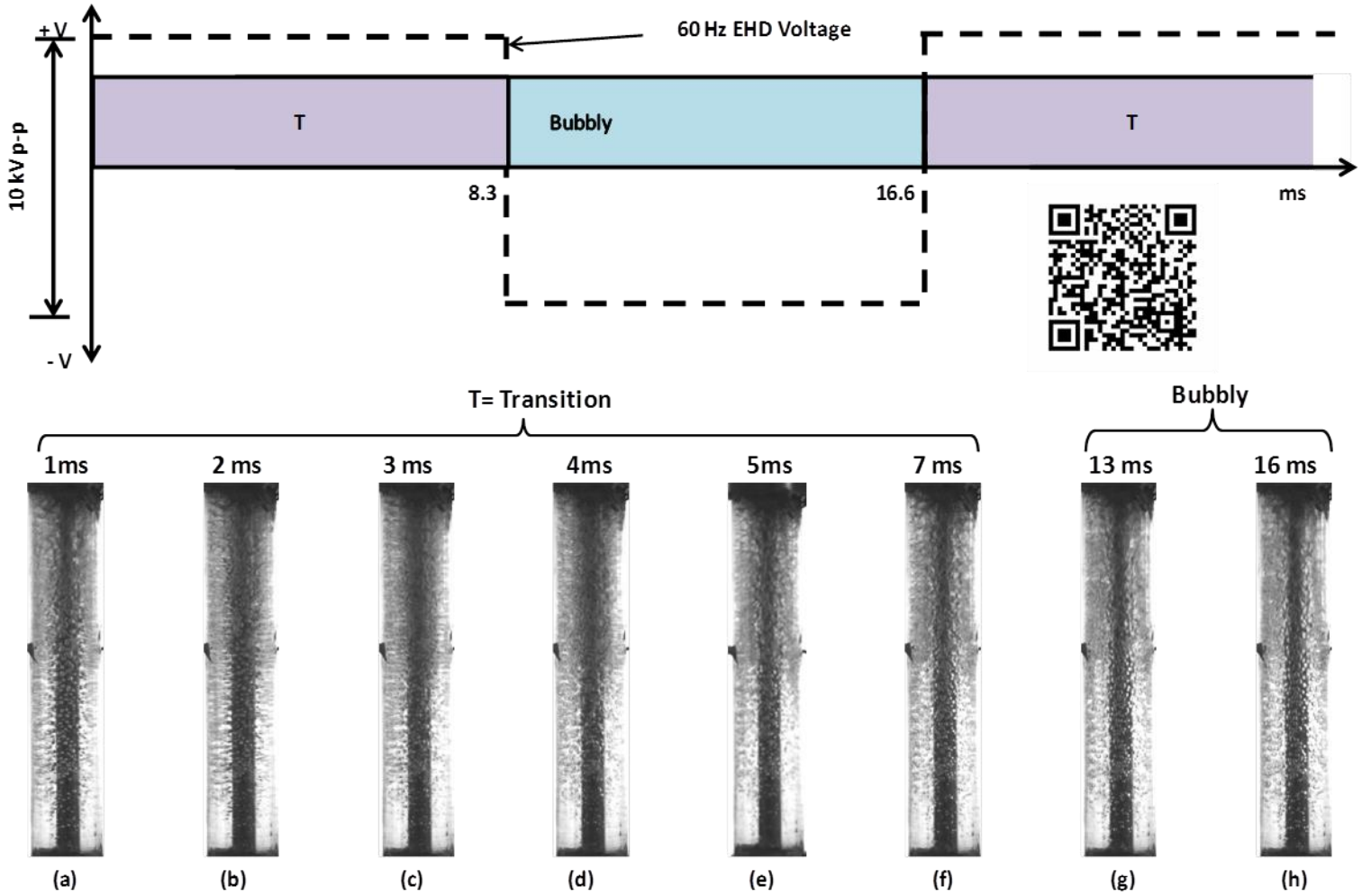


Figure 6-21. Voltage and flow regime cycles for G=100 kg/(m$^2$ s), $q''$=6 kW/m$^2$ , V=10 kV$_{p-p}$ at 100 Hz

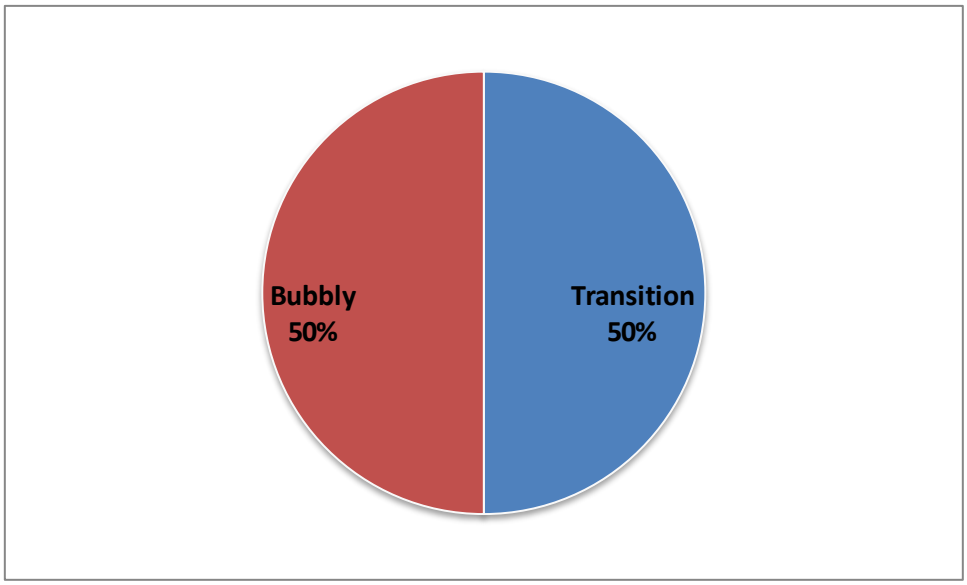


Figure 6-22. Percentage time for each flow regime at 60 Hz, 10 kV p-p

## 6.4 Frequency effect at higher heat flux

In this set of experiments the mass flux was again set at 100 kg/(m$^2$ s) and the voltage at 10 kV$_{p-p}$ with AC frequency of 1, 10, 60, 100, 500 and 1000 Hz), but with the higher heat flux of 16 kW/m$^2$. The HTC and enhancement results are shown in Figure 6-23.

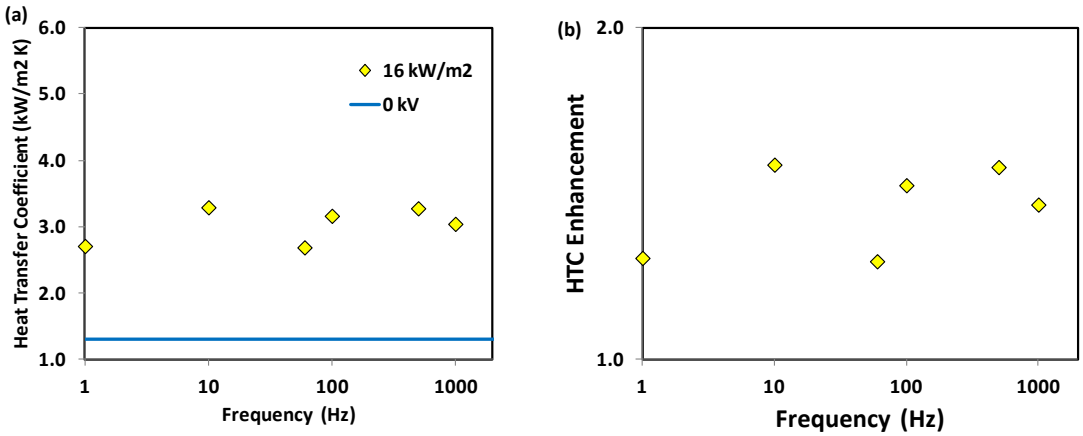


Figure 6-23. (a) HTC vs the frequency, (b) HTC enhancement vs frequency for G=100 kg/(m$^2$ s), q$^{//}$=16 kW/m$^2$ , V=10 kV$_{p-p}$ and f=1 - 1000 Hz

Figure 6-23 shows that maximum HTC of 3.3 kW/(m$^2$ K) and associated enhancement occurred of 1.6 occurred at 10 Hz. However, the peak at 10 Hz is not as prominent as the lower heat flux case. Figure 6-24 shows this better where the HTC

and enhancement are plotted for the lower and higher heat flux cases on the same plots. As it is shown, not only is the peak much less pronounced, but the enhancement is generally lower over all frequencies tested.

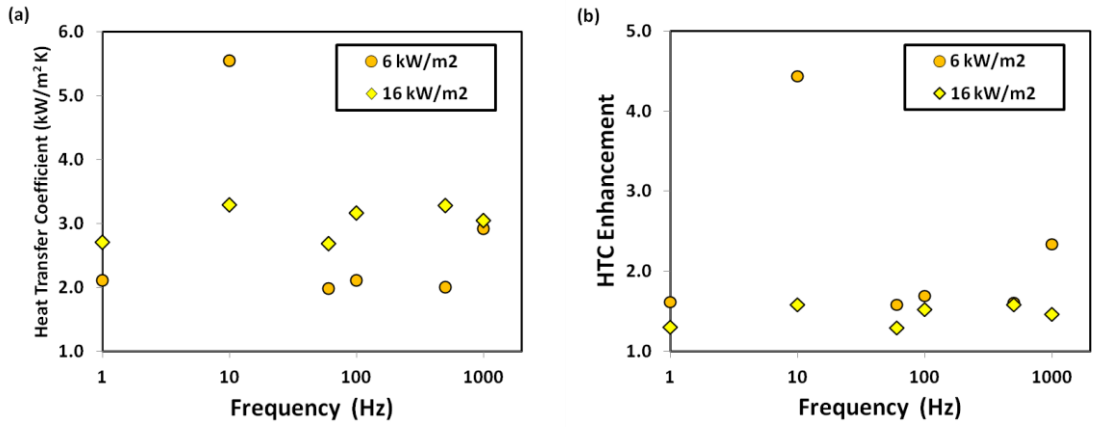


Figure 6-24. Comparing high and low heat flux Results (a) HTC vs the frequency (b) HTC enhancement vs frequency

With regard to the off-peak frequencies i.e. 1 Hz, 60 Hz, 100 Hz etc., there is no major difference with regard to the EHD dynamics with the flow. The main reason for the lower enhancement is simply due to the fact that with the higher heat flux, the boiling is already more rigorous and thus the impact of EHD, although measurable, is not as large because the baseline bubbly flow is already more effective. The still images in Figure 6-25 illustrate this to some extent. For the frequencies >10 Hz the bubbles zigzag at the frequency of the applied AC voltage, but as the figure shows, the high heat flux has associated with it a higher local quality and thus higher density of bubbles. The bubbles not only interfere with one another, which may affect their ability to move transversely to the flow, but are also inhibited from interacting with the wall region due to the high density of bubbles there. Therefore, although there is enhanced mixing and heat transfer, the actual enhancement is not as pronounced. However, for the 1 Hz and 10 Hz cases, the enhancement mechanism, as discussed earlier, was more associated with the full vapour contraction to the electrode and subsequent dispelling of the vapour to cause a churn flow to be established. The difference in the enhancement was then related to the relative portion of time of the cycle that the churn flow occupied. Figure 6-25 (a) shows the flow regime at 10 Hz at the end of the transition (T) phase for the higher heat flux. Although it qualitatively

looks similar to the lower heat flux case there is a very important different which will be discussed next.

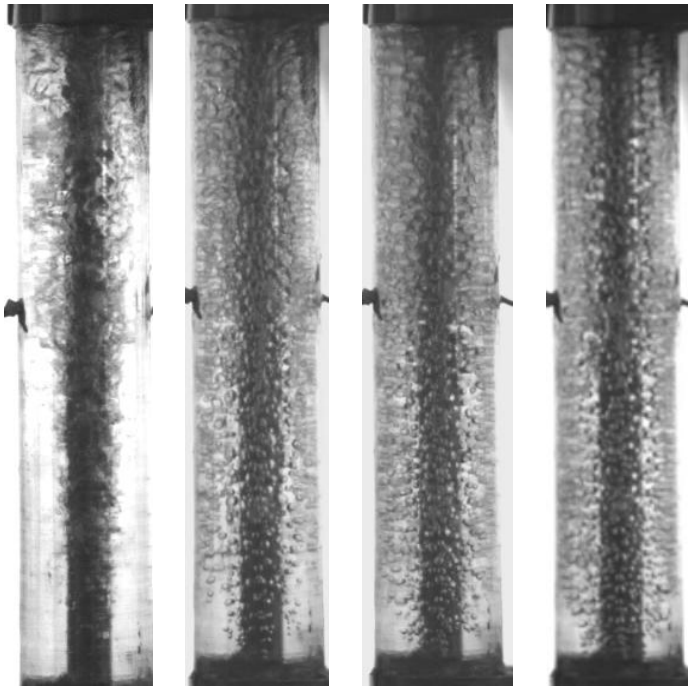

(a) (b) (c) (d)

Figure 6-25. Over all test section images 100 kg/($m^2$ s), 10 kV, 16 kW/$m^2$. (a) 10 Hz (b) 60 Hz (c) 100 Hz (d) 500 Hz

Figure 6-26 shows the flow regimes and sequence of events under 10 Hz 10 $kV_{p-p}$ electric field at 16 kW/$m^2$ and can be compared with the lower heat flux case in Figure 6-19. Consistent with the lower heat flux case, the switching on of the +10 kV attracts the vapour to the electrode during a Transition (T) phase that lasts ~ 5 ms (Figure 6-26 (a, b)). However, for the low heat flux case the vapour is observed to nearly disappear from sight as it is held tightly to the electrode forming a thin film during the VC phase. Here however, Figure 6-26 (c,d) shows that, due to the much higher volume of vapour associated with this heat flux, the VC phase is not as dramatic and large bubbles still exist in the core flow, which are continually generated by being sheared from the vapour mass around the electrode. This release of vapour back into the core flow is termed Transition 2 (T2) in Figure 6-26. It thus seems that the higher vapour volume diminished the intensity of the VC phase leaving and expelling significant vapour in the core flow and mix with new generated bubbles during a second transition phase T2. The subsequent effect is that when the vapour

near the electrode is finally discharged and released back into the flow, the churn flow that is created is also much less dramatic and very much shorter (~6 ms) after which bubbly-type flow start once again develops. The bubbly flow continues for ~80 ms until the next AC cycle commences.

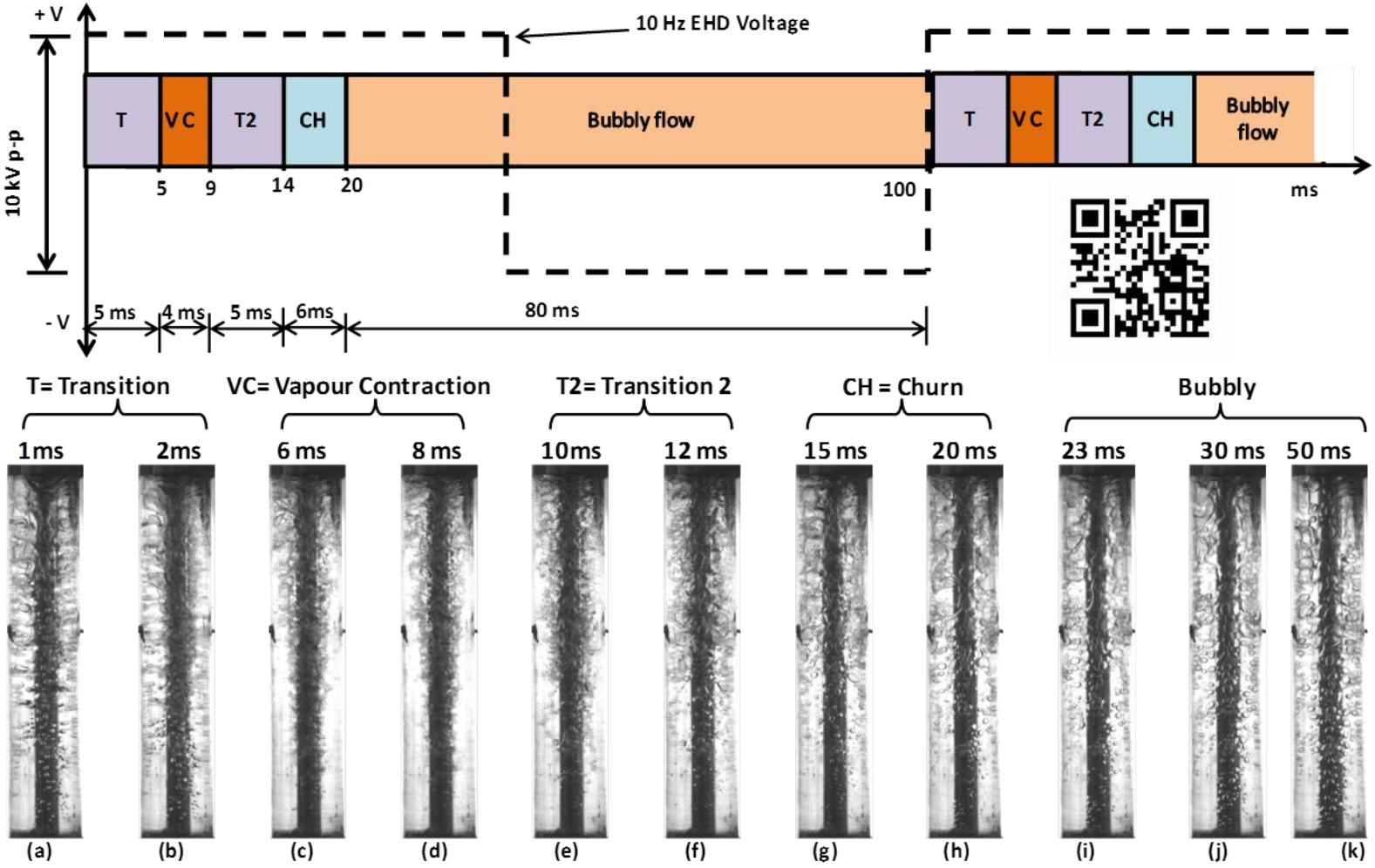


Figure 6-26. Voltage and flow regime cycles for G=100 kg/(m$^2$ s), $q^{//}$=16 kW/m$^2$ , V=10 $kV_{p-p}$ at 10 Hz

It thus appears that the more rigorous boiling and vapour generation associated with the higher heat flux interferes with the ability of EHD to create a vigorous and sustained churn flow and this inhibits EHD from enhancing the heat transfer to the same extent that the lower heat flux could. This is highlighted in Figure 6-27 which can be compared with Figure 6-20 for the low heat flux case. The most striking difference is that the portion of the cycle associated with EHD augmentation of the flow (T/VC/T2/CH) only occurs for about 30% of the cycle, whereas for the low heat flux case this was 100%, and this accounts for the lower HTC and HTC enhancement at 10 kHz.

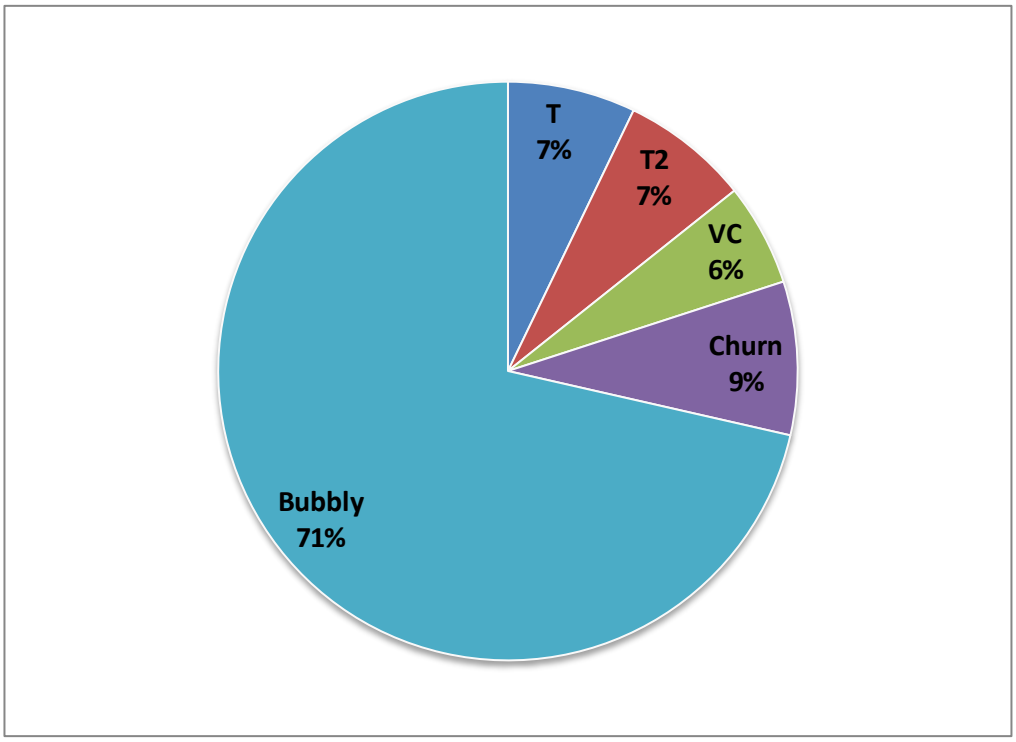


Figure 6-27. Percentage time for each flow regime at 10 Hz, 10 $kV_{p-p}$, 16 $kW/m^2$ k

## 6.5 **Conclusion**

To the best of knowledge, this is the first study of vertical upflow boiling with EHD augmentation that included local heat transfer measurements with detailed visualization of the flow regimes and phase interactions. One very striking conclusion is that, for the bubbly flow regime considered, there is very strong electrophoretic interaction with the phases, and this is not what has been observed for horizontal flows where liquid extraction (dielectrophoretic) dominates the EHD effect. The

electrophoretic force interaction is clear from the fact that bubbles are attracted to the electrode, which is in the opposite direction of the dielectrophoretic forces, and for higher AC frequencies the bubbles zigzag at the frequency of the applied voltage, where the dielectrophoretic force would respond at double this frequency. The repercussion of this new finding is not only relevant for vertical two phase flows, but also for microgravity convective boiling since they will have generally similar flow regimes as those considered here.

The interaction with the phases was best illustrated for the lower heat flux case at 6 kW/($m^2$ K). The step input of +10 kV appears to inject charge to the fluid which accumulated on the bubbles causing them to be attracted by electrophoretic forces to the negative electrode, and this was termed the Transition (T) phase, lasting on the order of O~10ms. The force was strong enough to pull the entire vapour mass out of the core flow and attach it to the electrode, and this was called the Vapour Contraction (VC) phase and lasted on the order of O~100 ms. It is postulated that the VC phase is associated with a discharge of electricity until the vapour film collapses and expels the vapour back into the bulk liquid. The uncharged vapour bubbles and clusters are then acted on by the dielectrophoretic force, pushing them to the wall and starts a very well mixed churn-type (CH) flow regime, which lasted on the order of O~100 ms. Over time the churning settles and the bubbly flow regime re-establishes until the next +10 kV step input.

By changing the applied AC voltage frequency it was found that the level of enhancement over the baseline bubbly flow was influenced by the proportion of time that the flow was within the EHD augmented phases, in particular the churn flow regime. For the 1 Hz case the EHD augmented phase is short compared to the 1000 ms period of the AC voltage signal so that the bubbly flow regime lasts a considerable time and thus the enhancement is good, but not exceptional. For 10 Hz, the EHD augmentation lasts about the same amount of time as the period of the voltage signal (O~100 ms) and is thus is always in an enhanced heat transfer state. Here the overall enhancement is quite high, at about 5 times the baseline, and the HTC is commensurate with what would be expected for churn flow. For frequencies on the order of O~100 Hz the flow is continually passing in and out of the Transition (T)

phase at the frequency of the applied electric field, causing the bubbles to zigzag as they move upward with the core flow. Here there is enhanced heat transfer due to the zigzagging bubbles interacting with the wall region, however the period is too short (O~10 ms) to enter the VC and CH regimes so the enhancement is, like the 1 Hz case, good but not exceptional.

In terms of EHD interaction with the phases, the higher heat flux showed similar general flow regimes. The main difference was that the higher volume of vapour in the core flow, associated with the higher vapour quality, seemed to impede the EHD interaction with the phases and, overall, reduced enhancement. This was particularly true for the 10 Hz high heat flux test case where the Transition (T) phase did not transit to a full Vapour Contraction (VC) phase, and notable vapour was still entrained in the core flow. This tended to reduce the aggressiveness and overall duration of the churn flow regime and resulted in lower HTC and significantly lower enhancement compared with the lower heat flux case.

The behaviour of flow dynamic and HTC measurements give the impression that there is a combined action of the possible enhanced nucleation and enhanced convection. Being not a linear relationship between the increase of the superheat at the wall and the number of active sites for nucleation, during the intermittent boiling at the wall some heat is stored increasing local superheat with a consequent activation of sites; also, the electric field influences the moment when the bubble are detached from the wall. As a consequence of the effect of the electric field frequency on the number of active sites and on the dynamics of bubble formation, there is an influence on the amount of vapour formed at the wall and on the motion of bubbles inside the vapour. This causes as a second step an influence on the convective contribution since affects average flow velocity in the axial direction and gives a component to the velocity perpendicular to the flow direction.

# Chapter 7. Conclusions and Future Work

An experimental investigation of upward vertical flow boiling for HFE 7000 has been performed in a tubular heat exchanger. Three distinct flow patterns have been observed: bubbly flow, slug flow and churn flow. The experimental flow regimes are compared to seven existing maps for vertical two phase flows available in the literature. The Bennett et al. [44] flow map was determined to be the most suitable for the experimental conditions tested in this work with ~80% of the flow regimes correctly predicted. The flow maps developed for adiabatic flows using the superficial liquid and vapour velocities poorly predicted the present data.

The experiments were then expanded to investigate the heat transfer for upward vertical flow boiling for HFE 7000 in a circular and annular heat exchanger. Results shows that the heat transfer coefficient is a very strong function of imposed heat flux, which is evidence to suggest that the dominant heat transfer mechanisms are associated with the local bubble activity opposed to convective influences. In particular the boiling dictates the flow regime and an interesting result is that the boiling heat transfer coefficient asymptotically matches a linear line for nucleate boiling at lower heat fluxes and a higher slope linear line at higher heat fluxes for the more rigorous slug and churn flow regimes. The inflection region was observed to occur at the transition from bubbly flow to slug flow. Tests were performed to study the influence of mass flux between 50-150 kg/($m^2$ s) as well as semi-confinement. The measurements showed no significant influence of these parameters.

The experimental boiling heat transfer data for HFE 7000 were then compared against seven predictions correlations for vertical upflow convective boiling. Each correlation has a unique behaviour in predicting the experimental results as each accounted for the influence of convection and boiling on the overall heat transfer in different ways. The results demonstrate good agreements between experimental data and the prediction of the Wattelet et al. correlation [65] with MRD, MAD, and RMS of 21%. The Shah [71] and Gungor & Winterton [75] correlations show acceptable agreements, while the Kandlikar [66] correlation predicted result that are outside of

what can be considered acceptable. The Gungor & Winterton [73], Chen correlation [67] and Jung & Radermacher [77] correlations display a largest deviation and must be used with caution. The end result was that correlations that showed the least sensitivity to flow rate and used the Cooper pool boiling correlation were the most accurate. Finally, the Cooper pool boiling correlation was tested against the experimental measurements and, consistent with some earlier and more recent published studies, the correlation did a very good job at predicting the vertical upflow convective boiling data for the range of parameters tested. This result tends to support the conclusion that the nucleate boiling activity at the heated surface is the dominant mechanism of heat transfer for the cases studied.

In the final phase of this study, EHD augmentation of the flow and heat transfer for vertical upflow convective boiling was investigated. To the best of knowledge, this is the first study of vertical upflow boiling with EHD augmentation that included local heat transfer measurements with detailed visualization of the flow regimes and phase interactions. One very striking conclusion is that, for the bubbly flow regime considered, there is very strong electrophoretic interaction with the phases, and this is not what has been observed for horizontal flows where liquid extraction (dielectrophoretic) dominates the EHD effect. The electrophoretic force interaction is clear from the fact that bubbles are attracted to the electrode, which is in the opposite direction of the dielectrophoretic forces, and for higher AC frequencies the bubbles zigzag at the frequency of the applied voltage, where the dielectrophoretic force would respond at double this frequency. The repercussion of this new finding is not only relevant for vertical two phase flows, but also for microgravity convective boiling since they will have generally similar flow regimes as those considered here.

The interaction with the phases was best illustrated for the lower heat flux case at 6 $kW/m^2$. The step input of +10 kV appears to inject charge to the fluid which accumulated on the bubbles causing them to be attracted by electrophoretic forces to the negative electrode, and this was termed the Transition (T) phase, lasting on the order of O~10ms. The force was strong enough to pull the entire vapour mass out of the core flow and attach it to the electrode, and this was called the Vapour Contraction (VC) phase and lasted on the order of O~100 ms. It is postulated that the VC phase is

associated with a discharge of electricity until the vapour film collapses and expels the vapour back into the bulk liquid. The uncharged vapour bubbles and clusters are then acted on by the dielectrophoretic force, pushing them to the wall and starts a very well mixed churn-type (CH) flow regime, which lasted on the order of O~100 ms. Over time the churning settles and the bubbly flow regime re-establishes until the next +10 kV step input.

By changing the applied AC voltage frequency it was found that the level of enhancement over the baseline bubbly flow was influenced by the proportion of time that the flow was within the EHD augmented phases, in particular the churn flow regime. For the 1 Hz case the EHD augmented phase is short compared to the 1000 ms period of the AC voltage signal so that the bubbly flow regime lasts a considerable time and thus the enhancement is good, but not exceptional. For 10 Hz, the EHD augmentation lasts about the same amount of time as the period of the voltage signal (O~100 ms) and is thus is always in an enhanced heat transfer state. Here the overall enhancement is quite high, at about 5 times the baseline, and the HTC is commensurate with what would be expected for churn flow. For frequencies on the order of O~100 Hz the flow is continually passing in and out of the Transition (T) phase at the frequency of the applied electric field, causing the bubbles to zigzag as they move upward with the core flow. Here there is enhanced heat transfer due to the zigzagging bubbles interacting with the wall region, however the period is too short (O~10 ms) to enter the VC and CH regimes so the enhancement is, like the 1 Hz case, good but not exceptional.

In terms of EHD interaction with the phases, the higher heat flux showed similar general flow regimes. The main difference was that the higher volume of vapour in the core flow, associated with the higher vapour quality, seemed to impede the EHD interaction with the phases and, overall, reduced enhancement. This was particularly true for the 10 Hz high heat flux test case where the Transition (T) phase did not transit to a full Vapour Contraction (VC) phase, and notable vapour was still entrained in the core flow. This tended to reduce the aggressiveness and overall duration of the churn flow regime and resulted in lower HTC and significantly lower enhancement compared with the lower heat flux case.

## 7.1 **Future Work**

The main contribution in this research is that the electrophoretic force has been exposed for the first time, which opens the door for more detailed investigations to gain a better understanding of this new finding. It is suggested that future work should focus on more basic experiments, like pool boiling with a single nucleation site and then flow boiling with a single nucleation site, where the focus should be on stripping back the complexity of the two-phase flow and getting a correct understanding of the core physics and using this to develop correct physical and mathematical models. With a correct understanding of the physics behind this newly observed phenomena, the more complex two phase flows can then be revisited in order to determine optimal fluid properties, EHD parameters (frequency/voltage) and geometrical configurations etc. that will result in well-engineered EHD augmented two phase heat exchangers.

# REFERENCES


[1] S. G. Kandlikar, “High Flux Heat Removal with Microchannels—A Roadmap of Challenges and Opportunities,” *Heat Transf. Eng.*, vol. 26, no. 8, pp. 5–14, Oct. 2005.

[2] X. Fang, Y. Yuan, A. Xu, L. Tian, and Q. Wu, “Review of correlations for subcooled flow boiling heat transfer and assessment of their applicability to water,” *Fusion Eng. Des.*, vol. 122, pp. 52–63, Nov. 2017.

[3] M. Piasecka, “An application of enhanced heating surface with mini-reentrant cavities for flow boiling research in minichannels,” *Heat Mass Transf.*, vol. 49, no. 2, pp. 261–275, Feb. 2013.

[4] “Flow boiling heat transfer in microgravity: Recent results | SpringerLink.” [Online]. Available: https://link.springer.com/article/10.1007/BF02915738. [Accessed: 21-Mar-2018].

[5] P. Di Marco and W. Grassi, “Overview and prospects of boiling heat transfer studies in microgravity,” December 18, 2.

[6] H. Ohta, T. Ohno, F. Hioki, and Y. Shinmoto, “Development of a High-Performance Boiling Heat Exchanger by Improved Liquid Supply to Narrow Channels,” *Ann. N. Y. Acad. Sci.*, vol. 1027, no. 1, pp. 217–234, Nov. 2004.

[7] L. Doretti, G. A. Longo, S. Mancin, G. Righetti, and C. Zilio, “Flow boiling heat transfer on a Carbon/Carbon surface,” *Int. J. Heat Mass Transf.*, vol. 109, pp. 938–948, Jun. 2017.

[8] M. Law and P.-S. Lee, “Comparative Study of Temperature and Pressure Instabilities During Flow Boiling in Straight- and 10° Oblique-Finned Microchannels,” *Energy Procedia*, vol. 75, pp. 3105–3112, Aug. 2015.

[9] G. Rufino and M. Grassi, “Multi-Aperture CMOS Sun Sensor for Microsatellite Attitude Determination,” *Sensors*, vol. 9, no. 6, pp. 4503–4524, Jun. 2009.

[10] “Fujitsu Develops Thin Cooling Device for Compact Electronics - Fujitsu Global.” [Online]. Available: http://www.fujitsu.com/global/about/resources/news/press-releases/2015/0312-01.html. [Accessed: 21-Mar-2018].

[11] “Heaping Pile Of Heat Pipes - Pipe Dreams: Six P35-DDR3 Motherboards Compared,” *Tom’s Hardware*, 05-Jun-2007. [Online]. Available: http://www.tomshardware.com/reviews/review-six-p35-ddr3-atx-motherboards-compared,1616-2.html. [Accessed: 25-Mar-2018].

[12] H. Qiu, “Multiphase Flow and Heat Transfer on Micro/Nanostructured Surfaces,” in *ResearchGate*, 2014.

[13] J. B. Copetti, M. H. Macagnan, F. Zinani, and N. L. F. Kunsler, “Flow boiling heat transfer and pressure drop of R-134a in a mini tube: an experimental investigation,” *Exp. Therm. Fluid Sci.*, vol. 35, no. 4, pp. 636–644, May 2011.

[14] C. Chen, P. Gao, S. Tan, H. Chen, and X. Chen, “Forced convective boiling heat transfer of water in vertical rectangular narrow channel,” *Nucl. Eng. Des.*, vol. 291, pp. 133–144, Sep. 2015.

[15] G. J. McGranaghan and A. J. Robinson, “The mechanisms of heat transfer during convective boiling under the influence of AC electric fields,” *Int. J. Heat Mass Transf.*, vol. 73, pp. 376–388, Jun. 2014.

[16] H. Sadek, C. Y. Ching, and J. Cotton, "Characterization of heat transfer modes of tube side convective condensation under the influence of an applied DC voltage," *Int. J. Heat Mass Transf.*, vol. 53, no. 19–20, pp. 4141–4151, Sep. 2010.
[17] S. Laohalertdecha, P. Naphon, and S. Wongwises, "A review of electrohydrodynamic enhancement of heat transfer," *Renew. Sustain. Energy Rev.*, vol. 11, no. 5, pp. 858–876, Jun. 2007.
[18] A. Robinson, "AC Voltage Induced Electrohydrodynamic Two-Phase Convective Boiling Heat Transfer in Horizontal Annular Channels," 2012.
[19] "Enhancement of convection heat transfer using EHD conduction method - ScienceDirect." [Online]. Available: https://www-sciencedirect-com.elib.tcd.ie/science/article/pii/S0894177717304119. [Accessed: 21-Mar-2018].
[20] "EHD Pump Cools Space Hardware | Engineering360." [Online]. Available: https://insights.globalspec.com/article/4155/ehd-pump-cools-space-hardware. [Accessed: 25-Mar-2018].
[21] T. H. Phung, L. N. Nguyen, and K.-S. Kwon, "A Vector Printing Method for High-Speed Electrohydrodynamic (EHD) Jet Printing Based on Encoder Position Sensors," *Appl. Sci.*, vol. 8, no. 3, p. 351, Feb. 2018.
[22] G. R. Beitel, "Boiling Heat-Transfer Processes and Their Application in the Cooling of High Heat Flux Devices," p. 154, Jun. 1993.
[23] M. S. N. Kazi, Ed., *An Overview of Heat Transfer Phenomena*. InTech, 2012.
[24] S. Mehendale, A. M. Jacobi, and R. K. Shah, "Fluid Flow and Heat Transfer at Micro and Meso-Scales With Application to Heat Exchanger Design," *Appl. Mech. Rev.*, vol. 53, Jul. 2000.
[25] S. G. Kandlikar and W. J. Grande, "Evolution of Microchannel Flow Passages: Thermohydraulic Performance and Fabrication Technology," pp. 59–72, Jan. 2002.
[26] E. Adom, S. Z. Islam, and P. Kew, "Boiling Heat Transfer on the Outside of A Miniature Diameter Compact Tube Bundle," 2010.
[27] P. A. Kew and K. Cornwell, "Correlations for the prediction of boiling heat transfer in small-diameter channels," *Appl. Therm. Eng.*, vol. 17, no. 8, pp. 705–715, Aug. 1997.
[28] C. L. Ong and J. R. Thome, "Macro-to-microchannel transition in two-phase flow: Part 1 – Two-phase flow patterns and film thickness measurements," *Exp. Therm. Fluid Sci.*, vol. 35, no. 1, pp. 37–47, Jan. 2011.
[29] R. W. Johnson, *The Handbook of Fluid Dynamics*. Springer Science & Business Media, 1998.
[30] A. K. Vij and W. E. Dunn, "Modeling of Two-Phase Flows in Horizontal Tubes," Air Conditioning and Refrigeration Center. College of Engineering. University of Illinois at Urbana-Champaign., text, May 1996.
[31] A. Faghri and Y. Zhang, *Transport Phenomena in Multiphase Systems*. Academic Press, 2006.
[32] M. K. Dobson, "Heat Transfer and Flow Regimes During Condensation in Horizontal Tubes," Air Conditioning and Refrigeration Center. College of Engineering. University of Illinois at Urbana-Champaign., text, May 1994.
[33] A. H. Govan, G. F. Hewitt, H. J. Richter, and A. Scott, "Flooding and churn flow in vertical pipes," *Int. J. Multiph. Flow*, vol. 17, no. 1, pp. 27–44, Jan. 1991.

[34] G. F. Hewitt and A. H. Govan, “Phenomenological modelling of non-equilibrium flows with phase change,” *Int. J. Heat Mass Transf.*, vol. 33, no. 2, pp. 229–242, Feb. 1990.
[35] L. Cheng, G. Ribatski, and J. R. Thome, “Two-Phase Flow Patterns and Flow-Pattern Maps: Fundamentals and Applications,” *Appl. Mech. Rev.*, vol. 61, no. 5, pp. 050802–050802, Jul. 2008.
[36] A. W. Bennett, G. F. Hewitt, H. A. Kearsey, R. K. F. Keeys, and P. M. C. Lacey, “Flow Visualization Studies of Boiling at High Pressure.,” *Proc Inst Mech Eng Lond. 180 Pt 3C 260-701965-66*, Oct. 1967.
[37] G. F. Hewitt, “Churn and Wispy Annular Flow Regimes in Vertical Gas–Liquid Flows,” *Energy Fuels*, vol. 26, no. 7, pp. 4067–4077, Jul. 2012.
[38] J. M. Mandhane, G. A. Gregory, and K. Aziz, “A Flow Pattern Map for Gas-Liquid Flowing Horizontal Pipes,” *Int. J. Multiph. Flow*, vol. 1, pp. 537–553, Oct. 1974.
[39] Y. Taitel and A. E. Dukler, “A theoretical approach to the Lockhart-Martinelli correlation for stratified flow,” *Int. J. Multiph. Flow*, vol. 2, no. 5–6, pp. 591–595, Apr. 1976.
[40] N. Kattan, J. R. Thome, and D. Favrat, “Flow Boiling in Horizontal Tubes: Part 1—Development of a Diabatic Two-Phase Flow Pattern Map,” *J. Heat Transf.*, vol. 120, no. 1, pp. 140–147, Feb. 1998.
[41] Steiner, D, *Heat Transfer to Boiling Saturated Liquid*, vol. Hbb. Düsseldorf, 1993.
[42] Moreno Quibén, Jesús, “Experimental and analytical study of two-phase pressure drops during evaporation in horizontal tubes,” 2005.
[43] J. R. Thome and J. E. Hajal, “Two-Phase Flow Pattern Map for Evaporation in Horizontal Tubes: Latest Version,” *Heat Transf. Eng.*, vol. 24, no. 6, pp. 3–10, Nov. 2003.
[44] L. Wojtan, T. Ursenbacher, and J. R. Thome, “Investigation of flow boiling in horizontal tubes: Part I—A new diabatic two-phase flow pattern map,” *Int. J. Heat Mass Transf.*, vol. 48, no. 14, pp. 2955–2969, Jul. 2005.
[45] A. Bejan and A. D. Kraus, *Heat Transfer Handbook*. John Wiley & Sons, 2003.
[46] G. Hewitt, *Annular Two-Phase Flow*. Elsevier, 2013.
[47] C.-Y. Yang and C.-C. Shieh, “Flow pattern of air–water and two-phase R-134a in small circular tubes,” *Int. J. Multiph. Flow*, vol. 27, no. 7, pp. 1163–1177, Jul. 2001.
[48] G. F. Hewitt and D. N. Roberts, “Studies of Two-Phase Flow Patterns by Simultaneous X-Ray and Flast Photography,” Atomic Energy Research Establishment, Harwell, England (United Kingdom), AERE-M--2159, Feb. 1969.
[49] S. Guet and G. Ooms, “Fluid Mechanical Aspects of the Gas-Lift Technique,” *Annu. Rev. Fluid Mech.*, vol. 38, no. 1, pp. 225–249, 2006.
[50] Y. Taitel, D. Bornea, and A. E. Dukler, “Modelling flow pattern transitions for steady upward gas-liquid flow in vertical tubes,” *AIChE J.*, vol. 26, no. 3, pp. 345–354, May 1980.
[51] V. Bertola, *Modelling and Experimentation in Two-Phase Flow*. Springer, 2014.
[52] M. R. Ansari and R. Azadi, “Effect of diameter and axial location on upward gas–liquid two-phase flow patterns in intermediate-scale vertical tubes,” *Ann. Nucl. Energy*, vol. 94, pp. 530–540, Aug. 2016.

[53] T. Oya, “Upward Liquid Flow in Small Tube into which Air Streams : 1st Report, Experimental Apparatus and Flow Patterns,” *Bull. JSME*, vol. 14, no. 78, pp. 1320–1329, 1971.
[54] T. Fukano and A. Kariyasaki, “Characteristics of gas-liquid two-phase flow in a capillary tube,” *Nucl. Eng. Des.*, vol. 141, no. 1, pp. 59–68, Jun. 1993.
[55] G. W. Govier and W. L. Short, “The upward vertical flow of air-water mixtures: II. Effect of tubing diameter on flow-pattern, holdup and pressure drop,” *Can. J. Chem. Eng.*, vol. 36, no. 5, pp. 195–202, Oct. 1958.
[56] G. Hetsroni, A. Mosyak, Z. Segal, and E. Pogrebnyak, “Two-phase flow patterns in parallel micro-channels,” *Int. J. Multiph. Flow*, vol. 29, no. 3, pp. 341–360, Mar. 2003.
[57] D. P. Frankum, V. V. Wadekar, and B. J. Azzopardi, “Two-phase flow patterns for evaporating flow,” *Exp. Therm. Fluid Sci.*, vol. 15, no. 3, pp. 183–192, Oct. 1997.
[58] L. Huang, G. Li, and L. Tao, “Experimental investigation on the heat transfer characteristics and flow pattern in vertical narrow channels heated from one side,” *Heat Mass Transf.*, vol. 52, no. 7, pp. 1343–1357, Jul. 2016.
[59] X. Huo, L. Chen, Y. S. Tian, and T. G. Karayiannis, “Flow boiling and flow regimes in small diameter tubes,” *Appl. Therm. Eng.*, vol. 24, no. 8–9, pp. 1225–1239, Jun. 2004.
[60] G. P. Celata, M. Cuno, G. E. Farello, A. Mariani, and S. Solimo, “Flow pattern recognition in heated vertical channels: Steady and transient conditions,” *Exp. Therm. Fluid Sci.*, vol. 4, no. 6, pp. 737–746, Nov. 1991.
[61] R. Rozenblit, M. Gurevich, Y. Lengel, and G. Hetsroni, “Flow patterns and heat transfer in vertical upward air–water flow with surfactant,” *Int. J. Multiph. Flow*, vol. 32, no. 8, pp. 889–901, Aug. 2006.
[62] R. Revellin and J. R. Thome, “A new type of diabatic flow pattern map for boiling heat transfer in microchannels,” *J. Micromechanics Microengineering*, vol. 17, no. 4, p. 788, 2007.
[63] V. D. Hatamipour and M. A. Akhavan-Behabadi, “Visual study on flow patterns and heat transfer during convective boiling inside horizontal smooth and microfin tubes,” *World Acad. Sci. Eng. Technol.*, vol. 70, pp. 700–706, Sep. 2010.
[64] W. Chen and X. Fang, “A note on the Chen correlation of saturated flow boiling heat transfer,” *Int. J. Refrig.*, vol. 48, pp. 100–104, Dec. 2014.
[65] J. P. Wattelet, “Predicting boiling heat transfer in a small-diameter round tube using an asymptotic method,” in *Convective Flow Boiling*, 1995, pp. 377–382.
[66] S. G. Kandlikar, “A General Correlation for Saturated Two-Phase Flow Boiling Heat Transfer Inside Horizontal and Vertical Tubes,” *J. Heat Transf.*, vol. 112, no. 1, pp. 219–228, Feb. 1990.
[67] J. C. Chen, “Correlation for Boiling Heat Transfer to Saturated Fluids in Convective Flow,” *Ind. Eng. Chem. Process Des. Dev.*, vol. 5, no. 3, pp. 322–329, Jul. 1966.
[68] M. M. Shahs, “Evaluation of General Correlations for Heat Transfer During Boiling of Saturated Liquids in Tubes and Annuli,” *HVACR Res.*, vol. 12, no. 4, pp. 1047–1063, Oct. 2006.
[69] H. K. Forster and N. Zuber, “Dynamics of vapor bubbles and boiling heat transfer,” *AIChE J.*, vol. 1, no. 4, pp. 531–535, Dec. 1955.

[70] F. W. Dittus and L. M. K. Boelter, *Heat transfer in automobile radiators of the tubular type,*. Berkeley, Calif: University of California Press, 1930.
[71] M. M. Shah, "A New Correlation for heat Transfer During Boiling Flow Through Pipes," 1976.
[72] *Convective Boiling and Condensation*, Third Edition. Oxford, New York: Oxford University Press, 1996.
[73] K. E. Gungor and R. H. S. Winterton, "A general correlation for flow boiling in tubes and annuli," *Int. J. Heat Mass Transf.*, vol. 29, no. 3, pp. 351–358, Mar. 1986.
[74] M. G. Cooper, "SATURATION NUCLEATE POOL BOILING - A SIMPLE CORRELATION," in *First U.K. National Conference on Heat Transfer*, H. C. Simpson, G. F. Hewitt, D. Boland, T. R. Bott, B. N. Furber, W. B. Hall, P. J. Heggs, P. N. Rowe, E. A. D. Saunders, and D. B. Spalding, Eds. Pergamon, 1984, pp. 785–793.
[75] K. E. Gungor and R. H. S. Winterton, "Simplified general correlation for saturated flow boiling and comparisons of correlations with data," *Chem. Eng. Res. Des.*, vol. 65, no. 2, pp. 148–156, 1987.
[76] J. R. Thome, "Boiling of new refrigerants: a state-of-the-art review," *Int. J. Refrig.*, vol. 19, no. 7, pp. 435–457, Sep. 1996.
[77] D. Jung and R. Radermacher, "Prediction of evaporation heat transfer coefficient and pressure drop of refrigerant mixtures in horizontal tubes," *Int. J. Refrig.*, vol. 16, no. 3, pp. 201–209, Jan. 1993.
[78] W. Owhaib, "Experimental Heat Transfer, pressure drop, and Flow Visualization of R-134a in Vertical Mini/Micro Tubes," 2007.
[79] K. Stephan and M. Abdelsalam, "Heat-transfer correlations for natural convection boiling," *Int. J. Heat Mass Transf.*, vol. 23, no. 1, pp. 73–87, Jan. 1980.
[80] M. Narcy, E. de Malmazet, and C. Colin, "Flow boiling in tube under normal gravity and microgravity conditions," *Int. J. Multiph. Flow*, vol. 60, pp. 50–63, Apr. 2014.
[81] Z. Zhou, X. Fang, and D. Li, "Evaluation of Correlations of Flow Boiling Heat Transfer of R22 in Horizontal Channels," *Sci. World J.*, vol. 2013, Jul. 2013.
[82] J. E. Bryan and J. Seyed-Yagoobi, "Electrohydrodynamically Enhanced Convective Boiling: Relationship Between Electrohydrodynamic Pressure and Momentum Flux Rate," *J. Heat Transf.*, vol. 122, no. 2, pp. 266–277, Nov. 1999.
[83] H. Sadek, A. J. Robinson, J. S. Cotton, C. Y. Ching, and M. Shoukri, "Electrohydrodynamic enhancement of in-tube convective condensation heat transfer," *Int. J. Heat Mass Transf.*, vol. 49, no. 9–10, pp. 1647–1657, May 2006.
[84] N.-T. Nguyen, *Micromixers: Fundamentals, Design, and Fabrication*, 1 edition. William Andrew, 2008.
[85] K. Smith, G. Byrne, R. Kempers, and A. J. Robinson, "Electrohydrodynamic augmentation of a reflux thermosyphon," *Exp. Therm. Fluid Sci.*, vol. 79, pp. 175–186, Dec. 2016.
[86] J. Cotton, "Electrohydrodynamic condensation heat transfer modulation under dc and ac applied voltages in a horizontal annular channel," *IEEE Trans. Dielectr. Electr. Insul.*, vol. 16, no. 2, pp. 495–503, Apr. 2009.

[87] A. J. R. Gerard McGranaghan, “EHD Augmented Convective Boiling: Flow Regimes and Enhanced Heat Transfer,” *Heat Transf. Eng.*, vol. 35, no. 5, 2014.
[88] J. Cotton, A. J. Robinson, M. Shoukri, and J. S. Chang, “A two-phase flow pattern map for annular channels under a DC applied voltage and the application to electrohydrodynamic convective boiling analysis,” *Int. J. Heat Mass Transf.*, vol. 48, no. 25–26, pp. 5563–5579, Dec. 2005.
[89] S. Laohalertdecha and S. Wongwises, “Effects of EHD on heat transfer enhancement and pressure drop during two-phase condensation of pure R-134a at high mass flux in a horizontal micro-fin tube,” *Exp. Therm. Fluid Sci.*, vol. 30, no. 7, pp. 675–686, Jul. 2006.
[90] K. Ng, C. Y. Ching, and J. S. Cotton, “Transient Two-Phase Flow Patterns by Application of a High Voltage Pulse Width Modulated Signal and the Effect on Condensation Heat Transfer,” *J. Heat Transf.*, vol. 133, no. 9, pp. 091501–091501, Jul. 2011.
[91] G. D. Harvel, B. Komeili, C. Y. Ching, and J.-S. Chang, “Electrohydrodynamically enhanced capillary evaporator,” *IEEE Trans. Dielectr. Electr. Insul.*, vol. 16, no. 2, pp. 456–462, Apr. 2009.
[92] J. Cotton, D. Brocilo, M. M. Shoukri, T. Smith-Pollard, and J. S. Chang, “Mechanisms of electrohydrodynamic flow boiling heat transfer in coaxial flow channels of dielectric refrigerant R-134a,” in *Conference on Electrical Insulation and Dielectric Phenomena, 1998. Annual Report*, 1998, vol. 1, pp. 178–181 vol. 1.
[93] J. E. Bryan and J. Seyed-Yagoobi, “Influence of Flow Regime, Heat Flux, and Mass Flux on Electrohydrodynamically Enhanced Convective Boiling,” *J. Heat Transf.*, vol. 123, no. 2, pp. 355–367, May 2000.
[94] S. Nangle-Smith and J. S. Cotton, “EHD-based load controllers for R134a convective boiling heat exchangers,” *Appl. Energy*, vol. 134, pp. 125–132, Dec. 2014.
[95] H. Sadek, C. Y. Ching, and J. Cotton, “The effect of pulsed electric fields on horizontal tube side convective condensation,” *Int. J. Heat Mass Transf.*, vol. 53, no. 19–20, pp. 3721–3732, Sep. 2010.
[96] H. Sadek, J. S. Cotton, C. Y. Ching, and M. Shoukri, “Effect of Frequency on Electrohydrodynamic Enhanced Tube-Side Condensation,” in *International Conference on Thermal Issues in Emerging Technologies: Theory and Application, 2007. THETA 2007*, 2007, pp. 145–149.
[97] H. Sadek, J. S. Cotton, C. Y. Ching, and M. Shoukri, “Effect of frequency on two-phase flow regimes under high-voltage AC electric fields,” *J. Electrost.*, vol. 66, no. 1–2, pp. 25–31, Jan. 2008.
[98] H. Sadek, C. Y. Ching, and J. S. Cotton, “The Effect of Frequency and Duty Cycle on Heat Transfer and Pressure Drop for Convective Condensation under Pulsed Electric Field,” vol. 3, pp. 133–137, 2009.
[99] J. S. Cotton, D. Brocilo, J. S. Chang, M. Shoukri, and T. Smith-Pollard, “Numerical simulation of electric field distributions in electrohydrodynamic two-phase flow regimes,” *IEEE Trans. Dielectr. Electr. Insul.*, vol. 10, no. 1, pp. 37–51, Feb. 2003.
[100] H. Y. Choi, “Electrohydrodynamic Condensation Heat Transfer,” *J. Heat Transf.*, vol. 90, no. 1, pp. 98–102, Feb. 1968.

[101] A. B. Didkovsky and M. K. Bologa, “Vapour film condensation heat transfer and hydrodynamics under the influence of an electric field,” *Int. J. Heat Mass Transf.*, vol. 24, no. 5, pp. 811–819, May 1981.
[102] M. K. Bologa, V. P. Korovkin, and I. K. Savin, “Mechanism of condensation heat transfer enhancement in an electric field and the role of capillary processes,” *Int. J. Heat Mass Transf.*, vol. 38, no. 1, pp. 175–182, Jan. 1995.
[103] M. Wawzyniak and J. Seyed-Yagoobi, “Experimental Study of Electrohydrodynamically Augmented Condensation Heat Transfer on a Smooth and an Enhanced Tube,” *J. Heat Transf.*, vol. 118, no. 2, p. 499, 1996.
[104] H. R. Velkoff and J. H. Miller, “Condensation of Vapor on a Vertical Plate With a Transverse Electrostatic Field,” *J. Heat Transf.*, vol. 87, no. 2, pp. 197–201, May 1965.
[105] H. Y. Choi and J. M. Reynolds, “STUDY OF ELECTROSTATIC EFFECTS ON CONDENSING HEAT TRANSFER.,” May 1965.
[106] A. Al-Ahmadi and R. K. Al-Dadah, “A new set of correlations for EHD enhanced condensation heat transfer of tubular systems,” *Appl. Therm. Eng.*, vol. 22, no. 18, pp. 1981–2001, Dec. 2002.
[107] T. Dyakowski, J. Trommelmans, and J. Berghmans, “Theoretical investigation of the effect of an electric field upon vertical plate condensation heat transfer,” presented at the Proceedings of the International Heat Transfer Conference, 1983, vol. CS11, pp. 65–70.
[108] K. Cheung, M. M. Ohadi, and S. V. Dessiatoun, “EHD-assisted external condensation of R-134a on smooth horizontal and vertical tubes,” *Int. J. Heat Mass Transf.*, vol. 42, no. 10, pp. 1747–1755, May 1999.
[109] K. Yamashita and A. Yabe, “Electrohydrodynamic Enhancement of Falling Film Evaporation Heat Transfer and its Long-Term Effect on Heat Exchangers,” *J. Heat Transf.*, vol. 119, no. 2, pp. 339–347, May 1997.
[110] Y. Liu, R. Li, F. Wang, and H. Yu, “The effect of electrode polarity on EHD enhancement of boiling heat transfer in a vertical tube,” *Exp. Therm. Fluid Sci.*, vol. 29, no. 5, pp. 601–608, Jun. 2005.
[111] “3M™ Novec™ 7000 Engineered Fluid.” [Online]. Available: https://www.3m.com/3M/en_US/company-us/all-3m-products/~/3M-Novec-7000-Engineered-Fluid/?N=5002385+3290667267&rt=rud. [Accessed: 11-Mar-2018].
[112] P. Young, T. Brackbill, and S. Kandlikar, “Estimating Roughness Parameters Resulting From Various Machining Techniques for Fluid Flow Applications,” *Proc. 5th Int. Conf. Nanochannels Microchannels Minichannels ICNMM2007*, Jan. 2007.
[113] “Restore Session.” [Online]. Available: about:sessionrestore. [Accessed: 15-Sep-2017].
[114] S. Kline and F. Mcclintock, “Describing Uncertainties in Single-Sample Experiments,” *Mech. Eng.*, vol. 75, pp. 3–8, 1953.
[115] John Thome, *Flow regimes under diabatic boundary conditions*. 2017.
[116] R. Jenkins, C. D. Brún, R. Kempers, R. Lupoi, and A. J. Robinson, “Thermal-hydraulic performance of convective boiling jet array impingement,” *J. Phys. Conf. Ser.*, vol. 745, no. 3, p. 032120, 2016.
[117] W. Frost, *Heat Transfer at Low Temperatures*. Springer Science & Business Media, 2013.

[118] N. Kattan, J. R. Thome, and D. Favrat, “Flow Boiling in Horizontal Tubes: Part 2—New Heat Transfer Data for Five Refrigerants,” *J. Heat Transf.*, vol. 120, no. 1, pp. 148–155, Feb. 1998.

[119] K. Cornwell and P. A. Kew, “Boiling in Small Parallel Channels,” in *Energy Efficiency in Process Technology*, Springer, Dordrecht, 1993, pp. 624–638.

[120] R. A. Buchanan and T. A. Shedd, “Extensive Parametric Study of Heat Transfer to Arrays of Oblique Impinging Jets With Phase Change,” *J. Heat Transf.*, vol. 135, no. 11, pp. 111017-111017–13, Sep. 2013.

[121] R. Jenkins, C. de Brún, T.L. Lupton, R. Lupoi, R. Kempers, A.J. Robinson, “Convective Boiling of Confined Impinging Jet Arrays,” *Exp. Therm. Fluid Sci.*, vol. (in press), 2017.

[122] A. J. R. G.J. McGranaghan, “The mechanisms of heat transfer during convective boiling under the influence of AC electric fields,” *Int. J. Heat Mass Transf.*, vol. 73, pp. 376–388, 2014.

[123] H. Sadek, A. J. Robinson, J. S. Cotton, C. Y. Ching, and M. Shoukri, “Electrohydrodynamic enhancement of in-tube convective condensation heat transfer,” *Int. J. Heat Mass Transf.*, vol. 49, pp. 1647–1657, 2006.

[124] “Water, Density, Specific enthalpy, Viscosity.” [Online]. Available: https://www.thermexcel.com/english/tables/eau_atm.htm. [Accessed: 16-Sep-2017].

# Appendices

## Appendix A. Pre-Heater Power Requirement

In order to choose the power supply for the pre-heater, the resistance of the tube and the heating required has to be calculated for the worst case, here close to be where the temperature near to saturation and the mass flux is G=200 kg/(m²s.

The heat transfer required to boil the refrigerant to a specific quality can be calculated from the expression:

$$Q_{refr} = m_{refr}[C_{P\,refr}\,(T_9 - T_{sat})] \tag{99}$$

From Table 4-1, the Specific Heat for the refrigerant ($C_{Prefr}$ = 1300) (J·/kg K).

The power required can be calculated for the maximum and minimum cases, ΔT is the sub cooling required for the refrigerant to protect the pump, at the minimum power the mass flux is 50 kg/($m^2$ s) at the maximum power the mass flux is about 200 kg/($m^2$ s).

Table 7-1. maximum and minimum power required for pre heater

| | **ΔT** | **G (kg/($m^2$ s)** | **m (kg/s)** | $Q_{refr}$ (w) |
|---|---|---|---|---|
| Min | 10 | 50 | 0.0046 | **2.3** |
| Max | 10 | 200 | 0.0275 | **55** |

This heat supplied by the electric heater:

$$Q_{refr} = VI \tag{100}$$

To select the power supply, the resistance of the heater calculated using the following formula:

$$R = \frac{\sigma_{stainless\_steel} \cdot L}{A} \quad (101)$$

Where $\sigma_{stainless\_steel}$ is the electrical resistivity of the steel, L is the length of the stainless steel pipe and A is the cross sectional area of the section which can be calculated as follow:

$$A = \frac{\pi}{4}(D^2 - d^2) \quad (102)$$

The table below presents the various characteristics of the heater.

Table 7-2. Pre heater electrical resistance

| $D_{out}$(mm) | $D_{in}$(mm) | A ($m^2$) | L(m) | $\sigma_{stainless\_steel}$ (Ohm .m) | R (Ohm .m) |
|---|---|---|---|---|---|
| 12.8 | 10.8 | $3.71 \times 10^{-4}$ | 2.95 | $6.9\times 10^{-7}$ | 0.055 |

The specification of the power (V & I) can be determined using equation below:

$$V = \sqrt{PR} \quad (103)$$

$$I = \sqrt{\frac{P}{R}} \quad (104)$$

Table 7-3. pre heater power requirement

| | Power (watt) | V (Volt) | I (A) |
|---|---|---|---|
| Min | 2.3 | 0.36 | 6.5 |
| Max | 55 | 1.7 | 31.6 |

# Appendix B: Selection of Material for use as Sapphire Tube Supports

The material used for the pieces to support the sapphire tube had to possess adequate structural strength, high electrical insulation and chemical resistance to HFE7000. It also had to have good long-term resistance to hot water. The following table details a range of engineering polymers investigated. Several were suitable, of which the most economic was found to be polypropylene.

| Material | Comment |
|---|---|
| Acrylic | Clear, usable up to 80°C, susceptible to cracking/crazing |
| Polycarbonate | Not resistant to hot water |
| Polypropylene | low water absorption, resistant to hot water, cheap, good insulator |
| Polyurethane | Low water absorption, water immersion good, Softens above ambient temp |
| PTFE | Poor adhesion, expensive. |
| PEEK | High temp resistance, resistant to hot water, low water absorption, expensive, |
| Acetyl (Delrin) | Black, difficult to bond, limited resistance to hot water, not insulating |
| Nylon | Attacked by water, absorption a problem |
| PPS | Not electrically insulating |
| PVC | Low glass transition temperature (70°C) 60°C max service temp, cheap, low water absorption, easy to bond |
| PVDF | Difficult to bond – HFE7000 |
| Polyester | Easy to bond and weld , not good long term with water over 60°C |
| Polyethylene | Low water absorption, poor with hot water, 80°C difficult to bond, |
| Tufnol | Low voltage only, medium water absorption rate |
| ABS | Good in all respects but not resistant to hot water/washing |

# Appendix C: Optical Transmission Qualities of ITO coating

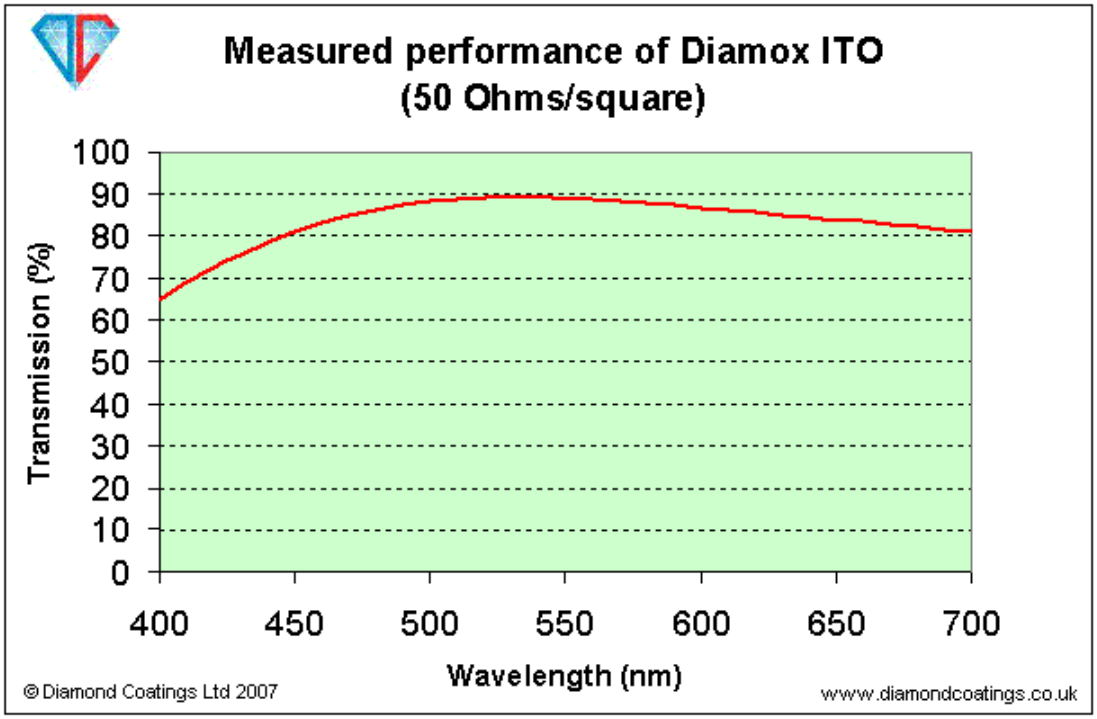


Figure 7-1. Optical transmissibility of Diamox ITO coating at 300Ω/m$^2$

**Sheet Resistance.**

Sheet resistances are available from 2.5 to1000 ohms/square. The standard tolerance is +/-20%

Source: Diamond Coatings Ltd, Unit 2a, Harvey Works Industrial Estate, Shelah Road, Halesowen, West Midlands , B63 3PG , England

## Appendix D Refrigerant HFE7000 properties

The flowing graphs prepared from look-up property table for HFE7000 and water in Excel. Best-fit polynomial curves and lines were then derived with a high accuracy. These polynomials were then input into Labview to determine fluid properties based on the temperature.

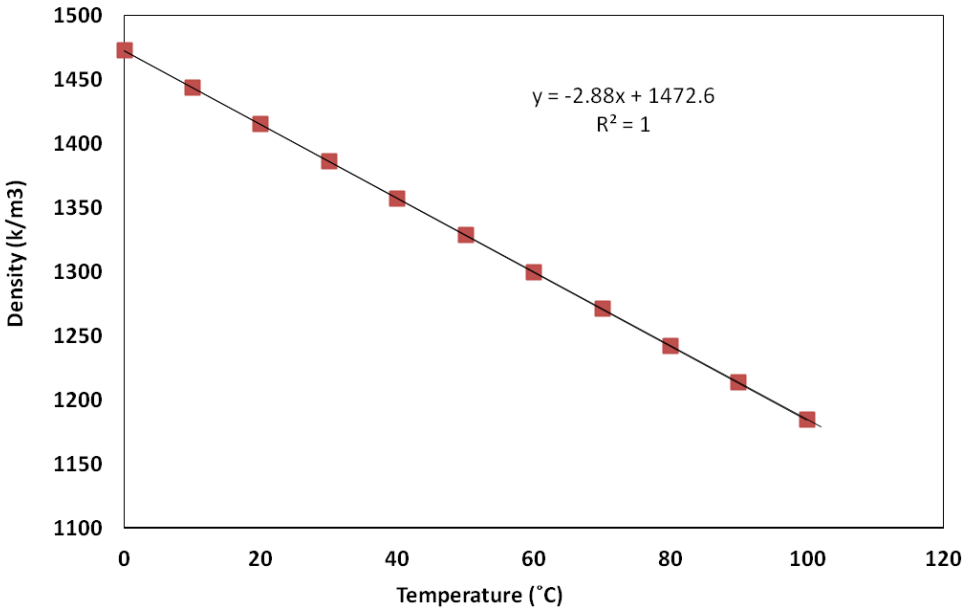


Figure 7-2. Variation of Density of HFE7000 with temperature

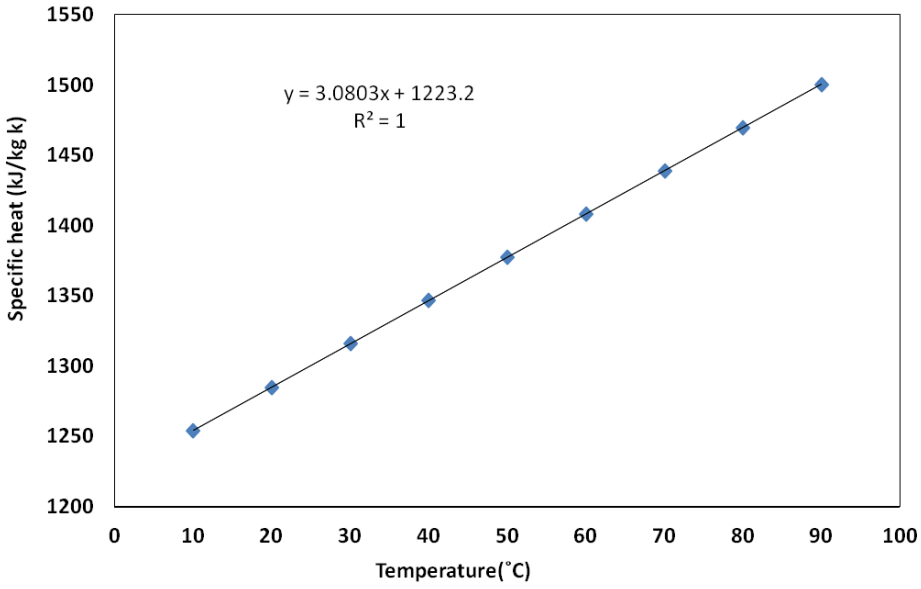


Figure 7-3. Variation of specific heat of HFE7000 with temperature

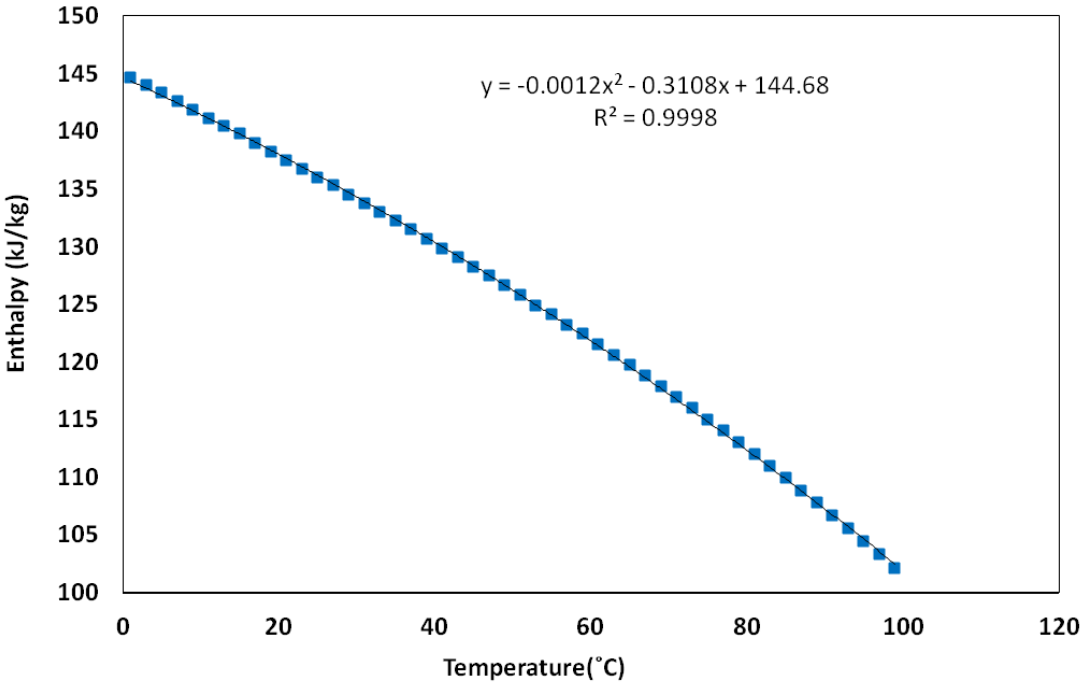


Figure 7-4. Variation of latent heat of vaporisation of HFE7000 with temperature

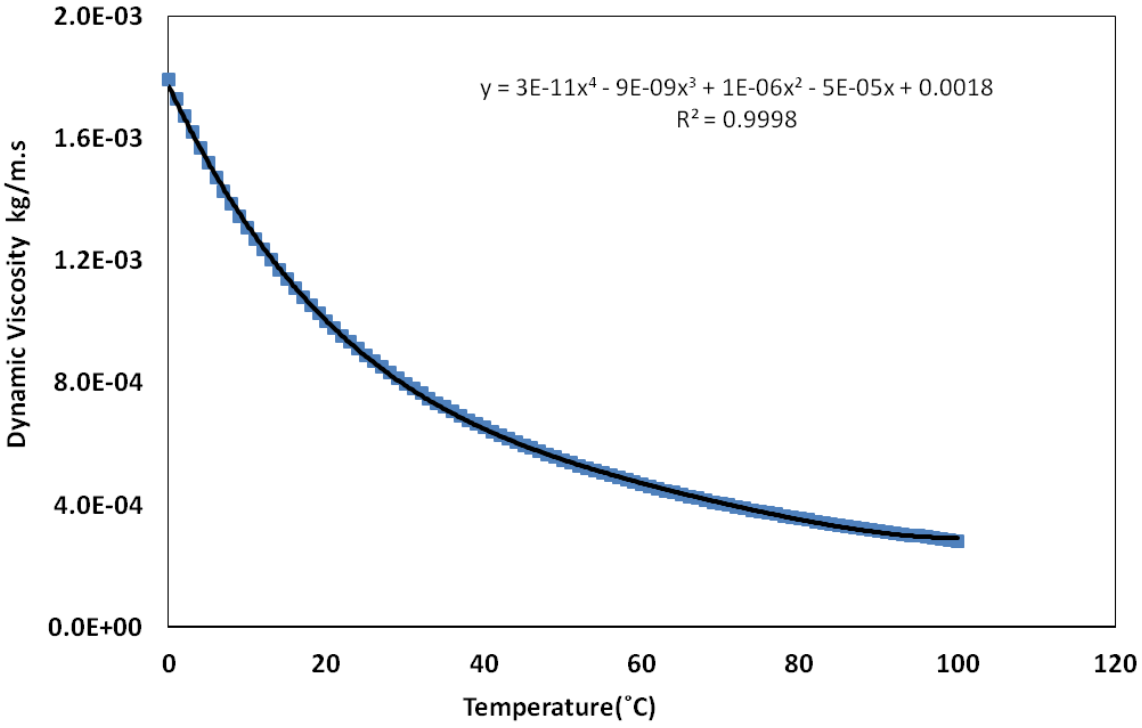


Figure 7-5. Variation of dynamic viscosity against temperature for water, source [124]

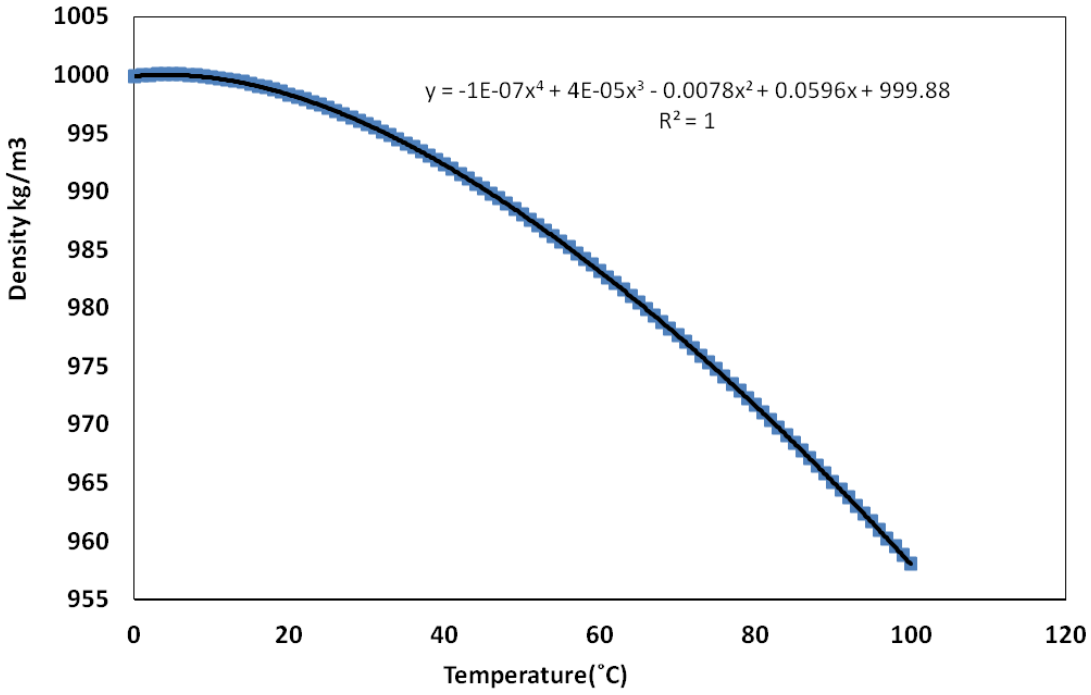


Figure 7-6. Variation of Density viscosity against temperature for water, source [124]

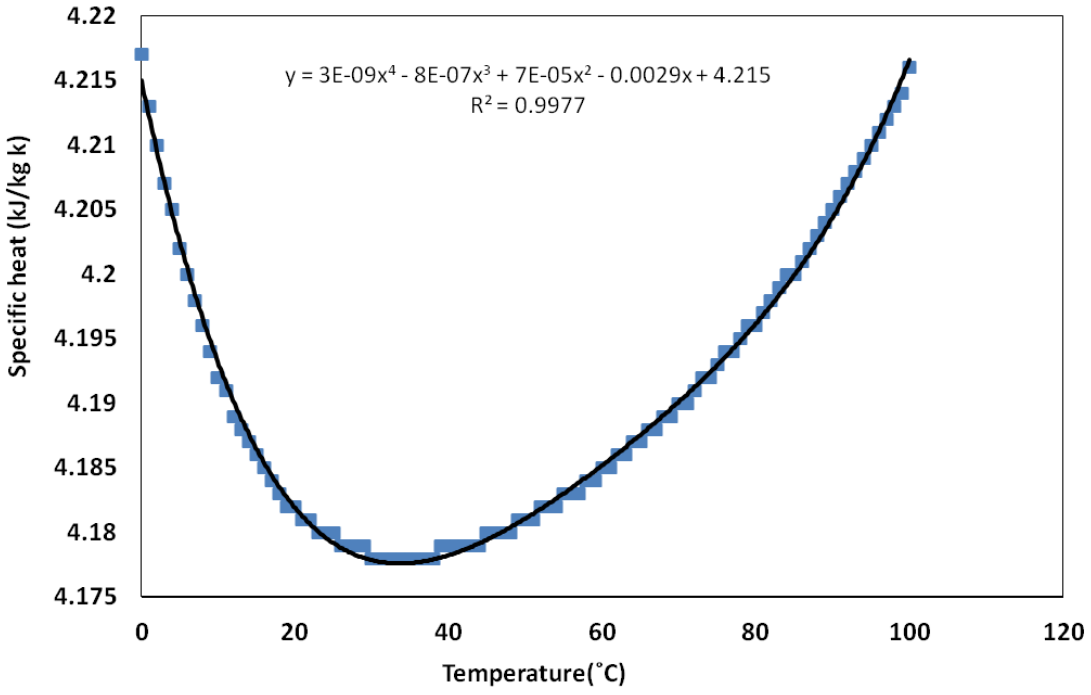


Figure 7-7. Variation of Density viscosity against temperature for water, source [112]

# Appendix E Combined Convection and Radiation losses from Test Section

The combined convection and radiation losses from test section are calculated by, measuring the temperature along the tube surface, the ambient temperature and the electrical power supplied to heat the sapphire tube.

$$Q_{total} = V \times I \tag{105}$$

With no fluid flowing in the tube, the total heat added to the test section transfer only to the environment by convection and radiation, and depends on the $T_{wall}$ and $T_{\infty}$.

$$Q_{total} = h_o A_o (T_{wall} - T_{\infty}) \tag{106}$$

The test section is heated to reach the same circumstance of an actual test, the actual test surface temperature is from 35 ˚C to 45 ˚C.

At steady state, the total heat transfer coefficient is equal to:

$$h_o = \frac{V \times I}{A_o (T_{wall} - T_{\infty})} \tag{107}$$

| $Q_{total}\,(W)$ | $T_{wall}$ | $T_{\infty}$ | $h_o$ |
|---|---|---|---|
| 1.02 | 22.18 | 17.60 | 14.14 |
| 2.04 | 28.04 | 17.60 | 12.44 |
| 2.97 | 32.91 | 17.60 | 12.34 |
| 3.90 | 33.87 | 17.60 | 15.24 |
| 5.01 | 39.28 | 18.00 | 14.99 |
| 5.90 | 44.65 | 18.30 | 14.25 |

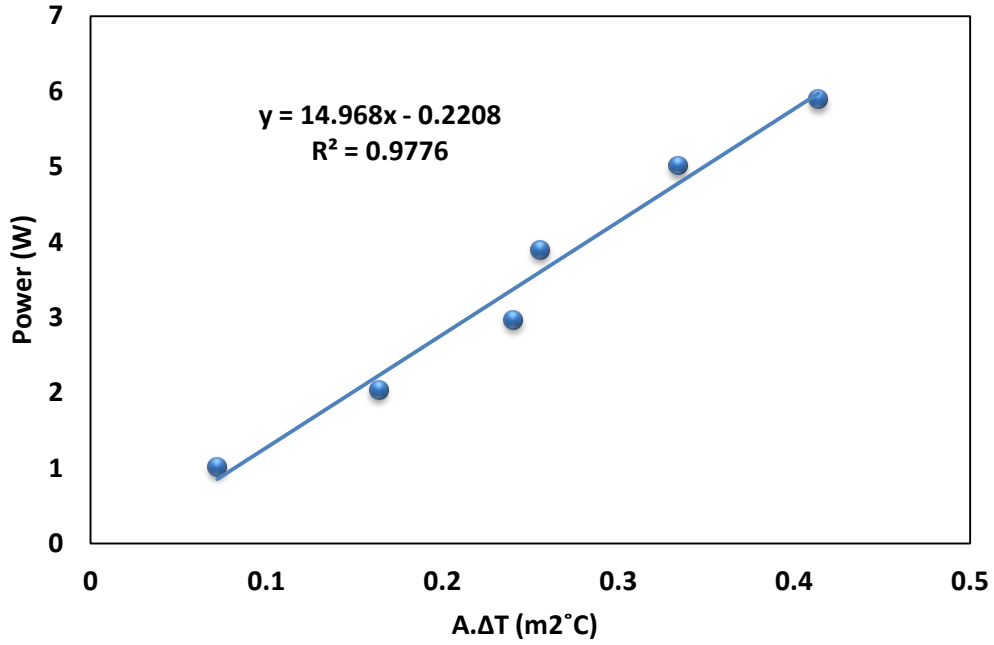


Figure 7-8. Heat input vs. (A. ΔT) for determining the combined convection radiation heat transfer coefficient

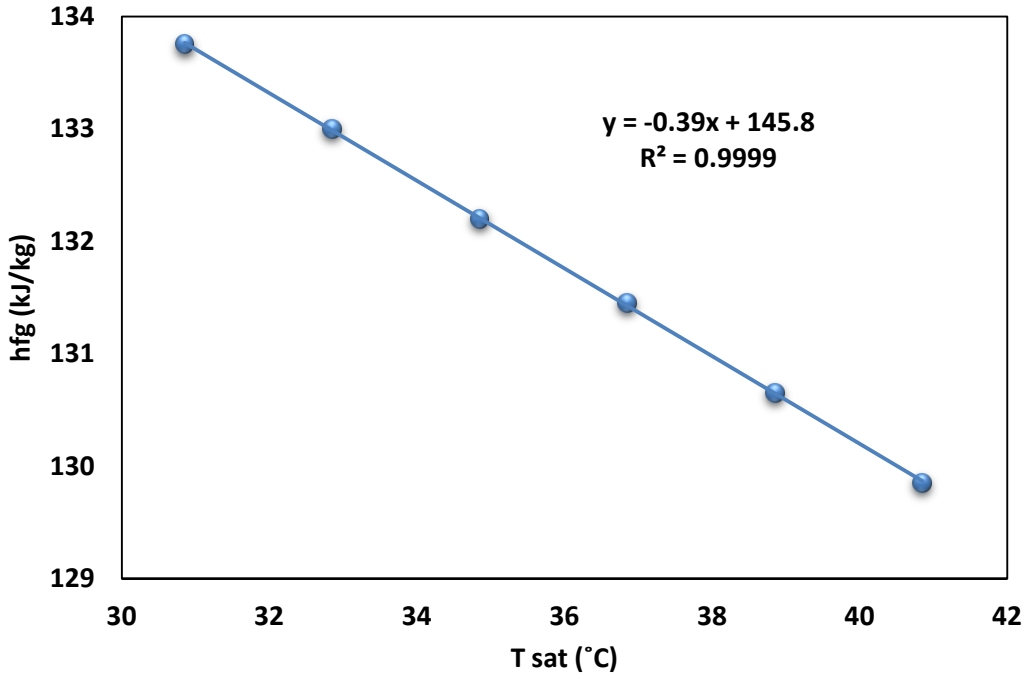


Figure 7-9. Variation of latent heat of vaporisation of HFE7000 with Temperature

# Appendix F Sapphire Properties

F.1: physical properties of sapphire

| Chemical formula | $Al_2 O_3$ |
|---|---|
| Crystal class | Hexagonal system, rhomboidal class 3 m |
| Lattice constants, A | a=4.785, c=12.991 |
| Density, $g/cm^3$ | 3.98 |
| Hardness | 2000 with 2000 gidenter (Knoop) 9 (Mohs) |
| Optical transmission range, μm | 0.17 - 5.5 |
| Refractive index at 0.532 μm | $n_o$ =1.7717, $n_e$ =1.76355 |
| Water absorption | nil |
| Young Modulus, Gpa | 345 |
| Shear Modulus, Gpa | 145 |
| Bulk Modulus, Gpa | 240 |
| Bending Modulus (Modulus of Rupture), Mpa | 420 at 20 ºC280 at 500ºC |
| Elastic Coefficient | C11=496, C12=164, C13=115 C33=498, C44=148 |

F. 2: Thermal properties of sapphire

| Melting point, K | 2303 |
|---|---|
| Specific heat, J/(kg x K) | 105 at 91K 761 at 291K |
| Thermal coefficient of linear expansion, K-1, at 323K | 5.66 x 10-6 parallel to optical axis 5 x 10-6 perpendicular to optical axis |
| Thermal conductivity, W/(m x K) at 300K | 23.1 parallel to optical axis 25.2 perpendicular to optical axis |

Source: Tydex, Domostroitelnaya str. 16, 194292 St.Peterburg, Russia